IRE
Transactions
on ANTENNAS and PROPAGATION

Volume AP-8 MAY, 1960 Number 3

Published Bimonthly

In This Issue

PUBLISHED BY THE
rofessional Group on Antennas and Propagation

IRE TRANSACTIONS® PGAP IS A PUBLICATION DEVOTED TO EXPERIMENTAL AND THEORETICAL PAPERS ON RADIO ANTENNAS, ON GUIDED OR UNGUIDED PROPAGATION OF RADIO WAVES, AND ON ALLIED FIELDS OF RADIO PHYSICS SUCH AS RADIO ASTRONOMY

MANUSCRIPTS should be submitted to Sidney A. Bowhill, Editor, 222 Electrical Engineering, Pennsylvania State University, University Park, Pa. Manuscripts should be original typewritten copy, double spaced, plus one carbon copy and two sets of copies of illustrations. Original illustrations will be called for if the paper is accepted. References should appear as footnotes and include author's name, title, journal, volume, initial and final page numbers, and date. Each paper must have a summary of not more than 200 words. News items concerning PGAP members and group activities should be sent to the News Editor, R. C. Hansen, Space Technology Laboratories, P.O. Box 95001, Los Angeles 45, Calif.

ORIGINAL ILLUSTRATIONS should be submitted as follows: All line drawings (graphs, charts, block diagrams, cutaways, etc.) should be inked uniformly and ready for reproduction. If commercially printed grids are used in graph drawings, author should be sure printer's ink is of a color that will reproduce. All halftone illustrations (photographs, wash, airbrush, or pencil renderings, etc.) should be clean and ready to reproduce. Photographs should be glossy prints. Call-outs or labels should be marked on a registered tissue overlay, not on the illustration itself. No illustration should be larger than 8 x 10 inches.

Copies can be purchased from **THE INSTITUTE OF RADIO ENGINEERS, 1 East 79 St., New York 21, N.Y. PRICE PER COPY:** members of the Professional Group on Antennas and Propagation, $2.80; members of the IRE $3.45; nonmembers, $6.90. **ANNUAL SUBSCRIPTION PRICE:** PGAP members, included in PGAP fee of $4.00; IRE members, $8.50; Colleges and public libraries, $10.00; nonmembers, $17.00. IRE TRANSACTIONS ON ANTENNAS AND PROPAGATION. Printed in U.S.A. Published by George Banta Co., Inc., Curtis Plaza, Menasha, Wisconsin.

Second-class postage paid at MENASHA, WISCONSIN, and additional mailing offices under the act of August 24, 1912. Acceptance for mailing at a special rate of postage is provided for in the act of February 28, 1925, embodied in Paragraph 4, Section 412, P. L. & R., authorized October 26, 1927.

IRE Transactions on Antennas and Propagation

Volume AP-8 MAY, 1960 Number 3

TABLE OF CONTENTS

Editorial Comment

"TO PUBLISH or not to publish . . . ": this is a question which editors must continually answer regarding material submitted to them. However, it is also a question which every research worker asks himself, at one time or another. Only when the question is answered in the affirmative does the result find its way to an editor's desk. Publication of an article in a journal carries with it a high measure of professional prestige; yet many workers are only imperfectly aware of what constitutes publishable material. This is especially the case if they happen to be working in an environment where publication in a professional journal is not a normal method for disseminating results. In this editorial, some of the motives for publication are discussed, in the hope that one or two new authors may be prompted to venture into publication.

Whether or not a researcher immediately thinks about publishing a completed piece of work depends on his research situation. In modern jargon, one may classify research as "publication-oriented" or as "result-oriented." Nearly all classifications of this kind are misleading; for instance, this arbitrary division is not the same as that between pure and applied research. "Publication-oriented" research is undertaken after a study of all prior publications in that particular field, and has publication of the results as the avowed end-product of the program. "Result-oriented" research, on the other hand, is undertaken primarily for some commercial or military end, and publication of the results is a by-product which is not essential to the main purpose of the work at hand. There are, of course, various intermediate stages between these two classifications; however, they will be retained, because the problems confronting the aspiring author differ in the two cases.

In publication-oriented research, the worker selects, or has selected for him, a field which is believed to be on the "frontier of knowledge" as delineated by the work published in the field as of that time. Finding where this frontier is, in the complicated n-dimensional space represented by knowledge, is not an easy matter. Having completed a piece of publication-oriented research, the worker is frequently unsure in his own mind whether his final results lie inside the frontier, and therefore add nothing new; whether they lie outside, and merit immediate publication; or whether, more subtly, the results are new but so specialized that no one else would be interested in them. We ourselves have experienced this dilemma in a particularly acute form. Some work which we had left unpublished, thinking it to be of little interest, was found to be closely related to a later publication by another individual (who, be it said, made full acknowledgment to the previous results). In discussion of this matter, he expressed a view which we believe to be the correct one: "Well, we waited and waited and you never put your work into print, so we went ahead and published our own version. It's always safer to publish everything." "Everything?" we asked. "Well, everything of interest, which is related to someone else's current work, or to something already published." Of course, there is occasionally the stunning new discovery which cries out for publication, however unrelated it may be to previously published material.

Under some circumstances, for example, at some universities, publication in a professional journal is raised to the level of a fetish. A recent study[1] has uncovered the interesting fact that university professors are frequently hired on the strength of the number of publications which stand in their name, although their professional activity may lie entirely in the field of teaching. It also cites instances of a highly competent educational staff being discharged through failure to publish regularly. There is, however, no doubt that carrying out and publishing scientific work is an index of intellectual activity; here perhaps the universities have the rights of the matter.

The researcher in a result-oriented field is in a difficult situation, particularly if he is inexperienced in the writing of technical papers. He has probably written several reports, circulated inside his organization, in which he has described the results of his work and how he obtained them. He feels he would like to publish his results in the form of a paper, and knows that some different type of approach is called for, but perhaps does not know exactly what that approach should be. Under these circumstances, his best plan is to contact some person who is outstanding in the particular field and has many publications already issued under his name, and ask his frank opinion. It is almost unknown for an approach of this kind to be rebuffed. Alternatively, he may wish to put his results in the form of a paper, modeling his approach on other published papers, and then submit the paper for publication to a journal. Part of the function of the reviewing procedure of any reputable journal is the constructive criticism of papers submitted. These are then returned to the author with the reviewers' comments, and the author is asked to revise his paper and resubmit it.

This process of writing, criticism, and rewriting is the most satisfactory procedure we know for a new author to "break the publication barrier." It certainly takes time and effort, but having one's results appear in printed form is, in the end, the greatest reward that research has to offer.

[1] T. Caplow and R. J. McGee, "The Academic Market Place," Basic Books, 1959.

contributions

Propagation at 36,000 MC in the Los Angeles Basin*

W. L. FLOCK†, R. C. MACKEY†, AND W. D. HERSHBERGER†

Summary—**Fading characteristics at 36 kmc over a line-of-sight path in the Los Angeles basin have been shown to be closely correlated with meteorological conditions, particularly with the relatively persistent, low-level temperature inversion of the area. No positive evidence of the influence of atmospheric pollutants has been found, but it has been shown that suitably located microwave paths can be of value for locating and monitoring temperature inversions when they are accompanied by sufficient variation in water-vapor content. The relation of diurnal variations in propagation characteristics to diurnal variations in the temperature inversion and in atmospheric turbulence indicate that the refraction mechanism is the predominant one in causing the observed large fading amplitudes. The view is further strengthened by the relatively noncritical relation of fading to the proximity of the inversion layer.**

Introduction

MICROWAVE propagation studies, at a frequency of approximately 36,000 mc, have been carried out in the Los Angeles Basin. The basin is characterized by the presence of the relatively persistent, low-level temperature inversion of the eastern edge of the Pacific anticyclone, and this inversion is responsible for the trapping of atmospheric pollutants. The index of refraction profile associated with the temperature inversion strongly influences microwave propagation. An 11.4-mile path from the City Hall to the University of California, Los Angeles campus, was set and used for obtaining experimental data. Operation was carried out during certain periods in 1956, 1957, and 1958.

The purpose of the investigation was to study the influences of meteorological factors and atmospheric pollutants on propagation and, conversely, to see if propagation studies could provide information about meteorological conditions and associated atmospheric pollution. Attention was primarily concentrated on the role of the inversion layer.

The Transmission System

The transmitter for the propagation studies was installed on the twenty-fourth floor of the Los Angeles City Hall, and the receiver was located on the roof of the Physics-Biology building of the University of California, Los Angeles. QK 292 klystrons were used for both the transmitter and the local oscillator of the receiver. The transmitting and receiving antennas were identical horns with apertures of 12 inches by 12 inches and with dielectric lenses. The measured antenna gains were 39 db. The transmitted power was in the order of 10 milliwatts.

The elevation of the transmitting antenna was 590 feet, and that of the receiving antenna was 500 feet. The path was a good optical path and provided adequate clearance of all obstructions, even after the construction of a large building near the transmitting site during the course of the study. The path is indicated by a dashed line in the upper left portion of Fig. 1.

* Manuscript received by the PGAP, June 25, 1959; revised manuscript received January 14, 1960. This work was supported in part by the State of California, through an Air Pollution Grant to the Dept. of Engrg.

† Dept. of Eng., University of California, Los Angeles.

Fig. 1—Map of Los Angeles Basin showing transmitter and receiver sites.

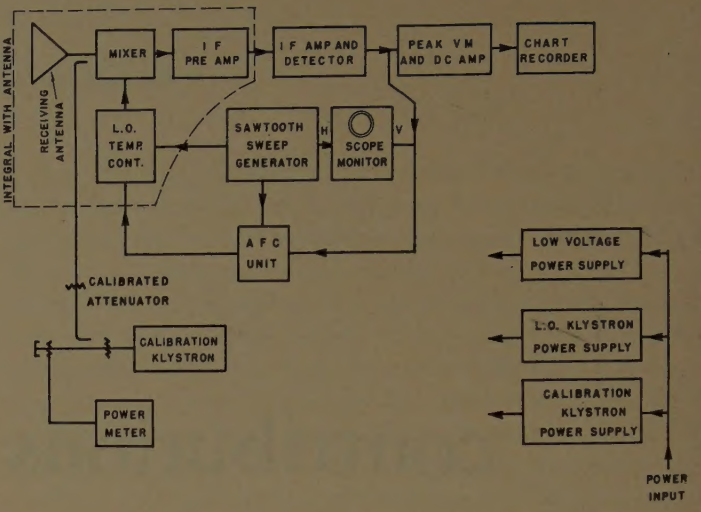

Fig. 2—8.6-mm microwave receiver.

The transmitter klystron of the system was operated at a constant frequency, while the local oscillator of the receiver was swept in frequency at a rate of 60 cps by a saw-tooth voltage waveform. This mode of operation provided a pulse whenever the difference between the incoming signal frequency and the local oscillator frequency was in the pass-band of the IF amplifier. A dc voltage proportional to the amplitude of the pulses was then obtained, and the dc voltage was applied to a recorder. A block diagram of the receiver is shown in Fig. 2. Additional details of the system are described elsewhere.[1]

The Temperature Inversion of the Los Angeles Basin[2,3]

The temperature inversion of the California coast is a subsidence inversion associated with the eastern edge of the Pacific anticyclone. Beneath the inversion there is a layer of moist marine air, while above the inversion there is a deep layer of much drier, warmer air. The mean depth of the marine layer is about 1500 feet along the southern California coastline, but there is considerable variation from near zero to three or four thousand feet. The inversion extends westward to the region of Hawaii, but becomes weaker and higher to the west. In the vicinity of Hawaii the average height is approximately 6000 feet. The temperature inversion along the California coast tends to be the lowest and most persistent in the late summer and autumn, but can be present at any time of the year, except when destroyed by cyclonic storms.

At times winds from the interior sweep the marine layer to sea and replace it with warm, dry, desert air. A temperature inversion may also result under these conditions. Strong winds from the interior provide adequate ventilation for the Los Angeles basin, but bad air pollution conditions may occur under conditions of weak interior winds. In any case there is a relatively small variation in index of refraction in the vertical profile, as contrasted to the situation when the marine layer is present.

Propagation Characteristics

Relation to Temperature Inversion

Fading ranges on the City Hall-UCLA path were generally small (as low as 0.5 db and less) when no temperature inversion was present or when the elevation of the temperature inversion was greater than approximately 900 feet. (The elevation of the transmitting antenna was 590 feet, that of the receiving antenna was 500 feet, and the length of the path was 11.4 miles.) When the temperature inversion started at the surface or at elevations less than 900 feet, large fading ranges were frequently observed. (The system was capable of measuring fading ranges ≤ 30 db, and fading ranges as great as 30 db were noted.)

At times, especially during days of bad smog attacks, fading was severe throughout the day. More commonly a diurnal variation was prominent. In such a case the fading range was usually rather large throughout the night and small during the middle of the day. Maximum fading ranges frequently occurred in the early morning or late afternoon hours.

The elevation of the inversion was given approximately by radiosonde data supplied by the U. S. Weather Bureau from Clover Field, Santa Monica. This field is located approximately four miles south of the UCLA terminal of the path. The height and profile of the tem-

[1] W. L. Flock, R. C. Mackey, and W. D. Hershberger, "Propagation at 36,000 Megacycles in the Los Angeles Basin," Dept. of Engrg., Univ. of Calif., Los Angeles, Rept. 58-14; February, 1958.

[2] M. Neiburger and J. Edinger, "Meteorology of the Los Angeles Basin," Air Pollution Foundation, Los Angeles, Calif., Rept. No. 1; April, 1954.

[3] J. G. Edinger, "The Meteorology of Los Angeles' Polluted Layer," Dept. of Meteorology, Univ. of Calif., Los Angeles, Final Rept. for Los Angeles County Air Pollution Control Dist.; January, 1958.

perature inversion varies with distance and time, but the Santa Monica soundings are representative of conditions along the path to the degree that rather good correlation with propagation was observed. Furthermore, information provided by the Department of Meteorology, University of California, Los Angeles, shows that near the coast the elevation of the inversion is normally less than or equal to the elevation at inland stations. Thus the Santa Monica soundings place a lower bound on the inversion height at inland points.

An additional means of estimating the height of the inversion is sometimes available. It is provided by the afternoon sea breeze which frequently clears pollutants from beneath the inversion layer near the coast. This may result in the appearance of a sharp line on the horizon, looking inland, between clear air above and polluted air beneath the inversion. The sharp line represents the base of the temperature inversion. On an afternoon when fading over a 30-db range was observed (4 P.M., November 16, 1956), the sharp line appeared to be extremely close to the top of City Hall where the transmitter was located. On other occasions when the inversion base appeared to be higher above the City Hall, smaller, but still moderately large, fading ranges (*e.g.*, 2 to 4 db) were observed.

Further study of the meteorological data reveals a diurnal variation which corresponds well with the diurnal variation in propagation conditions. In general the inversion weakens and tilts upward in the inland direction during the middle of the day. Edinger[3] reports that in July 1957 determinations, the average height of the inversion near City Hall was approximately 100 feet above that at UCLA at 9 A.M., whereas at 11 A.M. and 12 Noon the corresponding average figure was near 550 feet. By 4 P.M. the differential had dropped to 150 feet.

It is, of course, the index of refraction profile associated with the temperature inversion which actually influences propagation. Normally the air under the inversion is relatively moist, and that above it is dry. A drop of up to 70 N units in index of refraction may be encountered in upward passage through the inversion. (The value of an N unit is 10^{-6}.) The index of refraction profile may be computed from radiosonde data, although it is to be expected that radiosonde data will not correctly indicate the sharpness of the drop. Microwave refractometer data can be expected to be much more satisfactory in this respect. The Naval Missile Air Test Center at Point Mugu, California, has carried out a program of microwave refractometer measurements,[4] and conditions in the Los Angeles area should be somewhat similar.

During the day the drop in index of refraction associated with the inversion layer frequently decreases to one-half and less of the value during the night. This factor helps to explain the tendency towards small fading ranges in the middle of the day. In fact since the tendency towards "steady" operation during the middle of the day is also characteristic of propagation on various commercial microwave paths in the area the weakening of the inversion would appear to be generally as important or more important than the elevation changes.

On occasion, particularly in the autumn when winds come from inland directions, the fading range was small at all times of the day even when a temperature inversion was present. This condition is explained by the small variation in index of refraction on such occasions of low humidity.

Table I gives some representative data showing fading range as related to inversion conditions. Samples of chart records appear in Figs. 3 through 10 (next page).

TABLE I

SELECTED DATA ILLUSTRATING CITY-HALL-UCLA MICROWAVE LINK OPERATION FALL 1956

No.	Date	Hour	Fading Range—db	Inv. Height*
1	9–13	7 P.M.	3	459
2	9–14	1 A.M.	6.6	Surf
3	9–14	7 A.M.	13	Surf
4	9–14	1 P.M.	3	381
5	9–14	7 P.M.	4	Surf
6	9–15	7 P.M.	6.6	Surf
7	9–17	7 P.M.	15	Surf
8	9–20	7 A.M.	0.6	1378
9	9–26	7 A.M.	5.6	Surf
10	9–27	7 A.M.	15	Surf
11	9–28	7 A.M.	15	Surf
12	10–1	7 A.M.	0.5	2329
13	10–2	7 A.M.	1	4856
14	10–4	7 A.M.	0.3	None
15	10–5	7 A.M.	0.4	None
16	10–8	7 A.M.	1	1903
17	10–9	7 A.M.	12	Surf
18	10–10	7 A.M.	10	Surf
19	10–11	7 A.M.	0.4	4003
20	10–15	7 A.M.	3	660
21	10–18	7 A.M.	0.5	2329
22	10–19	7 A.M.	0.2	2231
23	10–22	7 A.M.	3	886
24	10–23	7 A.M.	0.5	None
25	10–24	7 A.M.	0.6	5348
26	10–25	7 A.M.	2	Surf
27	10–26	7 A.M.	7	Surf
28	11–13	7 A.M.	0.2	2297
29	11–14	7 A.M.	0.5	Surf
30	11–15	7 A.M.	1.2	564
31	11–16	7 A.M.	0.5	Surf
32	11–19	7 A.M.	0.5	Surf
33	11–20	7 A.M.	0.5	Surf
34	11–27	7 A.M.	0.5	Surf

* Inversion height at Clover Field, Santa Monica, as given by radiosonde data.

Notes:

1) The index of refraction profile is highly variable and unsuitable for description in a table. However an idea of order of magnitude can be gained by noting that for entries 1–5 the variation through the inversion layer was 53 to 70 N units. On the other hand entry 33 was for a day when the relative humidity was 16 per cent and the variation in *N* units was approximately 10.
2) The above data are from chart records. The signal was also monitored by an oscilloscope, and the 30 db fading range reported for November 16, 1956, for example, was from an oscilloscope observation. The time constant of the recorder was a limiting factor in the chart records, so the above figures are in some cases, particularly for large fading ranges, minimum figures.

[4] T. R. Carr, *et al.*, Tropospheric Propagation Study Reports for 1955, 1956, and 1957, U. S. Naval Air Missile Test Ctr., Point Mugu, Calif.

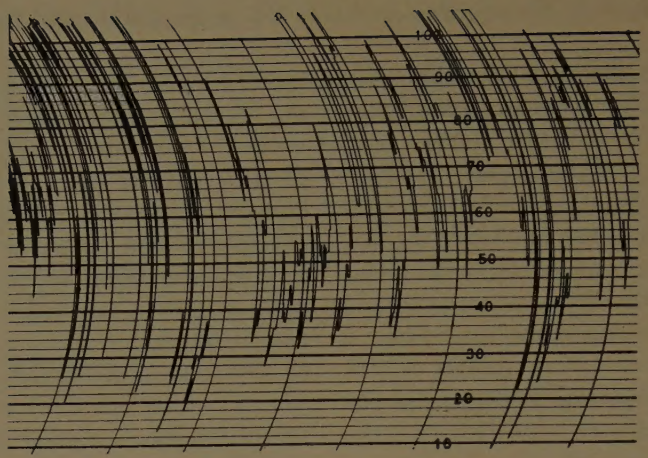

Fig. 3—Portion of 24-hour record showing large amplitudes of fading, September 14, 1956. (One horizontal division represents 15 minutes.)

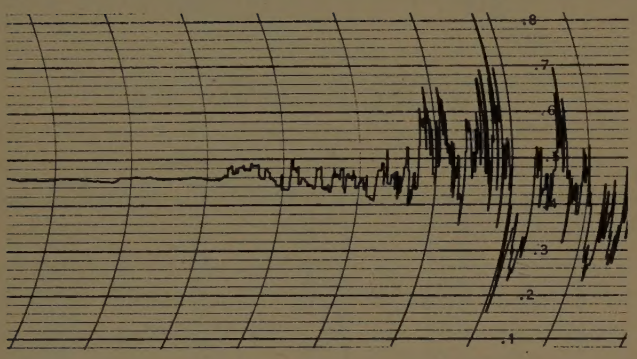

Fig. 4—Portion of 24-hour record showing transition from relatively large fading amplitude to steady signal operation, April 4, 1956. (One horizontal division represents 15 minutes, small fading range commences at approximately 8:30 A.M.)

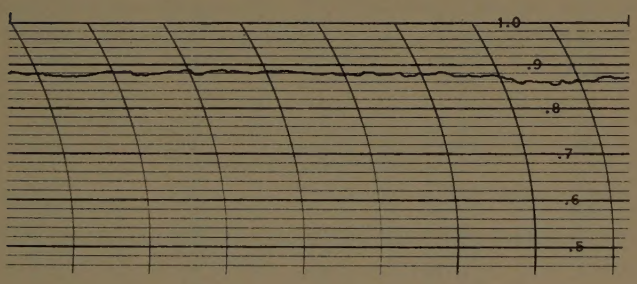

Fig. 5—Portion of 24-hour record showing small fading range, April 8, 1956. (One horizontal division represents 15 minutes.)

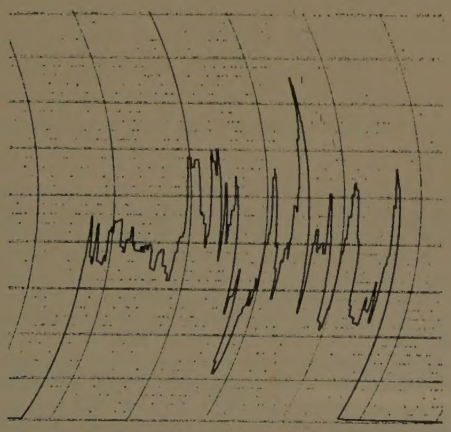

Fig. 6—One-hour record, 7:00 A.M., October 10, 1956, showing large fading range with periods in order of five minutes. (One horizontal division represents 15 minutes.)

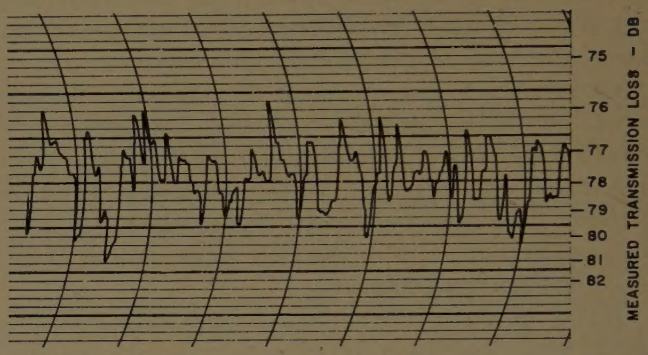

Fig. 7—Record showing moderately-large fading range, 4:00 P.M., August 14, 1957. (One horizontal division represents 18 seconds.)

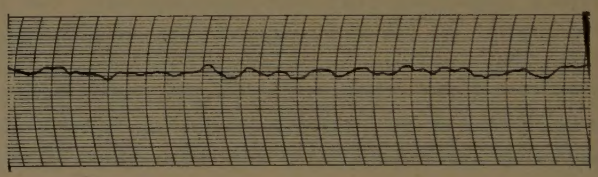

Fig. 8—Signal scintillation during cyclonic storm, no precipitation along path, April 3, 1958. (One horizontal division represents 1 second, fading range approximately 0.5 db.)

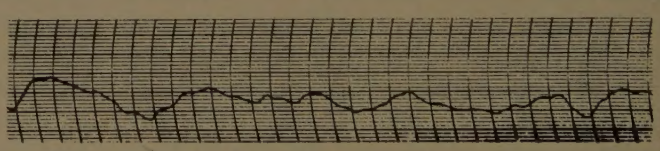

Fig. 9—Fading pattern, September 13, 1957. (One horizontal division represents 1 second, fading range approximately 3.6 db.)

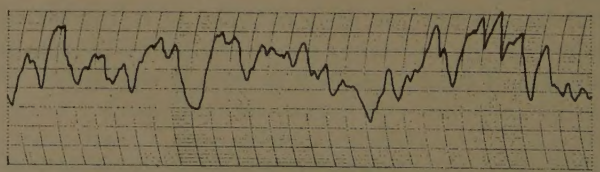

Fig. 10—Fading pattern, April 15, 1958. (One horizontal division represents 1 second, fading range approximately 7 db.)

Records were originally taken for 24-hour intervals with a 2.5-second time constant in the receiver detecting circuit and with an Esterline-Angus recorder operating at a speed of 3 inches per hour. To obtain more detail the recorder was operated at a rated speed of 3 inches per minute with a receiver time constant of 0.1 second. With this operation, response was limited by the recorder characteristics, so later records were taken with a Brush recorder and the 0.1 second time-constant circuit in the receiver. It is the latter type of short-duration record whose spectrum was determined.

Noninversion Conditions

During the cyclonic storms of winter and during strong winds, small fading ranges were observed, except for attenuation due to precipitation. The expected high attenuation during rainfall was noted. Cyclonic storms destroy the inversion condition and provide clean air for Los Angeles. In general, however, the inversion condition is only temporarily destroyed and may return with the passage of the storm.

On occasion a signal scintillation with a fairly regular period in the order of 2 seconds was observed during periods of cyclonic storms. Such a condition is shown in Fig. 8.

Relation to Atmospheric Pollutants

It has been conjectured that the presence of atmospheric pollutants might have a noticeable influence on propagation. In particular, it has been suspected that some absorption of energy might be detectable. Such absorption, however, would be difficult to measure under the fading conditions normally associated with a strong concentration of pollutants. No positive evidence of the influence of atmospheric pollutants has been obtained.

It has been shown, however, that appropriately located microwave links could be of value in locating and monitoring inversion conditions, when the inversion is accompanied by sufficient variation in moisture content.

Spectra of Fading

Visual examination of records indicates prominent periods in the range from 5 minutes to the order of seconds in various records. Spectra of two representative portions of a typical record showing higher-frequency variations were computed by the staff of the Radio Propagation Engineering Division, National Bureau of Standards, Boulder, Colorado, and are shown in Fig. 11. The spectra show significant energy content in a higher-frequency range than in 8.6 mm spectra reported by the University of Texas for Texas and Colorado locations.[5]

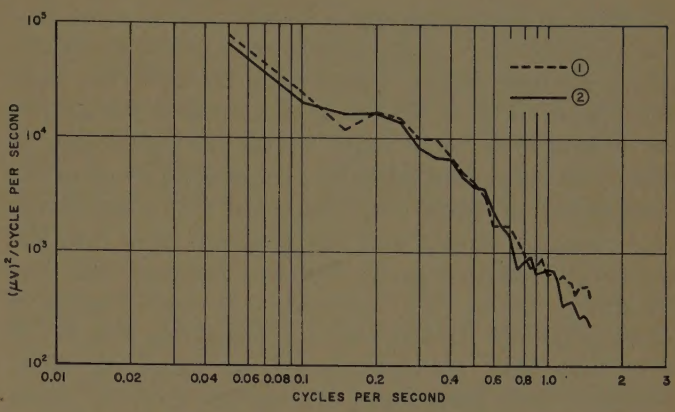

Fig. 11—Spectrum of fading, April 10, 1958. (Computed by staff of Radio Propagation Engineering Division, National Bureau of Standards, Boulder, Colorado.)

Spectra for overwater propagation in the Gulf of Mexico also determined at the University of Texas,[6] were more nearly comparable with those obtained from the Los Angeles data. It is also of interest to note that the fading ranges observed in the California operations were generally greater, for the same distance, than in the Texas and Colorado studies. On the other hand, fading ranges were more nearly comparable for overwater propagation in the Gulf of Mexico and for propagation in the presence of the inversion layer of the Los Angeles basin.

Microwave Refractometer Data

In June, 1958, microwave refractometer data were taken at the receiving terminal of the City Hall-UCLA link using a refractometer loaned by Dr. C. M. Crain. The typical 24 hour record showed very small fluctuations in index of refraction during the night, with 1-6 N fluctuations during the daytime. The average index of refraction increased considerably during the night with respect to daytime values. Only limited propagation tests were carried out during this period, but signal fading was observed to be small during the daytime hours. The diurnal variation in turbulence, indicated by the refractometer, appears to generally bear an inverse relationship to the diurnal variation in fading. Examples of refractometer records are shown in Fig. 12, next page.

Propagation Mechanisms

The large amplitudes of fading observed on the City Hall-UCLA link can be explained on the basis of multipath operation involving the refraction mechanism. This mechanism fits in well with diurnal variations in meteorological conditions and with the relatively noncritical relationship of fading to inversion height.

Scattering due to atmospheric turbulence may be responsible for some of the observed fading, particularly in the presence of cyclonic storms. In scattering theory,

[5] C. W. Tolbert, *et al.*, "Propagation Studies at 8.6-Millimeter Wavelength on 3.5-, 7-, and 12-Mile Paths," Elec. Engrg. Res. Lab., University of Texas, Austin, Rept. No. 69, June 26, 1953; also "Propagation of 8.6-Millimeter Radio Waves Over a 50 Mile Path," No. 70, October 30, 1953; also "Amplitude and Phase Difference Fluctuations of 8.6 Mm and 3.2 Cm Radio Waves on Line-of-Sight Path," Rept. No. 78, March 16, 1956.

[6] A. W. Straiton, *et al.*, "Propagation of Millimeter Radio Waves in Low-Level Overwater Ducts," Elec. Engrg. Res. Lab., Univ. of Texas, Austin, Rept. No. 74; October 15, 1954.

however, scattered energy is largely concentrated in a cone having a half angle, θ, of $\lambda/2\pi l_0$ radians where l_0 is a characteristic length. Values from 20 to 500 feet have been reported for l_0. When λ equals 8.6 mm, θ is seen to be an extremely small angle. To see the significance of this small value for θ, consider a simplified picture of the atmosphere in which a marine layer, with a uniformly high moisture content and with a normal lapse rate, lies below an inversion layer. Further, consider that the boundary between the marine and inversion layers is sharply defined. Atmospheric systems of this type of the California coast are characterized by a high degree of stability, but, particularly during the daytime when there is heating due to solar radiation, there is some mixing between the moist air of the marine layer and the drier air above. The mixing can be expected to be the greatest at the boundary between the marine layer and the inversion layer (that is, at the base of the inversion layer), and conditions for scattering due to atmospheric turbulence can be expected to be much more favorable in the close vicinity of the boundary than elsewhere in space. Therefore, remembering the small value of θ it would appear that a line-of-sight path would have to lie very close to the boundary for the scattering mechanism to be responsible for fading ranges much greater than those for paths far removed from the boundary. With a given fixed path, a highly critical relationship between fading and inversion height is thus implied.

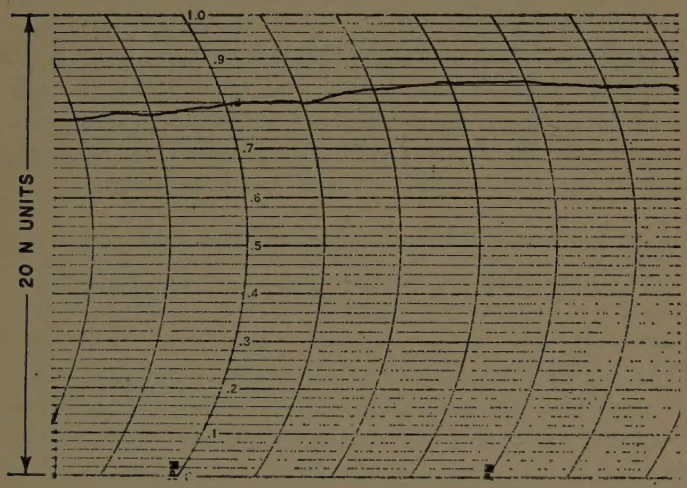

(a)

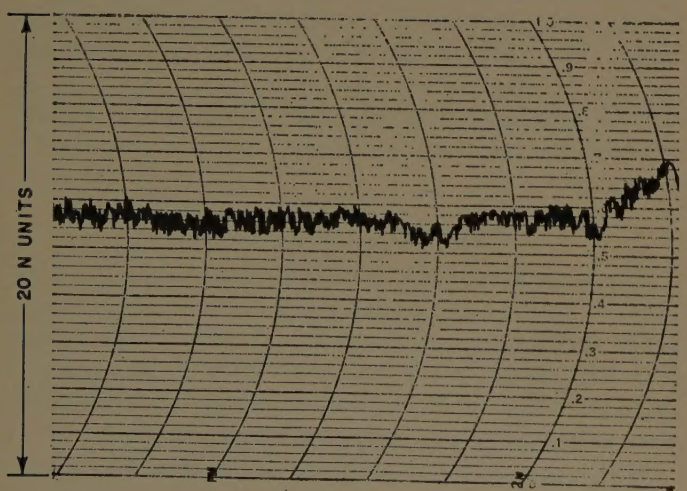

(b)

Fig. 12—Samples of index of refraction records. (a) Approximately 8:20 P.M. to 10:20 P.M., June 4, 1958. (b) Approximately 11:45 A.M. to 1:45 P.M., June 5, 1958.

In the case of the refraction mechanism, however, the relationship between fading and inversion height is not as critical as indicated in the preceding paragraph. The situation can be analyzed by reference to Fig. 13 and (1).

$$x(y) \cong \int_0^y \frac{dy}{\sqrt{\alpha_0^2 - 2[n_0 - n(y)]}}. \qquad (1)$$

This expression gives the horizontal projection, x, of a ray path, as a function of height, y, for an initial angle, α_0, with respect to the horizontal.[7] The integration can be accomplished if n is assumed to have a constant value n_0 below the temperature inversion layer AA_1, and to decrease linearly within the inversion layer. The assumed variation of n is shown by Fig. 14 and (2).

[7] D. E. Kerr, "Propagation of Short Radio Waves," McGraw-Hill Book Co., Inc., New York, N. Y., p. 48; 1951.

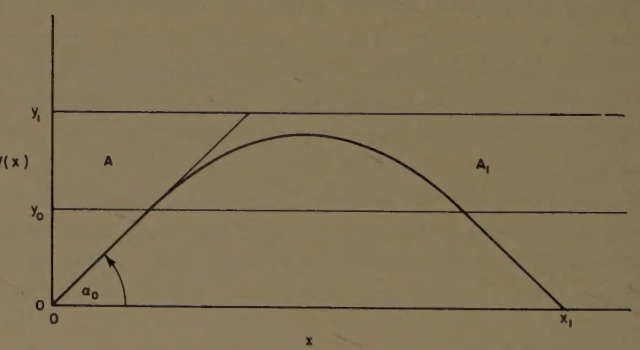

Fig. 13—Simplified picture of ray path in presence of temperature inversion.

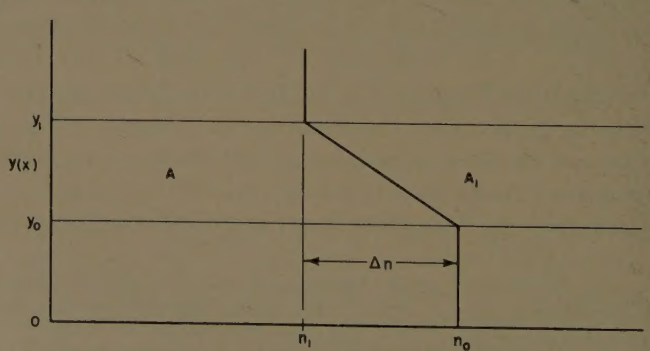

Fig. 14—Assumed variation of n with height.

$$n = n_0, \qquad 0 < y < y_0$$

$$n = n_0 - \frac{\Delta n}{t}(y - y_0), \qquad y_0 < y < y_1$$

$$n = n_1, \qquad y_1 < y < \infty$$

$$\Delta n = n_0 - n_1, \qquad t = y_1 - y_0. \tag{2}$$

The solution of (1) for $y_0 < y < y_1$ is

$$x = \frac{y_0}{\alpha_0} + \frac{t}{\Delta n}\left[\alpha_0 - \sqrt{\alpha_0^2 - 2\frac{\Delta n}{t}(y - y_0)}\right]. \tag{3}$$

If $\alpha_0^2 < 2\,[n_0 - n(y)]$, it can be seen that expressions (1) and (3) are complex. Reflection will occur for this condition. The critical condition for reflection is $\alpha_0^2 = 2\Delta n\,[n_0 - n(y)]$, or, in (3),

$$\alpha_0^2 = \frac{2\Delta n}{t}(y - y_0).$$

For this critical condition (3) becomes

$$x_m = \frac{y_0}{\alpha_0} + \frac{t}{\Delta n}\alpha_0, \tag{4}$$

where x_m is half the path length for the critical ray. If Δn is taken as 70 N units and the thickness t is estimated as 100 feet, α_0 is calculated to be 0.0118 radian or 0.68°. If x_m is then set at 30,000 feet, or half the path length, y_0 is found to be equal to 154 feet. This is the maximum height that the base of the 70 N inversion layer can be above the path to cause the critical ray to reach the receiving terminal, in the simplified picture considered. If the thickness of the layer were taken as zero, y_0 would be equal to approximately 350 feet, which agrees with the experimental data. A finite thickness must be assumed for the inversion layer, however, so the figure of 350 feet must be doubted. It is still true, however, that the mechanism appears to be less sensitive to the height of the layer than the scattering mechanism.

The combination of a signal which has traveled a curved path, such as shown in Fig. 13, and a signal which has taken a direct path from transmitter to receiver would give a total signal of variable amplitude, since the relative phase of the two component signals would vary in a random fashion. The actual situation, of course, may be more complicated than that depicted, and energy may reach the receiver via several paths. Such phenomena have been described previously in the literature,[8] though not for a frequency of 36,000 mc.

Additional detailed studies are desirable, to more thoroughly define the roles of the various factors possibly influencing propagation. These include reflection, scattering, and absorption. Although propagation beyond the horizon is considerably different in many respects from line-of-sight propagation, it can be expected that line-of-sight experiments can be of assistance in understanding the mechanisms involved in both cases. Suitable experiments under a variety of meteorological conditions, including those of the California coast, should be valuable.

[8] A. B. Crawford and W. C. Jakes, "Selective fading of microwaves," *Bell Sys. Tech. J.*, vol. 31, pp. 68–90, January, 1952; also O. E. DeLange, "Propagation studies at microwave frequencies by means of very short pulses," pp. 91–103.

Two Statistical Models for Radar Terrain Return*

L. M. SPETNER† AND I. KATZ†

Summary—A statistical approach to radar backscattering from terrain is taken in this paper. The normalized radar cross section, σ_0, has been computed for two different terrain models. The value of σ_0 is obtained for both models as a function of grazing angle, θ, and radiation wavelength, λ. The first model is a distribution of isolated independent scatterers such as corner reflectors. For such surfaces a wavelength dependence for σ_0 is obtained, and, depending upon the density of scatterers and their average size, the theoretical results indicate that the local dependence of σ_0 on λ can be as λ^{-6}, λ^{-4} or λ^{-2}. For such surfaces, σ_0 is independent of θ.

Where reflection occurs from specularly reflecting facets on the surface and where the distribution of surface slopes is Gaussian, the θ dependence turns out to be of the form

$$e^{-k \cot^2 \theta/2s_0^2}$$

where s_0 is the standard deviation of the surface-slope distribution. The precise form of σ_0 depends upon the space spectrum of the slopes. Two cases are worked out, one where such a spectrum is flat out to some cutoff, and the other where the space spectrum has a single peak at a particular wave number. In either case, for small enough λ, σ_0 varies as λ^{-2}. As the wavelength becomes large compared to the facet size, the facet no longer behaves as a specular reflector and instead becomes more like an isotropic scatterer.

For any particular wavelength one may expect that the radar return be the result of the addition of two types of backscattering. The large facets will behave as specular-type reflectors, while the smaller facets will act as the isotropic scatterers discussed in the first model.

Introduction

In this paper we shall attempt to formulate a theory to explain radar return from land and sea surfaces. We shall set up models of such surfaces and from these models compute the normalized radar cross section as a function of radiation wavelength and of radar depression angle. Other investigators have treated radar return from sea surfaces, usually with emphasis on very small depression angles. The work of Goldstein represents the pioneering effort in this field and consisted both of experimental investigations and theoretical treatment.[1,2] A later treatment of sea clutter, by Katzin,[3] applies both to small and to large depression angles. In the present paper we shall investigate the normalized radar cross section for both land and sea surfaces over the entire angular range with no particular emphasis on the extremely small angles.

* Manuscript received by the PGAP, July 15, 1959; revised manuscript received, January 9, 1960. This work was supported by the Navy Bureau of Ordnance under Contract NOrd 7386.

† Applied Physics Lab., The Johns Hopkins University, Silver Spring, Md.

[1] H. Goldstein, "Frequency dependence of the properties of sea echo," *Phys. Rev.*, vol. 70, pp. 938–946; December, 1946.

[2] D. E. Kerr, "Propagation of Short Radio Waves," McGraw-Hill Book Co., Inc., New York, N. Y., pp. 481–527; 1951.

[3] M. Katzin, "Mechanisms of radar sea clutter," PROC. IRE, vol. 45, pp. 44–54; January, 1957.

Random-Scatterer Model

We shall assume that the radar return from the earth's surface is composed of the summation of returns from a large number of incoherent independent scatterers. One might think of such a surface as a random array of corner-type reflectors distributed upon a nonreflecting surface. It is conceivable that this model may correspond to a barren rocky surface or perhaps to a city or other built-up cultural areas. The normalized radar cross section from such an array of scatterers, as from any surface, is the scattering cross section per unit surface area. If the scatterers are independent and incoherent then the normalized radar cross section is the product of the density of scatterers per unit area, p_S, and the average radar cross section of a single scatterer σ_1; *i.e.*,

$$\sigma_0 = p_S \sigma_1. \tag{1}$$

Let us now examine (1) to obtain the functional dependence of σ_0 upon the radar depression angle, θ, and the radiation wavelength, λ. It is useful at this point to make a distinction between what we shall call *effective* scatterers and *real* or *physical* scatterers. At sufficiently short wavelengths, the effective scatterers are to be identified with the real scatterers; while at the longer wavelengths an effective scatterer is equivalent to several nearly coherent real scatterers. For sufficiently short wavelengths the average density of effective scatterers on the surface is independent of wavelength. As the wavelength gets longer, neighboring scatterers become more coherent with each other and hence must be grouped as a single scatterer. Thus for long enough wavelength p_S is proportional to λ^{-2}. Let p_0 represent the number of real scatterers per unit area of the surface. Then the density of effective scatterers is given by

$$p_S = \begin{cases} p_0, & \lambda < (C_1/p_0)^{1/2} \\ C_1/\lambda^2, & \lambda > (C_1/p_0)^{1/2}. \end{cases} \tag{2}$$

Here C_1 is a dimensionless constant of the order of unity. At this point in the theory it would be unrealistic to attempt to specify the value of C_1 more precisely.

From the definition of p_S it is easily seen that p_S is independent of θ. Whether or not a scatterer exists is independent of the radar depression angle. The scatterer's reradiation pattern may be a function of θ, but its existence should be independent of θ. Hence we will use (2) to represent both the λ and the θ dependence of p_S.

Let us now examine the wavelength dependence of the average scatterer cross section, σ_1. For wavelengths which are small compared to the dimensions of the scatterer we may think of its scattering action somewhat as follows. The scatterer snatches from the beam an amount of power proportional to its geometrical area. Some of this power is dissipated. The rest of it is scattered. The only part of the scattered power in which we are interested here is that scattered back to the radar. We can now write

$$\sigma_1 = A_S \rho \frac{4\pi A_S}{\lambda^2}, \qquad \lambda \text{ small}, \tag{3}$$

where A_S is the effective area of the scatterer, ρ is its power reflection coefficient which essentially describes how much of the power is not absorbed, and the remaining term in (3) represents the gain of the scatterer as if it were an antenna reradiating back in the direction of the radar. We have written the gain just as one would write it for an ordinary radar dish and have used the same effective area A_S as was used for the determination of the amount of power intercepted by the scatterer. For wavelengths which are very large compared to the scatterer dimensions, however, one would expect a Rayleigh-type scattering, and, in particular, the scattering cross section would be given by

$$\sigma_1 = C_2 v^2/\lambda^4, \qquad \lambda \text{ large}, \tag{4}$$

where v is the volume of the scatterer. The constant C_2 in (4) is expected to be large compared to unity; for example, for the scattering cross section of a small dielectric sphere with large index of refraction one gets an expression for σ_1, as in (4), with a C_2 of approximately 1100.

Eqs. (3) and (4) taken together give the λ dependence of σ_0. For the isotropic-type scatterers discussed in this model, all the parameters appearing in the expressions for σ_0 are independent of θ. Let us arbitrarily denote by λ_0 the wavelength that marks the transition from the applicability of (3) to the applicability of (4). Thus these two equations can be rewritten as

$$\sigma_1 = \begin{cases} A_S \rho \dfrac{4\pi A_S}{\lambda^2}, & \lambda < \lambda_0 \\ C_2 v^2/\lambda^4, & \lambda > \lambda_0. \end{cases} \tag{5}$$

Now let us combine (2) and (5) to obtain the final expression for σ_0. Table I gives the four possible expressions for σ_0 in various wavelength regions. Fig. 1 shows in graphic form the wavelength dependence of σ_0. Note that in Fig. 1 the magnitude of the breakpoint λ_0 can be either greater or smaller than that of the breakpoint $(C_1/p_0)^{1/2}$ and the final curve will still have the same general shape.

TABLE I

	$\lambda < \lambda_0$	$\lambda > \lambda_0$
$\lambda < (C_1/p_0)^{1/2}$	$\sigma_0 = \dfrac{4\pi p_0 \rho A^2_S}{\lambda^2}$	$\sigma_0 = \dfrac{C_2 p_0 v^2}{\lambda^4}$
$\lambda > (C_1/p_0)^{1/2}$	$\sigma_0 = \dfrac{4\pi C_1 \rho A^2_S}{\lambda^4}$	$\sigma_0 = \dfrac{C_1 C_2 v^2}{\lambda^6}$

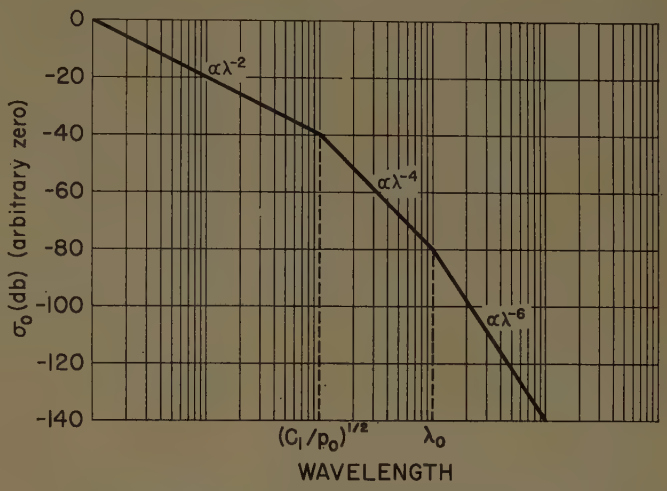

Fig. 1—Wavelength dependence of normalized radar cross section (random scatterer model).

Specular Point Model

Let us now consider another model for a terrain surface. Here we shall assume that the surface is reflecting, is of irregular shape but continuous, and has continuous derivatives. We shall also say that the contribution to the radar return comes predominantly from two sources: the energy which is reflected from large facets of the surface which are oriented perpendicular to the line of sight, and the energy which is scattered isotropically by the small scatterers. Here again we refer to the expression for σ_0 given by (1). In our present case (1) must be modified to take account of the fact that we are dealing with two separate kinds of scatterers. Thus we write

$$\sigma_0 = p_{SS}\sigma_{1S} + p_{SL}\sigma_{1L} \tag{6}$$

where p_{SS} and p_{SL} are, respectively, the scatterer densities for small and large scatterers, and σ_{1S} and σ_{1L} are, respectively, the radar cross sections of small and large scatterers. The first term on the right-hand side of (6) is the same expression we obtained in the previous section for the case of random scatterers, but here it is only valid for large λ.

Let us now concern ourselves with the second term on the right-hand side of (6). The average number of facet-type scatterers per unit area, p_{SL}, is the average density of points on the surface which are oriented normal to the line of sight. We shall call these points specular

points. In order to compute p_{SL} let us write the probability density of the surface slopes as

$$q(z_x, z_y)dz_x dz_y \tag{7}$$

where z represents the height of the surface above some datum plane and where

$$z_x = \partial z/\partial x \quad \text{and} \quad z_y = \partial z/\partial y.$$

In order for a point (x, y) to be a specular point, the slopes z_x and z_y at the point must be such that the surface is normal to the line of sight. We shall represent this condition by

$$z_x = \alpha(x, y),$$
$$z_y = \beta(x, y).$$

Now let us replace the z_x and z_y in (7) by $\alpha(x, y)$ and $\beta(x, y)$. Next replace $dz_x dz_y$ by

$$\begin{vmatrix} \partial z_x/\partial x & \partial z_x/\partial y \\ \partial z_y/\partial x & \partial z_y/\partial y \end{vmatrix} dxdy.$$

Then the probability density of the slopes becomes

$$q[\alpha(x, y), \beta(x, y)] \left| z_{xx}z_{yy} - z_{xy}^2 \right| dxdy, \tag{8}$$

where

$$z_{xx} = \partial^2 z/\partial x^2, \quad z_{xy} = \partial^2 z/\partial x \partial y \quad \text{and} \quad z_{yy} = \partial^2 z/\partial y^2.$$

Eq. (8) is, however, just the probability that in the area, $dzdy$, there is a point where the surface is normal to the line of sight (*i.e.*, there is a specular point) on the condition that the second derivatives are given by the particular values z_{xx}, z_{xy}, and z_{yy}. If it is assumed that these second derivatives of z are statistically independent of the first derivatives, then an average may be taken over the second derivatives to obtain the probability per unit area that a specular point exists. Thus, p_{SL} becomes

$$p_{SL} = \langle \left| z_{xx}z_{yy} - z_{xy}^2 \right| \rangle \, q(\alpha, \beta). \tag{9}$$

One can write α and β as functions of the depression angle as

$$\alpha = z_x = \cot \theta$$
$$\beta = z_y = 0.$$

Eq. (9) can then be written as

$$p_{SL} = \langle \left| z_{xx}z_{yy} - z_{xy}^2 \right| \rangle q(\cot \theta, 0).$$

If z_x and z_y are jointly Gaussian with zero means and with equal variances, s^2, and if they are statistically independent, *i.e.*, if

$$q(z_x, z_y) = \frac{1}{2\pi s^2} \exp\left[-(z_x^2 + z_y^2)/2s^2\right],$$

then p_{SL} becomes

$$p_{SL} = \frac{\langle \left| z_{xx}z_{yy} - z_{xy}^2 \right| \rangle}{2\pi s^2} \exp\left(-\cot^2 \theta/2s^2\right),$$

or

$$p_{SL} = p_{SL}(90°) \exp\left(-\cot^2 \theta/2s^2\right).$$

We must now determine p_{SL} (90°) and σ_{1L} as functions of λ. In order to do this we must make some assumptions about the slope spectrum of the surface. Let us consider first the case of a flat-slope spectrum as shown in Fig. 2. Here the ordinate is in units of (slope)^2/wave number and the abscissa is in units of wave number. We shall define the cutoff of this spectrum as the point $\nu = \lambda_2^{-1}$ as shown in Fig. 2. We must note that p_{SL} (90°) and σ_{1L} depend not only upon the nature of the surface, but also on the wavelength of the radiation.

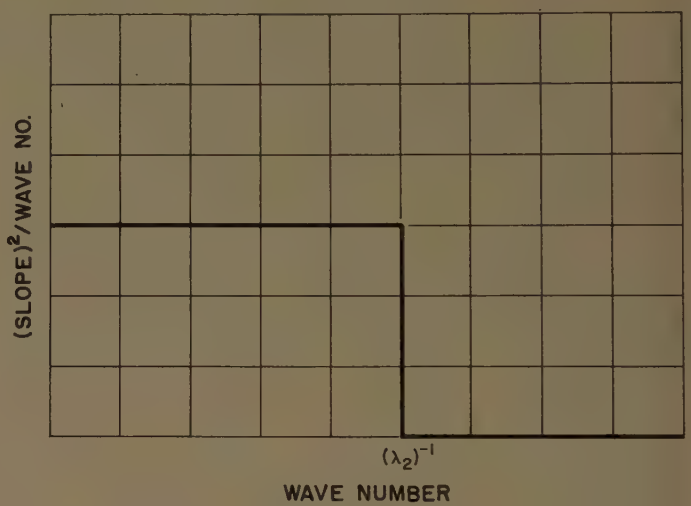

Fig. 2—Flat slope spectrum (one dimensional representation).

Let us define s_0^2 as the variance of the slope measured on the surface; then s^2 must be the *effective* slope variance which depends upon the wavelength. The two quantities s and s_0 may in certain cases be quite different; in particular they will differ when the dimensions of the surface structure are much finer than the wavelength. The effective slope variance must be obtained by first smoothing the surface with a smoothing length of approximately λ and then measuring the variance of the slope of the smoothed surface. Thus it is seen that as the wavelength increases, more facet-type scatterers are lost, but more random-type scatterers are gained. One can see that the effective mean squared slope for the slope spectrum shown in Fig. 2 is given by

$$s^2 = \begin{cases} s_0^2, & \lambda < \lambda_2 \\ s_0^2\lambda_2/\lambda, & \lambda > \lambda_2. \end{cases} \tag{10}$$

The density of horizontal facets, p_{SL} (90°), is, for small wavelengths, proportional to λ_2^{-2}. For wavelengths longer than λ_2, the density of horizontal scatterers is proportional to λ^{-2}. Thus we can say

$$p_{SL}(90°) = \begin{cases} C_3/\lambda_2^2 & \lambda < \lambda_2 \\ C_3/\lambda^2, & \lambda > \lambda_2 \end{cases} \tag{11}$$

where it is expected that the dimensionless number C_3 is of the order of unity. Here we must note that the cutoff wave number λ_2^{-1} defines the fineness of the structure of the surface, and, hence, λ_2 must be related to the size of the scatterer.

Let us now examine the radar cross section of a single facet-type scatterer. This can be handled in a way similar to that in the first model. For facet-type reflections, only those facets which are oriented perpendicular to the line of sight are important in backscattering. In this case, the radar cross section would be expected to have the same form as that for a flat plate, which is also the same as (3). We write

$$\sigma_{1L} = \frac{4\pi A_S \rho}{\lambda^2}, \tag{12}$$

where the symbols have the same meaning as in (3). As the scatterer becomes small compared to a wavelength, the higher-order multipole terms which contribute to its radiation become progressively less significant and in the limit, when λ is very large compared to the size of the scatterer, only the dipole term is of importance and the cross section becomes that normally associated with Rayleigh-type scattering. This type of scatterer has a cross section given by

$$\sigma_{1S} = \frac{C_4 \rho}{\lambda^4}. \tag{13}$$

Thus we see that for the cross section of a single facet, (12) is applicable for small λ and (13) is applicable for large λ. The transition region between the applicability of (12) and (13) corresponds to a value of λ which is related to the size of the scatterer; but this is the role played by λ_2 in (10) and (11). Here too, we shall use the same λ_2 to mark the transitions from (12) to (13). Now we can combine (12) and (13) to obtain

$$\sigma_1 = \begin{cases} 4\pi A_S \rho/\lambda^2, & \lambda < \lambda_2 \\ C_4 \rho/\lambda^4, & \lambda > \lambda_2. \end{cases} \tag{14}$$

We are now prepared to write the final expression for the normalized radar cross section of an irregular reflecting surface having a Gaussian slope distribution and a flat slope spectrum which is sharply cut off at $\nu = \lambda_2^{-1}$.

$$\sigma_0 = \begin{cases} \dfrac{4\pi A_S C_3 \rho}{\lambda_2^2} \dfrac{1}{\lambda^2} e^{(-\cot^2\theta/2s_0^2)}, & \lambda < \lambda_2 \\ \dfrac{C_3 C_4}{\lambda^6} e^{(-\cot^2\theta)\lambda/2s_0^2\lambda^2} + \dfrac{C_5}{\lambda^6}, & \lambda > \lambda_2. \end{cases} \tag{15}$$

The term C_5/λ^6 is the contribution from the small scatterers. In the case where $C_5 > C_3C_4$, the exponential term has a minor effect for $\lambda > \lambda_2$. If, however, $C_5 < C_3C_4$, then over some region of $\lambda > \lambda_2$, the exponential term predominates. For sufficiently large λ, however, σ_0 again goes as C_5/λ^6. Note that in both cases of (15) the θ dependence is situated in the $\cot^2\theta$ term in the exponential.

Fig. 3 shows in graphical form the wavelength dependence of σ_0 for a Gaussian surface having a flat slope spectrum which is sharply cut off at a wave number of λ_2^{-1}. In Fig. 3 we have assumed, for illustrative purposes, that $C_5 < C_3C_4$.

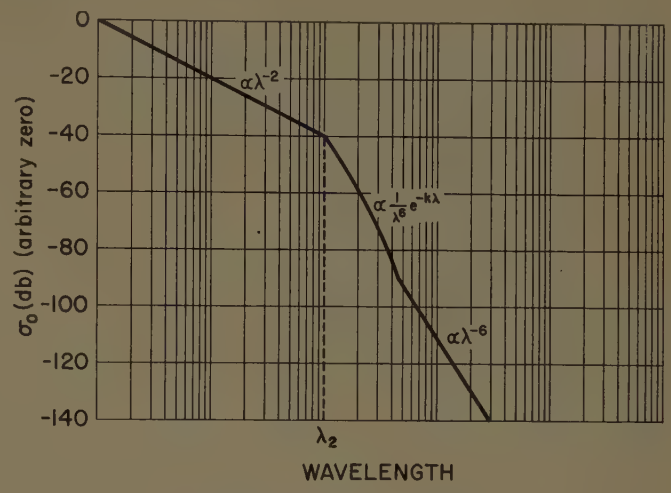

Fig. 3—Wavelength dependence of normalized radar cross section (specular point model).

As a second example of a facet-type surface we examine the case where the slope spectrum has a single sharp peak at a wave number equal to λ_2^{-1}. In this case, for wavelengths greater than λ_2, the entire surface is effectively flat and horizontal. Hence, the average density of horizontal scatterers, for our purposes, is 0.[4] Thus we write the average density of horizontal scatterers as

$$p_{SL}(90°) = \begin{cases} C_6/\lambda_2^2, & \lambda < \lambda_2 \\ 0, & \lambda > \lambda_2, \end{cases}$$

where we have assumed that for wavelengths shorter than λ_2, p_{SL} (90°) is proportional to λ_2^{-2}; the proportionality constant C_6 is of the order of unity. The effective slope variance s^2 is equal to the actual slope variance s_0^2 for wavelengths smaller than λ_2. For wavelengths larger than λ_2, however, the surface is effectively flat as pointed out above. Hence, the effective slope variance is 0. Thus we may write the effective slope variance as

$$s^2 = \begin{cases} s_0^2, & \lambda < \lambda_2 \\ 0, & \lambda > \lambda_2. \end{cases}$$

We find that for the facet-type surface which has a slope spectrum consisting of only one narrow peak the normalized radar cross section is given by

$$\sigma_0 = \begin{cases} \dfrac{4\pi A_S \rho C_6}{\lambda_2^2} \dfrac{1}{\lambda^2} e^{-\cot^2\theta/2s_0^2}, & \lambda < \lambda_2 \\ C_5/\lambda^6 & \lambda > \lambda_2. \end{cases}$$

[4] Taking the density of horizontal scatterers to be 0 for a flat surface gives the correct result for all depression angles other than 90°. For the case of exactly 90°, however, one must drop the assumption of facet reflections and assume instead reflection from a plain mirror; *i.e.*, the concept of σ_0 is no longer applicable.

It is important to note that for this case there may be a sharp drop in σ_0 at $\lambda=\lambda_2$ as it makes the transition from one region to the other. The sharpness of this drop depends upon the magnitude of C_6 and also upon the detailed shape of the spectral peak, which we have, for simplicity, taken here to be an impulse-type function. For any particular shape of spectral peak one could compute in detail the actual transition of the expression for σ_0 from one region of wavelength to the other.

The λ-dependence of σ_0 will be much like that shown in Fig. 3 except that the $\lambda^{-6}e^{-k\lambda}$ portion will not appear.

Note that here too the dependence of σ_0 on depression angle is contained in the $\cot^2\theta$ term in the exponential. Fig. 4 illustrates this θ dependence of σ_0.

It should be remarked that the customary $\sin\theta$ illumination term does not appear in our expressions for σ_0. The reason for this is that the areas used in the calculations of the expressions for σ_0 represent either the areas of facets which are oriented normal to the line of sight or areas containing isolated isotropic scatterers, and it is only from these that radar power is assumed to be returned.

Note that the curves in Fig. 4 have as a parameter s_0, the RMS slope of the surface. It is clear that the rate at which the σ_0 curve falls with decreasing θ depends markedly on the value of s_0. These parameters, as well as other parameters which come into our expressions and which are functions of the surfaces, must be determined by measurement.

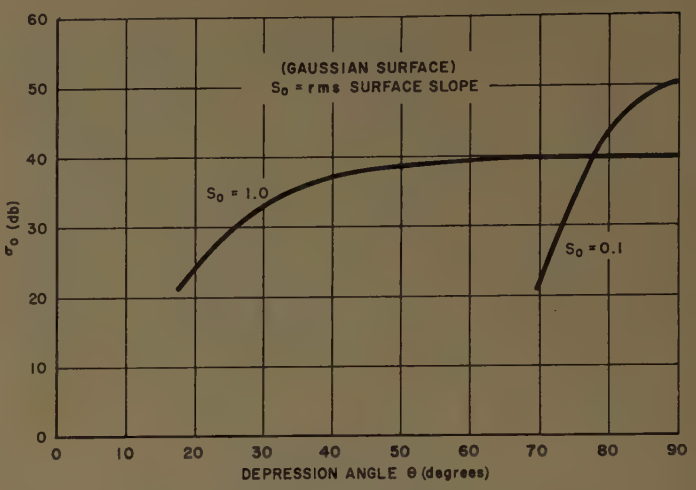

Fig. 4—Depression-angle dependence of radar terrain return (specular point model).

Conclusion

In a study of radar terrain return we have presented two models of a reflecting surface: the first consists of isolated scatterers distributed over a nonreflecting surface and the second is an irregular but continuous reflecting surface. In the latter case we treated two examples of the two dimensional slope spectrum.

No attempt is made here to draw a strict correspondence between these models and actual terrain surfaces. The next logical step is to examine existing experimental data in the light of these models to determine accuracy of the predictions of the λ- and θ-dependence.

Radar Terrain Return Measured at Near-Vertical Incidence*

A. R. EDISON†, R. K. MOORE†, and B. D. WARNER†

Summary—**An experimental program to investigate the reradiation properties of terrain at near-vertical incidence was carried out. Data were obtained at 415 and 3800 mc, using narrow-pulse type radar at altitudes of 2000 to 12,000 feet over many different target areas.**

At frequencies over 400 mc most terrain acts as a scatterer of energy even at near-vertical incidence with a backscattering "radiation pattern" that drops off rapidly as the angle of incidence is increased. An exception occurs for heavily wooded areas which appear as nearly isotropic scatterers.

At 415 mc, the radar cross section per unit area at vertical incidence ranges between values of 0.7 for woods to approximately 4 for city targets, while at 3800 mc, the variation ranges between values of 0.8 for woods to about 18 for some city targets. If the ground were a lossless isotropic scatterer, the radar cross section per unit area would be 2 at vertical incidence.

For a wide beam antenna, the fading range between the level exceeded by 95 per cent of the return pulses and the level exceeded by only 5 per cent of the return pulses is generally between 12 and 17 db, except for a few very smooth areas which give considerable specular (nonfading) type of return and have a smaller fading range.

Introduction

An experimental program was undertaken to investigate the reradiation of electromagnetic energy from terrain at near-vertical incidence.[1] This program set out to determine the effects on the signal

* Manuscript received by the PGAP, February 1, 1960. The experimental program was carried out by the Sandia Corporation. The work reported here was carried out at the University of New Mexico Engineering Experiment Station, sponsored by the Naval Ordnance Test Station, China Lake, California, under Contract N123 (60530) 18138A and was described in Tech. Rept. EE 24.

† Electrical Engrg. Dept., University of New Mexico, Albuquerque, N. M.

[1] R. K. Moore and C. S. Williams, Jr., "Radar terrain return at near-vertical incidence," Proc. IRE, vol. 45, pp. 228–238; February, 1957.

returned to the radar of altitude, terrain, and such parameters of the radar as frequency, antenna pattern, pulse shape and repetition rates. A C-47 aircraft was equipped with 415- and 3800-mc radar gear, appropriate calibration equipment[2] and cameras, and was flown to obtain measurements of radar return from many different "target" areas in the United States.

The results indicate that even at vertical incidence most terrain reradiates toward the radar a large scattered (incoherent) signal and a relatively small specular or coherent component at the frequencies considered. The average radar cross section per unit area σ_0, sometimes called the scattering coefficient, is a function of the angle of incidence for any particular type of terrain. The scattering coefficient was found to decrease fairly rapidly as the angle of incidence was increased (vertical is zero) over smooth areas, fields covered with green vegetation, and over water; heavily wooded areas appeared to be nearly isotropic scatterers. To some extent, the scattering coefficient is also a function of the azimuthal angle, but no attempt was made to determine such dependence. Fresnel (specular) reflection predominates over a limited number of targets, such as smooth water or some desert areas. Typical curves showing the scattering cross section as a function of the angle of incidence are shown.

A lossless terrain with the properties of an isotropic scatterer would have a radar cross section per unit area of 2 for backscatter at vertical incidence. At 415 mc, the values of the scattering coefficient at vertical incidence varied from 0.7 for dense woods to 4 for certain city targets, while at 3800 mc, the variation was from 0.8 for woods to 18 for some city targets. For slightly rough water, the values of the scattering cross section per unit area reached 50 at 415 mc and 200 at 3800 mc for near vertical incidence.

The range of fading (defined here as the range between the level below which only 5 per cent of the return power is found and the level below which 95 per cent is found) varied from about 3 db, for some smooth water surfaces exhibiting principally specular return, to about 19 db for certain nonhomogeneous target areas. At 3800 mc, the average range of fading for all targets was about 16 db, and at 415 mc, about 15 db. The theoretical range of fading for a randomly scattering ground for which the signal amplitudes are Rayleigh distributed is 17.5 db. The range of fading did not appear to be a useful measure of the ratio of power returned by specular reflection to power returned by scattering, except in a gross sense, that is, to separate out those few targets that act almost completely as specular reflectors.

A "path attenuation" factor has been defined as the attenuation in db experienced by the pulse from the time it leaves the transmitting antenna until it returns to the receiving antenna. The "path attenuation" is affected by such factors as the altitude, type of terrain, shape of pulse and antenna pattern and, therefore, is not directly applicable to other situations where one or more of these parameters may be different. The "path attenuations" for several typical target areas are included.

Theoretical Model

A model has been used in which the vector nature of the waves is neglected and the return is resolved into a coherent and an incoherent component.[3] This model will give useful information where linear polarization is involved since the linearly-polarized electromagnetic wave can be completely described in terms of one component of a vector and is therefore essentially scalar in nature. Depolarization by the ground has the same effect on the receiving antenna as absorption, and the effects are lumped together.

The approach has been to assume that the terrain is made up of individual scatterers varying in height about a mean ground level, and that each individual scatterer does not greatly differ in size from the others. The actual return from an individual scattering facet is then divided into a coherent component whose phase is the same as that for return from the mean ground plane at that point and whose amplitude is the average value of all components with such phases and is divided also into another component whose phase and amplitude are determined by the vertical displacement of the facet from the mean ground plane. The first is described as the "specular component" and the second as the "scatter component." The heights of the facets are assumed to be distributed in accordance with a "normal distribution" about the mean ground plane.[4]

An approximate form for the scattering coefficient, whose angular variation might be termed an antenna pattern for the ground, has been derived[5] and can be expressed as

$$\sigma_0(\theta) = \frac{\theta a^2 \csc\theta}{4\pi\sigma^2} \exp\left\{-\frac{a^2}{4\sigma^2}\tan^2\theta\right\} \qquad (1)$$

where

σ_0 is scattering coefficient,
a is horizontal correlation distance for vertical displacements,
σ is standard deviation of vertical displacements,
θ is angle of incidence.

[2] F. J. Janza and R. E. West, "Accurate radar attenuation measurements achieved by inflight calibration," IRE Trans. on Instrumentation, vol. PGI-4, pp. 23–31; October, 1955.

[3] R. K. Moore, "Resolution of Vertical Incidence Radar Return into Random and Specular Components," University of New Mexico, Albuquerque, Engrg. Exp. Stat. Tech. Rept. EE-6; July, 1957.

[4] H. Davies, "The reflection of electromagnetic waves from a rough surface," *J. IEE (London)*, pt. 4, vol. 101, pp. 209–215; August, 1954.

[5] J. A. Cooper, "Comparison of Observed and Calculated Near-Vertical Radar Ground Return Intensities and Fading Spectra," M.S. thesis, University of New Mexico, Albuquerque, also Engrg. Exp. Stat. Tech. Rept. EE-10; May, 1958.

The rough ground has been described by two arbitrary parameters σ and a. The second-order probability distribution of heights above the mean ground plane is so chosen that the corresponding autocorrelation of ground heights as a function of their separation is e^{-r^2/a^2}, where r is the distance between points to be correlated.[4]

The field at the antenna has been divided into a nonfading and a fading component for a rough perfectly conducting ground. The mean value of the nonfading (specular) component is reduced from that for a smooth ground by a factor[3] which is expressed as

$$x = \exp\left\{-2\left[\frac{2\pi\sigma}{\lambda}\right]^2\right\} \tag{2}$$

where σ is the standard deviation of heights of the scattering sources about the mean ground plane as before and λ is the wavelength. The factor x serves to reduce the nonfading component of the field by an amount determined by the frequency and the roughness of the ground because of the loss of energy from the unidirectional specular return into scattering.

The power returned by specular reflection is then

$$P_{spec} = \frac{x^2K^2P_TG^2(0)\lambda^2}{(4\pi)^2(2h)^2} \tag{3}$$

where

P_T is transmitted power,
G is antenna gain,
h is altitude,
K is Fresnel reflection coefficient.

The Fresnel reflection coefficient takes into account absorption in and transmission into the ground. Since the nonfading, or specular, power return is reduced by a factor x^2 for the case of lossless terrain, the fading or scattered component must be modified from what it would be for a perfect scatterer by $(1-x^2)$. The scattered power can now be written as[1]

$$P_{scatt} = (1-x^2)\beta\int\frac{P_TG^2\lambda^2\sigma_0}{(4\pi)^3r^4}\,dA \tag{4}$$

where β accounts for absorption and depolarization in an imperfect ground and r is the slant range to an area element dA.

Probability density functions for signal amplitudes from several possible types of terrain have been investigated. These include a purely scattering ground for which the Rayleigh distribution is appropriate[6] and grounds for which one, two, or three facets contribute enough signal in comparison to the background to modify the distribution. Density curves for the scattering ground plus a single strong source are shown in Fig. 1, where $p(P)$ is probability of finding return power between P and $P+dP$.

[6] S. O. Rice, "Mathematical analysis of random noise," *Bell Sys. Tech. J.*, vol. 23, pp. 282–332, July, 1944; vol. 24, pp. 46–156, January, 1945.

While a study of the probability density functions appears to be a promising means of classifying terrains, it has not proved to be practical. No consistent relationship has been found in the experimental data.

The fading of signals from the ground is the same statistically as fluctuation of the amplitude of a single sine wave in noise, where the sine wave corresponds to the specular return and the noise corresponds to the scattered return. The range of fading will increase as the ratio of the power in the sine wave to the power in the noise is reduced. Since the scattered power varies with the illuminated area and the specular power does not, the fading distributions are functions of the size of the illuminated area and consequently of antenna beamwidth and pulse duration. (See Fig. 2.)

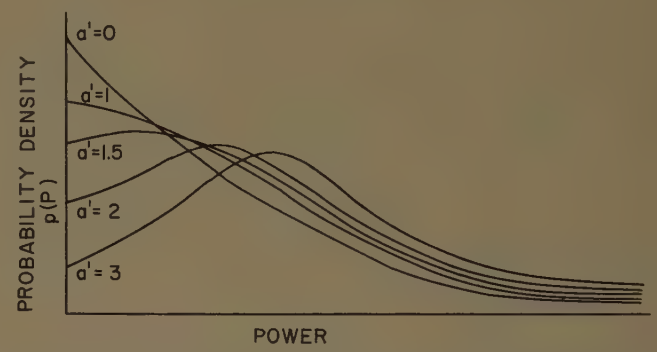

Fig. 1—Probability densities of the power return. a' is defined as the ratio of the power from the strong source to the power from the random scattering ground.

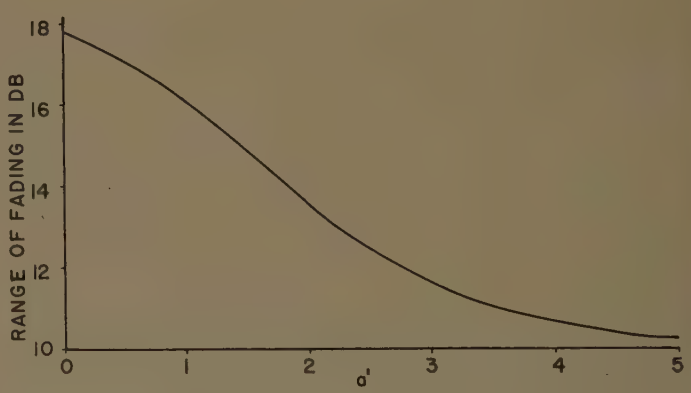

Fig. 2—Theoretical fading range for a signal composed of return from a random scattering ground which includes a single strong scatterer.

Design of the Experiment

The experiment, regarding the nature of the power returned to a radar, was intended to provide information for the radio altimeter designer. Of particular importance are information on the variation of scattering coefficient with angle, data on fading ranges and rates, and measurements of the reflection coefficient. A pulse type radar was selected for ease of instrumentation, although

the results may be adapted to frequency-modulated and other systems.

A broad-beam antenna was selected to simulate conditions for a radio altimeter, to insure a power return from a large collection of independent scatterers, and to permit measurements of scattering from a wide range of angles on each pass over a target. A narrow transmitted pulse was used so that the illuminated area was effectively limited by the pulse width. This meant that the illuminated area began as a small circle when the leading edge of the pulse first touched the ground and then developed into an expanding annulus bounded by the leading and trailing edges of the pulse, finally to disappear (effectively) at the "edge" of the antenna pattern.

Each point on the "A-scope trace" of the return pulse corresponds to power returned from a certain annular area on the ground. Independent calculations of the scattering coefficient for various angles of incidence can thus be made from a single pulse, providing the return for a particular range of angles is from an area that does not overlap the area contributing to the signal for another range of angles. The altitude, pulse duration, and antenna beamwidth will limit the number of independent zones for a particular case. When a horizontal flight path is used, the returns from ahead of the aircraft show a positive doppler shift while those from behind show a negative shift. This means that the return signal will be distributed over a band of frequencies near the carrier frequency.

The ground can be thought of as a population of oscillators with amplitudes determined by the strength of the incident transmitted pulse, with random phase, and with frequencies shifted from the carrier by an amount equal to the doppler shift for each particular scatterer. This frequency shift creates a random modulation function which is sampled each time a received pulse is recorded. This process may also be thought of as sampling a fixed space pattern due to randomly phased ground oscillators at the carrier frequency.

There is a problem in obtaining adequate statistical samples of such wave patterns.[7] It is desirable to minimize the length of the flight path in order to keep to a minimum the number of new scatterers introduced into the target area during the run. This is necessary to keep the process as close to stationary as possible. On the other hand, a short flight path means that a small number of independent samples is obtained. This paradox is particularly evident at low altitudes and low frequencies

The necessity of obtaining absolute values for the transmitted and received pulses complicated the measurement problem. The fact that the equipment was assembled and used in an aircraft meant that the environment was not ideal for making precise measurements at high frequencies. An inflight calibration procedure was adopted to determine the system characteristics just before and just after a data run was made. This resulted in usable data being obtained even though the system characteristics drifted somewhat during the flight. In addition, over-all system checks were made at times by flying over smooth water, from which the return may be calculated accurately from theory.

The 3800-mc unit had a measured antenna pattern which was almost circularly symmetric about its axis and was described to a good approximation through the region of interest by

$$G(\theta) = 14.14 \cos^2 2\theta \qquad (5)$$

where G is the power gain and θ is the angle measured from the axis, which was oriented normal to the earth during the experiment. The 415-mc antenna pattern was assumed to be circularly symmetric and was described by

$$G(\theta) = 3.80 \cos 2\theta \qquad (6)$$

over the region $0 < \theta < 20°$ and by the constant 2.81 over the region $20° < \theta < 25°$.

Data Reduction Procedure

The amplitude of the signal returned by the ground was recorded pulse by pulse, on 35-mm film. The start of the sweep was delayed until shortly before the first return, and the sweep duration was just sufficient to display all significant returns from angles within about 45° of the vertical. Each individual pulse was thus available for analysis although, for many runs, only deflections of pulses that were far enough apart to be statistically independent were measured on the film.

Calculations based on the distribution curves were then used to obtain fading ranges, probability density curves, and median and mean values of the power returns. Because of the relatively wide range of fading, and the independence of fading in different parts of the return pulse, adjacent pulses do not look much like a mean pulse or like each other. (See Fig. 3, next page).

A theoretical analysis of the power return from a large homogeneous area leads to a surface integral which contains the scattering coefficient.[1] Since a narrow-pulse radar was used, the illuminated annulus on the ground corresponds to a rather narrow range of angles, except at low altitudes and except immediately adjacent to the vertical. This made it possible to assume that the scattering coefficient remained constant over the range of integration; thus it was removed from under the integral sign. By using the median[8] returned pulse and the transmitted pulse it was possible to calculate a representative value of the scattering coefficient. In cases where the scattering coefficient varied rapidly with angle, a first estimate so obtained was modified by putting the angular variation into the integral.

[7] R. A. Hessemer, Jr., "The Sampling Problem in Low Frequency Radar Terrain Return," Sandia Corp., Albuquerque, N. M., Tech. Memo. 193-55-54; September, 1955.

[8] The median rather than the mean value of the returned pulse was selected for ease of computation in the data reduction process.

$$\beta'\sigma_0(t) = \frac{P_r(t)}{\frac{c\lambda^2}{64\pi^2}\int_{t_1}^{t_2}\frac{P_T(d-t)G^2(t)}{\left(h+\frac{ct}{2}\right)^3}dt} \qquad (7)$$

where

P_r = median value of received power,
P_T = transmitted power,
G = antenna gain,
h = altitude,
c = velocity of light,
λ = wavelength,
d = radar delay time from start of transmitted pulse,
t = time measured from start of received pulse
θ = angle of incidence,
σ_0 = radar cross section per unit area,
$\beta' = (1-x^2)\beta$ where β is a scatter power dispersion factor and x^2 is a measure of the ratio of specular power to total power return and t_2 and t_1 are time limits on the pulse.

The angle of incidence θ is related to the time t by

$$\cos\theta = \frac{h}{h+\frac{ct}{2}}. \qquad (8)$$

The scattering cross sections are shown in Figs. 4–10. The experimental points were determined from (7); a theoretical scattering curve described by (1), was then fitted to the values computed from the measured signal.

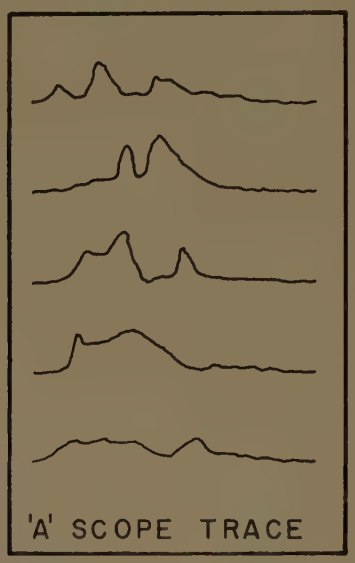

Fig. 3—Sample film strip for woods showing the rapidity of fading Pulse repetition rate, 400 pps; air speed, 120 mph; freq., 415 mc.

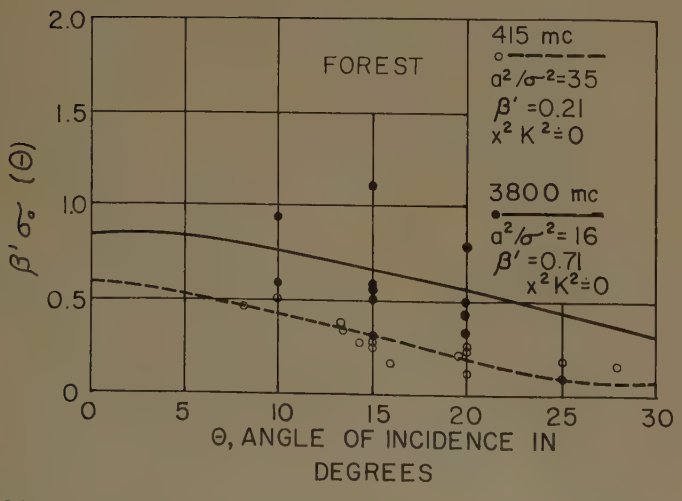

Fig. 4—Median scattering curves for woods at Pine Island, Minn. a^2/σ^2, β' and x^2K^2 are parameters used in attempting to fit the experimental data to a theoretical model.

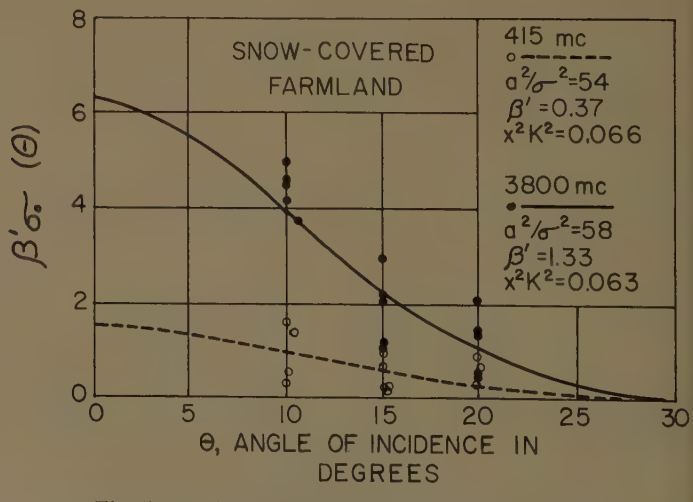

Fig. 5—Median scattering curves for snow covered farmland near Wahpeton, N. D.

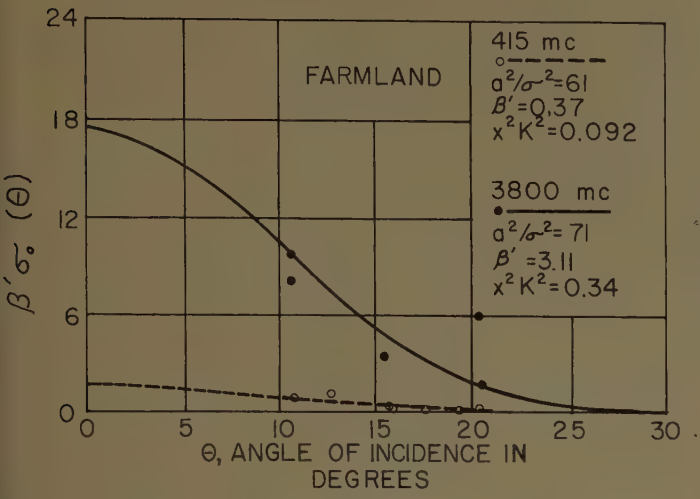

Fig. 6—Median scattering curves for farmland near Cameron, Mo.

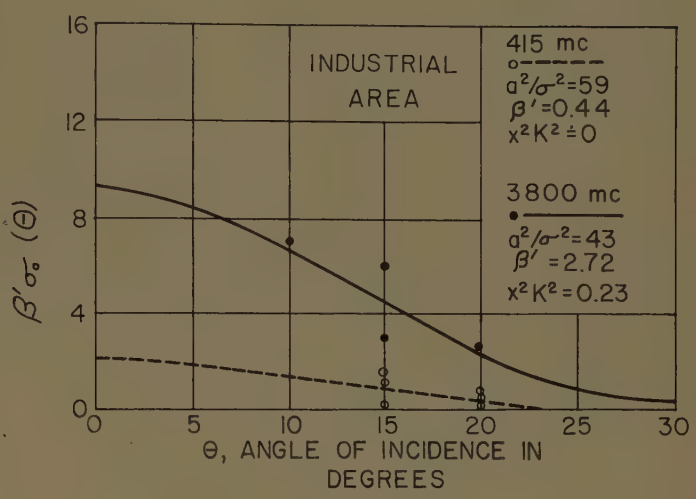

Fig. 7—Median scattering curves for industrial area in Minneapolis, Minn.

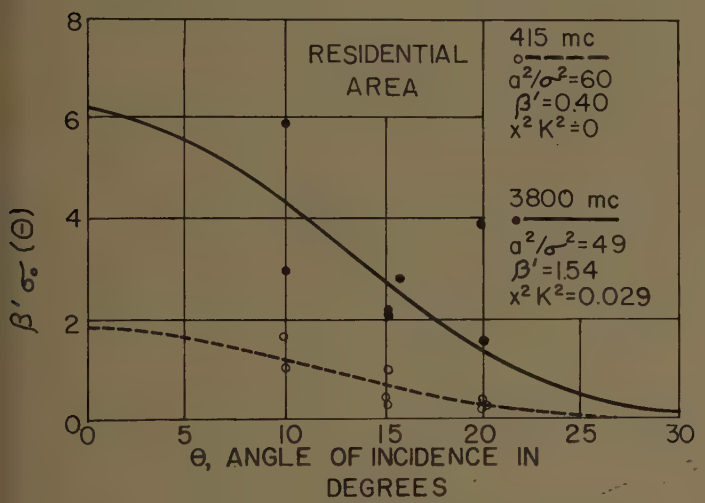

Fig. 8—Median scattering curves for residential area in Minneapolis, Minn.

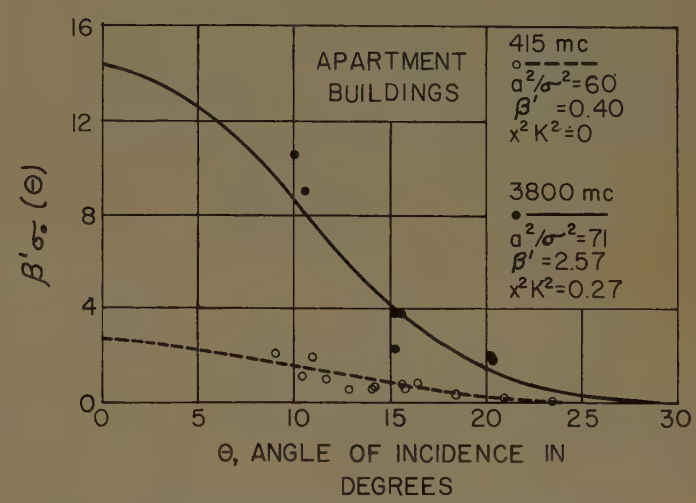

Fig. 9—Median scattering curves for an area of apartment buildings in Kansas City, Mo.

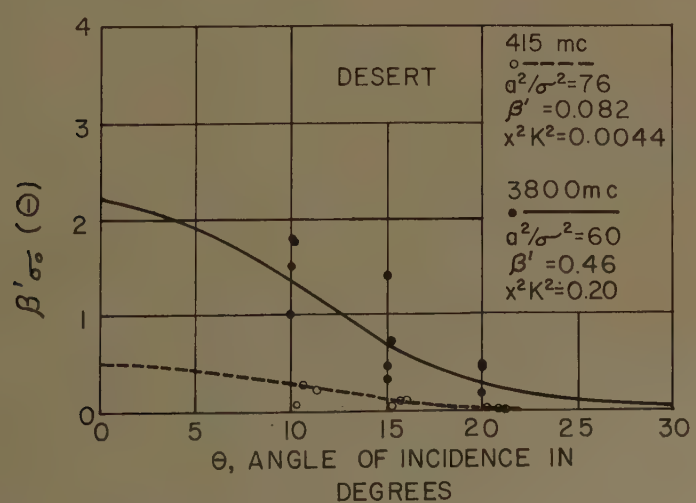

Fig. 10—Median scattering curves for a desert area near Salton Sea, Calif.

This was done in the region away from the leading edge of pulse so that no power returned by specular reflection would be present. Extrapolating the theoretical curve into the region where specular power was possible, an estimate was made of the amount of specular power in the return pulse. This estimated specular power is at best an approximation and depends on the validity of extrapolating the theoretical scattering coefficient to very small angles of incidence. A better method of performing this separation has not been developed at this time. A new experiment specifically designed to allow separation of specular and scatter components will be necessary to confirm the values for reflection coefficients.

Targets Exhibiting Specular Return

Although most of the targets investigated gave very little specular return, there were a few exceptions. Specular return is indicated by two characteristics: 1) the return pulse has the same width as the transmitted pulse and 2) the range of fading is very small.

The specular reflection coefficient for power has been written as $(xK)^2$ where x^2 is the proportionality constant between specular and scattered power and K is the Fresnel reflection coefficient. In the cases considered in the following table, x was assumed to be unity.

$$x^2K^2 = \frac{64\pi^2h^2P_r}{\lambda^2G^2(0)P_T}. \tag{9}$$

TABLE 1

Target	Fading Range db	K	K^*
Elephant Butte Reservoir (calm)	2.7	0.79	0.80
Bonneville Salt Flats (wet)	—	0.95	0.92
Frozen Lake	3.9	0.42	0.30
Irrigated Farmland (wet)	7.6	0.69	0.73
Yucca Lake Bed (moist)	2.6	0.74	0.73
Sandy Flats (dry)	5.8	0.42	0.33

* Theoretical value.

Path Attenuation

The prediction of the power return from a target for a particular type of radar requires knowledge of the reradiating characteristics of the ground as well as information on the geometry involved and the mode of operation of the radar. These many factors have been lumped together and described as a path attenuation experienced by the pulse in traveling from the antenna to the earth and back again to the antenna. This quantity is defined as

$$A = 10 \log \frac{P_TG^2}{P_R} \tag{10}$$

where P_T is the peak value of the transmitted pulse, P_R is the peak value of the received pulse, and G is a representative value of the antenna power gain over the region which returns the peak value of P_T.

Experimental values of the path attenuation for various targets are shown in Figs. 11–16. The upper and lower extremities on the bar graphs correspond to attenuations exceeded by 5 and 95 per cent, respectively, of the pulses considered. The median value of the path attenuation is indicated by a circle on each graph. The path attenuations at 3800 mc have been normalized to 415 mc by removing the effects of frequency on the effective antenna area[9] and are shaded on the graphs.

The computed path attenuation makes it possible to predict the radar return from a variety of targets for radars having similar pulse characteristics and operating on similar flight paths. In computing the values of path attenuation for this report, the pulse width was normalized to 0.2 μsec. It is important to note that the attenuation figures cannot be applied directly to radars with different operating characteristics. Within relatively narrow limits, the values obtained may be applied to radars having different transmitter pulse durations by assuming that P_R is directly proportional to pulse length. This assumption is better for rough targets like woods than for smooth ones like water or desert.

Conclusions

Since terrain generally appears to a radar as a rough surface at frequencies over 400 mc, the back scattering of energy predominates over the specular or coherent form of power return. Moreover, the rough ground shows a definite "antenna pattern" for back scattering. The radar cross section per unit area for terrain decreases as the angle of incidence becomes larger. A very rough target such as a heavily wooded area appears to be nearly an isotropic scatterer, while a smoother target such as farmland or grassland will have an "antenna pattern" that peaks up sharply at near-vertical incidence. When the angle of incidence reaches 25° from the vertical, the return signal from most farmland and city areas is down about 20 db from the value at normal incidence. For goods the decrease is less than 20 db at 25° and for water it is generally greater than 20 db at 25° from the vertical position.

Specular or coherent return (when it is present) comes from the direction of normal incidence, and the width of that portion of the return pulse associated with it is the same as the width of the transmitted pulse. This is not the case for scattered or incoherent return. Return signals caused by the scattering process are extended over a period of time determined by the beamwidth of the antenna, the back scattering antenna pattern of the ground and the pulse width. If a broad-beam antenna

[9] The path attenuation normalized to 415 mc is defined by

$$10 \log \left(\frac{P_TG_i^2\lambda_i^2}{P_R\lambda_n^2} \right)$$

where subscripts i and n refer to 3800 and 415 mc, respectively.

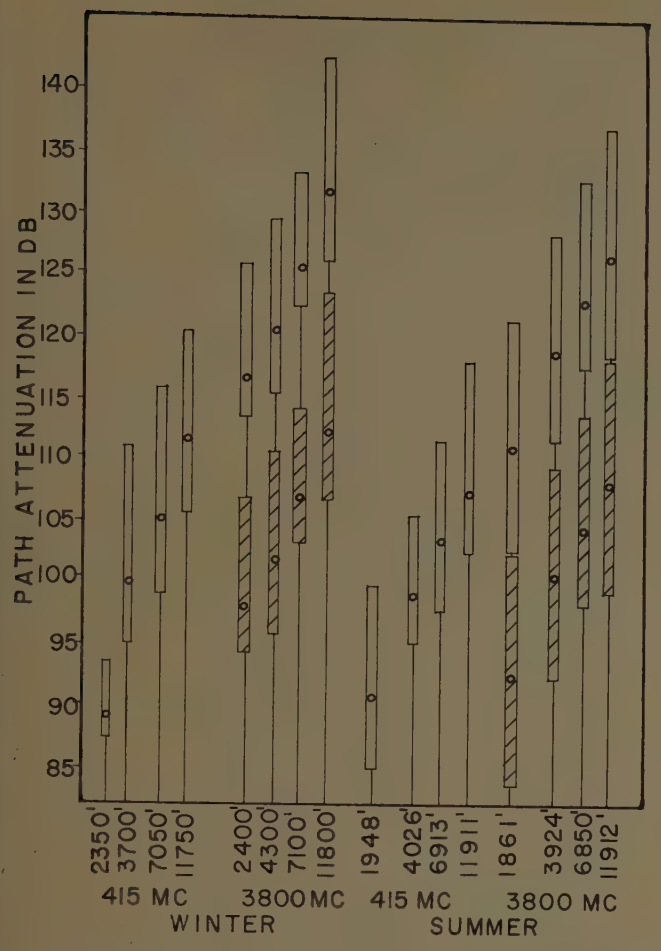

Fig. 11—Path attenuation for a farmland target near Wahpeton, N. D. Shaded bars show path attenuation normalized to 415 mc.

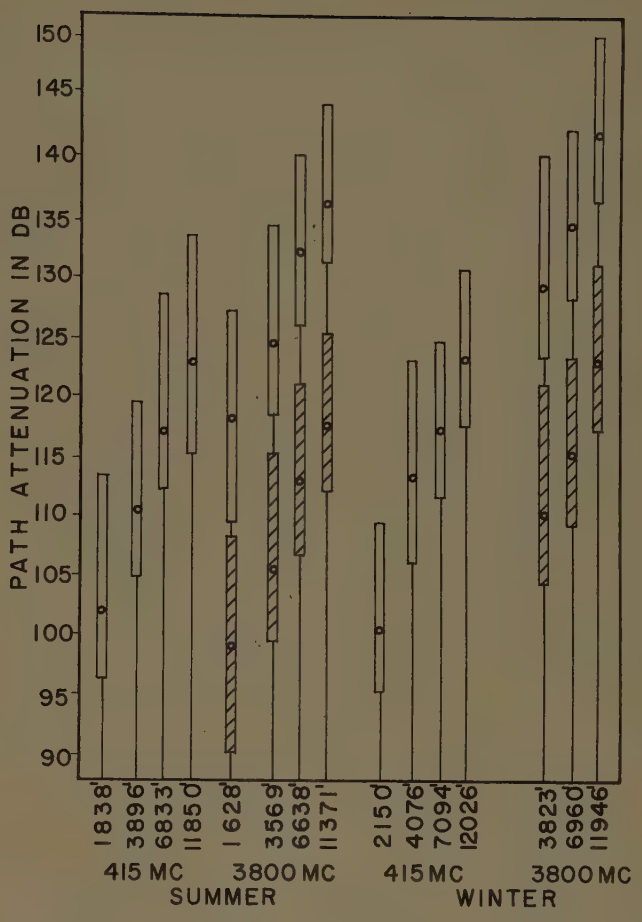

Fig. 12—Path attenuations for woods at Pine Island, Minn.

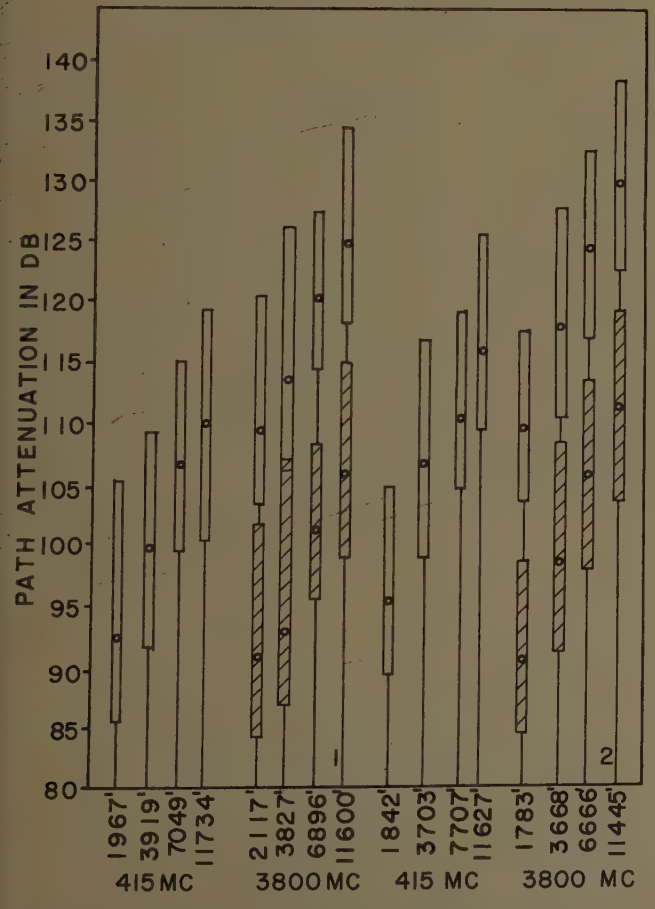

Fig. 13—Path attenuations for residential areas in 1) Kansas City, Mo. and 2) Minneapolis, Minn.

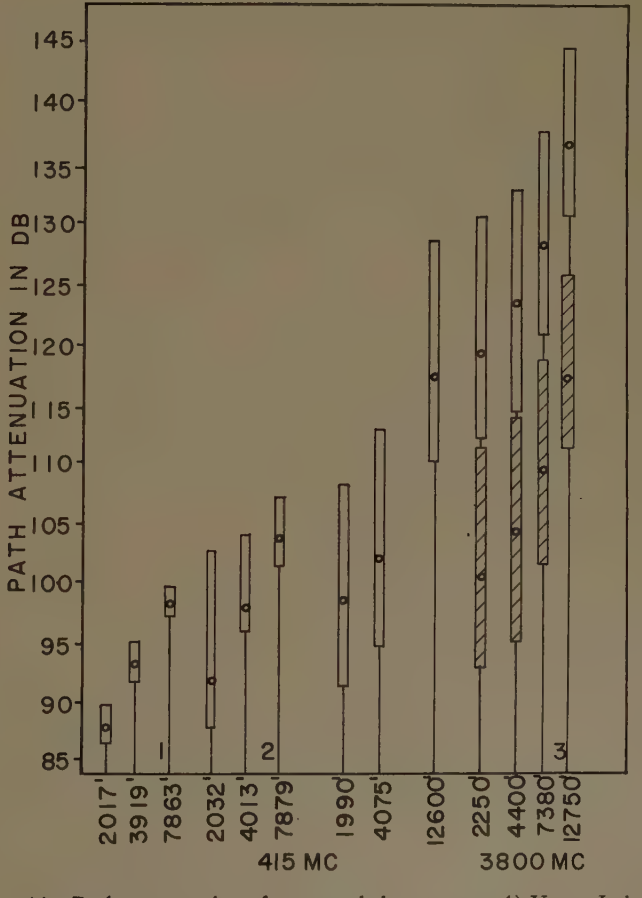

Fig. 14—Path attenuations for several desert areas. 1) Yucca Lake Bed, very moist; 2) Sandy Flats near Yucca Lake; 3) Desert near Salton Sea.

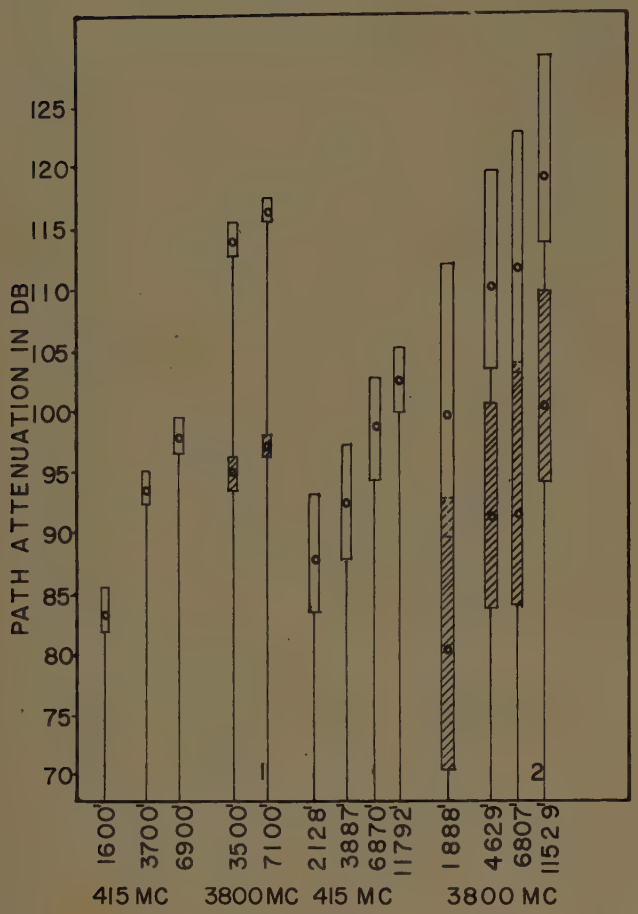

Fig. 15—Path attenuations for fresh water targets. 1) Elephant Butte Reservoir, water very smooth. 2) Lake Bemidji, water rough.

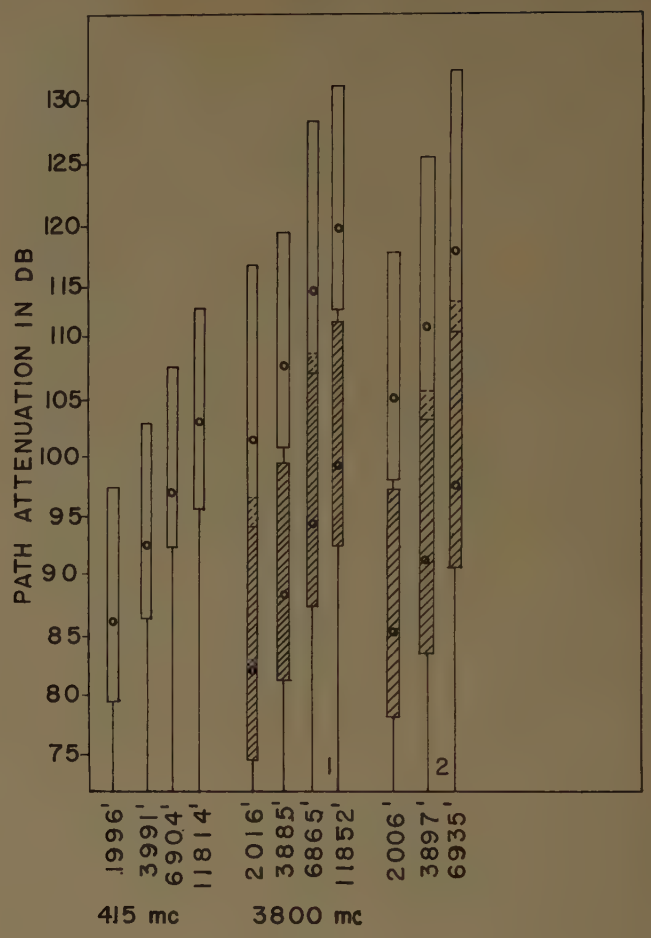

Fig. 16—Path attenuations for salt water targets. 1) Salton Sea, Calif. 2) Pacific Ocean.

is used, a narrow transmitted pulse will be returned to the receiver as a much wider pulse.

The range of fading experienced by the return signal depends upon the type of terrain illuminated and upon the antenna pattern. When using a broad-beam antenna at altitudes of 2000 feet or more, a very smooth surface will return a signal which fades only a few db while the majority of targets return signals which fade 12 to 16 db. The range of fading could be expected to diminish if a narrow-beam antenna were used. The actual range of fading experienced for a particular target has proven to be an unsatisfactory means of classifying the target except into the very broad categories of a smooth or a rough terrain.

For a very particular case, the path attenuation is a rough means of describing the action of the ground in reradiating energy. This factor is useful in predicting the radar return to a system similar to that used in the experiment when operated over a similar target at the same altitude. The path attenuation figure cannot, however, be easily extended for use with other types of radar, although some altitude extrapolation is permissible when the general character of the variation of σ_0 with angle is known. In this experiment the path attenuation is from 15 to 20 db higher at 12,000-foot than at 2000-foot altitude. Over the range of altitudes considered, the return signal variation is between "inverse square" and "inverse cube" with altitude.

A New Mathematical Approach for Linear Array Analysis*

D. K. CHENG† AND M. T. MA†

Summary—**It is well known that linear antenna arrays are representable mathematically by polynomials. However, even for the simplest case of a uniform array, properties of its radiation pattern are conventionally analyzed by examining the transcendental form of the array factor and some of its important characteristics have been determined only approximately. For a more general array, a closed form of the associated polynomial is usually not obtained and the analysis becomes quite difficult. This paper proposes a new approach for linear array analysis. Basically, the current distribution in the discrete elements of a linear array is considered as the sampled values of a continuous function. Known relations in Z transforms developed for sampled-data systems can then be used to express the array polynomial in a closed form. Mathematical techniques for determining important properties of the array pattern are developed. Typical examples illustrating the applications of this new approach are given.**

Introduction

SCHELKUNOFF[1] has shown that linear antenna arrays are representable mathematically by polynomials and that important characteristics of the radiation pattern of any linear array can be analyzed in terms of the properties of its associated polynomial. However, except for uniform and binomial arrays, a closed form of the polynomial is not obtained, and investigation of array characteristics by examining the many terms in the polynomial for a multielement array is quite tedious and frequently unfruitful. Even for the simplest case of a uniform array the usual approach has been to consider the transcendental form of the array factor. Because of the difficulty in solving transcendental equations, important characteristics such as the location and the level of sidelobes and the beamwidth have been determined only approximately. At the present time there exists no general technique which can be used to analyze the radiation characteristics of a linear array with nonuniform amplitude distribution.

Consider the linear array of n equally spaced, identical, elements in Fig. 1. The polynomial associated with such an array can be written as

$$E(z) = a_0 + a_1 z^{-1} + a_2 z^{-2} + \cdots + a_{n-1} z^{-(n-1)} = \sum_{k=0}^{n-1} a_k z^{-k} \tag{1}$$

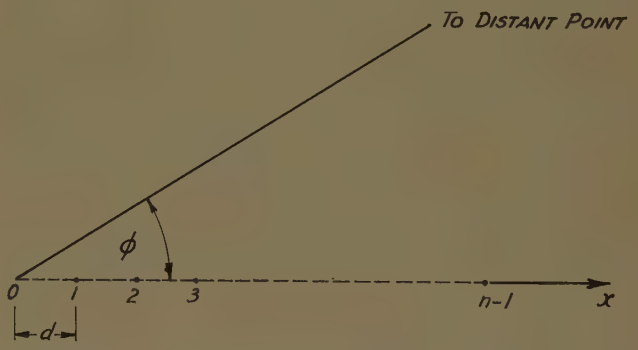

Fig. 1—A linear array of n equally spaced elements.

where

$$z = \epsilon^{-i\psi}\ ^{2} \tag{2}$$

with

$$\psi = \beta d \cos \phi + \alpha. \tag{3}$$

In (3), $\beta = 2\pi/\lambda$ is the phase constant and α is the progressive phase lead of the excitation in an element compared to that in its neighbor on the left. The coefficients, $a_0, a_1, a_2, \cdots, a_{n-1}$, in the polynomial represent the excitations in the elements and can in general be complex. For most practical arrays, a progressive phase shift α exists along the array and the a-coefficients are real.

When all the a's are equal, a uniform array results. In such a case, $a_k = a_0$ for all k's, the polynomial in (1) can be easily summed up:

$$E(z) = a_0 \left(\frac{1 - z^{-n}}{1 - z^{-1}} \right). \tag{4}$$

The usual approach in analyzing a uniform array is to rearrange (4) as follows:

$$E(z) = a_0 z^{-(n-1)/2} \left(\frac{z^{n/2} - z^{-n/2}}{z^{1/2} - z^{-1/2}} \right)$$

or, in terms of ψ,

$$E'(\psi) = a_0 \epsilon^{i(n-1)\psi/2} \left(\frac{\sin n\psi/2}{\sin \psi/2} \right). \tag{5}$$

* Manuscript received by the PGAP, October 1, 1959. A part of the work reported in this paper was done under Contract No. AF 30(602)-1640 sponsored by Rome Air Development Center, Griffiss Air Force Base, Rome, N. Y. Presented at the 15th Natl. Electronics Conf., Chicago, Ill., October 14, 1959.

† Elec. Engrg. Dept., Syracuse University, Syracuse, N. Y.

[1] S. A. Schelkunoff, "A mathematical theory of linear arrays," *Bell Sys. Tech. J.*, vol. 22, pp. 80–107; January, 1943.

[2] Note that the notation for z in (2) is different from the usual definition which does not include the negative sign in the exponent. This change of notation is necessary in order to conform with the conventional form of the Z transform of a function to be introduced later in (9).

The expression in (5) is obtained by noting the relation in (2). Although this approach is straightforward, it does not make full use of the algebraic character of the array function. An exact analysis of transcendental expressions such as that in (5) is a difficult job unless we wish to plot the whole function graphically.

For a nonuniform array, the a coefficients in (1) will not be all equal and the simple forms for $E(z)$ in (4) and $E'(\psi)$ in (5) do not apply. We are then faced with the formidable task of having to analyze a polynomial of n terms. The polynomial could be put in terms of sine and cosine functions, but this would only make the resultant expression even harder to handle.

In the following sections a new approach for the analysis of linear arrays is described. The discrete linear array will be treated as a sampled-data system. Known relations in Z transforms developed for sampled-data systems enable us to express the array polynomial in a closed form, even for nonuniform arrays. Analysis of the important characteristics of the radiation pattern can then be done conveniently. Several useful formulas concerning this technique will also be developed.

Discrete Array as a Sampled-Data System

Supose that the envelope of the amplitude distribution of the excitations in a linear array can be described by a continuous function $f(x)$ within the range $0 \leq x \leq (n-1)d$. Then the a coefficients in (1) can be written as

$$\begin{aligned} a_0 &= f(0) \\ a_1 &= f(d) \\ a_2 &= f(2d) \\ &\vdots \\ a_{n-1} &= f[(n-1)d] \end{aligned} \tag{6}$$

and the array polynomial becomes

$$\begin{aligned} E(z) &= f(0) + f(d)z^{-1} + f(2d)z^{-2} + \cdots \\ &\quad + f[(n-1)d]z^{-(n-1)} \\ &= \sum_{k=0}^{n-1} f(kd)z^{-k}. \end{aligned} \tag{7}$$

We may also rewrite (7) as

$$E(z) = \sum_{k=0}^{\infty} f(kd)z^{-k} - \sum_{k=n}^{\infty} f(kd)z^{-k}. \tag{8}$$

Now, the first term on the right side of (8) is exactly what is called the Z transform[3] of the function $f(x)$, or of the sampled function $f^*(x)$, the sampling period being d.

$$\begin{aligned} \sum_{k=0}^{\infty} f(kd)z^{-k} &= \mathrm{Z}[f(x)] = \mathrm{Z}[f^*(x)] \\ &= F(z). \end{aligned} \tag{9}$$

[3] D. K. Cheng, "Analysis of Linear Systems," Addison-Wesley Publishing Co., Reading, Mass., ch. 10; 1959.

The second term on the right side of (8) can also be expressed in terms of the Z transform of a function:

$$\begin{aligned} \sum_{k=n}^{\infty} f(kd)z^{-k} &= f(nd)z^{-n} + f(nd+d)z^{-(n+1)} + \cdots \\ &= z^{-n}[f(nd) + f(nd+d)z^{-1} + \cdots] \\ &= z^{-n}\mathrm{Z}[f(nd+x)] = z^{-n}G(z). \end{aligned} \tag{10}$$

Substituting (9) and (10) in (8), we have

$$E(z) = F(z) - z^{-n}G(z). \tag{11}$$

Eq. (11) is an important relation because both $F(z)$ and $G(z)$ can be expressed in closed forms for well-behaved envelope function $f(x)$. A general relation exists between $G(z)$ and $F(z)$, but it is seldomly needed. For most practical arrays the amplitudes of the excitations in the two end elements are equal and it suffices to recognize that if

$$f[(n-1)d + x] = \pm f(x) \tag{12}$$

then

$$\begin{aligned} G(z) &= \mathrm{Z}[f(nd+x)] \\ &= \sum_{k=0}^{\infty} f(nd+kd)z^{-k} \\ &= \sum_{k=0}^{\infty} f[(n-1)d + (k+1)d]z^{-k} \\ &= \pm \sum_{k=0}^{\infty} f[(k+1)d]z^{-k} \\ &= \pm z[F(z) - f(0)] \end{aligned} \tag{13}$$

where $f(0)$ is the excitation in the first element and the shifting relation[3]

$$\mathrm{Z}[f(x+d)] = z[F(z) - f(0)] \tag{14}$$

has been used. Substituting (13) in (11), we obtain

$$E(z) = [1 \mp z^{-(n-1)}]F(z) \pm f(0)z^{-(n-1)} \tag{15}$$

where the $\pm$ signs follow those in (12).

It is important to note that, since the Z transforms of many useful nonuniform envelope functions $f(x)$ exist in closed form, $E(z)$ in (15) is expressible as a closed function of z, instead of as a polynomial of n terms. Note further that increasing the number of elements, n, in an array does not increase the complexity of the expression for $E(z)$. The application of (15) can best be illustrated by examples.

Example 1: Uniform Array of n Elements

The amplitude of the excitation can be assumed to be unity with no loss of generality. In this case,

$$f_A(x) = U(x), \tag{16}$$

$$f_A[(n-1)d + x] = f_A(x), \tag{17}$$

$$F_A(z) = \mathrm{Z}[U(x)] = \frac{1}{1 - z^{-1}}. \tag{18}$$

Substituting (16)–(18) in (15) and using the upper signs, we obtain

$$E_A(z) = \frac{1 - z^{-(n-1)}}{1 - z^{-1}} + z^{-(n-1)} = \frac{1 - z^{-n}}{1 - z^{-1}} \tag{19}$$

which checks with the result in (4) for $a_0 = 1$.

Example 2: Linear Array of n Elements with Sinusoidal Amplitude Distribution

In this case, the amplitude distribution in the elements of the array is shown in Fig. 2. The array polynomial obtained by summing the contributions due to all elements in the array would be

$$E_B(z) = \sin(0) + (\sin \beta d)z^{-1} + (\sin 2\beta d)z^{-2} + \cdots + [\sin(n-1)\beta d]z^{-(n-1)}. \tag{20}$$

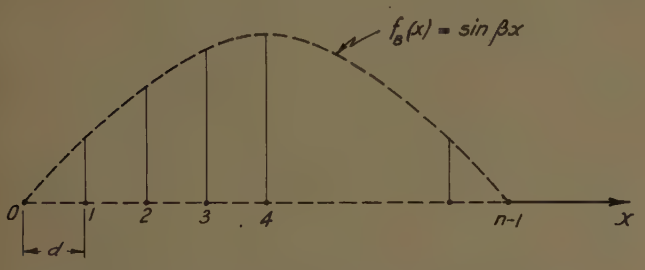

Fig. 2—Linear array with sine amplitude distribution.

We are confronted with difficulty here because it is not obvious that the polynomial in (20) can be summed up in a neat form, without which further analysis cannot proceed in general terms. For a general amplitude distribution function $f(x)$, it would also appear that increasing the total number of elements, n, in an array would increase the complexity of the expression for $E(z)$ since $E(z)$ would be a polynomial of n terms.

Let us now use the new approach. For the distribution in Fig. 2, we have

$$f_B(x) = \sin \beta x. \tag{21}$$

In this particular case, $(n-1)\beta d = \pi$,

$$f_B[(n-1)d + x] = -f_B(x) \tag{22}$$

and

$$F_B(z) = \mathcal{Z}[\sin \beta x] = \frac{z \sin \beta d}{z^2 - 2z \cos \beta d + 1}. \tag{23}$$

Substituting (21)–(23) in (15) and using the lower signs, we obtain

$$E_B(z) = \frac{[1 + z^{(n-1)}]z \sin \beta d}{z^2 - 2z \cos \beta d + 1} \tag{24}$$

which is indeed a neat expression and is the closed form for the polynomial in (20). Eq. (24) can be used as the starting point for further investigation on the properties of the array pattern.

Array Factor in Terms of Z Transforms

Although array functions obtained by using (15) are quite general, antenna engineers are interested primarily in the magnitude $|E(z)|$. It is not a simple matter to derive $|E(z)|$ from a general $E(z)$ since z itself is a complex quantity. Of course, one could always write z as $(\cos \psi - j \sin \psi)$ and take the square root of the sum of the squares of the real and imaginary parts of $E(z)$, but this would result in helplessly complicated expressions. In this section we will show a simple way of deriving $|E(z)|^2$ from $E(z)$. $|E(z)|^2$ describes the power pattern of the array and is sometimes called the *array factor*. Characteristics of $|E(z)|^2$ completely specify those of $|E(z)|$.

$|E(z)|^2$ can be derived from $E(z)$ by noting that

$$z^* = z^{-1} = \epsilon^{j\psi}. \tag{25}$$

Hence,

$$|E(z)|^2 = E(z)E(z^{-1}) = \left(\sum_{k=0}^{n-1} a_k z^{-k}\right)\left(\sum_{k=0}^{n-1} a_k z^{k}\right). \tag{26}$$

Using (15), we have the general formula

$$|E(z)|^2 = [2 \mp z^{(n-1)} \mp z^{-(n-1)}]F(z)F(z^{-1}) - f(0)\{[1 \mp z^{(n-1)}]F(z) + [1 \mp z^{-(n-1)}]F(z^{-1})\} + f^2(0). \tag{27}$$

Here again the $\pm$ signs follow those in (12). Let us now find the array factors for the two arrays for which the array functions have been found in the examples in the last section.

Uniform Array of n Elements

$$E_A(z) = \frac{1 - z^{-n}}{1 - z^{-1}}. \tag{19}$$

$$E_A(z^{-1}) = \frac{1 - z^{n}}{1 - z}. \tag{28}$$

Therefore,

$$|E_A(z)|^2 = E_A(z)E_A(z^{-1}) = \frac{2 - (z^n + z^{-n})}{2 - (z + z^{-1})}. \tag{29}$$

Substituting $\epsilon^{-j\psi}$ for z, we obtain

$$|E_A'(\psi)|^2 = \frac{2 - (\epsilon^{-jn\psi} + \epsilon^{jn\psi})}{2 - (\epsilon^{-j\psi} + \epsilon^{j\psi})} = \left|\frac{\sin n\psi/2}{\sin \psi/2}\right|^2$$

or

$$|E_A'(\psi)| = \left|\frac{\sin n\psi/2}{\sin \psi/2}\right| \tag{30}$$

which agrees with the known result.

Linear Array for n Elements with Sinusoidal Amplitude Distribution

$$E_B(z) = \frac{[1 + z^{-(n-1)}]z \sin \beta d}{z^2 - 2z \cos \beta d + 1}, \tag{24}$$

$$E_B(z^{-1}) = \frac{[1 + z^{(n-1)}]z^{-1} \sin \beta d}{z^{-2} - 2z^{-1} \cos \beta d + 1}, \tag{31}$$

$$|E_B(z)|^2 = \frac{[2 + z^{(n-1)} + z^{-(n-1)}] \sin^2 \beta d}{(2 + z^2 + z^{-2}) - 4(z + z^{-1}) \cos \beta d + 4 \cos^2 \beta d}. \tag{32}$$

Two points about both (29) and (32) are worthy of note: First, the number of terms in $|E(z)|^2$ for a given $f(x)$ does not increase or decrease wtih the number of elements, n, in the array. As a matter of fact, the denominator of $|E(z)|^2$ is, as a rule, independent of n. Second, the terms z^k and z^{-k} always appear in pairs. In other words, $|E(z)|^2$ is symmetrical with respect to the z^0 (constant) term. The second observation suggests a new symbol, say y, for $(z+z^{-1})$. Other pairs (z^k+z^{-k}) can also be expressed in terms of y. This materially simplifies subsequent manipulations of the array factor. Thus,

$$z + z^{-1} = 2 \cos \psi = y, \tag{33}$$

$$z^2 + z^{-2} = (z + z^{-1})^2 - 2 = y^2 - 2, \tag{34}$$

$$z^3 + z^{-3} = (z + z^{-1})^3 - 3(z + z^{-1}) = y^3 - 3y, \tag{35}$$

$$z^4 + z^{-4} = (z + z^{-1})^4 - 4(z^2 + z^{-2}) - 6 = y^4 - 4y^2 + 2, \tag{36}$$

$$z^5 + z^{-5} = (z + z^{-1})^5 - 5(z^3 + z^{-3}) - 10(z + z^{-1}) = y^5 - 5y^3 + 5y, \tag{37}$$

. . . . . .

For a uniform array of 6 elements, we can reduce (29) to the following simple form:

$$P_A(y) = (y + 2)(y^2 - 1)^2. \tag{38}$$

The location of nulls, maxima, and half-power points can all be found conveniently from (38).

Nulls: It is obvious that the nulls of the radiation pattern occur at the following points:

$$y = -2, \quad \text{or} \quad \psi = 180°,$$
$$y = +1, \quad \text{or} \quad \psi = \pm 60°,$$
$$y = -1, \quad \text{or} \quad \psi = \pm 120°.$$

Maxima: To find the maximum points of $P_A(y)$, we set [remembering from (33) that y is a function of ψ]

$$\frac{dP_A(y)}{dy}\frac{dy}{d\psi} = \frac{dP_A(y)}{dy}(-2 \sin \psi) = 0. \tag{39}$$

We note that $\psi = 0$ $(y = 2)$ and $\psi = \pi$ $(y = -2)$ always satisfy (39). $\psi = 0$ always corresponds to the principal maximum, but $\psi = \pi$ may or may not have physical meaning depending upon the values of βd and α since the value of ψ is restricted to the range $\alpha \pm \beta d$. For the present example, $\psi = \pi (y = -2)$ is a null point.

Principal maximum: $y = 2$, $P_A(2) = 36$.

Minor maxima:

$$\frac{dP_A(y)}{dy} = (y^2 - 1)(5y^2 + 8y - 1) = 0.$$

The first factor gives $y = \pm 1$ which are null points. The second factor yields

$$y = 0.116(\psi = \pm 86.6°),$$
$$P_A(0.116) = 2.06(-12.4 \text{ db}),$$
$$y = -1.716(\psi = \pm 149.2°),$$
$$P_A(-1.716) = 1.074(-15.3 \text{ db}).$$

Beamwidth: Setting $P_A(y)$ in (38) equal to one-half of the value $[P_A(2) = 36]$ at the principal maximum, we have

$$(y + 2)(y^2 - 1)^2 = 18$$

or

$$y^5 + 2y^4 - 2y^3 - 4y^2 + y - 16 = (y - 1.784)(y^4 + 3.78y^3 + 4.75y^2 + 4.48y + 8.98) = 0.$$

The only positive real root is $y = 1.784$, which corresponds to $\psi = \pm 27°$. Since y must be real $(-2 \leq y \leq +2)$ and since the value of y at half-power points must lie near to that $(y = 2)$ at the principal maximum, the single positive real root is not difficult to determine even though the equation is of a high degree. To find the 3-db beamwidth we must first convert the values of ψ at the two half-power points to corresponding values of ϕ by (3). The beamwidth is then the angle of ϕ subtended between these two points.

For an array of 6 elements with a sine amplitude distribution, the important characteristics of the array factor are also easy to determine. We have, from (32),

$$P_B(y) = \sin^2\left(\frac{\pi}{5}\right)(y + 2)\left(y + 2 \cos \frac{\pi}{5} - 1\right)^2.$$

Nulls:

$$y = -2, \quad \text{or} \quad \psi = 180°$$
$$y = -0.618 \quad \text{or} \quad \psi = \pm 108°.$$

Maxima:

Principal maximum: $y = 2$, $P_B(2) = 9.47$.

Minor maxima:

$$\frac{dP_B(y)}{dy} = \sin^2\left(\frac{\pi}{5}\right)\left(y + 2 \cos \frac{\pi}{5} - 1\right) \cdot \left(3y + 2 \cos \frac{\pi}{5} + 3\right) = 0.$$

Null points are given by $y = 1 - 2 \cos (\pi/5)$. Hence, only the last factor yields minor maxima:

$$y = -1.54(\psi = \pm 140.3°),$$
$$P_B(-1.54) = 0.135(-18.5 \text{ db}).$$

Beamwidth: At half-power points we have

$$\sin^2\left(\frac{\pi}{5}\right)(y+2)\left(y+2\cos\frac{\pi}{5}-1\right)^2 = 4.74$$

which can be rearranged as follows:

$$(y-1.390)(y^2+4.63y+9.29) = 0.$$

The only positive real root is $y=1.390$, which corresponds to $\psi = \pm 46°$.

A Theorem for Composite Excitation Functions

When the amplitude distribution in an array can be decomposed into two or more component functions, the resultant array factor can be expressed in terms of the component array functions. The problem is somewhat more involved than simple superposition because array factor is the square of the magnitude of array function. The following theorem applies: If the envelope of the amplitude distribution of the excitations in a linear array is a linear combination of two component functions such that

$$f(x) = C_A f_A(x) + C_B f_B(x), \quad 0 \leq x \leq (n-1)d \tag{40}$$

then the array factor can be expressed as

$$\begin{aligned} |E(z)|^2 &= [C_A E_A(z) + C_B E_B(z)][C_A E_A(z^{-1}) + C_B E_B(z^{-1})] \\ &= C_A^2 |E_A(z)|^2 + C_B^2 |E_B(z)|^2 \\ &\quad + C_A C_B[E_A(z)E_B(z^{-1}) + E_A(z^{-1})E_B(z)] \end{aligned} \tag{41}$$

where $E_A(z)$ and $E_B(z)$ are the component array functions. Note that cross terms exist in (41). The extension of the above statement to cases where there are more than two component functions is obvious.

With the aid of (41) we can determine the pattern characteristics of an array which has an amplitude distribution shown in Fig. 3. We write

$$\begin{aligned} f_C(x) &= f_A(x) + f_B(x) \\ &= U(x) + \sin \beta x. \end{aligned} \tag{42}$$

Substituting $E_A(z)$ and $E_B(z)$ for the component arrays with uniform and sine amplitude distributions in (41) and using relations (33) through (37), we obtain the resultant array factor

$$P_C(y) = (y+2)\left[y^2 - 1 + \left(y + 2\cos\frac{\pi}{5} - 1\right)\sin\frac{\pi}{5}\right]^2. \tag{43}$$

Analysis of $P_C(y)$ in (43) proceeds in the normal manner.

Nulls:

$$\begin{aligned} y &= -2, && \text{or } \psi = 180°, \\ y &= 0.556, && \text{or } \psi = \pm 73.8°, \\ y &= -1.144, && \text{or } \psi = \pm 124.9°. \end{aligned}$$

Maxima:

Principal maximum: $y=2$, $P_C(2)=82.1$.

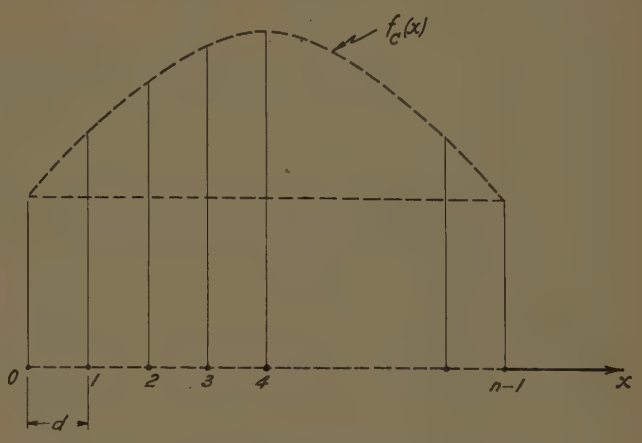

Fig. 3—Linear array with sine-over-a-pedestal amplitude distribution.

Minor maxima:

$$\frac{dP_C(y)}{dy} = \left[y^2 - 1 + \left(y + 2\cos\frac{\pi}{5} - 1\right)\sin\frac{\pi}{5}\right] \cdot (5y^2 + 9.76y + 1.714) = 0.$$

The first factor gives null points, and the second factor yields minor maxima:

$$\begin{aligned} y &= -0.195 (\psi = \pm 95.6°), \\ P_C(-0.195) &= 0.918 (-19.5 \text{ db}). \\ y &= -1.757 (\psi = \pm 151.5°), \\ P_C(-1.757) &= 0.484 (-22.3 \text{ db}). \end{aligned}$$

Beamwidth: At half-power points we have

$$(y+2)\left[y^2 - 1 + \left(y + 2\cos\frac{\pi}{5} - 1\right)\sin\frac{\pi}{5}\right]^2 = 41.1$$

which can be rearranged as follows:

$$(y-1.72)(y^4 + 4.90y^3 + 9.83y^2 + 14.3y + 23.3) = 0.$$

The only positive real root is $y=1.72$ which corresponds to $\psi = \pm 30.7°$.

Conclusion

In this paper we have shown that the amplitude distribution of the currents in the discrete elements of a linear array can be considered as the sampled values of a continuous function and that known relations in Z transforms developed for sampled-data systems can be used to express the array polynomial in a closed form. Analysis of the important properties of the radiation pattern of an array can proceed conveniently from a closed, algebraic, expression of the array factor, instead of from a polynomial of many, many terms. Simplified techniques for determining the location of the nulls, the principal maximum, the location and the level of sidelobes, and the half-power beamwidth have been developed. A method for deriving the array factor of an array with a composite amplitude distribution in terms of component array functions is also discussed. It is believed that the proposed approach offers decided advantages over the conventional approach.

Log Periodic Dipole Arrays*

D. E. ISBELL†

Summary—**A new class of coplanar dipole arrays is introduced. The antennas described provide unidirectional radiation patterns of constant beamwidth and nearly constant input impedances over any desired bandwidth. The broad-band properties are achieved by making use of the principles of log periodic antenna design. Models are discussed which are capable of providing 8- to 9-db directive gain with an associated input standing wave ratio of 1:2:1 on a 75-ohm feeder, and this performance is independent of frequency. The free-space properties of several of these arrays have been measured and the results are presented. The antenna configuration is simple, permitting practical methods of fabrication, and the design should prove useful in many applications. It makes possible, for example, the construction of "all-wave" rotatable beams of very low cross section for use in the hf to uhf spectrum.**

I. Introduction

LOG periodic antenna design has been the subject of several papers over the past few years. The concept was first introduced in connection with a plane slot radiator having bidirectional linearly-polarized radiation patterns of constant beamwidth and essentially constant input impedance over better than ten to one bandwidths.[1] Since that time many extensions of the original structure have been introduced providing a large choice of electrical characteristics, all of which are virtually independent of frequency.[2,3] Log periodic antenna designs are available, for example, which provide omnidirectional, bidirectional, or unidirectional radiation patterns and either linear or circular polarization. The basic unidirectional elements all have moderate directive gains, and it has been shown that high gains are possible through application of array techniques[4] or by using the antennas as primary sources for large reflectors.[5,6]

The antennas discussed in the following paragraphs provide electrical characteristics which are similar to those of some of the antennas described in the above referenced papers, but they represent a departure in form. The log periodic designs which have been introduced to date have all been variations of a basic type involving combinations of a single composite element which is shaped to provide the log periodic characteristics. The antennas introduced here demonstrate that the log periodic principles can be applied to the design of arrays of conventional elements with frequency independent performance resulting. An important consequence of this, as will be seen, is that these antennas permit at least a qualitative analysis of their operation in terms of familiar ideas, and they further tend to increase insight with respect to the operation of the original log periodic antennas.

II. Some General Considerations

Although it has not, as yet, been possible to obtain precise physical understanding of the operation of the successful frequency independent antennas, it is possible to put forth certain qualitative arguments in that direction. The following is an attempt to induce these arguments into the design of a wide-band array using conventional elements.

If frequency independent performance is sought from a structure composed of resonant elements it is clear that the resonances must be staggered in order that as frequency is varied the function of the resonant element is transferred smoothly from one element to the next. In the case of an antenna array composed of similar discrete elements this means that the physical dimensions of the elements must be scaled from one to the next in such a way that the desired frequency range is covered with elements of overlapping response characteristics. Since the characteristics of antenna elements are determined in part by their surroundings, it is necessary also to scale the environment.

Considering now a coplanar array of side-by-side dipoles in accordance with the above ideas, an arrangement of the type shown in Fig. 1 is obtained. The lengths of the dipoles are related by a constant scale factor as defined in the figure. That is, given the length L of the element of order 0 in the array, the length of the elements of order n will be given by $\tau^n L$ where n takes on all integral values, positive or negative. Since it is also necessary to scale the environment, the spacings Δs between elements must be related in the same manner. If carried to the limit the array converges to the point 0 on the left as $n \rightarrow -\infty$ and becomes infinite in extent on the right as $n \rightarrow \infty$. If the elements of Fig. 1

* Manuscript received by the PGAP, July 2, 1959; revised manuscript, received January 6, 1960. This work was performed at the University of Illinois under contract with the United States Air Force, Wright Air Dev. Ctr., Wright Patterson Air Force Base, Ohio. It has been published by the University of Illinois as Antenna Lab. Tech. Rept. No. 39, June 10, 1959.

† Electro-Dynamics Staff, Transport Div., Boeing Airplane Co., Seattle, Wash.

[1] R. H. DuHamel and D. E. Isbell, "Broadband logarithmically periodic antenna structures," 1957 IRE National Convention Record, pt. 1, pp. 119–1280. Also, University of Illinois Antenna Laboratory Tech. Rept. No. 19, Contract AF 33(616)-3220, Wright Air Dev. Ctr.; May, 1957.

[2] D. E. Isbell, "Non-planar logarithmically periodic antenna structures," *Abstracts of the Seventh Annual Symposium on the USAF Antenna Research and Development Program*, October, 1957. Also, University of Illinois Antenna Lab. Tech. Rept. No. 30, Contract AF 33(616)-3220, Wright Air Dev. Ctr.; February, 1958.

[3] R. H. DuHamel and F. R. Ore, "Logarithmically periodic antenna designs," 1958 IRE National Convention Record, pt. 1, pp. 139–151.

[4] R. H. DuHamel and D. G. Berry, "Logarithmically periodic antenna arrays," 1958 IRE WESCON Convention Record, pt. 1, pp. 161–174.

[5] D. E. Isbell, "A log-periodic reflector feed," Proc. IRE, vol. 47, pp. 1152–1153; June, 1959.

[6] R. H. DuHamel and F. R. Ore, "Log periodic feeds for lens and reflectors," 1959 IRE National Convention Record, vol. 7, pt. 1, pp. 128–137.

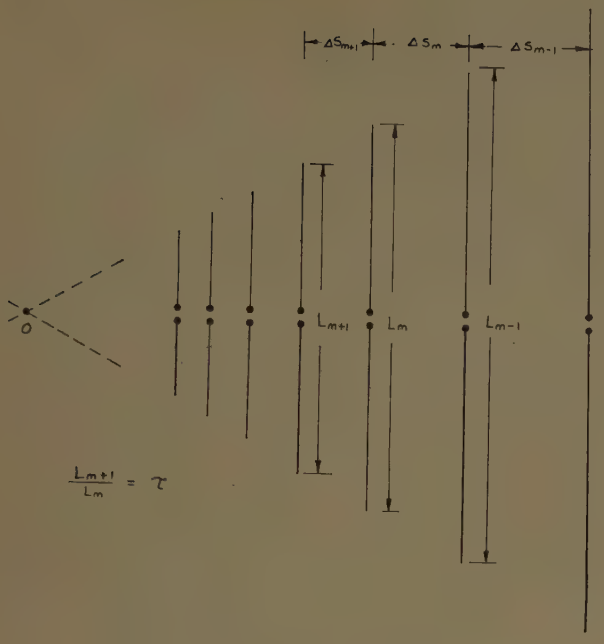

Fig. 1—Side-by-side coplanar array.

are fed in series by means of a common feeder from a generator located at point 0, the infinite structure will possess the property of logarithmic periodicity. That is, whatever the fields produced by an excitation frequency f they will be reproduced (apart from a change of scale) at all other frequencies given by $\tau^n f$. The variation in the fields between these frequencies will depend upon the degree of overlap in the individual element responses.

To be useful as a practical broad-band radiator it must be possible to truncate the array so that at all frequencies above some lower limit the truncated antenna performs like the infinite structure. This imposes a requirement for rapid attenuation of the incident wave along the feeder so that only negligible energy is reflected from the truncated end. If this situation occurs it follows that the array characteristic will be periodic in periods of bandwidth $1/\tau{:}1$. If, furthermore, the variation in performance is negligible over a period then the antenna may be broad banded to any desired degree by simply adding elements according to the general scheme.

Consideration must now be given to the method of feeding the array. Two methods of introducing the common feeder are shown in Fig. 2. In both cases the dipole elements are attached to the feeder so that their respective terminal impedances appear in parallel across the line at the logarithmically varying intervals Δs. In Fig. 2(a) the currents in the elements have the same relationship as the terminal phases so that, considering the elements closely spaced, the phase progression of the currents in the array is to the right. In Fig. 2(b), however, the elements are connected so that a phase constant of π radians is added to the terminal phase of each element. This is accomplished mechanically by twisting the feeder 180° between each element.

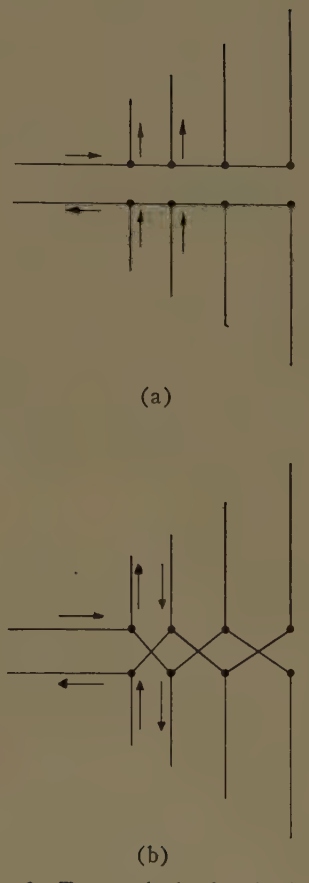

Fig. 2—Two methods of excitation.

A choice between these methods of feeding can be made on the basis of the following reasoning. If the array is to have the property of unlimited bandwidth with constant electrical characteristics, then it is clear that at any given frequency only a portion of the dipole elements can be excited. These elements must be such that the length of the excited portion of the array will be approximately constant in terms of the normalized distance x/λ measured from the array vertex. The elements which are not excited by the feeder should make no contribution to the performance so that coupling with the radiated field would be undesirable. It appears then that the radiation pattern of the array should have a null in the direction of the incident energy on the line. It has been pointed out that the array of Fig. 2(a), is fed so that the element phase progresses to the right, and since this type of excitation is a condition for endfire in that direction this would seem to be an unsatisfactory method. Qualitative consideration of the array of Fig. 2(b), however, provides a more promising picture. In this case the short closely spaced elements are seen to be almost in phase opposition and hence radiate very little energy. Further out along the array where the spacing is larger and the elements are longer, the elements will radiate and the mechanical phase reversal effects a reversal in the direction of phase progression so that the radiation pattern is endfire in the direction of the input terminals. With this method of feeding, the

elements which radiate the most energy will be those near resonant lengths and their combined radiation pattern is toward the array apex as desired. As the frequency is increased the radiating elements appear closer to the apex of the array by an amount proportional to the change in wavelength so that the normalized array length remains approximately constant as the frequency is varied.

An experimental program was carried out to determine the electrical properties of arrays of the type shown in Fig. 2(b), and it was found that this antenna, for certain parameter values, has essentially frequency independent performance over any desired bandwidth.

III. Experimental Results

A. Model Description

The parameters describing the experimental arrays are shown in Fig. 3. The structure is defined in terms of the geometric ratio τ, the angle α, and the characteristic impedance of the feeder. The feeder impedance has not been found to be critical, and for most of this investigation 105 ohm, rigid, open wire line was used. The method of obtaining the 180° phase reversal between elements is shown in the sketch of Fig. 4. The array is fed by means of a coaxial cable brought to the input terminals through one of the balanced line conductors. No balun is required for this method of feeding.

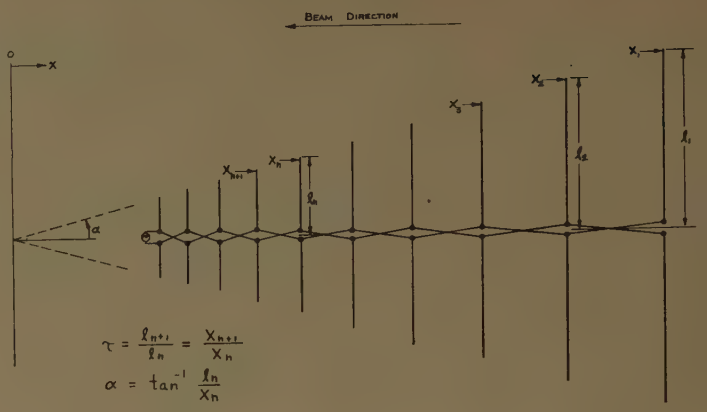

Fig. 3—Schematic diagram of the array.

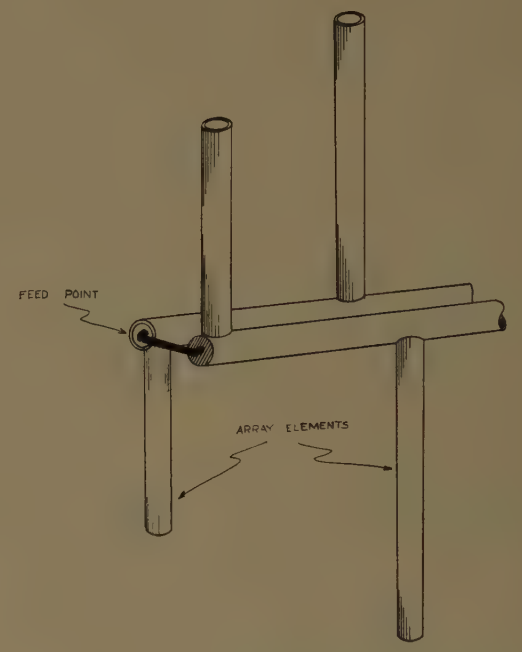

Fig. 4—Connection of elements to balanced feeder.

B. Effect of Truncation

One of the first things to be determined experimentally is the effect of truncation of the array. It is necessary that the electrical properties of the truncated structure converge to characteristic values as the frequency is increased. As previously mentioned, it should be the case that above some low-frequency limit, determined by the maximum physical dimension of the array, the properties are identical to those of the infinite structure.

If the antenna array is thought of as a linear-passive four-terminal network with input terminals at the apex and output terminals at the truncated end then it may be considered as shown in Fig. 5. It is required that for the truncated antenna, the transmitted power P_t, through the network, be only a negligible part of the net power input, $P_i - P_r$. In other words, the transmission coefficient S_{12} of the network, must be small. It is essential that the antenna configuration convert, efficiently, the power incident on the feeder to radiated power P_R. The radiating efficiency is defined as

$$\eta_R = \frac{P_R}{P_i - P_r}.$$

In terms of the scattering coefficients this becomes

$$\eta_R = \frac{1 - |S_{11}|^2 - |S_{12}|^2}{1 - |S_{11}|^2}.$$

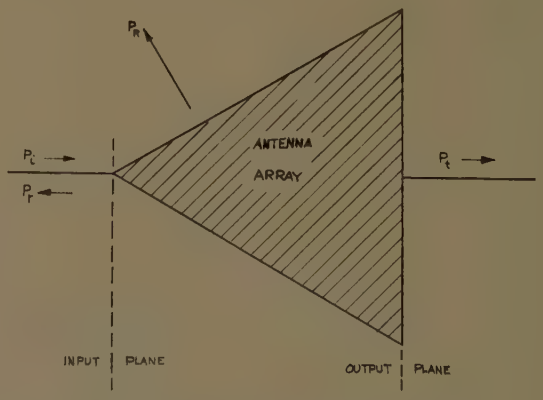

Fig. 5—The array as a two-port network.

Note that the efficiency so defined does not take into account the conductor losses in the elements, and is therefore the true radiating efficiency only in the lossless case.

A simple method of determining the scattering parameters of a two-port network was introduced by Deschamps.[7] With this method, the image of the unit circle in the output plane is determined experimentally and plotted in the input reflection coefficient plane. This is accomplished by a simple series of slotted line measurements of the input reflection coefficient as a function of pure reactive terminations at the output terminals. Determination of the unit image circle and its iconocenter is sufficient for determination of the scattering matrix elements.

The experimental apparatus for making this measurement is shown in Fig. 6. The individual antenna elements were made from thin copper strips formed at one end so that they snap in place on the conductors of the open wire line. This procedure was found to be both simple and satisfactory although care was necessary in making the elements to ensure that they stood perpendicular to the feeder. The pure reactive termination was obtained with a sliding short on the balanced line beyond the antenna elements.

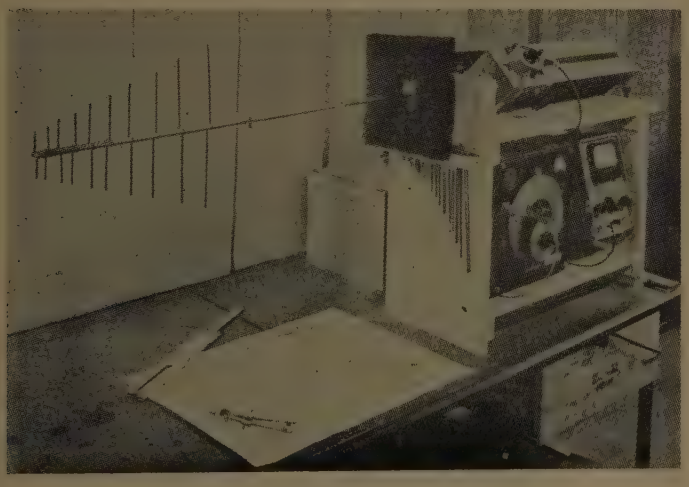

Fig. 6—Measurement apparatus.

The radiating efficiency was measured for several of the arrays as a function of size. This was accomplished by starting with a few small elements near the apex in place and then measuring the scattering coefficients of the network as each additional element was snapped in place. A curve of radiation efficiency as a function of array size is shown in Fig. 7 for one of the models tested. Notice that by the time an element of length $\lambda/2$ is added nearly 80 per cent of the power is being radiated.

[7] G. A. Deschamps, "Determination of reflection coefficients and insertion loss of a waveguide junction," *J. Appl. Phys.*, vol. 24, pp. 1046–1050; August, 1953.

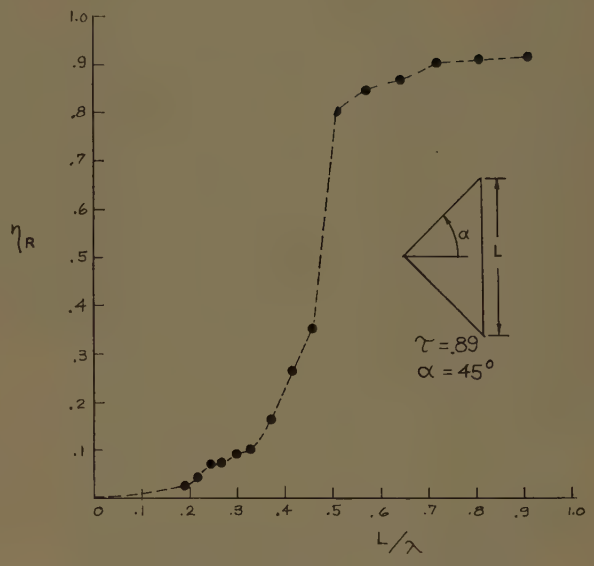

Fig. 7—Radiating efficiency vs antenna size.

C. Input Impedance

The input impedances of the experimental models were measured using the same set up as shown in Fig. 6. The array elements were arranged so that the terminals of the shortest dipole appeared at the junction between the coaxial cable and the balanced line. This procedure effectively truncates the array at both ends providing upper and lower frequency limits accordingly. Between these frequency limits the input impedance was found to behave in a manner characteristic of the design parameters τ and α, and several combinations were investigated.

The results of the impedance measurements are shown in Figs. 8–10. Each figure shows the variation of the input impedance as a function of α for a given value of τ. The solid curve represents the approximate mean resistance level R_0 of the impedance locus and the dashed curve shows the corresponding voltage standing-wave ratio with respect to R_0. If, for example, a 75-ohm coaxial cable is used to feed an array having $\tau = 0.89$ and α of approximately 17°, then the resulting standing-wave ratio on the line will be about 1.2:1 over any desired range, depending on the locations of the two truncations. All impedances were measured with the balanced feeder terminated in a short circuit a distance $l_1/2$ beyond the largest element.

D. Radiation Patterns

The characteristic radiation pattern is an endfire beam in the negative x direction, as indicated in Fig. 3. The beamwidths are nearly constant in both principal planes and the directivity is a function of both τ and α. It is not, therefore, possible to control the pattern independently of the input impedance, but it should be possible to make satisfactory compromises when selecting parameters.

Radiation patterns were measured for the same range of parameters as were the impedances. Figs. 11–13 show how the characteristic radiation patterns vary with α for three values of τ. The estimated directive gain as a function of α is shown in Fig. 14. Cross polarization for these antennas is considerably better than 20 db below pattern maximum, if care is taken with regard to mechanical symmetry. Pattern measurements, like the impedance measurements, were made with the balanced feeder terminated in a short circuit a distance $l_1/2$ beyond the terminals of element l_1.

E. Bandwidth Control

Since the log periodic dipole array may be truncated at both ends and still provide nearly frequency independent performance over some range of frequencies, it is clear that, in the interest of saving size and weight, a particular antenna should be designed to meet the minimum required bandwidth. The upper and lower frequency limits will be determined by lengths of the shortest and longest elements of the array respectively.

To determine this bandwidth for a particular array the antenna shown in Fig. 15 was constructed. This antenna is defined by a τ of 0.95, α equal to 10°, l_1 equal to $2\frac{1}{2}$ inches, and the shortest element half the length of the longest. The array is $7\frac{1}{2}$ inches long and there are a total of fifteen dipoles included.

Radiation patterns for this array are shown in Figs. 16–18 over the band 1100 to 1800 mc, and the directive gain, estimated on the basis of half-power beamwidth, is shown in Fig. 19. The minimum front-to-back ratio is 17 db and the directivity is better than 9 db over isotropic from 1130 to 1750 mc. The variations in the directivity curve correspond closely to the periodicity τ.

A scaled-up model of the array was assembled on the balanced line of the impedance measuring set up of Fig. 6, and its input impedance was measured over a range corresponding to that of the radiation patterns above.

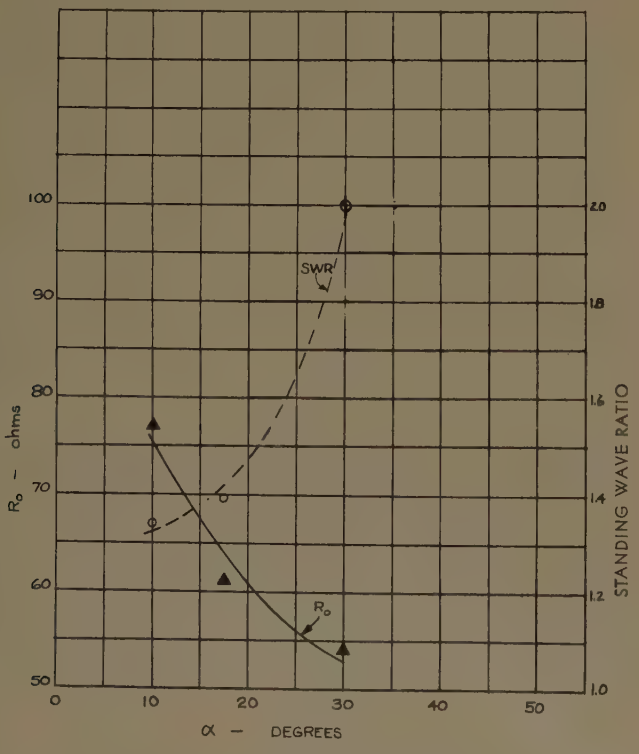

Fig. 8—Input impedance; $\tau = 0.95$.

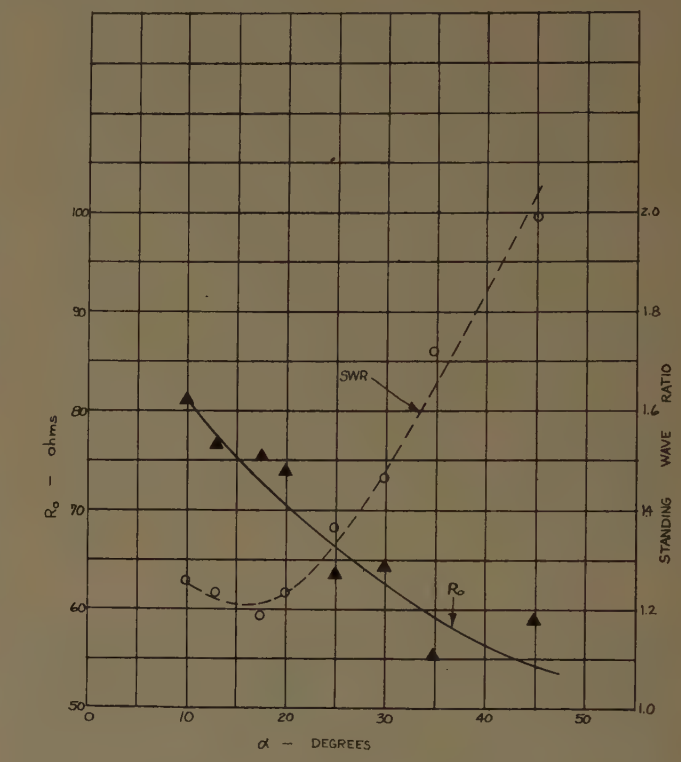

Fig. 9—Input impedance; $\tau = 0.89$.

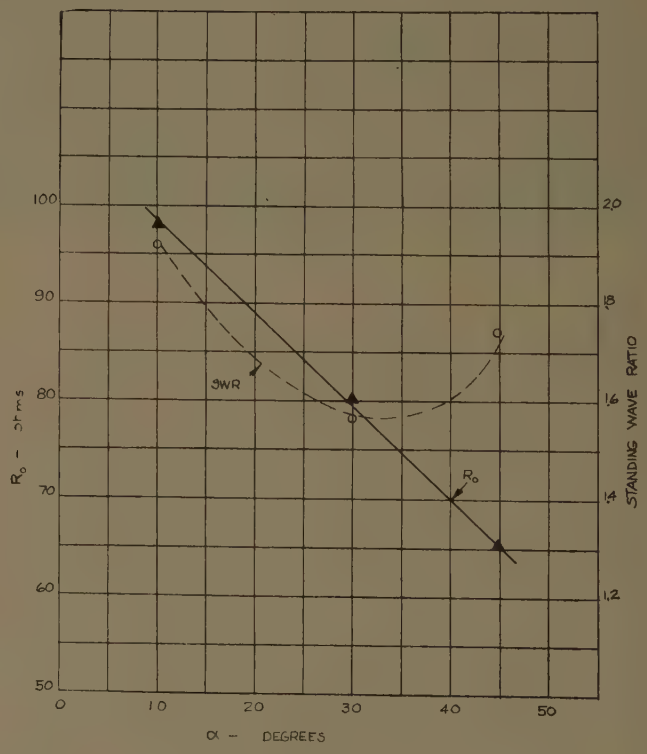

Fig. 10—Input impedance; $\tau = 0.81$.

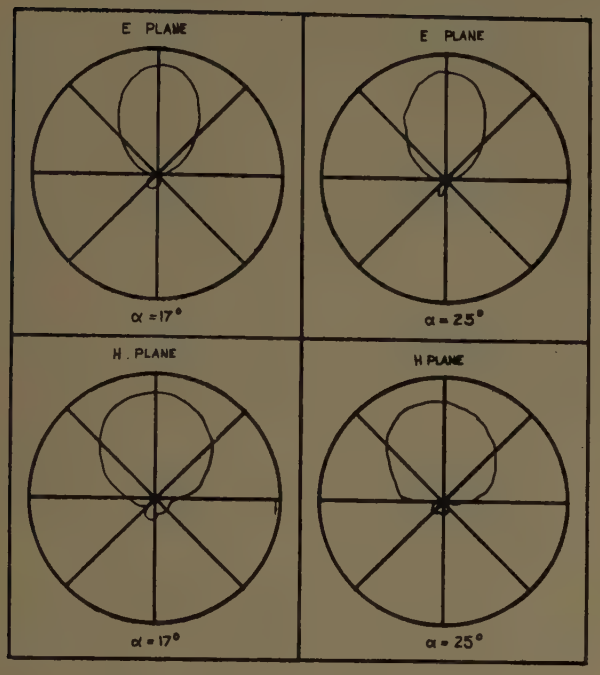

Fig. 11—Typical field patterns; $\tau = 0.95$.

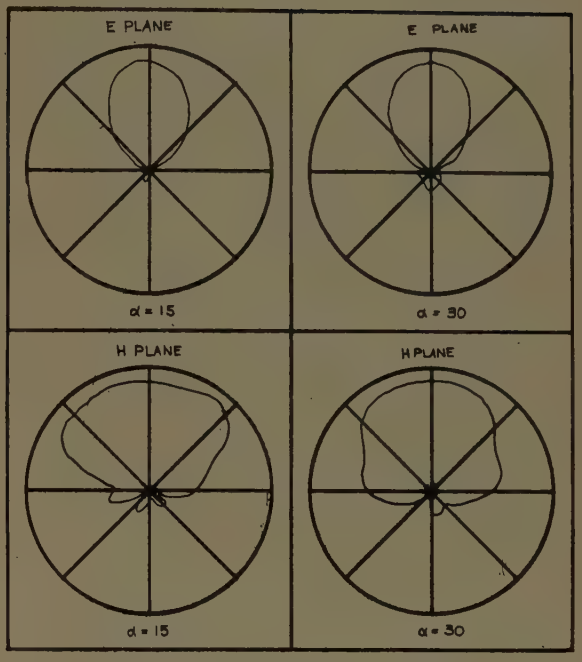

Fig. 13—Typical patterns; $\tau = 0.81$.

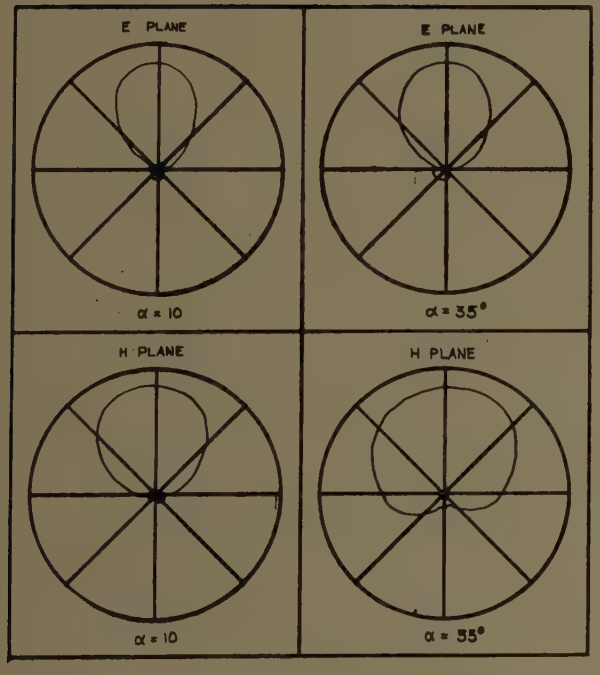

Fig. 12—Typical field patterns; $\tau = 0.89$.

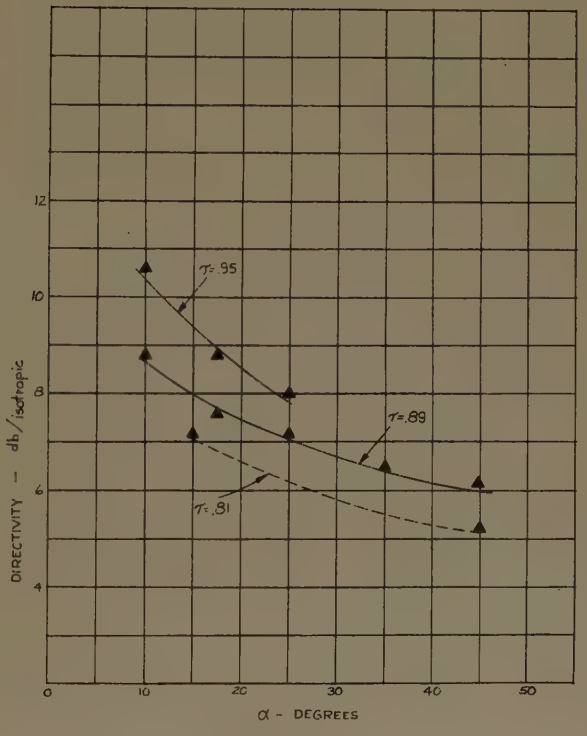

Fig. 14—Directivity vs τ and α.

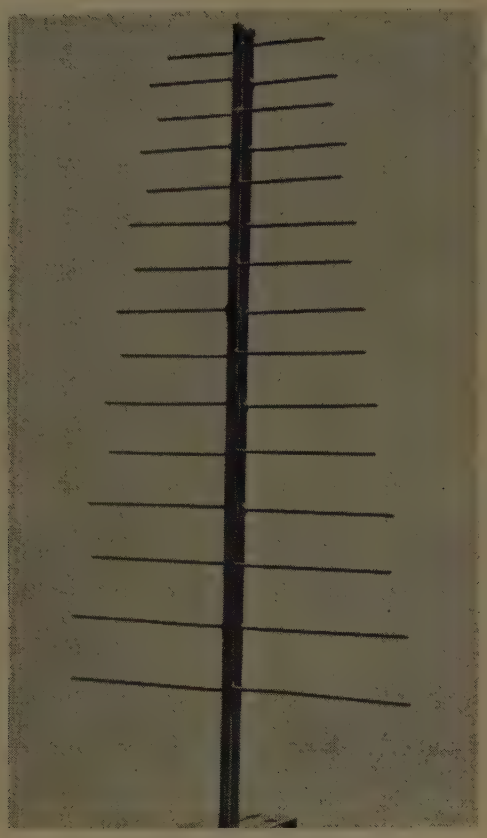

Fig. 15—Bandwidth control model.

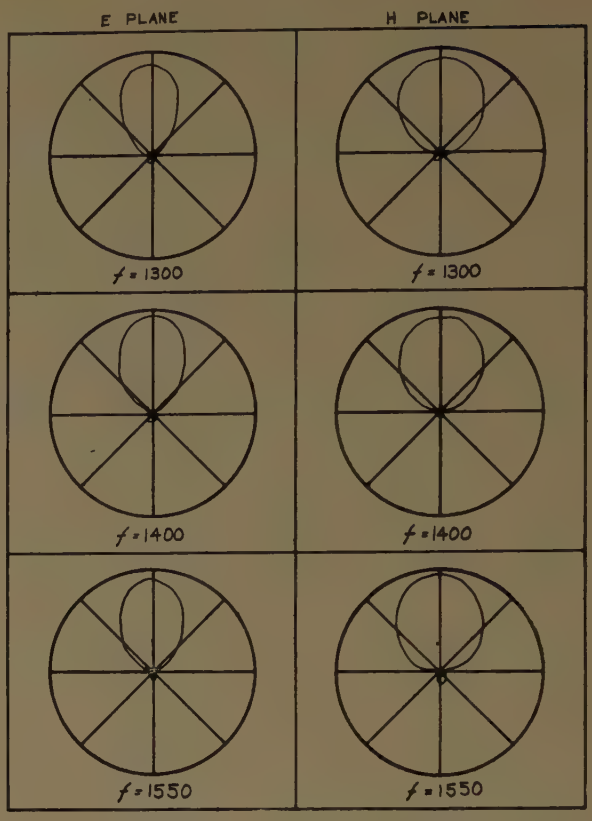

Fig. 17—Field patterns of bandwidth control model.

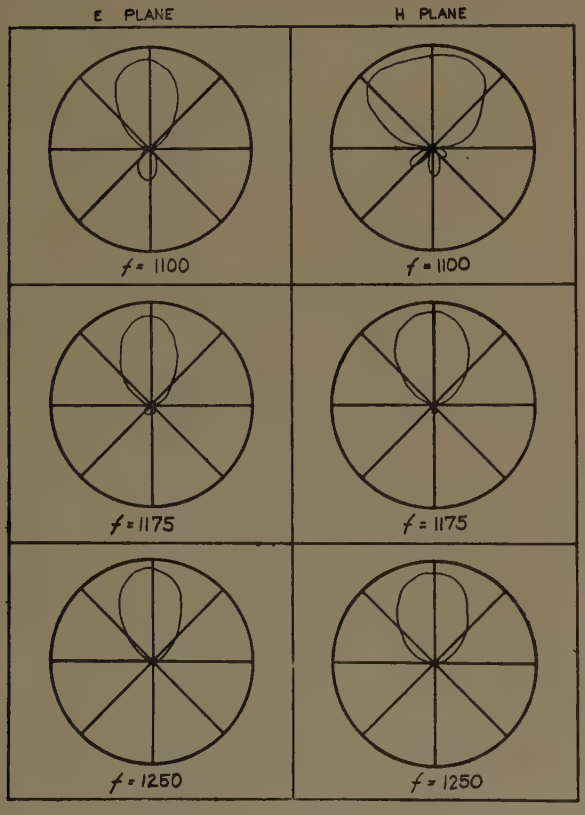

Fig. 16—Field patterns of bandwidth control model.

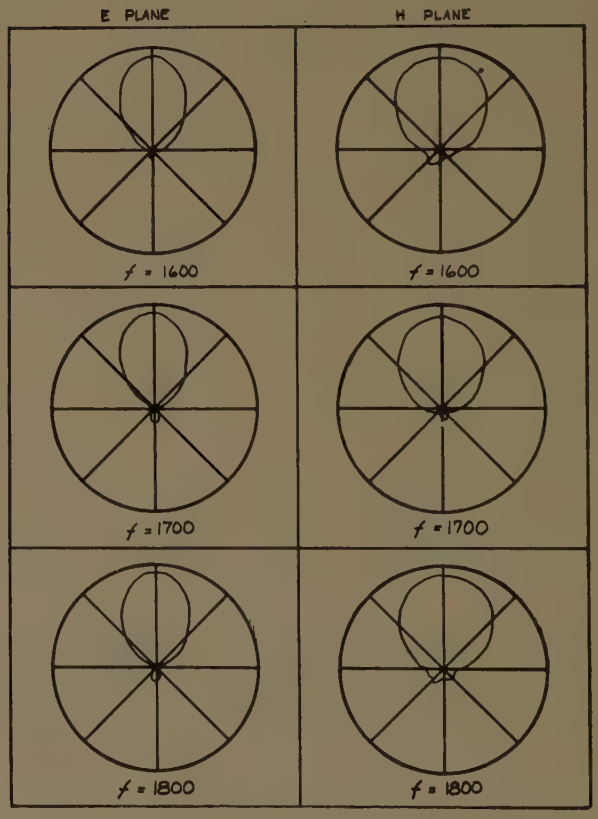

Fig. 18—Field patterns of bandwidth control model.

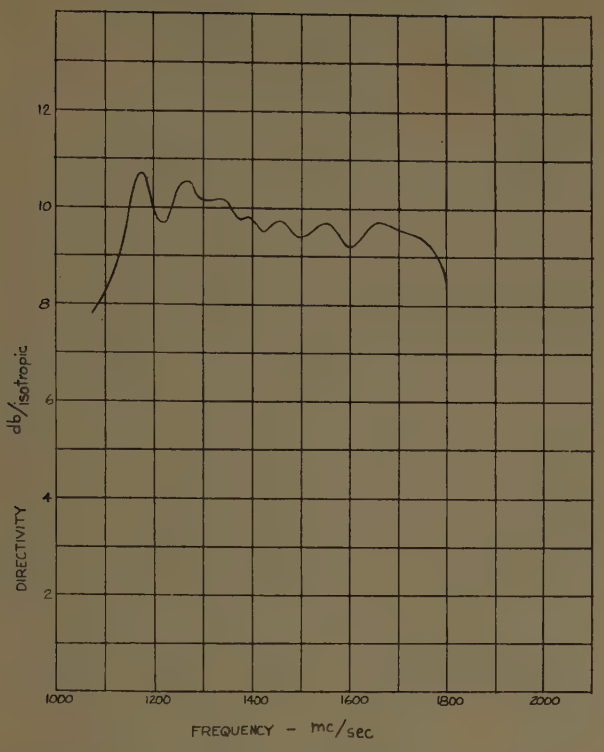

Fig. 19—Directive gain of bandwidth control model.

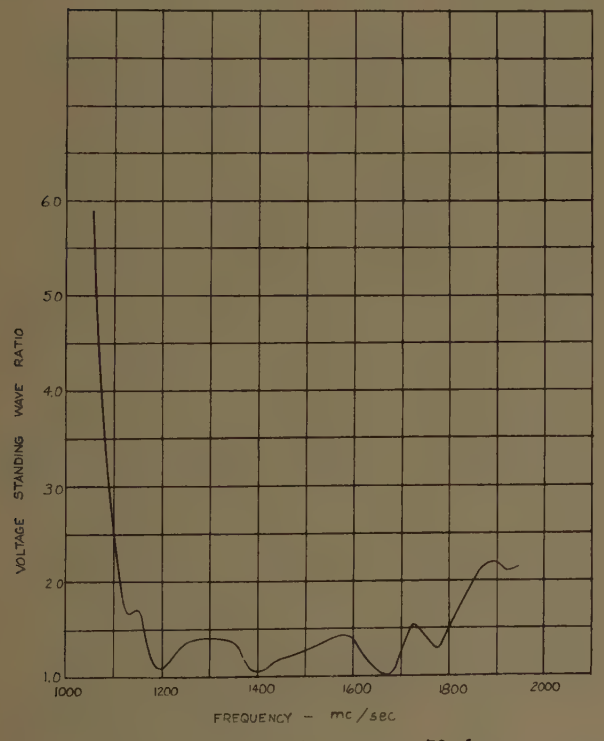

Fig. 20—VSWR with respect to 72 ohms.

The results of this measurement are shown in Fig. 20 in terms of the standing wave ratio produced on a 72-ohm transmission line.

If the usable bandwidth of this antenna is taken to be the range from 1100 to 1800 mc then the size of the antenna for any desired bandwidth is defined. That is, the longest dipole element should be approximately 0.47 frequency long at the lower limit and the shortest element should be about 0.38 wavelength long at the higher wavelength. There will, of course, be some minimum number of elements necessary to provide a suitable front to back ratio at the low frequency limit.

IV. Conclusions

The arrays discussed in the foregoing paragraphs should prove useful in several applications. The model used to demonstrate bandwidth control shows that these antennas will make excellent rotatable beams, superior in many respects to the parasitic types currently in use. It is interesting to compare, for example, the antenna of Fig. 15 to a 5-element Yagi.

A wide-spaced five-element Yagi adjusted to provide a midband front-to-back ratio of 25 db, will provide a 7 per cent bandwidth with a front-to-back ratio of approximately 15 db at the edges. The midband directive gain of this antenna is slightly better than 10 db over isotropic, and its length is about 0.85 wavelength. The log periodic beam of Fig. 15 has fifteen elements but is only 0.73 wavelength long at the low-frequency end. The directivity stays above 9 db with the front-to-back ratio better than 17 db through a bandwidth of 43 per cent, and the elements need no adjusting for this performance.

DuHamel and Berry have shown that the original log periodic elements can be arrayed to provide directivities of up to 20 db, and those same principles may be applied to the dipole array where higher gains are required. Omnidirectional horizontal polarization and unidirectional circular polarization should be achievable by using the methods introduced by DuHamel and Ore.

In addition to the practical usefulness of the log periodic dipole arrays there is another equally interesting and important aspect of the design. The fact that these structures are made up of conventional linear elements seems to invite analysis in terms of familiar transmission line and array theory. To be sure, the problem is not a simple one even so, but its solution would be well worth while in the study of frequency independent antennas. This problem is presently being considered.

Beam Pointing Errors of Long Line Sources*

M. LEICHTER†

Summary—**The relation between the statistics of the antenna beam pointing direction and the phase and amplitude errors at the source has been obtained to first order in the mean-square errors, under certain restrictions, for long line sources. It is shown that when the desired phase at the source is a constant, the results are, to first order, independent of the amplitude errors. When the desired amplitude is also constant, there is a simple formula for computing the allowable rms-phase error at the source when the pointing direction is required to lie in a given angular range with a given probability. When the amplitude distribution corresponds to the Taylor-modified (sin x)/x pattern, the allowed rms-phase error is obtained from the constant-amplitude case by a multiplicative factor which depends only on the one parameter characterizing the Taylor distribution. This function is plotted for the range corresponding to sidelobe ratios of 13.2 to 40 db. At 40 db the allowed rms-phase errors are about three fourths of the allowed rms-phase errors at 13.2 db (constant amplitude) for the same uncertainty in the pointing direction. The results are applied to a hypothetical example and to an actual "Mills Cross" for illustrative purposes.**

I. Introduction

FOR large antennas, as for all complex systems, the analysis of the expected performance must take into account the random errors inherent in the system. Although a substantial number of papers have considered the effects of errors on gain and sidelobe levels,[1] there apparently are very few papers dealing with the effect of such errors on the pointing direction. In a paper on radio astronomy Mills *et al.*[2] derived the mean-square errors in the pointing direction of a linear array consisting of a large number of independent elements with the desired phase constant along the antenna. Rondinelli[3] performed a similar calculation for a two-dimensional array and obtained numerical values for square arrays in which both the desired amplitude and phase were constants. The calculations here are restricted to continuous line sources but the results can, under certain conditions, be compared with the results obtained for linear arrays.[2] Although the radiators of interest are often arrays, there are two reasons why the study of a continuous source was undertaken. First, integrations are much easier to handle than summations; and second, it is not obvious to what extent *the model* of point radiators (independent or not) more accurately characterizes an actual array than the continuous model does.

The desired amplitude and phase are assumed to be symmetric about the center of the antenna but are otherwise arbitrary. However, it is pointed out in Section IV that the results can readily be extended to the scanning of the above antennas. The assumptions made in this paper about the nature of the errors at the source are determined largely by the fact that the continuous source model is used to approximate an array of weakly coupled or independent elements. The errors in amplitude and phase are assumed to be independent with the amplitude errors at each point assumed proportional to the desired amplitude. The proportionality "constant" is assumed to be a stationary, Gaussian random process. The phase errors are also assumed stationary and Gaussian with the autocorrelation function for both phase and amplitude assumed exponential with a decay length very small compared with the antenna length. These points are discussed more fully as they arise. In addition to the above assumptions, many approximations are made in order to obtain a reasonably simple and useful result. It is believed, however, that the essential aspects of the problem have been retained and that the final results are reliable. Some of the more detailed mathematical computations are outlined in the appendixes.

Although this paper is not concerned with the average radiation pattern, it will be discussed in the first part of the analysis because it conveniently introduces the notation, the assumptions, and some of the approximations (which are also used later) without introducing the additional complications that arise in the discussion of the pointing direction.

II. Analysis

A. Average Radiation Pattern

For a one-dimensional line source the field pattern (when the element factor is neglected) is given by

$$E(u) = \int_{-L}^{L} A(x) e^{i\phi(x)} e^{ikux} dx \qquad (1)$$

where the geometry is shown in Fig. 1, and

Fig. 1—Geometry for line source.

$$u = \sin\theta \qquad k = 2\pi/\lambda$$
$$A(x) = \text{amplitude at } x \qquad \phi(x) = \text{phase at } x. \qquad (2)$$

* Manuscript received by the PGAP, February 8, 1960. This paper has been partially supported under Contract No. AF 30(602)-1718, Rome Air Dev. Ctr., Air Res. and Dev. Command.

† System Development Corp., Santa Monica, Calif.; formerly with Microwave Lab., Hughes Aircraft Co., Culver City, Calif.

[1] For further references see R. S. Elliott, "Mechanical and electrical tolerances for two-dimensional scanning antenna arrays," IRE Trans. on Antennas and Propagation, vol. AP-6, pp. 114–120; January, 1958.

[2] B. Y. Mills, A. G. Little, K. V. Sheridan, and O. B. Slee, "A high resolution radio telescope for use at 3.5 m," Proc. IRE, vol. 46, pp. 67–84; January, 1958.

[3] L. A. Rondinelli, "Effect of random errors on the performance of antenna arrays of many elements," 1959 National IRE Convention Record, pt. 1, pp. 174–189.

The radiation pattern $P(u)$ is given by the squared magnitude of (1):

$$P(u) = |E(u)|^2$$

$$= \int\int A(x)A(x')e^{i[\phi(x)-\phi(x')]}e^{iku(x-x')}dxdx'. \quad (3)$$

The limits of integration in (3), as well as in all that follows, are $-L$ and L unless otherwise specified. It will be assumed that the amplitude and phase functions include some random errors, and therefore, they will be written in the form

$$A(x) = A_0(x) + a(x) \qquad \phi(x) = \phi_0(x) + \delta(x) \quad (4)$$

where $A_0(x)$ and $\phi_0(x)$ are the desired amplitude and phase functions. Because of the presence of the random functions $a(x)$ and $\delta(x)$, the antenna pattern can now only be described statistically.

The average radiation pattern is obtained from (3) by averaging the right side. Some assumptions about the statistical properties of $a(x)$ and $\delta(x)$ must be made to carry out this averaging process. First, it is assumed that $a(x)$ and $\delta(x)$ are independent. Physically this means that the amplitude and phase are assumed to be independently controllable. From this assumption it follows that

$$\overline{P(u)} = \int\int \overline{A(x)A(x')}\ \overline{e^{i[\phi(x)-\phi(x')]}}e^{iku(x-x')}dxdx'. \quad (5)$$

For computation of the averages indicated in (5) further assumptions have to be made about the statistics of $a(x)$ and $\delta(x)$. They will be assumed to be normally distributed. Strictly speaking, neither the amplitude errors $a(x)$ nor the phase errors $\delta(x)$ can be normally distributed; the former cannot because the total amplitude $A(x)$ cannot be negative (and hence $a(x)$ cannot be less than $-A_0(x)$), and the latter cannot because it is restricted to the finite interval $(-\pi, \pi)$. However, in many applications the rms error in the phase δ is sufficiently small compared with π so that for all practical purposes the entire area under the normal curve would be included in the interval $(-\pi, \pi)$. In such cases, the effect on the calculations of actually extending the limits on δ to infinity would be negligible. (Even for the rather extreme case of $\sigma_\delta = \pi/2$, the area under the normal curve in the interval $(-\pi, \pi)$ is 0.95.) A similar argument is valid for amplitude errors also, *i.e.*, the rms percentage error $\{\overline{[a(x)/A_0(x)]^2}\}^{1/2}$ may be expected to be small compared to unity and hence, $|a(x)|$ will be generally much less than $A_0(x)$.

With this assumption, the amplitude average indicated in (5) becomes

$$\overline{A(x)A(x')} = A_0(x)A_0(x') + \overline{a(x)a(x')} \quad (6)$$

where use has been made of the fact that odd moments of $a(x)$ vanish. The second term on the right side of (6) is the autocorrelation function of $a(x)$. It will be further assumed that the amplitude errors are proportional to the desired amplitude $A_0(x)$; that is

$$a(x) = \alpha(x)A_0(x) \quad (7)$$

where $\alpha(x)$ is assumed to be a stationary, Gaussian random process. Then

$$\overline{A(x)A(x')} = A_0(x)A_0(x')[1 + \overline{\alpha(x)\alpha(x')}] \quad (8)$$

where $\overline{\alpha(x)\alpha(x')}$ is the autocorrelation function of $\alpha(x)$. It is, however, more convenient to express $\overline{\alpha(x)\alpha(x')}$ in terms of the normalized autocorrelation ρ_α

$$\overline{\alpha(x)\alpha(x')} = \sigma_\alpha^2\rho_\alpha(x - x') \quad \text{where} \quad \sigma_\alpha^2 = \overline{\alpha^2}. \quad (9)$$

Substitution of (9) into (8) yields the desired average in terms of the statistics of the basic random variable $\alpha(x)$:

$$\overline{A(x)A(x')} = A_0(x)A_0(x')[1 + \sigma_\alpha^2\rho_\alpha(x - x')]. \quad (10)$$

If it is assumed that $\phi(x)$ is strictly Gaussian (that is, all joint densities required are also Gaussian), then from the properties of its characteristic function,[4] the phase average indicated in (5) can readily be shown to be given by

$$\overline{e^{i[\phi(x)-\phi'(x)]}} = e^{-\sigma_\delta^2}e^{\sigma_\delta^2\rho_\delta(x-x')}e^{i[\phi_0(x)-\phi_0(x')]} \quad (11)$$

where $\rho_\delta(x)$ is the normalized autocorrelation function of $\delta(x)$. Substitution of (1) and (10) into (5) yields the expression for the average radiation pattern which becomes

$$\overline{P}(u) = e^{-\sigma_\delta^2}\Big[\int\int A_0(x)A_0(x')e^{i[\phi_0(x)-\phi_0(x')]} \cdot e^{\sigma_\delta^2\rho_\delta(x-x')}e^{iku(x-x')}dxdx' + \sigma_\alpha^2\int\int A_0(x)A_0(x')e^{i[\phi_0(x)-\phi_0(x')]}\rho_\alpha(x - x') \cdot e^{\sigma_\delta^2\rho_\delta(x-x')}e^{iku(x-x')}dxdx'\Big] \quad (12)$$

$$= e^{-\sigma_\delta^2}[I_1 + \sigma_\alpha^2 I_2] \quad (13)$$

where I_1 and I_2 are the two integrals above. The above formulation is similar to that of Ruze,[5] where the average radiation pattern is studied in more detail by expanding the integrand as a power series in σ_δ^2. Here, however, we shall need only the "zero-order" approximation which is obtained by keeping only the first term in the expansion. Using also the fact that σ_α^2 has been assumed to be small compared to one, the zero-order approximation for (13) is

$$\overline{P}_0(u) = e^{-\sigma_\delta^2}P_d(u) \quad (14)$$

where $P_d(u)$ is the desired radiation pattern.

[4] J. L. Lawson and G. E. Uhlenbeck, "Threshold Signals," McGraw-Hill Book Co., Inc., New York, N. Y., p. 46; 1950.

[5] J. Ruze, "The effect of aperture errors on the antenna radiation pattern," *Nuovo Cim. Suppl.*, vol. 9, pp. 364–380; 1952.

B. Pointing Direction

The pointing direction will be defined as the "angle" u_p at which the slope S of the radiation pattern is zero; *i.e.*, u_p is the angle such that

$$S(u_p) = \left[\frac{dP}{du}\right]_{u=up} = 0. \tag{15}$$

Although the slope will be zero at the peaks of all the sidelobes as well as at the peak of the main lobe, only the latter will be considered. As emphasized by the quotation marks, u_p is not an angle since $u = \sin\theta$. However, the angles of interest will always be so small that for all practical purposes u and θ will be equal.

The statistics of u_p are found by computation of $S(u)$ in general and by the use of (15) and (3):

$$S(u) = \iint ik(x - x')A(x)A(x') \cdot e^{i[\phi(x)-\phi(x')]}e^{iku(x-x')}dxdx'. \tag{16}$$

For any particular $A(x)$ and $\phi(x)$, the pointing direction u_p is obtained by solving

$$S(u) = 0. \tag{17}$$

This, of course, cannot be done in general. However, for small errors, it is to be expected that for most functions, $A(x)$ and $\phi(x)$, u_p will be quite small and therefore (17) can be replaced by a linear approximation

$$S(u) \cong S(0) + S'(0)u = 0, \tag{18}$$

the solution of which yields the pointing direction.

It is convenient to denote $S(0)$, the slope at $u=0$, by v and to denote $-S'(0)$, the negative of the curvature at $u=0$ (which is negative), by w. Then the solution of (18) may be written as

$$u_p = v/w. \tag{19}$$

Since the random variable w is expected to be sharply peaked about its large average value $\bar{w}$, the above expression can be further simplified without significant error by replacing w by $\bar{w}$.

On the other hand v, the slope at $u=0$, is just as likely to be positive as negative, and since its value is determined by the contributions from a large number of sources, it may be assumed to be normally distributed. Then u_p is also normally distributed, and only its dispersion $\overline{u_p^2}$ need be calculated (since $\overline{u_p}$ is obviously zero):

$$\overline{u_p^2} = \overline{v^2}/\bar{w}^2. \tag{20}$$

For the computation of $\bar{w}$, the explicit expression for w is obtained from its definition and (16):

$$w = k^2 \iint (x - x')^2 A(x)A(x')e^{i[\phi(x)-\phi(x')]}dxdx'. \tag{21}$$

The calculation $\bar{w}$ is essentially the same as the calculation of $\overline{P}$ of Section II-A. Furthermore, since $\bar{w}$ is large, only the zero-order approximation $\bar{w}_0$ is needed, which, by analogy with (14), is given by

$$\bar{w}_0 = e^{-\sigma\delta^2}\left[\frac{dS_d(u)}{du}\right]_{u=0} = e^{-\sigma\delta^2}\left[\frac{d^2P_d(u)}{d^2u}\right]_{u=0}. \tag{22}$$

Next, consider the numerator in (20). Using the definition of v and (16) the expression for $\overline{v^2}$ becomes

$$\overline{v^2} = -k^2 \iiiint (x - x')(x'' - x''')\overline{A(x)A(x')A(x'')A(x''')} \cdot \overline{e^{i[\phi(x)-\phi(x')+\phi(x'')-\phi(x''')]}}\, dxdx'dx''dx'''. \tag{23}$$

With the use of (4), (7), and (9) the above amplitude average may be written as

$$\overline{A(x)A(x')A(x'')A(x''')} = \mathfrak{A}_0(x, x', x'', x''') + R_\alpha(x, x', x'', x''') + Q(x, x', x'', x''') \tag{24}$$

where

$$\mathfrak{A}_0 = A_0(x)A_0(x')A_0(x'')A_0(x''') \tag{25}$$

$$R_\alpha = \mathfrak{A}_0\sigma_\alpha^2[\rho_\alpha(x - x') + \rho_\alpha(x - x'') + \rho_\alpha(x - x''') + \rho_\alpha(x' - x'') + \rho_\alpha(x' - x''') + \rho_\alpha(x'' - x''')]. \tag{26}$$

and

$$Q = \mathfrak{A}_0\overline{\alpha(x)\alpha(x')\alpha(x'')\alpha(x''')}. \tag{27}$$

For the derivation of (24), use has been made of the fact that for a Gaussian process all the odd moments vanish. The right side of (27) can be expressed in terms of σ_α and ρ_α,[6] but since it turns out to be of fourth order in σ_α and of second order in ρ_α, Q shall be neglected in the calculations.

The evaluation of the average of the exponential in (23) is similar to the process leading to (11) and the result is

$$\overline{e^{i[\phi(x)-\phi(x')+\phi(x'')-\phi(x''')]}} = e^{-2\sigma\delta^2}e^{i\psi_0(x,x',x'',x''')}e^{-\sigma\delta^2 R_\delta(x,x',x'',x''')} \tag{28}$$

where

$$\psi_0 = \phi_0(x) - \phi_0(x') + \phi_0(x'') - \phi_0(x''') \tag{29}$$

and

$$R_\delta = \rho_\delta(x - x'') + \rho_\delta(x' - x''') - \rho_\delta(x - x') - \rho_\delta(x - x''') - \rho_\delta(x' - x'') - \rho_\delta(x'' - x'''). \tag{30}$$

Substitution of (28) and (24) into (23) yields

$$\overline{v^2} = k^2e^{-2\sigma\delta^2} \iiiint (x - x')(x'' - x''')(\mathfrak{A}_0 + R_\alpha)e^{i\psi_0} \cdot e^{-\sigma\delta^2 R_\delta}dxdx'dx''dx''' \tag{31}$$

or

$$\overline{v^2} = -k^2e^{-2\sigma\delta^2}[L_1 + L_2] \tag{32}$$

[6] H. J. Laning and R. H. Battin, "Random Processes in Automatic Control," McGraw-Hill Book Co., Inc., New York, N. Y., p. 83; 1956.

where L_1 and L_2 are the two integrals corresponding to the A_0 and R_α respectively in (31). The integral involving Q has been dropped for the reasons mentioned above. Exp $(-\sigma_\delta^2 R_\delta)$ is expanded in a power series in σ_δ^2, (as it is by Ruze[5]) and L_1 and L_2 are written in the form

$$L_1 = \sum_{m=0}^{\infty} \frac{(-1)^m}{m!} \sigma_\delta^{2m} L_{1m} \qquad L_2 = \sum_{m=0}^{\infty} \frac{(-1)^m}{m!} \sigma_\delta^{2m} L_{2m} \quad (33)$$

where

$$L_{1m} = \int\int\int\int (x - x')(x'' - x''') \mathcal{A}_0 \cdot e^{i\psi_0} R_\delta^m dx dx' dx'' dx''' \quad (34)$$

and

$$L_{2m} = \int\int\int\int (x - x')(x'' - x''') R_\alpha \cdot e^{i\psi_0} R_\delta^m dx dx' dx'' dx'''. \quad (35)$$

The terms in (33) will in general decrease rapidly with m and L_1, and L_2 will be computed only to the first order. The $m=0$ term in L_1 is of zero order but in L_2 the $m=0$ term is of first order since R_α is proportional to σ_δ^2 (26). Since the slope is generally very small, it might be expected that the zero-order contribution to $\overline{v^2}$ would vanish. This can easily be seen to be the case from (34) because both $\mathcal{A}_0$ and ψ_0 are even functions (whenever the desired amplitude $A_0(x)$ and phase $\phi_0(x)$ are even functions) so that the four integrands obtained from (34) are all odd, and hence, $L_{10}=0$. Thus, there remains the problem of evaluating the two terms L_{11} and L_{20}. The L_{11} term may be written as the sum of six terms since R_δ (30) is the sum of six terms:

$$L_{11} = \sum_{m=1}^{6} L_{11}^{(m)}. \quad (36)$$

To compute the individual terms in (36), it is necessary to make some specific assumption about the phase-correlation function $\rho_\delta(x)$. We shall only assume that the correlation $\rho_\delta(x)$ goes to zero rapidly for $x>\Delta$, where Δ is a distance which depends on the geometry and physics of the particular antenna and is very small compared to the length of the antenna. It is convenient to choose $\rho_\delta(x)$ to be given by

$$\rho_\delta(x) = e^{-|x|/\Delta}. \quad (37)$$

The first term on the right side of (36) is therefore given by

$$L_{11}^{(1)} = \int\int\int\int (x - x')(x'' - x''') \mathcal{A}_0 \cdot e^{i\psi_0} e^{-|x-x''|/\Delta} dx dx' dx'' dx''' \quad (38)$$

where (37) has been used. The other five terms of (36) are the same as (38) except that the argument of the autocorrelation function $|x-x''|$ is replaced by some other appropriate argument as given by (30). These integrals are evaluated in Appendix I and the final result for L_1 is

$$L_1 \cong -\sigma_\delta^2 L_{11} = -4\Delta\sigma_\delta^2 [D \mid E_d(0) \mid^2 + \mathrm{Re}\{C^* E_d^2(0)\}] \quad (39)$$

where

$$D = \int_{-L}^{L} [x A_0(x)]^2 dx \qquad C = \int_{-L}^{L} [x A_0(x) e^{i\phi_0(x)}]^2 dx \quad (40)$$

and $E_d(0)$ is the desired amplitude at $u=0$:

$$E_d(0) = \int_{-L}^{L} A_0(x) e^{i\phi_0(x)} dx. \quad (41)$$

The term L_{20} can also be written as the sum of six terms since R_α (26) is the sum of six terms:

$$L_{20} = \sum_{m=1}^{6} L_{20}^{(m)}. \quad (42)$$

To evaluate the above, we assume that the amplitude-correlation function is also given by (37). Then, since R_α and R_δ are very similar functions, the results of Appendix I can be used also to evaluate L_{10} by making the appropriate change in variables and signs. The final result for L_2 is

$$L_2 \cong L_{20} = 4\Delta\sigma_\delta^2 [\mathrm{Re}\{C^* E_d^2(0)\} - D \mid E_d(0) \mid^2]. \quad (43)$$

Eqs. (43) and (39) combine with (32) to become

$$\overline{v^2} \cong \Delta(2ke^{-\sigma_\delta^2})^2 \{ D(\sigma_\delta^2 + \sigma_\alpha^2) \mid E_d(0) \mid^2 + (\sigma_\delta^2 - \sigma_\alpha^2) \mathrm{Re}\,[C^* E_d^2(0)] \}. \quad (44)$$

This essentially concludes the calculation of the statistics of the pointing direction u_p, since both the numerator and denominator of (20) have now been computed. Hence $\overline{u_p^2}$ is now explicitly expressed in terms of the mean-square phase and amplitude errors as given by (44) and (22).

Sometimes one is interested not only in the relation between the mean-square errors in phase, amplitude, and pointing direction but also in the probability, $P(\gamma)$, that the pointing direction lies in the angular range $(-\gamma, \gamma)$. Since u is normally distributed, the required relation is given by

$$\frac{\gamma^2}{a_P} = \sigma_p^2 = \frac{\overline{v^2}}{\bar{w}_0^2} \quad (45)$$

where a_P is the argument of the error integral corresponding to the given $P(\gamma)$. Of course u_p is normally distributed only in a restricted range which will be discussed in Section IV.

III. Application to Constant Phase Antennas

The above results will be applied to two particular aperture distributions both having constant phase $\phi_0=0$. In the first case the amplitude will be constant $(A_0=1)$ while in the second example a Taylor-modified $(\sin x)/x$

distribution (hereafter referred to simply as a Taylor distribution) will be assumed. (Although the constant distribution is a special case of a Taylor distribution, the calculations are so much simpler in this special case that is it worthwhile treating it as a separate example.)

The condition $\phi_0=0$ leads to a considerable simplification in the expression for $\overline{v^2}$ (44). From (40) it can be seen that in this case $C=D$, and both C and $E_d(0)$ (41) are real. Under these conditions (44) becomes

$$\overline{v^2} = 2\Delta C[2k\sigma_\delta E_d(0)e^{-\sigma_\delta^2}]^2. \tag{46}$$

An interesting point to note is that the results are independent of σ_α^2; *i.e.*, if the desired aperture distribution has no phase variation, the statistics of the pointing direction are, to first order in σ_α^2, independent of the amplitude errors. (The fact that amplitude errors yield only second-order effects for constant-phase antennas, has been noted also by Mills, *et al.*[2].)

A. Constant Amplitude

When $A_0(x)=1$, $\overline{v^2}$ and $\overline{w}_0$ can be evaluated explicitly. First, consider $\overline{w}_0$, which is given by (22). This calculation requires the determination of the desired radiation pattern $P_d(u)$ which is obtained from the desired amplitude field pattern $E_d(u)$:

$$E_d(u) = \int_{-L}^{L} e^{ikux}dx = 2L\frac{\sin\beta}{\beta} \tag{47}$$

where

$$\beta = kuL. \tag{48}$$

Therefore,

$$P_d(u) = \left[2L\frac{\sin\beta}{\beta}\right]^2 \tag{49}$$

and the combination of this with (22) gives the result

$$\bar{w}_0^2 = \left[\frac{2}{3}(2kL^2)^2e^{-\sigma_\delta^2}\right]^2. \tag{50}$$

In $\overline{v^2}$, as given by (46), the only unknown factor is C defined in (40):

$$C = \int_{-L}^{L} x^2dx = \frac{2}{3}L^3. \tag{51}$$

The combination of the above expressions with (45) for the solution of σ_δ yields the following:

$$\sigma_\delta = \frac{kL\gamma}{a_P}\sqrt{\frac{L}{3\Delta}}. \tag{52}$$

It is preferable to express the above in terms of the ratio γ/γ_0 where γ_0 is the angle to the first null given by $\gamma_0=\lambda/2L$. Then the relation between the allowed rms error in phase σ_δ, the specified angular accuracy γ, and the specified probability P is, for constant phase and amplitude, given by

$$\sigma_\delta(P,\gamma) = \frac{\pi}{a_P}\frac{L}{3\Delta}\frac{\gamma}{\gamma_0}. \tag{53}$$

B. Taylor-Modified (sin x)/x Distribution

The Taylor distribution function[7] is given by

$$A_0(x) = J_0(ib\sqrt{L^2-x^2}) \tag{54}$$

where J_0 is the usual Bessel function. When $b=0$, the above reduces to the previous example, thus providing a useful check in the following calculations which are much more involved than the ones above. As in the first example, the desired field pattern and the constant C must be computed in order to express σ^2 in terms of the antenna parameters.

Fortunately, the field pattern corresponding to (54) is known to be[7]

$$E_d(u) = \frac{2L\sin\sqrt{\beta^2-\alpha^2}}{\sqrt{\beta^2-\alpha^2}} \tag{55}$$

where

$$\beta = kuL \quad \text{and} \quad \alpha = bL. \tag{56}$$

(The parameter b used here is related to the parameter B in Taylor[7] by $bL=\pi B$.) Again, after computation of the denominator of (48) which requires the calculation of the second derivative of $[E_d(u)]^2$ at $u=0$, the result, after some algebra, is

$$\bar{w}_0 = 2\left(\frac{2kL^2}{\alpha^2}\right)^2\sinh\alpha(\alpha\cosh\alpha-\sinh\alpha)e^{-\sigma_\delta^2}. \tag{57}$$

The determination of C requires the evaluation of the integral

$$C = \int_{-L}^{L} x^2J_0^2(ib\sqrt{L^2-x^2})dx. \tag{58}$$

The integration is outlined in Appendix II. The result is

$$C = \left(\frac{L}{2\alpha}\right)^3G(\alpha) \tag{59}$$

where

$$G(\alpha) = (4\alpha^2-1)\int_0^{2\alpha} I_0(x)dx + 2\alpha[I_0(2\alpha)-2\alpha I_1(2\alpha)] \tag{60}$$

and $I_0(x)$ and $I_1(x)$ are the usual modified Bessel functions. The integral in (60) has been tabulated.[8] The

[7] T. T. Taylor, "One Parameter Family of Line Sources Producing Modified Sin $\pi u/\pi u$ Patterns," Hughes Aircraft Co., Tech. Memo. No. 324, p. 5; September, 1953.

[8] M. Rothman, "Table of $\int_0^x I_0(x)dx$," *Quart. J. Appl. Math.*, vol. 2, pp. 212–217; April, 1949.

combination of (59), (57), (55), and (47) with (45) for the solution of σ_δ^2 yields the generalization of (53) to antennas with Taylor distributions (characterized by the parameter α) which is

$$\sigma_\delta(P, \gamma, \alpha) = f(\alpha)\sigma_\delta(P, \gamma, 0) \tag{61}$$

where

$$f(\alpha) = 4\sqrt{3}\,\frac{\cosh \alpha - \sinh \alpha}{\alpha\sqrt{\alpha G(\alpha)}} \tag{62}$$

and $\sigma_\delta(P, \gamma, 0)$ is given by (53). The above result implies that $f(o) = 1$ which is verified below.

As α increases, $A_0(x)$ becomes more sharply peaked, and the beamwidth increases. Under these conditions it would be expected that the allowable phase errors decrease for a given accuracy in the pointing direction. This means that $f(\alpha)$ should be a decreasing function of α. In Fig. 2, $f(\alpha)$ is plotted in the range $(0, 1.75\pi)$ corresponding to sidelobe ratios from 13.2 to 40 db.[7]

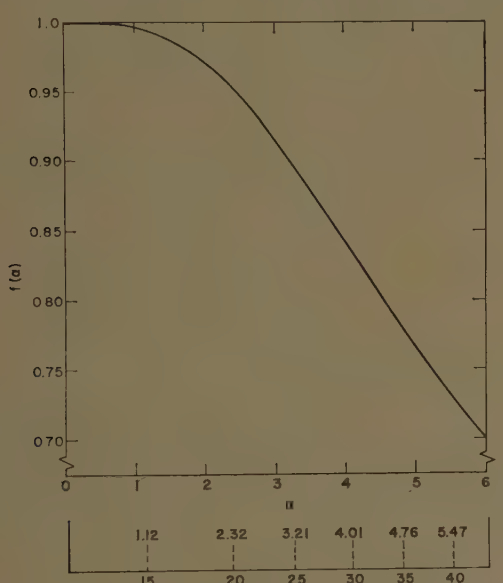

Fig. 2—Plot of $f(\alpha)$, multiplicative factor which converts allowed rms error for uniform distribution to the corresponding value for Taylor-modified $(\sin x)/x$ distributions characterized by the parameter a. The values of a corresponding to the sidelobe ratios (in $-$db) are indicated in the lower scale.

For α, beyond the range plotted in Fig. 2, $f(\alpha)$ is given approximately by

$$f(\alpha) \cong 2\pi^{1/4}\alpha^{-3/4} \qquad \alpha > 6.$$

IV. Discussion

A. Scanning

Although the calculation above is based on the assumption that the desired phase and amplitude are symmetrical, only a slight modification is necessary to extend the results to the scanning of such antennas. If the antenna is scanned to point in the direction θ_s, then it is only necessary to multiply all lengths measured along the antenna by $\cos \theta_s$ since for moderate scan angles the antenna now is effectively shorter by the factor $\cos \theta_s$.[9] In applying this correction to the result given in (53), it is to be noted that the ratio L/Δ remains unchanged but the factor γ_0 is replaced by $\gamma_{0s} = \gamma_0/\cos \theta_s$. Therefore, the allowed rms error as given by (53) (for constant amplitude) becomes

$$\sigma_{\delta,s}(P, \gamma) = \cos \theta_s \sigma_\delta(P, \gamma).$$

It is of course reasonable that the tolerance in error becomes smaller because the antenna is effectively shorter. In the more general result given by (61) no further changes are necessary since α is unaffected by scanning. Therefore, for scanned antennas with Taylor distributions that allowed rms error in phase is related to the broadside case by the factor $\cos \theta_s$ (just as in the constant-amplitude case).

At the end of Section II, it was mentioned that the range of validity of the Gaussian approximation for the distribution of the pointing direction would be discussed. It will be recalled that the Gaussian distribution was a result of the linear approximation assumed in (21). Therefore, it is necessary to investigate the conditions under which the higher-order terms are in fact negligible compared with the ones retained. The details will not be given here,[10] but it is clear that for small errors the range of validity of the linear approximation is determined primarily by the desired radiation pattern. If it is assumed that the linear approximation is "good" when the first neglected term is less than one-tenth of the last term retained, then it can be shown that for the constant-amplitude case the Gaussian distribution is good to about 0.2 γ_0 where γ_0 is the angle to the first null. For the Taylor distribution, the corresponding range increases and at 40 db it is about 1.4 of the original value.

B. Application to Linear Arrays

If the continuous line source is an approximation to a linear array of independent elements, then, as mentioned earlier, it is reasonable to choose Δ in (37) to be the element spacing because the correlation function would be expected to go rapidly to zero when that distance is exceeded. Two particular arrays will now be considered to illustrate the results derived above.

1) Let the given array consist of 250 elements spaced a half-wavelength apart, and assume that the pointing direction is to lie in the range (-0.001 radian, 0.001 radian) with 0.99 probability. The amplitude distribution is to be Taylor with 30-db sidelobe ratio. The allowed rms-phase error is desired.

The required answer is given by (61) with $P = 0.99$, $\gamma = 0.001$ and $\alpha = 4$ (the last value is obtained either

[9] R. W. Bickmore, "A note on the effective aperture of electrically scanned arrays," IRE Trans. on Antennas and Propagation, vol. AP-6, pp. 194–197; April, 1958.

[10] M. Leichter, "Beam Pointing Errors of Long Line Sources," Hughes Aircraft Co., Tech. Memo. No. 588, pp. 26–28; April, 1959.

from Taylor[7] or from the information in Fig. 2). The second factor in (61) represents the allowed rms error for the constant-amplitude case and is given by (53). Since the spacing between elements is $\lambda/2$, Δ is also chosen as $\lambda/2$ and antenna length $=2L=250\lambda/2=125\lambda$ and hence, $\gamma_0=\lambda/2L=1/125$. Finally, the value of a_P, as found in tables of the error integral, corresponding to $P=0.99$, is 2.58. Substitution of these values into (53) yields σ_δ (0.99, 0.001) $=0.78$ radian. From Fig. 2 it is found that $f(4)=0.85$ and therefore, the required answer is

$$\sigma_\delta(0.99, 0.001, 4) \cong 38 \text{ degrees.}$$

2) As a second example, a particular "Mills Cross" array will be considered for which the rms error in pointing direction has been obtained on the assumption that the elements are independent.[2] The given data are $2L=1500$ feet, number of elements $=250$, and wavelength$\cong$11.5 feet. In an earlier paper[11] the distribution for this antenna is specified as Gaussian, and, according to the data given, the distribution corresponds approximately to a Taylor distribution with $\alpha=4$.

In this example, only the relation between the rms-phase error and the rms-pointing error is required. Therefore, since $\sigma_p=\gamma/\partial_P$, (61) and (52) combine to yield

$$\sigma_\delta = f(\alpha)\frac{\pi\sigma_p}{\gamma_0}\sqrt{\frac{L}{3\Delta}}.$$

When the numerical values are substituted into the above, with $\Delta=2L/250=12$ feet, the relation between the two rms values becomes

$$\sigma_p \cong 4.3 \times 10^{-4}\sigma_\delta.$$

According to Mills *et al.*[2] "an rms-phase error of 10° leads to a probable collimation error of about $\frac{1}{4}$ minute of arc." For $\sigma_\delta=10°$, the above yields $\sigma=0.26$ minute which agrees with the quoted value.

Appendix I

To evaluate (38), note first that since $A_0(x)$ and $\phi_0(x)$ are even functions, the integrand is an odd function of x' and x'''. Therefore, of the four terms obtained from $(x-x')$ $(x''-x''')$, only one yields a nonvanishing integral

$$L_{11}^{(1)} = \left[\int\int_{-L}^{L} xx''A_0(x)A_0(x'') \cdot e^{-|x-x''|/\Delta}e^{i[\phi_0(x)+\phi_0(x'')]}dxdx'\right] \cdot \left[\int\int_{-L}^{L} A_0(x')A_0(x''')e^{-i[\phi_0(x')+\phi_0(x''')]}dx'dx'''\right]. \quad (63)$$

The second integral is just the square of the complex conjugate of the desired field pattern in the forward direction

$$\left[\int_{-L}^{L} A_0(x)e^{-i\phi_0(x)}dx\right]^2 = [E_d^*(0)]^2. \quad (64)$$

The first integral may be written as an iterated integral, and then (63) becomes

$$L_{11}^{(1)} = 2[E_d^*(0)]^2\int_0^{2L} e^{-y/\Delta}C(y)dy \quad (65)$$

where

$$C(y) = \int_{y-L}^{L} x(x-y)A_0(x)A_0(x-y)e^{i[\phi_0(x)+\phi_0(x-y)]}dx. \quad (66)$$

Since Δ is very small compared with $2L$, and since $C(y)$ is a slowly varying function for any reasonable antenna, the integral in (65) can be approximated by expanding $C(y)$ about the origin and extending the upper limit to infinity. This yields

$$L_{11}^{(1)} \cong 2\Delta C(0)[E_d^*(0)]^2 \quad (67)$$

where

$$C(0) = \int_{-L}^{L} x^2A_0^2(x)e^{2i\phi_0(x)}dx. \quad (68)$$

The second term $L_{11}^{(2)}$ differs from $L_{11}^{(1)}$ only in that the argument of the correlation function, as obtained from (4), is now $|x'-x'''|$. By proceeding then exactly as above, the result is

$$L_{11}^{(2)} = 2\Delta C^*(0)[E_d(0)]^2 = [L_{11}^{(1)}]^*. \quad (69)$$

In the third term $L_{11}^{(3)}$, the argument of the correlation function is $|x-x'|$. From (38) it can be seen that now the integrand is an odd function of x'' and x''' and hence, the integral vanishes:

$$L_{11}^{(3)} = 0. \quad (70)$$

The fourth term has $|x-x'''|$ for argument and also a minus sign according to (4); this yields

$$L_{11}^{(4)} = +2\Delta D(0)\,|\,E_d(0)\,|^2 \quad (71)$$

where

$$D(0) = \int_{-L}^{L} x^2A_0^2(x)dx. \quad (72)$$

Similarly the fifth term is

$$L_{11}^{(5)} = 2\Delta D(0)\,|\,E_d(0)\,|^2 = L_{11}, \quad (73)$$

and finally, the last term vanishes for the same reason as the third. By addition of the four terms the result is

$$L_{11} = 2\,\text{Re}\,L_{11}^{(1)} + 2L_{11}^{(4)} = 4\Delta\{D\,|\,E_d(0)\,|^2 + \text{Re}\,[C^*E_d^2(0)]\}. \quad (74)$$

[11] B. Y. Mills and A. G. Little, "A high resolution aerial system of a new type," *Aust. J. Phys.*, vol. 6, pp. 272–278; September, 1953.

By combination of this with (33) the result given in (29) is obtained.

Appendix II

To evaluate the integral in (58), let $x=L\cos\theta$; then,

$$C(\alpha) = 2L^3\int_0^{\pi/2} \sin\theta\cos^2\theta J_0^2(i\alpha\sin\theta)d\theta. \quad (75)$$

By introduction of Neumann's representation,[12] for $J_0^2(x)$,

$$J_0^2(x) = \frac{2}{\pi}\int_0^{\pi/2} J_0(2x\sin\gamma)d\gamma \quad (76)$$

and by interchange of the order of integration, (75) becomes

$$C(\alpha) = \frac{4L^3}{\pi}\int_0^{\pi/2} d\gamma \cdot\left[\int_0^{\pi/2} \sin\theta\cos^2\theta J_0(2i\alpha\sin\gamma\sin\theta)d\theta\right]. \quad (76a)$$

The integral in the brackets can be evaluated by applying Sonines' first integral,[13] and the result is

$$\sqrt{2}\Gamma(3/2)y^{-3/2}J_{3/2}(y) \quad (77)$$

where

$$y = 2i\alpha\sin\gamma. \quad (78)$$

Since the Bessel functions of half-integral order can be expressed in terms of sines and cosines, the expression for $C(\alpha)$ becomes

$$C = \frac{4L^3}{\pi}\int_0^{\pi/2}\left[\frac{\sin y}{y^3} - \frac{\cos y}{y^2}\right]d\gamma. \quad (79)$$

Although it is not strictly correct to write the above integral as the sum of the individual integrals since the separate integrands would have a γ^{-2} singularity at the origin, nevertheless it is convenient to do so. Then (79) becomes

$$C = a(C_2 - C_1) \quad (80)$$

where

$$C_1 = \frac{1}{v^2}g_1(v) \qquad g_1(v) = \int_0^{\pi/2}\frac{\cos(v\sin\gamma)}{\sin^2\gamma}d\gamma \quad (81)$$

$$C_2 = \frac{1}{v^3}g_2(v) \qquad g_2(v) = \int_0^{\pi/2}\frac{\sin(v\sin\gamma)}{\sin^3\gamma}d\gamma \quad (82)$$

$$v = 2i\alpha \qquad a = 4L^3/\pi. \quad (83)$$

From (81) and (82) it follows that

$$\frac{dg_2}{dv} = g_1, \quad (84)$$

which is useful because C can now be expressed entirely in terms of g_1 which can be evaluated. For this accomplishment (80) is multiplied by v^3 and differentiated:

$$\frac{1}{a}\frac{d}{dv}[v^3C(v)] = \frac{d}{dv}[v^3C_2(v)] - \frac{d}{dv}[v^3C_1(v)]$$

$$= g_1(v) - \frac{d}{dv}[vg_1(v)]. \quad (85)$$

Integration of the above yields

$$a^{-1}v^3C(v) = \int_0^v g_1(Z)dZ - vg_1(v) + c \quad (86)$$

where c is a constant of integration which will be determined later.

For the evaluation of the function $g_1(v)$, (81) is differentiated twice to yield

$$g_1'' = -\int_0^{\pi/2}\cos(v\sin\gamma)d\gamma = -\frac{\pi}{2}J_0(v) \quad (87)$$

where the last result may be found in Watson.[14] Integrating (87) twice and interchanging orders of integration, yields the required expression for $g_1(v)$:

$$g_1(v) = \frac{\pi}{2}\int_0^v (v - Z)J_0(Z)dZ + g_1(0). \quad (88)$$

When this expression is substituted into the right side of (86) and the order of integration in the first term is inverted, the following result is obtained:

$$a^{-1}v^3C(v) = \frac{\pi}{4}\left[v^2\int_0^v J_0(w)dw - \int_0^v w^2J_0(w)dw\right] + c. \quad (89)$$

Since $C(0)$ is finite, it follows that $c=0$. By use of the formula $[xJ_1(x)]'=xJ_0(x)$ and by integration by parts, the second integral can be reduced to the form

$$v^2J_1(v) + vJ_0(v) - \int_0^v J_0(w)dw, \quad (90)$$

and hence,

$$C(v) = \left(\frac{L}{v}\right)^3\left\{(v^2+1)\int_0^v J_0(w)dw - v[vJ_1(v) + J_0(v)]\right\}. \quad (91)$$

Finally, when v is replaced by $2i\alpha$ (83), the result given in (59) is obtained.

[12] G. N. Watson, "Theory of Bessel Function," Cambridge University Press, Cambridge, Eng., p. 32; 1952.
[13] *Ibid.*, p. 372.
[14] *Ibid.*, p. 21.

Mutual Impedance Effects in Large Beam Scanning Arrays*

P. S. CARTER, Jr.†

Summary—**An analysis is presented of the driving point impedance of the elements in a flat array of infinite vertical height but finite horizontal width. It is assumed that each of the elements is fed by a separate amplifier, having infinite internal impedance, and that the amplifiers can be phased to direct the beam at various positions in space. The radiating elements considered are infinitely long wires spaced on half-wavelength centers and half-wave dipoles spaced on half-wavelength centers, each backed by a conducting ground plane spaced one-quarter wavelength from the elements. Values of driving point impedance are computed for the 61 elements in arrays 30 wavelengths wide. Values of the driving point impedance near the center of the array are found to agree closely with the values computed for infinitely wide arrays while the driving-point impedance of elements near the edge of the array are found to deviate considerably from the values at the center.**

I. Introduction

When the direction of the beam of an antenna array is changed by varying the phase and, possibly, the amplitude of the currents in the array elements, mutual coupling of the elements causes the driving-point impedances to vary. In a large-aperture, two-dimensional array consisting of many separately driven elements, the impedances of the elements that are far enough from the edge of the array will exhibit nearly the same variation as the antenna beam is scanned. This effect (on the center elements only) may cause the transmitter to transfer power to the antenna less efficiently, decreasing the system gain. The uniform variation of impedance of the center elements does not by itself change the radiation pattern. However, since impedances of the elements near the edge of the array will vary differently from those in the center of the array, the deviation of the currents in these edge elements from the intended values may cause pattern distortion. For some scan angles, the resistive component of the impedance of the edge elements may even be negative. In this case the "generator" attached to such an element having a negative driving-point resistance would be required to absorb rather than to deliver power.

In this paper the driving-point impedance is computed for the various elements in a row of an antenna array of the type illustrated in Fig. 1, assuming that these elements are driven with constant-current generators that are properly phased to position the beam of the array at various angles in both the E and H planes. It is believed that these formulas will apply with good precision to all except the first few top and bottom rows of elements in an actual array that does not have an infinite vertical extent. Antenna arrays having both infinite wire radiators, with and without a reflector, and half-wavelength dipole radiators backed with a reflector, are considered here.

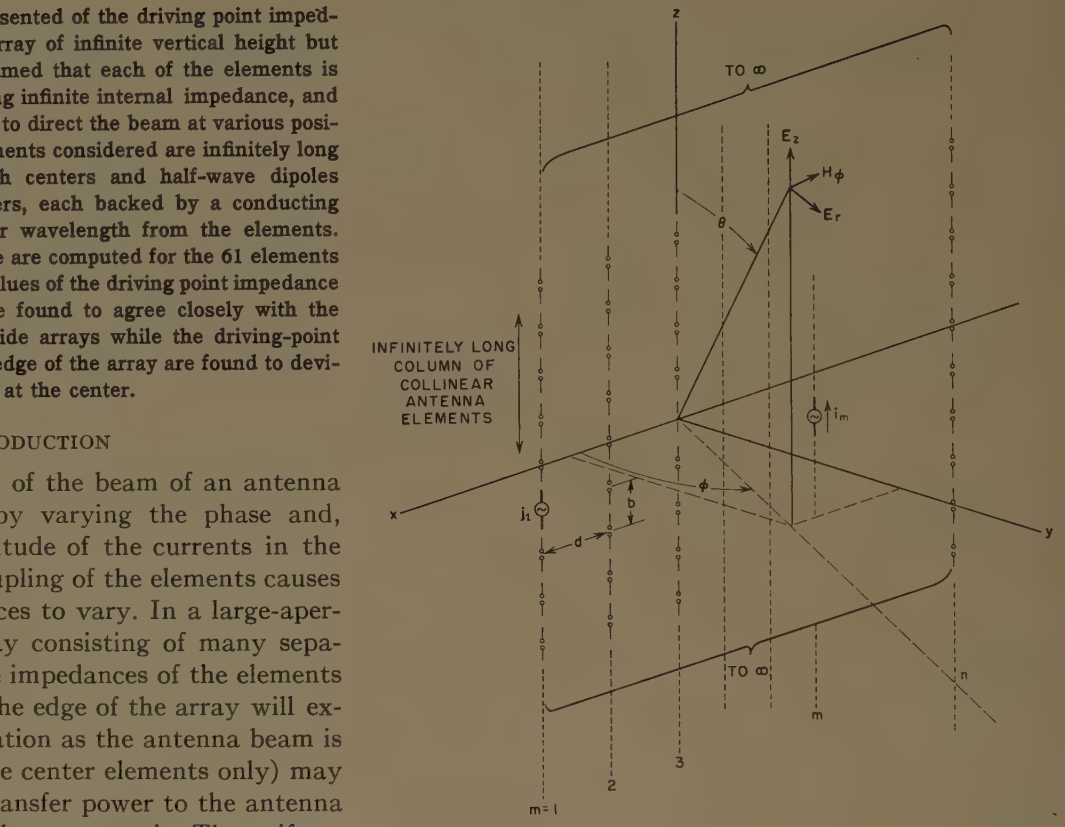

Fig. 1—Coordinates of array.

II. Summary of Analysis and Results

1) *Outline of Method*

The model of the antenna used in this analysis is illustrated in Fig. 1 and consists of a finite number of infinitely long collinear arrays of antenna elements—in this case, dipoles. The currents along each infinitely long row of dipoles are subjected to a Fourier analysis, the terms of which represent traveling waves of current along the Z axis. The electromagnetic fields, E_r, E_z, and H_θ, set up by each current mode, are given by a set of simple scalar potentials. The EMF method is then applied, using these fields and the circuit equations, to obtain the input impedance of a dipole in any mth row of the n total rows. This analysis and the derivation of results presented below appear in detail in Section III.

* Manuscript received by the PGAP, July 18, 1959; revised manuscript received, January 16, 1960. The work described in this paper was performed under Contract AF 19(604)-2240 with the Air Force Cambridge Research Center, Bedford, Mass.

† Stanford Research Institute, Stanford, Calif.

An analytical expression for the input impedance Z_m of an antenna element in the mth row for the case, shown in Fig. 1, of infinite impedance generators and no reflector, is

$$Z_m = \frac{1}{I_m} \sum_{p=1}^{p=n} Z_{m,p} I_p, \tag{1}$$

where

I_p = current in the pth element (*i.e.*, column),
$Z_{m,p}$ = mutual impedance, as defined in Section V, between an element in the mth column of antennas and pth column.

When a reflector is used, as would commonly be the case in order to achieve a unidirectional beam, (1) is modified to include the effect of the image currents $I_{p'} = -I_p$, *i.e.*,

$$Z_m = \frac{1}{I_m} \left\{ \sum_{p=1}^{p=n} Z_{m,p} I_p + \sum_{p'=1}^{p'=n} Z_{m,p'} I_{p'} \right\}, \tag{2}$$

where $Z_{m,p'}$ = mutual impedance, as defined in Section V, between mth element and image current $I_{p'}$ corresponding to the pth element.

2) *Infinite Wires With and Without Reflector*

The first type of antenna array considered here is the infinite wire model. Here, we have replaced the n infinite columns of discrete elements by n infinitely long wires each carrying a uniform current

$$I_p = |I_p| e^{-j(2\pi/\lambda) z \cos\theta} e^{-j(p-1)(2\pi d/\lambda) \cos\phi \sin\theta}. \tag{3}$$

For this case it can be shown (see Section V) that

$$Z_{m,p} = +j \frac{60}{r_0} \frac{(k^2 - h_0^2)^{1/2}}{k} \frac{H_0^{(2)}(\sqrt{k^2 - h_0^2} r_{m,p})}{H_1^{(2)}(\sqrt{k^2 - h_0^2} r_0)}, \quad m \neq p, \tag{4}$$

and

$$Z_{m,m} = +j \frac{60}{r_0} \frac{(k^2 - h_0^2)^{1/2}}{k} \frac{H_0^{(2)}(\sqrt{k^2 - h_0^2} r_0)}{H_1^{(2)}(\sqrt{k^2 - h_0^2} r_0)}, \quad m = p, \tag{5}$$

where

r_0 = radius of wire,
$r_{m,p} = |m - p| d$,
$k = 2\pi/\lambda$,
d = distance between wires, shown in Fig. 1,
$h_0 = k \cos\theta$,

and where θ and ϕ are the scan angles as defined in Fig. 1.

These mutual impedance coefficients $Z_{m,p}$ can be used along with (1) to calculate the driving impedance per unit length of the array of wires without a reflector as explained above. In order to include the effect of a reflector we use (2), where now the additional image-current mutual-impedance coefficients $Z_{m,p'}$ are given by

$$Z_{m,p'} = j \frac{60}{r_0} \frac{\sqrt{k^2 - h_0^2}}{k} \frac{H_0^{(2)}(\sqrt{k^2 - h_0^2} r_{m,p'})}{H_1^{(2)}(\sqrt{k^2 - h_0^2} r_0)}, \tag{6}$$

in which all the symbols are the same as above except for $r_{m,p'}$ which is given by

$$r_{m,p'} = [r^2_{m,p} + 4x^2]^{1/2} = [(|m - p| d)^2 + 4x^2]^{1/2},$$

where x = distance from plane of array to conducting sheet reflector.

3) *Array of Dipoles With and Without Reflector*

The formulas listed below apply to the case, common in practice, where the antenna elements shown in Fig. 1 are dipoles of radius r_0, along which the current is assumed to be distributed sinusoidally. The driving-point impedance, Z_m, as given by (1) and (2) is now actually the impedance between the terminals of any mth row dipole element. The formulas are summarized as follows:

$$Z_{m,p} = \sum_{i=-\infty}^{i=\infty} \frac{B_{imp}}{b} \left\{ \frac{\sin[(k_a + h_i)(l/4)]}{k_a + h_i} + \frac{\sin[(k_a - h_i)(l/4)]}{k_a - h_i} \right\}^2, \tag{7}$$

where

$r_{m,p} = |m - p| d$,
$h_i = k \cos\theta - (2i\pi/b)$,
$k = 2\pi/\lambda$,
$l/2$ = length of dipole,
$k_a = 2\pi/l$,
b = distance between centers of dipoles along line of dipoles as shown in Fig. 1,
d = distance between lines of dipoles as shown in Fig. 1,
r_0 = radius of dipole.

The coefficients B_{imp} are given by the following expressions:

$i = 0, m \neq p$

$$B_{omp} = -j \frac{60}{r_0} \frac{\sqrt{k^2 - h_0^2}}{k} \frac{H_0^{(2)}(\sqrt{k^2 - h_0^2} r_{m,p})}{H_1^{(2)}(\sqrt{k^2 - h_0^2} r_0)},$$

$i \neq 0, m \neq p$

$$B_{imp} = j \frac{60}{r_0} \frac{\sqrt{h_i^2 - k^2}}{k} \frac{K_0(\sqrt{h_i^2 - k^2} r_{m,p})}{K_1 \sqrt{h_i^2 - k^2} r_0)},$$

$i = 0, m = p$, i.e., $r_{m,p} = 0$

$$B_{omm} = -j \frac{60}{r_0} \frac{\sqrt{k^2 - h_0^2}}{k} \frac{H_0^{(2)}(\sqrt{k^2 - h_0^2} r_0)}{H_1^{(2)}(\sqrt{k^2 - h_0^2} r_0)},$$

$i \neq 0, m = p$, i.e., $r_{m,p} = 0$

$$B_{imp} = j \frac{60}{r_0} \frac{\sqrt{h_i^2 - k^2}}{k} \frac{K_0(\sqrt{h_i^2 - k^2} r_0)}{K_1(\sqrt{h_i^2 - k^2} r_0)},$$

in which

$$h_i = k\cos\theta - \frac{2i\pi}{b}.$$

For the case described by (2), which includes the reflector, the expressions for the mutual impedance coefficients $Z_{m,p'}$ are given again by (7) where only the first two expressions for B_{omp} and B_{imp} are used *including* the case $m=p'$. Also, $r_{m,p}$ is replaced by $r_{m,p'}$ where again

$$r_{mp'} = [r_{mp} + 4x^2]^{1/2} = [(|m-p|d)^2 + 4x^2]^{1/2},$$

in which x = distance from the plane of the array to the reflector.

4) *Infinite Grid Formulas*[1]

A considerable simplification, in some respects of the driving-point impedance formulas for the infinite wire array is achieved for the particular case where there are an infinite number of wires, *i.e.*, $n\to\infty$. In this case, formulas given by MacFarlane[2] and Marcuvitz[3] for the reactance of an infinite grid can be modified to give the driving point impedance per unit length of wire. The appropriate formulas are given as follows:

H-plane scan, without reflector,

$$Z_d = \frac{\eta}{d}\left\{\frac{\csc\phi}{2} + j\frac{d}{\lambda}\left[\ln\left(\frac{d}{2\pi r_0}\right) + F\left(\frac{d}{\lambda}, \phi - 90°\right)\right]\right\} \text{ ohms/meter;} \quad (8)$$

H-plane scan, with reflector,[4]

$$Z_d = \frac{\eta}{d}\left\{\frac{\csc\phi}{1 - j\cot(kx\sin\phi)} + j\frac{d}{\lambda}\left[\ln\left(\frac{d}{2\pi r_0}\right) + F\left(\frac{d}{\lambda}, \phi - 90°\right)\right]\right\} \text{ ohms/meter;} \quad (9)$$

E-plane scan, without reflector,

$$Z_d = \frac{\eta}{d}\left[\frac{\sin\theta}{2} + j\sin^2\theta\,\frac{d}{\lambda}\left\{\ln\left(\frac{d}{2\pi r_0}\right) + \frac{1}{6}\left(\frac{2\pi r_0}{d}\right)^2 + \frac{1}{2}\left(\frac{d\sin\theta}{\lambda}\right)\left[1 - \frac{1}{2}\left(\frac{2\pi r_0}{d}\right)^2\right]\right\}\right] \text{ ohms/meter;} \quad (10)$$

E-plane scan, with reflector,[5]

$$Z_d = \frac{\eta}{d}\left[\frac{\sin\theta}{1 - j\cot(ky\sin\theta)} + j\sin^2\theta\,\frac{d}{\lambda}\left\{\ln\left(\frac{d}{2\pi r_0}\right) + \frac{1}{6}\left(\frac{2\pi r_0}{d}\right)^2 + \frac{1}{2}\left(\frac{d\sin\theta}{\lambda}\right)\left[1 - \frac{1}{2}\left(\frac{2\pi r_0}{d}\right)^2\right]\right\}\right] \text{ ohms/meter.} \quad (11)$$

Eq. (8) is valid for wavelengths and incident angles in the range $d(1+\cos\phi)/\lambda<1$. According to Marcuvitz,[3] the results obtained by this formula are in error by less than 10 per cent. The factor $(F(d/\lambda, \phi-90°)$ has been calculated by Marcuvitz[3] and MacFarlane[2] and is presented in the form of graphs in their articles. Eq. (9) is derived using a plane wave assumption for the wave scattered from the grid. This assumption has been examined by Wait,[4] who gives additional corrections by which the accuracy of (9) can be increased. Eq. (10) is derived by means of a Babinet transformation using the formula given by Marcuvitz for a capacitive window. According to Marcuvitz this circuit equation is valid in the range $(d\sin\theta)/\lambda<1$, and is in error by less than about 10 per cent in the range $(4r_0/d)<0.5$. The accuracy of (11) is not known: it was derived, as was (9), using the assumption of plane wave scattering from the grid. It is presented here for the sake of completeness; presumably its accuracy could be examined by the theoretical methods employed by Wait.[4]

III. Discussion of Results

The formulas contained in Section II were used to calculate a number of cases of interest in order to show some of the important effects on the driving impedance encountered in electronic scanning. As stated, the driving impedance varies with both the scan angle and the position of the driven element within the array. Also, it was stated that "near the center" of the array the impedances do not vary very much, and are very close to the value which would be obtained from the infinite array formulas. The significance of these statements is made obvious from the calculations shown below for the infinite wire and half-wave dipole arrays. Finally, we should expect that in the case where a tapered current distribution is used to improve the sidelobe performance of the array, the low current levels at the edge of the array will prove difficult to maintain in their proper magnitude and phase, due to the increased magnitude of the coupled voltages compared to those in the non-tapered case. This effect is considered below in the calculations of the half-wave dipole array.

The first set of calculations which are shown in Figs. 2–6 are for the infinite wire array both with and without

[1] This approach using the infinite grid formulas was suggested by E. M. T. Jones, Stanford Res. Inst., Menlo Park, Calif.

[2] G. G. MacFarlane, "Surface impedance of an infinite parallel-grid at oblique angles of incidence," *J. IEE (London)*, vol. 93, pp. 1523–1527; 1951.

[3] N. Marcuvitz, "Waveguide Handbook," Rad. Lab. Ser., vol. 10, pp. 286–289, McGraw-Hill Book Co., Inc., New York, N. Y.; 1951.

[4] Approximate—for range of valid results and for additional correction terms, see J. R. Wait, "Reflection from a wire grid parallel to a conducting plane," *Canada J. Phys.*, vol. 32, pp. 571–579; September, 1954.

[5] Approximate—accuracy not yet evaluated.

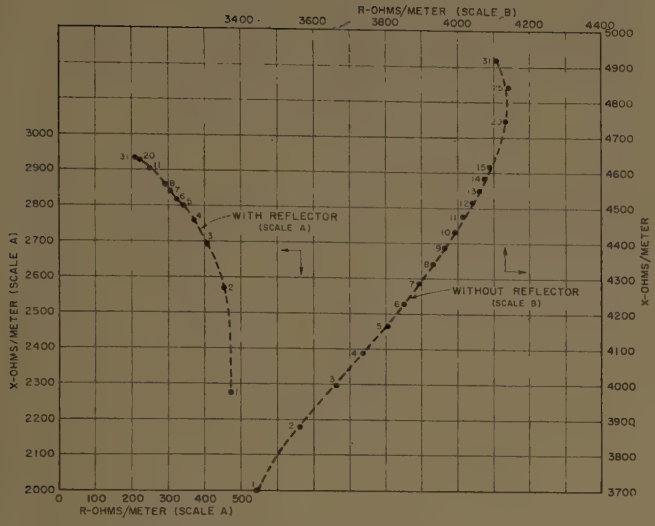

Fig. 2—Driving-point impedances of infinite wire array, $\theta=90°$, $\phi=3°$.

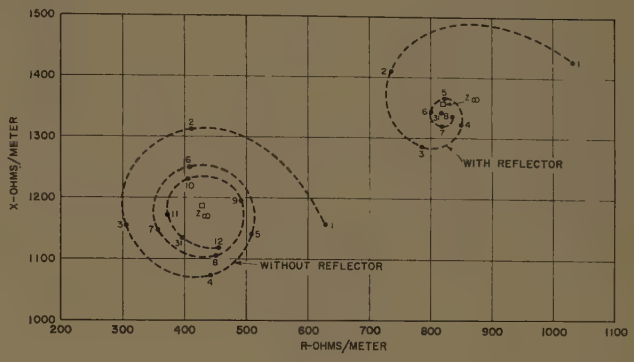

Fig. 3—Driving-point impedances of infinite wire array, $\theta=90°$, $\phi=60°$.

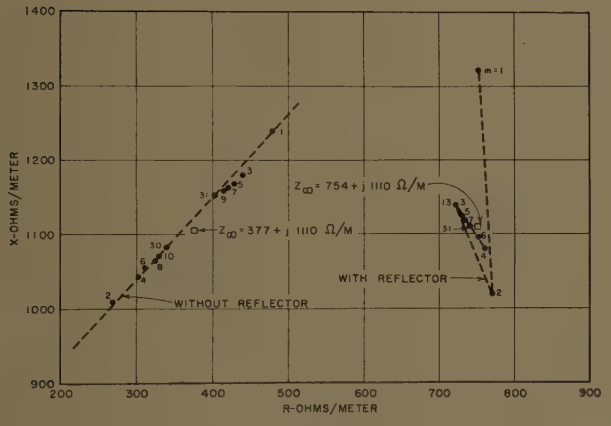

Fig. 4—Driving-point impedances of infinite wire array, $\theta=90°$, $\phi=90°$.

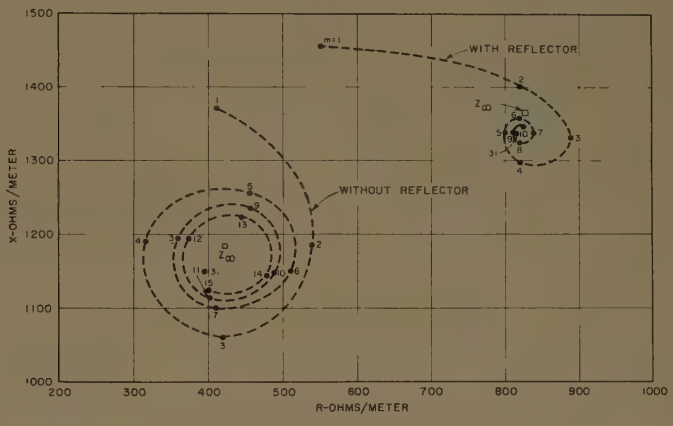

Fig. 5—Driving-point impedances of infinite wire array, $\theta=90°$, $\phi=120°$.

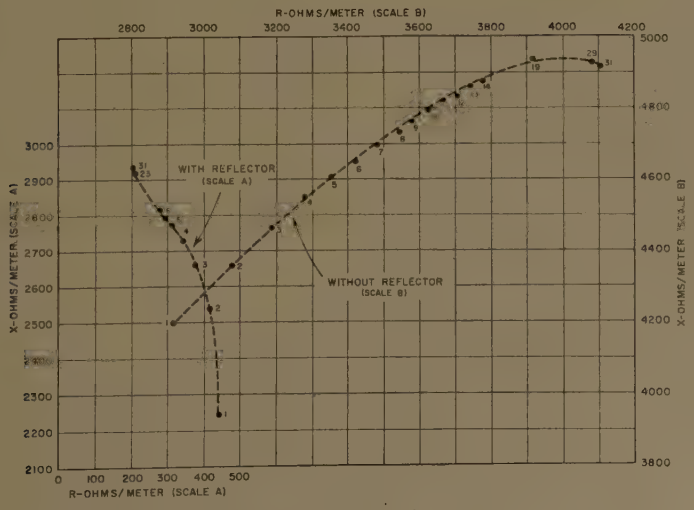

Fig. 6—Driving-point impedances of infinite wire array, $\theta=90°$, $\phi=177°$.

a reflector. The following array parameters were chosen and used in these calculations:

$r_0 = 0.005$ meter $= 0.5$ cm,
$\lambda = 1$ m,
$d = \frac{1}{2}$ m $= \lambda/2$,
$n = 61$ = number of elements in array,
$x = \frac{1}{4}$ m $= \lambda/4$ (in case where reflector is used).

Uniform illumination of the array was chosen in this case, *i.e.*, $|I_p| = I_0$. The array has 61 elements which are spaced one-half wavelength apart resulting in an array 30 wavelengths wide. H-plane scan angles (*i.e.*, the principal plane defined by $\theta = 90°$), were chosen ranging from $\phi = 3°$ to $\phi_2 = 177°$.[6] Because of the symmetry of the array, it is not necessary to calculate impedances beyond $m = 31$.[7]

The results of these calculations for the infinite wire array are shown in Figs. 2–6 in the form of $R-X$ diagrams. The calculated points are numbered $m = 1, 2, 3 \cdots$, indicating the element position in the array as shown in Fig. 1. It is instructive first to consider scan angles in the neighborhood of $\phi = 90°$ (*i.e.*, normal to the plane of the array). As we trace the locus of the impedance from the edge of the array, the driving impedance approaches a limiting value near the center of the array. It approaches this value most rapidly for the $\phi = 90°$ case and less rapidly as the scan angle is increased with respect to the array normal. Comparing the values with and without the reflector, we see that the impedance approaches a limiting value more rapidly in the case with the reflector. This is expected since, in effect, the addition of the reflector makes each element directive and thus reduces the coupling between elements.

For scan angles displaced from the normal ($\phi = 90°$) by more than around 45°, the impedance changes radically as a function of the position of the element within the array until, for scan angles around 0° and 180°, the impedance varies widely over the entire length of the array.

The impedance of even the center elements is a function of the H-plane scan angle ϕ. This is shown in Fig. 7, where the impedance is plotted as a function of scan angle for the thirty-first (center) element of the 61-element array, and also for an element of the infinite grid array from (8) and (9). The same parameters were used in the infinite grid formulas ($d = \lambda/2$, $\lambda = 1$, $r_0 = 0.005$ and $x = \lambda/4$) as were used in the calculations of the 61-element array. It is evident from these curves that, for small scan angles around the normal to the array, the variation of impedance is somewhat greater with the reflector than without it. We see also that the

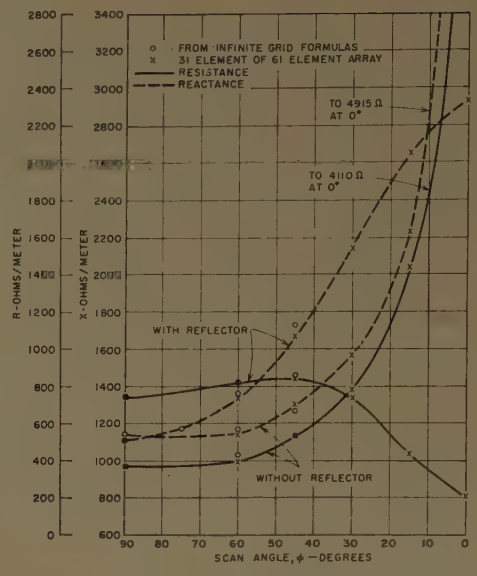

Fig. 7—Driving-point impedance vs scan angle of infinite wire array (element 31) and infinite grid.

driving resistance in the case with the reflector reaches a maximum, and then decreases for scan angles displaced by more than about 45° from broadside excitation. This behavior is easily understood from inspection of the equivalent circuit described in Section V, *C*. This equivalent circuit contains a reactance [see Fig. 14(b)] due to the reflector, which is shunted across the equivalent resistance, $n \csc \phi$, of free space. This reactance decreases with increasing scan angle, tending to reduce the value of radiation resistance seen from the driving terminals.

Driving-point impedances were calculated for the half-wave dipole array with a reflector. It was desired to make these calculations as realistic as possible and to include, therefore, a tapered current distribution as well as a reflector. The current distribution used is shown in Fig. 8. The height of the pedestal was chosen to be approximately one-third of the height of the peak of the distribution at the center of the array. A study of the radiation pattern of this distribution shows that the highest sidelobe levels are about 25 db below the main lobe maximum. A little analysis shows that the expression for the amplitudes of the currents $|I_p|$ in the elements of the 61-element array is

$$|I_p| = \left\{0.33 + 0.67 \cos^2\left[\frac{(p/2 - 15.5)}{30.5}\pi\right]\right\} I_0, \qquad (12)$$

where I_0 is the magnitude of the current in the center element of the array. It is assumed in this expression for $|I_p|$ that the distance d between elements is one-half wavelength.

The vertical distance (in the z direction) between the centers of the dipoles, $b = 0.5\lambda$, was chosen to allow a full 180° scan in the H plane. This is not unreasonable, even though for this spacing the ends of the dipoles would be touching, since the proximity of the dipole elements

[6] $\phi = 0°$, 180° was not used here, since this is the angle at which, for an element spacing of $\lambda/2$, an additional major lobe appears in the radiation pattern.

[7] That is to say, the impedance of the nth element for an angle ϕ, where $\phi < 90°$, is the same as the impedance of the $61-n$th element for angle $180° - \phi$.

would affect mainly the nonvarying component of the mutual reactance. Besides this, very little increase in vertical spacing b could be obtained by limiting the E-plane scan angle to less than the range $0<\theta<180$. For instance, if θ were limited to within the range $45°<\theta<135°$, the maximum spacing would be $b=0.58\lambda$, as compared with $b=0.5\lambda$ in the full 180° scan case.

Calculations of the driving-point impedance were made for the half-wave dipole array and are shown in Figs. 9–12. Included here are both E-plane and H-plane scan angles, as well as scan angles not located in either principal plane, *i.e.*, $\theta=45°$, $\phi=45°$.

The same general trends can be observed for the half-wave dipole array as for the infinite wire array discussed above. For example, at small scan angles, the

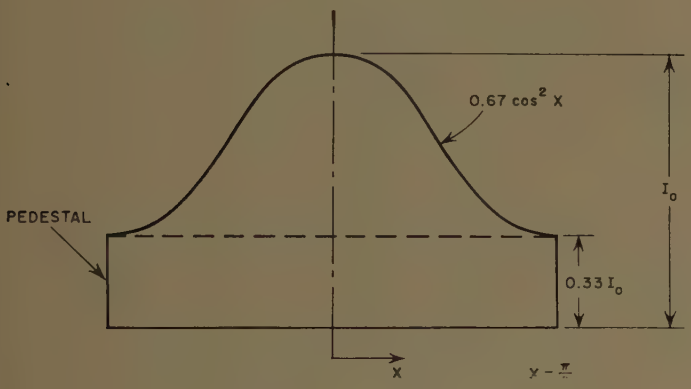

Fig. 8—Current distribution on half-wave dipole array.

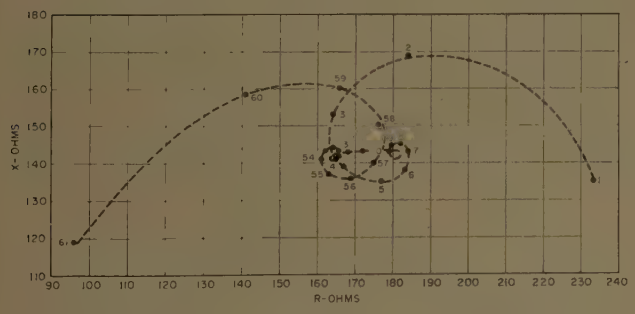

Fig. 9—Driving-point impedances of half-wave dipole array with reflector, $\theta=90°$, $\phi=45°$.

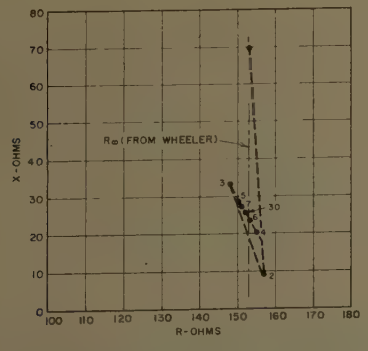

Fig. 10—Driving-point impedances of half-wave dipole array with reflector, $\theta=90°$, $\phi=90°$.

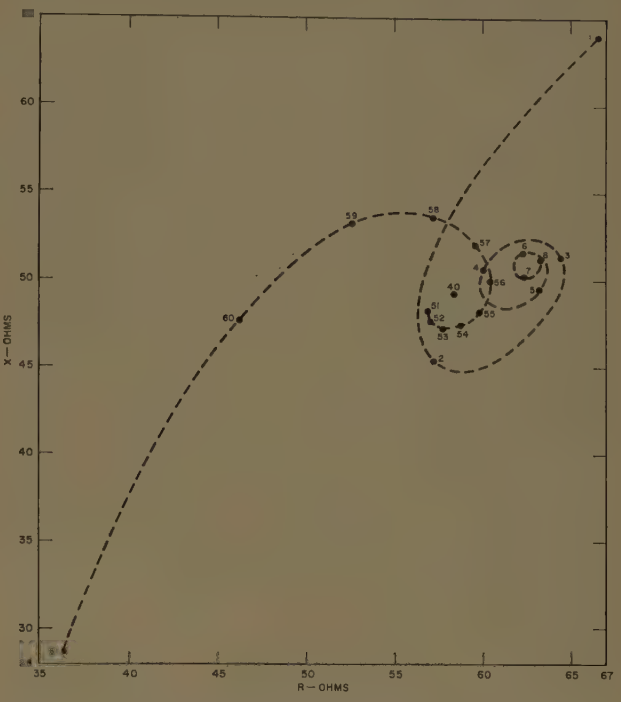

Fig. 11—Driving-point impedances of half-wave dipole array with reflector, $\theta=45°$, $\phi=45°$.

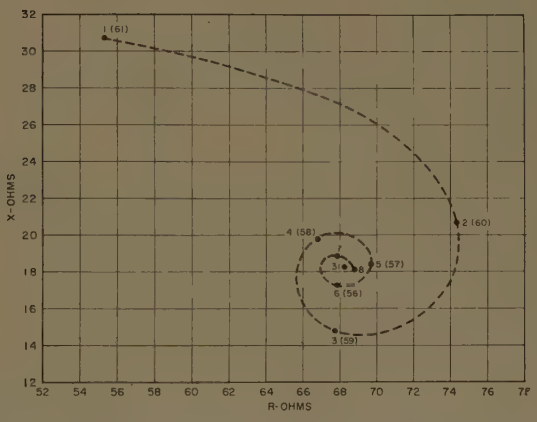

Fig. 12—Driving-point impedances of half-wave dipole array with reflector, $\theta=45°$, $\phi=90°$.

distances from the edge of the array at which variations in the driving point impedance decrease below a certain amount are about the same for both arrays. Also, the variation of impedance of the center elements with scan angle at least, for H-plane scan angles, is similar for both arrays. This last statement is illustrated in Fig. 13, which is a plot of the variation of impedance with scan angle of the thirty-first element of the half-wave dipole array.

It is to be noticed that none of the driving-point impedances in the figures contain a negative resistive component. Nevertheless, it is still reasonable to expect that one may observe a negative resistance in some of the elements for some other scan angles, since it appears

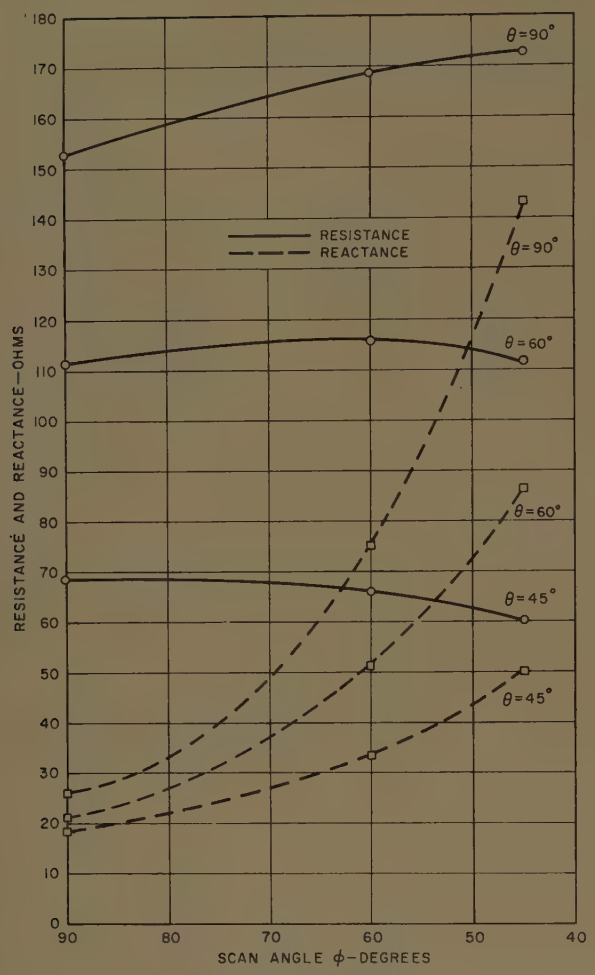

Fig. 13—Impedance vs scan angle of element 31 of half-wave dipole array with reflector.

to be possible for the component of resistance due to mutual effects to be negative and greater than the positive self-resistance of an element.

The validity of the impedance formulas and computations for the half-wave dipole array was established by a comparison with other methods of calculation. For instance, Wheeler[8] has shown how to calculate the driving point resistance of an infinite array of dipoles excited in phase (*i.e.*, to yield a broadside beam). Application of his formula, using the parameters $b=d=\lambda/2=\frac{1}{2}$, yields a value for the driving resistance, $R_\infty=153$ ohms. This may be compared to the value of resistance, $R_{31}=152$ ohms, shown in Fig. 10, for the thirty-first element of the 61-element array. Another check on the validity of the formulation was obtained from a calculation of the driving point impedance of a single infinitely long column of dipoles, *i.e.*, a calculation of $Z_{m,m}$ using (7). $Z_{m,m}$ was calculated for two values of θ: $\theta=45°$ and $\theta=90°$. This is compared in Table I below to a calculation made using the well-known formulas for the mutual impedance between two dipoles.[9] One would expect the result for this latter calculation to approach the result for the infinite column of dipoles as the number of dipoles is increased. The driving point impedances shown in column 2 in Table I were calculated from the formulas given in Carter's article,[9] assuming a column of nine collinear half-wave dipoles. The agreement between the two sets of results for the driving-point impedance indicates the validity of our formulas.

TABLE I

COMPARISON OF Z_{mm} OF INFINITE COLUMN OF COLLINEAR DIPOLES WITH CLASSICAL FORMULA ASSUMING COLUMN OF NINE COLLINEAR DIPOLES

θ-degrees	Center Dipole of Nine Collinear Dipoles (From Carter[9])	Infinite Column [Eq. (7)]
45	$49+j\times21.2$	$47.2+j\times17.4$
90	$121+j\times76.5$	$119.5+j\times74.2$

It has been assumed, in the calculations of driving impedances described in this paper, that the antenna elements were driven by infinite impedance generators and that the proper currents were thus established on the antenna elements. A more interesting result is, of course, the case where the antennas are fed with generators of finite impedance. This problem could, of course, be solved using conventional methods of circuit analysis and making use of the mutual impedance coefficients $Z_{m,n}$ derived in this paper. An exact solution of this problem would entail the reduction of determinants of order n where n is the number of columns of antenna elements. This calculation would be an extensive undertaking and, if found to be necessary, would undoubtedly require the services of a digital computer for a large antenna array.

IV. Conclusions

This paper has drawn attention to the variations of driving-point impedance that occur in an antenna array that positions the beam electronically. Methods and formulas have been derived by which calculations of the driving-point impedances of elements in large arrays can be conveniently made, and several typical examples were calculated to yield numerical results. These results indicate that these impedance variations may be large in the case of a large range of scanning angles. Special techniques such as current feedback and automatic impedance compensation will probably be necessary if a large scanning angle range is needed with a single antenna array.

[8] H. A. Wheeler, "The radiation resistance of an antenna in an infinite array or waveguide," Proc. IRE, vol. 36, pp. 478–487; April, 1948.

[9] P. S. Carter, "Circuit relations in radiating systems and applications to antenna problems," Proc. IRE, vol. 20, pp. 1004–1041; June, 1932.

V. Derivation of Formulas

A. Infinite Dipole Array

The basic formulas listed in Section I are easily derived from the scalar cylindrical wave functions for TM waves in the manner described by Stratton.[10] Using the scalar wave function $\psi(\theta, \phi, r)$, the fields outside the radius r_0, where r_0 equals radius of antenna element or wire, are given in this case by

$$E_{zi} = (k^2 - h_i^2)\psi_i, \tag{13a}$$

$$H_{\theta i} = \frac{-jk^2}{\omega\mu}\frac{\delta\psi_i}{\delta r}, \tag{13b}$$

$$E_{ri} = \mp h_i \frac{\delta\psi_i}{\delta r}. \tag{13c}$$

The scalar wave function ψ_i is given by

$$\psi_i = C_i H_0^{(2)}(\sqrt{k^2 - h_i^2}\, r)e^{\pm jh_i z}e^{j\omega t} \tag{14}$$

for the case $(k^2 - h_i^2) > 0$, and by

$$\psi_i = C_i K_0(\sqrt{h_i^2 - k^2}\, r)e^{\pm jh_i z}e^{j\omega t} \tag{15}$$

for the case $(h_i^2 - k^2) > 0$. As is obvious from the asymptotic forms of the above expressions for large values of r, ψ_i given by (14) may be used to represent a radiating or outward traveling wave; ψ_i given by (15) can be used to represent a surface or exponentially decreasing wave. The arbitrary constant C_i is evaluated from the boundary condition on the magnetic field at the surface of the wire; accordingly,

$$H_{\theta i}(r = r_0) = -\frac{I_i}{2\pi r_0}. \tag{16}$$

The current I_i is the ith Fourier or traveling-wave component of current along the infinitely long line of collinear dipoles and is given by

$$I_i = A_i e^{j[(2i\pi z)/b - \nu z + \omega t]} = A_i e^{-jh_i z + j\omega t}, \tag{17}$$

where

$$h_i = \nu - \frac{2i\pi}{b}.$$

The quantity ν is determined by the latitude of the beam; thus, $\nu = k\cos\theta = 2\pi/\lambda \cos\theta$. The coefficient A_i is the magnitude of the ith Fourier component of the current distribution along the line of dipoles. The evaluation of this coefficient for the case where the antenna elements are center-fed dipoles along each of which the current is sinusoidally distributed, and the centers of which are separated by the distance b, (see Fig. 1) gives,

$$A_i = \frac{1}{b}\left[\frac{\sin(k_a + h_i)\frac{l}{4}}{k_a + h_i} + \frac{\sin(k_a - h_i)\frac{l}{4}}{k_a - h_i}\right] I_0, \tag{18}$$

in which $k_a = 2\pi/l$, and I_0 = magnitude of current at the feed terminals of dipole. The derivation of this formula for A_i is given in Section VI.

The evaluation of the magnetic field at the surface of the wire using (13b) and the subsequent employment of the boundary condition given in (16) yields for the coefficients C_i

$$C_i = \frac{-jA_i}{2\pi r_0}\cdot\frac{\eta}{k\sqrt{k^2 - h_i^2}}\cdot\frac{1}{H_1^{(2)}(\sqrt{k^2 - h_i^2}\, r_0)}, \tag{19}$$

for the case where $k^2 - h_i^2 > 0$, and

$$C_i = \frac{+jA_i}{2\pi r_0}\frac{\eta}{k\sqrt{h_i^2 - k^2}}\frac{1}{K_1(\sqrt{h_i^2 - k^2}\, r_0)}, \tag{20}$$

for the case $h_i^2 - k^2 > 0$. The evaluation of the electric field E_{zi}, making use of (13a) gives

$$E_{zi} = \frac{-j\eta}{2\pi r_0}\frac{A_i\sqrt{k^2 - h_i^2}}{k}\frac{H_0^{(2)}(\sqrt{k^2 - h_i^2}\, r)}{H_1^{(2)}(\sqrt{k^2 - h_i^2}\, r_0)}e^{-jh_i z}, \tag{21}$$

for the case $k^2 - h_i^2 > 0$, and

$$E_{zi} = \frac{+j\eta}{2\pi r_0}\frac{A_i\sqrt{h_i^2 - k^2}}{k}\frac{K_0(\sqrt{h_i^2 - k^2}\, r)}{K_1(\sqrt{h_i^2 - k^2}\, r_0)}e^{-jh_i z}, \tag{22}$$

for the case $h_i^2 - k^2 > 0$.

The final step in the derivation is to calculate the self and mutual impedances, Z_{mm} and Z_{mp}. Basic analytical expressions for these two quantities are,[9]

$$Z_{mm} = \frac{-1}{I_0}\int_{-l/4}^{l/4} E_{zmm}(z)I(z)dz \tag{23}$$

and

$$Z_{mp} = \frac{-1}{I_0}\int_{-l/4}^{l/4} E_{zmp}(z)I(z)dz, \tag{24}$$

where

$I(z) = I_0 f(z)$,

Z_{mm} = driving-point impedance of any element in mth column of collinear elements in the absence of other columns of elements,

Z_{mp} = mutual impedance between the mth column and the pth column,

$E_{zmm}(z)$ = electric field along element in mth column due to a current $I(z)$ in the elements of the mth column,

E_{zmp} = electric field along element in mth column due to a current $I(z)$ in the elements of the pth column.

[10] J. A. Stratton, "Electromagnetic Theory," McGraw-Hill Book Co., Inc., New York, N. Y., pp. 349–361; 1941.

The current $I(z)$ is assumed, in our example, to be a cosine function of the distance along the dipole from the center of the dipole, *i.e.*, $I(z)=I_0 \cos(2\pi z/l)$ where l = twice the length of the dipole. The total electric field $E_{zmm}(z)$ or $E_{zmp}(z)$ is the sum of modes given by (21) and (22). Thus

$$E_{zmm}(z) = \sum_{i=-\infty}^{\infty} E_{zi}(r = r_0), \tag{25}$$

and

$$E_{zmp}(z) = \sum_{i=-\infty}^{\infty} E_{zi}(r = r_{mp}). \tag{26}$$

The rest of the derivation of the final results given in Section II is carried out using (23)–(26). In these formulas it has been assumed that the only case for which $k^2-h_i^2>0$ is for the index $i=0$. A little consideration shows that this is true for all scan angles $0<\theta<180°$ provided that the center-to-center spacing of the dipoles is less than or equal to $\lambda/2$. This condition is made obvious by a consideration of the result which is obtained in the case that $k^2-h_i^2>0$ for other values of i than $i=0$. In this case, there will be a second main lobe at an angle different from the primary main lobe. For the infinitely long array, the condition needed for all of the higher order current modes to be nonradiating or surface-wave modes is the same as the requirement on the element spacing in an array of finite length for there to be only one major lobe.

B. Infinite Wire Array

The infinite wire array is a special case of the infinite dipole array considered above, where the current amplitude distribution along the column is uniform and there are no particular sets of driving-point terminals. Thus, it is not necessary to use (23) and (24) to calculate the impedances, which are expressed as impedances per unit length. A brief consideration shows that in the infinite wire array all of the current modes are absent except for the term given by $i=0$. Further consideration shows that in this case $A_0=I_0$ = magnitude of current along wire. The self and mutual impedances given in (4) and (5) may therefore be written down by inspection from (21) after setting $i=0$. Notice, however, that the sign is changed in (4) and (5) from that in (21), to account for the fact that the impedance is proportional to the driving voltage which is 180° out of phase with, and equal in magnitude to, the induced voltage.

C. Infinite Grid Array

The formulas contained in Section I for the driving impedance of an infinite grid are easily obtained by a slight extension of the results for the reactance of a grid given by MacFarlane[2] or Marcuvitz.[3] These extensions of their formula are easily derived by considering the equivalent transmission-line circuits of the grid, and are shown in Fig. 14 for the cases of H-plane and E-plane scan and with and without the reflector. In Figs. 14(a) and 14(b), the quantity $\eta \csc \phi$ is the impedance looking in the direction normal to the plane of the array of a wave traveling at an angle ϕ with respect to the array and having its *electric* vector in the plane of the array. In Figs. 14(c) and (14(d), $\eta \sin \theta$ is the impedance of a wave traveling at an angle θ with respect to the plane of the array with its *magnetic* vector in the plane of the array. The equivalent circuit of a reflector is given in each case by

H-plane scan,

$$X_r = j\eta \csc \phi \tan(kx \sin \phi);$$

E-plane scan,

$$X_r = j\eta \sin \theta \tan(kx \sin \theta).$$

The expressions for the reactance of an infinite inductive grid have been given by Marcuvitz[3] and MacFarlane,[2] and are

H-plane scan,

$$X_g = \eta \frac{d}{\lambda}\left[\ln \frac{d}{2\pi r_0} + F\left(\frac{d}{\lambda}, 90° - \phi\right)\right];$$

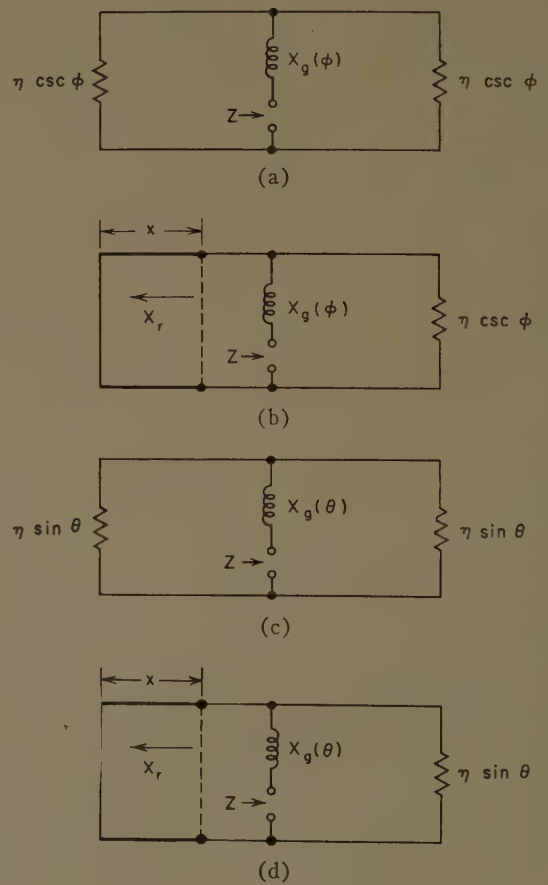

Fig. 14—Equivalent circuits of infinite grid and reflector. (a) H-plane scan without reflector. (b) H-plane scan with reflector. (c) E-plane scan without reflector. (d) E-plane scan with reflector.

E-plane scan,

$$X_g = \eta \sin^2\theta \frac{d}{\lambda}\left\{\ln\frac{d}{2\pi r_0} + \frac{1}{6}\left(\frac{2\pi r_0}{d}\right)^2 + \frac{1}{2}\left[\frac{d\sin\theta}{\lambda}\right]\left[1 - \frac{1}{2}\left(\frac{2\pi r_0}{d}\right)^2\right]^4\right\}.$$

The first of these two formulas requires reference to Marcuvitz[3] or MacFarlane[2] for the values of the correction factor $F(d/\lambda, 90°-\phi)$.

The application of the formulas listed above, together with the equivalent circuits shown in Fig. 14, yields the complete equations (8) through (11).

The infinite grid formula for the H-plane scan with reflector is reasonably accurate within certain restrictions on scan angle and reflector spacing which have been studied by Wait.[4] Reference should be made to his paper regarding these restrictions and their interpretation. It is not known, however, over what range of scan angles and reflector spacings (11) is accurate. It would be useful to extend the theory for close reflector spacings along the lines described by Wait in order to better evaluate results from this formula.

VI. Derivation of Fourier Coefficients of Currents on Infinite Column of Colinear Dipoles

We consider here one of the infinitely long columns of dipoles shown in Fig. 1. These dipole elements are assumed to be separated by a distance b between centers. An expression for the current on the nth dipole element (counting from the origin of coordinates, $z=0$), is given by

$$I_n(z) = I'\left[z - n\left(\frac{z}{b}\right)b\right]e^{-j\nu bn(z/b)}e^{j\omega t}, \tag{27}$$

in which

$$n\left(\frac{z}{b}\right) = \text{integer nearest } z/b,$$

$$\nu b = \frac{2\pi b}{\lambda}\sin\theta,$$

$I'(z)$ = current distribution along dipole element.

The phase function in this representation is a quantity increasing by steps, as indeed it must be since the elements are individually phased. According to Floquet's Theorem, a representation of the following form is possible:

$$I(z) = \sum_{i=-\infty}^{\infty} A_i e^{(j2i\pi/b)z - j\nu z} = \sum_{i=-\infty}^{\infty} A_i e^{-jh_i z}. \tag{28}$$

This representation is the one that is needed for the solution of the field components in terms of the scalar cylindrical functions ψ_i. A little consideration shows that $I(z)$ can be expressed also in the form

$$I(z) = I''(z)e^{-j\nu z}, \tag{29}$$

where

$$I''(z) = I'(z)e^{+j\nu[z - n(z/b)b]}.$$

The representation in the form $I''(z)$ is periodic, since the phase function $e^{j\nu[z-n(z/b)b]}$ is a sawtooth function. In fact, this phase function can be represented in the region $-(b/2)<z<(b/2)$ by the function $e^{j\nu z}$. Therefore by the Fourier Theorem,

$$I''(z) = \frac{1}{b}\sum_{i=-\infty}^{\infty}\int_{-(b/2)}^{b/2} I''(z')e^{(j2i\pi/b)(z-z')}dz'$$

$$= \sum_{i=-\infty}^{\infty}\frac{e^{j2i\pi z/b}}{b}\int_{-(b/2)}^{b/2} I'(z)e^{+j[\nu(-2i\pi/b)z']}dz'. \tag{30}$$

This expression when combined with (29) gives a representation equivalent to (28), which is what we set out to prove.

We shall compute the Fourier coefficients A_i for the case where the distribution of current along the dipole is a simple cosine function. In this case,

$$I'(z) = \cos\frac{2\pi z}{l} = \cos(k_a z), \qquad \frac{-l}{4} < z < \frac{l}{4}$$

$$= 0 \qquad \frac{-b}{2} < z < \frac{-l}{4}$$

$$= 0 \qquad \frac{l}{4} < z < \frac{b}{2}.$$

The insertion of this expression in (30) and the subsequent evaluation of the integral yields the expression for A_i given in Section V namely,

$$A_i = \frac{1}{b}\left\{\frac{\sin\left[\left(k_a + \nu - \frac{2i\pi}{b}\right)\frac{l}{4}\right]}{k_a + \nu - \frac{2i\pi}{b}} + \frac{\sin\left[\left(k_a - \nu + \frac{2i\pi}{b}\right)\frac{l}{4}\right]}{k_a - \nu + \frac{2i\pi}{b}}\right\}I. \tag{31}$$

VII. Acknowledgment

The assistance of, and the several important suggestions made by, Dr. E. M. T. Jones and Dr. S. B. Cohn in the carrying out of this investigation are gratefully acknowledged. Considerable credit is also due Mrs. T. Richardson and L. Leving for their part in programming the formulas for numerical computations on the digital computer.

Mutual Coupling Effects in Large Antenna Arrays: Part I—Slot Arrays*

S. EDELBERG† AND A. A. OLINER‡

Summary—**A periodic structure approach is presented for the analysis of the impedance properties of large antenna arrays. The method is applied to a two-dimensional array of slots, in which each slot is fed by a separate waveguide and the array radiates into a half-space. The slot spacing and progressive phasing in the array may be arbitrary, however. The periodic structure approach permits a waveguide-type analysis of the half-space which automatically includes all mutual coupling effects. Both the susceptance and conductance of the slot are evaluated for arbitrary scan angle, and the effects associated with the appearance of higher order beams are considered.**

I. Introduction

BECAUSE of mutual coupling effects, the input impedance of a radiating antenna when used as an element of an array is different from its impedance value when the same antenna is isolated. Furthermore, this difference between impedance values varies with the scan angle of the array. A lack of knowledge regarding the correct impedance value may result in errors in the desired pattern, in increased sidelobe level, or in array mismatch. The amount and type of error introduced depends also on the means by which the array is fed.

Considerable interest has been expressed lately in large two-dimensional arrays, particularly those which produce large scanning angles by means of electronic scanning techniques. The study of the behavior of *large* arrays divides itself naturally into two parts, one associated with the *central portion* of the array, and the second related to the *edge effects*. Each element of the central portion of the array "sees" essentially the same environment, so that this central portion, which actually constitutes the bulk of a large array, may be analyzed as if it were a portion of an infinite array. In this central portion, the effects of mutual coupling are to change the input or driving-point impedance of the radiating elements, and to produce a variation in this value as a function of scan angle. If each element of the array is fed independently, this variation will cause only a variation in the efficiency of the array, but will not produce pattern distortion or influence the sidelobe level. In the vicinity of the edge, however, the mutual coupling effect is different for each element, and consequently edge effects influence the sidelobe level and the pattern shape. If each element of the array is not fed by an independent line, but, for example, if the array elements are fed successively by a traveling wave, errors in the impedance values for the elements in the central portion will produce errors in the desired amplitude or phase distribution of the array, and in consequence affect the pattern shape.

The present paper is concerned with the calculation of array element input impedances, and consequently of mutual coupling effects, for the central portion of the array. The evaluation of edge effects and their influence on sidelobe level is presented in one of the companion papers, of this series, Part III.

A procedure commonly employed for the determination of the input (or driving-point, or active) impedance of an element in an array is to determine first the self impedance of the element and the mutual impedances between neighbors, and then to sum these appropriately to yield the input impedance which correctly accounts for the presence of all the other elements in the array. For example, when the radiating element is a dipole, the input impedance of a typical dipole in the array may be computed by means of Carter's[1] mutual impedance calculations, or by any of several modifications or improvements on his original results. However, since the sums involved are slowly convergent, the calculations required in this method are very tedious and this computation procedure is not practical.

The point of view adopted in this paper recognizes the *periodicity* present in an array[2] and utilizes this periodicity for the direct evaluation of the desired input impedance (or admittance). By this technique, which is a waveguide approach, the mutual impedance contributions from all of the other elements are taken into account *automatically* in a direct and simple fashion. The periodic structure point of view is described in Section II, where a rectangular slot is chosen as a representative element of a two-dimensional array radiating into a half-space. Each slot in the array is fed by a separate waveguide, but the slot spacing and progressive phasing is arbitrary. A slot array was chosen as the typical example both because results for it are of practical interest

* Manuscript received by the PGAP, August 17, 1959; revised manuscript received, December 28, 1959. The work reported in this paper was performed by Lincoln Laboratory, a center for research operated by the Massachusetts Institute of Technology. The work was supported by the U. S. Air Force.

† Lincoln Laboratory (M.I.T.), Lexington, Mass.

‡ Microwave Research Institute, Polytechnic Institute of Brooklyn, Brooklyn, N. Y.

[1] P. S. Carter, "Circuit relations in radiating systems and applications to antenna problems," PROC. IRE, vol. 20, pp. 1004–1041; June, 1932.

[2] H. A. Wheeler, "The radiation resistance of an antenna in an infinite array or waveguide," PROC. IRE, vol. 36, pp. 478–487; April, 1948. Wheeler is the first to present this point of view but he does not deduce any of the results quoted here. In particular, his pioneering paper does not consider the influence of scan angle or susceptance effects.

in themselves, and because it is possible to derive these results accurately for this example. The periodic structure approach employed in the analysis is not restricted to the method by which the array is fed, however. The method of feed considered here is chosen because it is widely used in conjunction with certain electronic scan methods. While the discussion is phrased in terms of radiation from the array, this approach is equally applicable to the case of reception by the array of an incoming wave.

By regarding the array as a junction between two waveguides, the feed guide and the "guide" in the half-space, the calculation of the slot input conductance and susceptance becomes a straightforward one which employs *ordinary waveguide methods*. A variety of interesting results are derived by this means in Section III, indicating, for example, the variation of admittance with the array dimensions, the jumps in conductance when certain grating lobes suddenly appear, etc.

Results for the conductance values are derived in Section IV for arbitrary scan angle;[3] they reduce correctly to values for special cases. It is of interest that the conductance varies strongly with scan angle, and that the variation is quite different for different directions of scan. Considerations appropriate to the analysis of the array as a receiving antenna are presented in Section V.

Expressions for the *susceptance* values of the slot array elements are derived and discussed in Section VI. It is shown there that a slot which is resonant when radiating by itself into a half-space can become either inductive or capacitive (but usually inductive), depending on the array spacings, when placed in an array.

II. Periodic Structure Point of View

The application of the periodic structure point of view to an array of radiating elements is independent of the type of element employed. In Fig. 1, a two-dimensional array of rectangular slots radiating into a half-space is shown as a typical example. It is seen in Fig. 1 that the slots are all identical and are arranged in a pattern with rectangular symmetry. If the end effects of the array are assumed negligible, or if a particular slot under consideration is far from an edge of the array, and if all slots are fed with the same amplitude but with a progressive phase difference between successive slots, then it is permissible to treat the array as a periodic structure. The slots are fed by some means below the plane shown in Fig. 1, but the periodic structure approach, which is a method for the treatment of the space into which the radiation occurs, is not influenced by the method used to feed the radiating elements.

It is useful to draw a unit cell around a typical slot in this periodic array, as indicated in Fig. 1; since the slot radiates into space, the unit cell extends indefinitely. When the slot array is radiating broadside, or receiving normally incident radiation, all slots are in phase and possess equal amplitudes. Then, due to the excitation in the slots and the symmetry of the array, the unit cell is bounded by electric and magnetic walls, as shown in Fig. 2. These walls do not perturb the field distribution but are present because of field symmetries. Once the walls are present, the field outside of the unit cell may be completely ignored and the unit cell may be regarded as a kind of waveguide. It is also seen that all mutual coupling effects due to neighbors are *automatically* taken into account by this viewpoint.

The dominant mode in the waveguide represented by the unit cell of Fig. 2 is the *TEM* mode. If the dimensions of the unit cell, or, alternatively, the spacings between successive slots, are small enough, no higher modes will propagate in the unit cell and, equivalently, no higher order beams will appear in the radiated field. In fact, it is shown below that the onset of higher modes in the unit cell corresponds exactly to the appearance

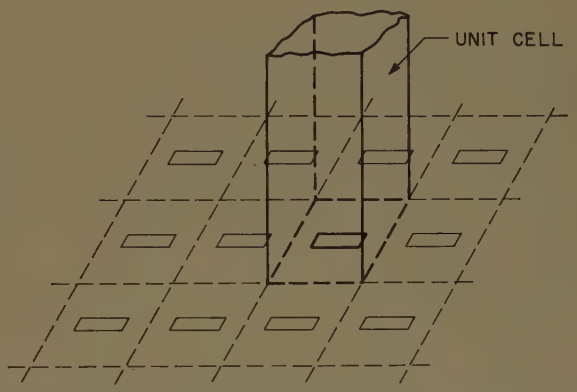

Fig. 1—Two-dimensional array of slots radiating into a half-space.

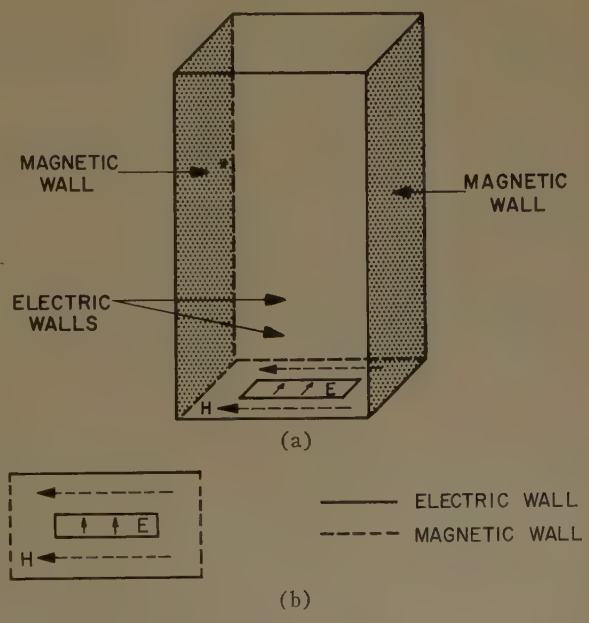

Fig. 2—Unit cell of slot array under conditions of broadside radiation or normally incident radiation. (a) Full view. (b) Top view.

[3] G. C. McCormick, "The Resonant Conductance of Slots in Linear and Two-Dimensional Arrays," presented at the URSI-IRE meeting in Washington, D. C., May, 1957. Some of the results derived here were also obtained by McCormick using a quite different approach.

of higher order beams in the radiation pattern. This equivalence is a check on the consistency of the representation.

When the array is scanned, the slots still possess equal amplitudes, but a constant phase difference appears between successive slots. The walls of the unit cell of Fig. 1 are now of a peculiar sort in that opposite walls are identical to each other except for a phase difference dependent on the scan angle. As an illustrative example, let the array be scanned in a direction parallel to the long dimension of the slots. If the scan angle θ is defined by Fig. 3 with respect to the ground plane, which is chosen as the xy plane, then the scanning occurs in the xz plane.

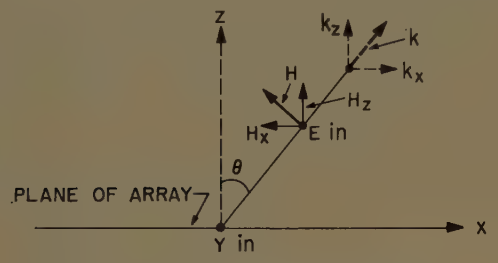

Fig. 3—Geometry for scanning in xz plane.

In the unit cell, the walls parallel to the long dimension of the slots remain electric walls, while the other pair of walls are of the periodic nature, differing by a phase shift. The modes in such waveguides are defined in Section IV. It is seen from Fig. 3, however, that the dominant mode in the unit cell waveguide is no longer a TEM mode, but is now an H (or TE) mode since a longitudinal component of field is present in the z direction. Scanning in the yz plane would produce an E (or TM) mode as the dominant mode in the unit cell, while scanning at an arbitrary angle results in both an H and an E mode or, alternatively, a single so-called H-type mode; further details are presented in Section IV.

For the dominant mode in the unit cell corresponding to scanning in the xz plane, one sees from Fig. 3 that the wavenumbers are:

$$k_x = k \sin \theta,$$
$$k_y = 0, \tag{1}$$

so that the transverse wavenumber k_t becomes

$$k_t = \sqrt{k_x^2 + k_y^2} = k \sin \theta. \tag{2}$$

For the higher modes in this unit cell, one has[4]

$$k_x = \left| k \sin \theta - \frac{2m\pi}{A} \right|,$$
$$k_y = \frac{2n\pi}{B}, \tag{3}$$

where A and B are the dimensions of the unit cell (see Fig. 2), so that k_t becomes

$$k_t = \sqrt{\left(k \sin \theta - \frac{2m\pi}{A} \right)^2 + \left(\frac{2n\pi}{B} \right)^2}. \tag{4}$$

If $A > B$, as is usually the case, the first higher mode is given by $m = 1$, $n = 0$, so that

$$k_t = \left| k \sin \theta - \frac{2\pi}{A} \right|. \tag{5}$$

To insure that this mode is below cutoff, we require $k < k_t$, or

$$k < \frac{2\pi}{A} - k \sin \theta;$$

since $k = 2\pi/\lambda$, we find

$$A < \frac{\lambda}{1 + \sin \theta} \tag{6}$$

as the condition on the wall spacing A of the unit cell in order to prevent any higher mode propagation. It is noted that this condition on A is a function of scan angle θ, and that it yields the familiar results that at broadside, $A < \lambda$, and at end-fire, $A < \lambda/2$, are required. Condition (6), however, is precisely the well-known criterion for the prevention of higher order beams in the radiation pattern, and illustrates the correspondence between these higher order beams and higher modes in the unit cell.

The periodic cell approach lends itself readily to an impedance (or admittance) description of the array. The details of this description, however, depend upon how the elements of the array are fed, and in the discussion below each slot is assumed to be fed by a separate rectangular waveguide. This method of feed is widely employed in certain electronic scan methods. The array is then regarded as a junction between two waveguides, the feed waveguide and the unit cell waveguide in the half-space, as shown in Fig. 4(a). The equivalent network corresponding to this geometrical configuration is given in Fig. 4(b) for the case of radiation from the array. For the receiving case, which is discussed in Section V, the network would be reversed since the incident power now enters the unit cell guide. The impedance properties of the array are specified by the values of the susceptance B and the conductance G, which can be evaluated by ordinary waveguide methods. The susceptance B is seen to be related to the sum of the stored powers on each side of the slot, while the input conductance G is simply the characteristic admittance of the unit cell waveguide brought through a transformer representing the change in guide cross section occurring at the junction between the two guides. Thus, the evaluation of B and G is a straightforward procedure which can be made as accurate as one pleases.

[4] N. Marcuvitz, "Waveguide Handbook," Rad. Lab. Series, vol. 10, McGraw-Hill Book Co. Inc., New York, N. Y., pp. 88, 89; 1951.

Since the field in the unit cell waveguide is that of the propagating mode carried by it, except in the vicinity of the slot, this field is undamped along the guide. When it is further recalled that the half-space consists of a two-dimensional array of these unit cell waveguides, one recognizes that the radiation field described by the periodic cell approach remains constant in amplitude as the radiated power travels away from the plane of the array. This field behavior is characteristic of the well-known features of the *Fresnel* region. The distance from the array plane at which this picture no longer describes the radiation field and at which the transition to the *Fraunhofer* region occurs is a function of the size of the array.

III. Radiation Conductance of Slot Array Elements for Broadside Radiation

For the case of broadside radiation, the walls of the unit cell waveguide are electric and magnetic walls, as shown in Fig. 2. If each slot in the array is fed by a separate rectangular waveguide of dimensions a by b, the geometrical configuration of Fig. 4(a) and the equivalent network of Fig. 4(b) are applicable, where the geometry of the junction between the guides is shown in Fig. 5. We note that the slot is centered in both the rectangular feed guide and the unit cell guide. The characteristic admittance Y and the propagation wavenumber κ characterize the transmission line representing the rectangular feed guide; the corresponding parameters for the unit cell guide will have the subscript p,

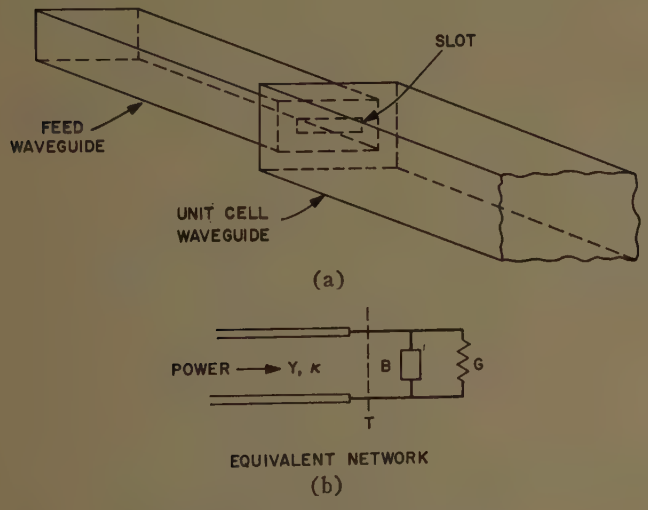

Fig. 4—Unit cell of array on radiation.

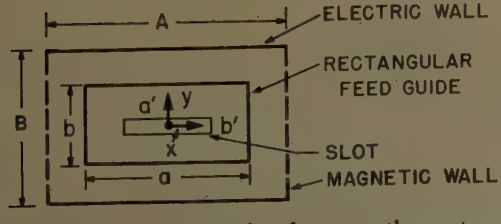

Fig. 5—Geometry of the junction between the rectangular feed waveguide and the unit cell waveguide, for the case of broadside radiation.

signifying "periodic," since the half-space is composed of these unit cells which exist in virtue of the periodicity of the array.

One may write, symbolically,

$$\frac{B}{Y} = \frac{\text{Stored Power}}{Y(V)^2} \tag{7}$$

$$\frac{G}{Y} = \frac{\text{Radiated Power}}{Y(V)^2}, \tag{8}$$

where B and G are normalized to the characteristic admittance of the rectangular feed guide, and where

$$Y = \frac{\kappa}{\omega\mu}, \qquad \kappa = 2\pi/\lambda_g = \sqrt{k^2 - (\pi/a)^2}, \tag{9}$$

since the dominant mode in rectangular waveguide is an H (or TE) mode. The voltage term in (7) and (8) is defined by

$$V = \iint_{\text{slot}} \boldsymbol{n} \times \boldsymbol{E} \cdot \boldsymbol{h}^* dS, \tag{10}$$

where the rectangular waveguide orthonormal mode function

$$\boldsymbol{h}(x) = \mathbf{x}_0 \sqrt{\frac{2}{ab}} \cos \frac{\pi x}{a} \tag{11}$$

is subject to the normalization

$$\iint_{\text{cross section}} \boldsymbol{h} \cdot \boldsymbol{h}^* dS = 1, \tag{12}$$

consistent with definition (9) for Y. The slot electric field E in (10) is chosen as

$$\boldsymbol{n} \times \boldsymbol{E} = \mathbf{x}_0 \cos \frac{\pi x}{a'}, \tag{13}$$

and is expected to be an excellent approximation when the slot is narrow and near resonance; $\mathbf{x}_0$ and $\boldsymbol{n}$ are the unit vectors parallel and normal to the slot, respectively, and dimensions a and a' are indicated in Fig. 5.

A. Single Main Beam Only

A single main beam in the radiation pattern corresponds to only a single mode propagating in the unit cell, or periodic, waveguide. This single mode in the unit cell of Fig. 2 is the TEM mode, for which the characteristic admittance Y_p is

$$Y_p = \sqrt{\frac{\epsilon}{\mu}} = \frac{k}{\omega\mu}, \tag{14}$$

and the orthonormal mode function $\boldsymbol{h}_p$, subject to normalization (12), is

$$\boldsymbol{h}_p = \mathbf{x}_0 \sqrt{\frac{1}{AB}}, \tag{15}$$

where A and B are the cross-section dimensions of the periodic waveguide. The radiated power in this guide can then be written as

$$P = Y_p | V_p |^2, \tag{16}$$

where the voltage term is

$$V_p = \iint_{\text{slot}} n \times E \cdot h_p^* dS, \tag{17}$$

E being the slot electric field given by (13).

We therefore have from (8),

$$\frac{G}{Y} = \frac{Y_p}{Y} \left| \frac{V_p}{V} \right|^2; \tag{18}$$

by using (10) and (17) we find

$$V = \sqrt{\frac{2}{ab}} \frac{2a'b'}{\pi} \frac{\cos(\pi a'/2a)}{1 - (a'/a)^2} \tag{19}$$

$$V_p = \frac{1}{\sqrt{AB}} \frac{2a'b'}{\pi}, \tag{20}$$

so that the radiation conductance normalized to the rectangular waveguide becomes

$$\left(\frac{G}{Y}\right)_p = \frac{\lambda_g}{\lambda} \frac{ab}{2AB} \left[\frac{1 - (a'/a)^2}{\cos(\pi a'/2a)}\right]^2, \tag{21}$$

where we have set $\kappa = 2\pi/\lambda_g$, and where the $(\ \ )_p$ signifies that the radiation occurs into the unit cell, or periodic, waveguide.

If the same slot is not an element of an array but is isolated and radiates into a *half-space*, and a cosine slot field is maintained, we have[5]

$$\left(\frac{G}{Y}\right)_{hs} = \frac{2\pi}{3} \frac{\lambda_g}{\lambda} \frac{ab}{\lambda^2} \left[\frac{1 - (a'/a)^2}{\cos(\pi a'/2a)}\right]^2 \cdot \left[1 - 0.374\left(\frac{a'}{\lambda}\right)^2 + 0.130\left(\frac{a'}{\lambda}\right)^4\right], \tag{22}$$

where terms of the order of $(b'/a')^2$ are neglected. If we take the ratio of (21) to (22), we find

$$\frac{\left(\frac{G}{Y}\right)_p}{\left(\frac{G}{Y}\right)_{hs}} = \frac{3}{\pi} \frac{(\lambda/2)^2}{AB} \frac{1}{\left[1 - 0.374\left(\frac{a'}{\lambda}\right)^2 + 0.130\left(\frac{a'}{\lambda}\right)^4\right]}. \tag{23}$$

Result (23) is the ratio between the conductance when all mutual coupling effects have been taken into account and the value for which no mutual effects are present. This ratio is sometimes denoted as the ratio of the "active" to the "self" conductances.

Expression (23) is very interesting. Recognizing that the value of the bracketed expression is nearly unity (in fact, for slots near resonance, $a'/\lambda \approx \frac{1}{2}$, so that the bracket equals approximately 0.9), we note that ratio (23) may be written as

$$\frac{\left(\frac{G}{Y}\right)_p}{\left(\frac{G}{Y}\right)_{hs}} \approx \frac{(\lambda/2)^2}{AB}. \tag{24}$$

Let us consider an array composed of X-band rectangular waveguides packed as closely together as possible. Then, neglecting the wall thickness, we have $a = A = 0.90''$ and $b = B = 0.40''$. Since midband operation corresponds roughly to $\lambda = 1.20''$, we find that for this situation (24) becomes

$$\frac{\left(\frac{G}{Y}\right)_p}{\left(\frac{G}{Y}\right)_{hs}} \approx 1.$$

If the waveguides are not directly adjacent to each other the A and B become larger and the ratio becomes somewhat less than unity.

We have the interesting result, then, that for practical broadside array conditions the conductance of a slot in a two-dimensional array is not very much different from that of the same slot when isolated. Thus, under certain fortuitous, but not unusual, conditions, very small error is introduced even if all mutual coupling effects are ignored.

B. Higher Order Beams

Higher order beams in the radiation pattern correspond to higher modes propagating in the periodic waveguide. For N propagating modes, the radiated power is written as

$$P = \sum_{i=1}^{N} Y_{pi} | V_{pi} |^2, \tag{25}$$

so that the expression for the conductance becomes

$$\left(\frac{G}{Y}\right)_p = \sum_{i=1}^{N} \frac{Y_{pi}}{Y} \left| \frac{V_{pi}}{V} \right|^2. \tag{26}$$

The sum (26) includes contributions from all propagating modes, whether E or H modes. However, the behavior of the added contribution from a higher mode will be different depending on whether the mode is an E or H mode.

1) *Contribution from Higher H Modes:* Suppose that the electric wall spacing B is maintained less than λ, but that the *magnetic wall spacing* A is increased to be

[5] This result appears in many places. In this specific form it is given in: A. A. Oliner, "Equivalent Circuits for Slots in Rectangular Waveguide," Rept. R-234-50, Microwave Res. Inst., Polytechnic Institute of Brooklyn, Brooklyn, N. Y., p. 121, eq. (3.118); 1951.

greater than λ. The first higher mode in this situation is an H mode with a field distribution of the type shown in Fig. 6. It is to be recalled that the slot is centered in the guide cross section.

All of the higher modes which would be present under these conditions are H modes due to the orientation and excitation of the slot. The characteristics of a typical higher mode of this type are:

$$k_{tn} = 2n\pi/A, \qquad \kappa_{pn} = \sqrt{k^2 - (2n\pi/A)^2} \tag{27}$$

$$Y_{pn} = \frac{\kappa_{pn}}{\omega\mu} \tag{28}$$

$$h_{pn} = \mathbf{x}_0 \sqrt{\frac{2}{AB}} \cos\frac{2n\pi x}{A}. \tag{29}$$

The corresponding mode voltage is then

$$V_{pn} = \iint_{\text{slot}} n \times E \cdot h_{pn}^* dS, \tag{30}$$

where the slot field is still given by (13). By using (29), (30) becomes

$$V_{pn} = \sqrt{\frac{2}{AB}} \frac{2a'b'}{\pi} \frac{\cos(n\pi a'/A)}{1 - (2na'/A)^2}. \tag{31}$$

When the characteristic admittances (9) and (28) are employed together with voltage terms (19) and (31) in expression (26) for the normalized conductance, and when these contributions are added to (21) for the dominant mode, (26) becomes

$$\left(\frac{G}{Y}\right)_p = \frac{\lambda_g}{\lambda} \frac{ab}{2AB} \left[\frac{1 - (a'/a)^2}{\cos(\pi a'/2a)}\right]^2 \left\{1 + 2\sum_{n=1}^{N} \cdot \sqrt{1 - \left(\frac{n\lambda}{A}\right)^2} \left[\frac{\cos(n\pi a'/A)}{1 - (2na'/A)^2}\right]^2\right\}, \tag{32}$$

when N higher H modes are propagating. One can also take the ratio of (32) to the half-space value (22) to obtain a result akin to (23), namely,

$$\frac{\left(\frac{G}{Y}\right)_p}{\left(\frac{G}{Y}\right)_{hs}} = \frac{3}{\pi} \frac{(\lambda/2)^2}{AB} \frac{\left\{1 + 2\sum_{n=1}^{N} \sqrt{1 - (n\lambda/A)^2} \left[\frac{\cos(n\pi a'/A)}{1 - (2na'/A)^2}\right]^2\right\}}{[1 - 0.374(a'/\lambda)^2 + 0.130(a'/\lambda)^4]}. \tag{33}$$

2) *Contributions from Higher E Modes:* Suppose now that the magnetic wall spacing A is maintained less than λ, but the *electric wall spacing* B is increased to be greater than λ. The higher modes arising in this situation are all E modes, due to the slot excitation and location, and the field configuration for the lowest of these modes is shown in Fig. 7.

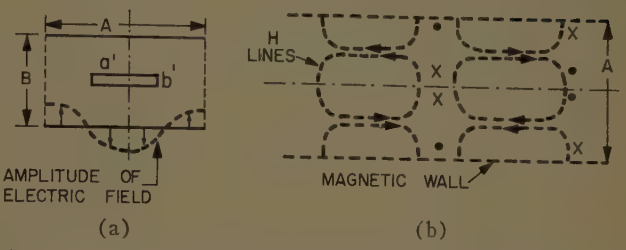

Fig. 6—First higher H mode in periodic waveguide under broadside radiation conditions. (a) Cross section view. (b) Top longitudinal view.

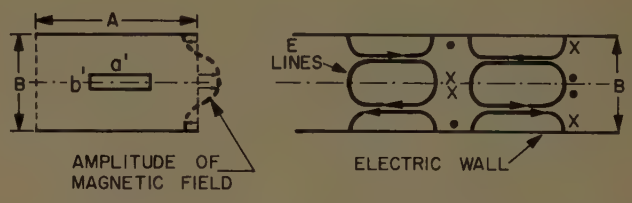

Fig. 7—First higher E mode in periodic waveguide under broadside radiation conditions. (a) Cross section view. (b) Top longitudinal view.

The characteristics of a typical higher E mode are:

$$k_{tn} = 2n\pi/B, \qquad \kappa_{pn} = \sqrt{k^2 - (2n\pi/B)^2} \tag{34}$$

$$Y_{pn} = \frac{\omega\epsilon}{\kappa_{pn}} \tag{35}$$

$$h_{pn} = \mathbf{x}_0 \sqrt{\frac{2}{AB}} \cos\frac{2n\pi y}{B}. \tag{36}$$

The mode voltage, obtained on use of (36) in (30), is now

$$V_{pn} = \sqrt{\frac{2}{AB}} \frac{2a'b'}{\pi} \left[\frac{\sin(n\pi b'/B)}{n\pi b'/B}\right]. \tag{37}$$

The use of characteristic admittances (9) and (35) and voltages (19) and (37) in (26), together with the dominant mode contribution (21), produces the following expression for the normalized conductance when N higher E modes are propagating:

$$\left(\frac{G}{Y}\right)_p = \frac{\lambda_g}{\lambda} \frac{ab}{2AB} \left[\frac{1 - (a'/a)^2}{\cos(\pi a'/2a)}\right]^2 \left\{1 + \sum_{n=1}^{N} \frac{2}{\sqrt{1 - (n\lambda/B)^2}} \left[\frac{\sin(n\pi b'/B)}{n\pi b'/B}\right]^2\right\}. \tag{38}$$

When result (38) is normalized to the half-space value (22) to obtain an expression similar to (23) or (33), one finds

$$\frac{\left(\frac{G}{Y}\right)_p}{\left(\frac{G}{Y}\right)_{hs}} = \frac{3}{\pi}\,\frac{(\lambda/2)^2}{AB}\,\frac{\left\{1+\sum_{n=1}^{N}\frac{2}{\sqrt{1-(n\lambda/B)^2}}\left[\frac{\sin\,(n\pi b'/B)}{n\pi b'/B}\right]^2\right\}}{[1-0.374(a'/\lambda)^2+0.130(a'/\lambda)^4]}. \tag{39}$$

A graphical indication of the way in which g_H and g_E vary with A/λ and B/λ, respectively, for the case $a'/\lambda = \frac{1}{2}$, is given in Figs. 8(a) and (b). It must be recalled that for g_H, $B<\lambda$, while for g_E, $A<\lambda$, and that the radiating slot is always centered in the periodic waveguide. We see from Fig. 8 that if the array spacings are accidentally such that g_H or g_E is unity, the neglect of mutual coupling has no effect. This fact may shed light on why difficulties occur in some array designs which neglect mutual coupling, but not in others. From the curves for g_E, it is seen that if spacing B is approximately one wavelength, the conductance value changes wildly. This effect may lead to erratic behavior if the wavelength is of this value and is changed slightly. If the array is scanned, the spacing at which the erratic behavior could occur is less than one wavelength, and varies between $\lambda/2$ and λ depending on the angle of scan.

3) *Discussion of Results:* Expressions (33) and (39) are the ratios of the conductance of the slot when it radiates in an array to that when it is isolated; they apply, respectively, to the cases for which the higher modes are H modes or E modes. Let us represent these ratios by g_H and g_E, respectively. It is seen that the manner in which a given higher mode contributes to g_H or g_E is very different. This difference is due to the location of the square root term under the summation, and is related to the different frequency dependence of the characteristic admittance for H and E modes. In g_H, the square root term occurs in the numerator of the added terms so that at cutoff for the higher mode, as it just begins to contribute, $A=n\lambda$, and the square root is zero. The contribution from the additional H mode is thus *zero* as the mode contribution just begins. In strong contrast, in g_E the square root term appears in the denominator of the added terms. Thus, at cutoff, when $B=n\lambda$, the square root again becomes zero, but now the contribution from the additional mode is *infinite* as the mode contribution just begins.

The curves for g_H and g_E are identical for A/λ and B/λ less than unity, of course, since only the dominant mode is present then. As A/λ or B/λ approaches infinity, these curves do not asymptotically approach unity. These asymptotic values will depend upon B/λ for g_H and A/λ for g_E, and are also a function of a'. As $A\rightarrow\infty$, the geometrical configuration reduces to a one-

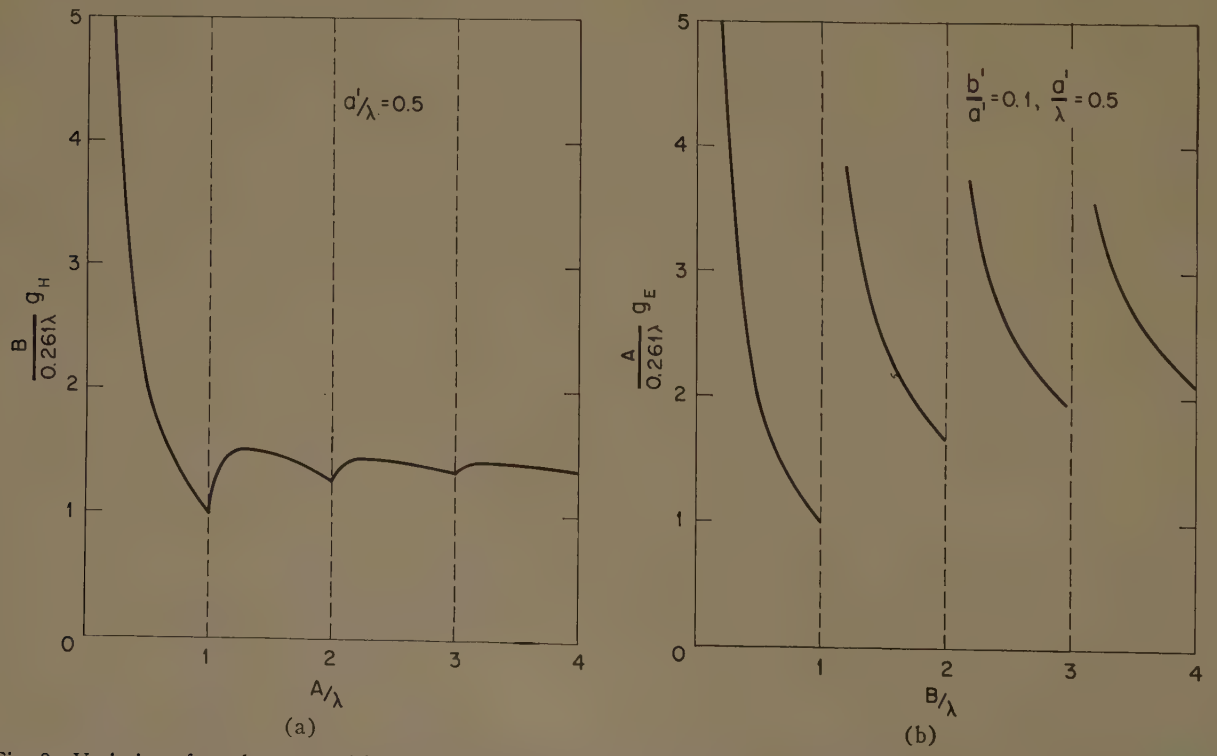

Fig. 8—Variation of conductance with array dimensions for higher order beams. (a) Higher H modes. (b) Higher E modes.

dimensional array of slots which produce broadside radiation, or, alternatively, a single slot radiating into a parallel plate region. As a check on the result for g_H, the asymptotic value of (33) was obtained as A and $N \to \infty$, while maintaining $B < \lambda$, and was found for $a' = \lambda/2$ to be

$$g_H \to \frac{1}{2.75} \frac{\lambda}{B},$$

in exact agreement with Gruenberg,[6] after a change in notation and an appropriate transformation from his longitudinal shunt slot resistance to our conductance.

IV. Variation of Slot Conductance With Array Scan Angle

In Section III, the slot conductance was evaluated for various situations, but for broadside radiation only. When the array is scanned, the radiated beam actually points off in some direction, but the periodic structure approach considers the "propagation" still to occur in the z direction along the unit cell, normal to the array. The walls of the unit cell then become phase-dependent, as discussed in Section II. Furthermore, depending on the direction of scan, the dominant mode in the unit cell waveguide may be different, resulting in different scanning behavior because the functional dependences of the characteristic admittances are not the same.

The dependence of conductance on scan angle is determined first for two special cases: scanning in the plane parallel to the long dimension of the slots, and scanning in the plane perpendicular to it. The results for these special cases are of interest in themselves. The expression for arbitrary scan angle is then derived.

A. Plane of Scan Parallel to Slots

When the array is scanned in the plane parallel to the long dimension of the slots, the electric walls of spacing B of the unit cell remain as before, and the magnetic walls are replaced by ones of phase-dependent character. The geometry of Fig. 3 is appropriate to this case of scanning in the xz plane, and, as discussed in Section II, indicates that the dominant mode in the unit cell, or periodic, waveguide is an *H mode*. Furthermore, the propagation wavenumber κ_p of this mode is

$$\kappa_p = k \cos \theta, \tag{40}$$

where θ is the angle the radiating plane wave makes with the normal to the array. The mode function of the dominant mode then becomes

$$h_p(x) = \mathbf{x}_0 \frac{1}{\sqrt{AB}} e^{-jk_x x}, \tag{41}$$

with

$$k_x = k \sin \theta. \tag{42}$$

The mode function (41), which takes into account the phase difference between the opposite walls of spacing A, is still subject to the normalization condition (12). The associated characteristic admittance is

$$Y_p = \sqrt{\frac{\epsilon}{\mu}} \cos \theta. \tag{43}$$

Employing (41) and field assumption (13) in (17), we find for the dominant mode voltage in the periodic waveguide

$$V_p = \frac{1}{\sqrt{AB}} \frac{2a'b'}{\pi} \frac{\cos (k_x a'/2)}{1 - (k_x a'/\pi)^2}, \tag{44}$$

or

$$V_p = (V_p)_{\theta=0} \frac{\cos \left(\frac{\pi a'}{\lambda} \sin \theta \right)}{1 - \left(\frac{2a'}{\lambda} \sin \theta \right)^2}, \tag{45}$$

where the voltage for $\theta = 0$ is given by (20).

Employment of (18) and comparison with the $\theta = 0$ result (21) permits the expression for the normalized conductance to be written as

$$\left(\frac{G}{Y} \right)_\theta = \left(\frac{G}{Y} \right)_{\theta=0} \frac{\cos \theta \cos^2 \left(\frac{\pi a'}{\lambda} \sin \theta \right)}{\left[1 - \left(\frac{2a'}{\lambda} \sin \theta \right)^2 \right]^2}. \tag{46}$$

The angle dependent factor in (46) varies with angle somewhat like $\cos \theta$ alone, but a bit more rapidly. The conductance for this scan direction thus *decreases* with scan angle.

B. Plane of Scan Perpendicular to Slots

The beam is now scanned in the yz plane, so that in the unit cell the magnetic walls of spacing A remain while the electric walls of spacing B are replaced by phase-dependent walls. Since an E_z component of field is introduced by the scan, the dominant mode now becomes an *E mode*. Thus, while the propagation wavenumber κ_p is still given by (40), the characteristic admittance now becomes

$$Y_p = \sqrt{\frac{\epsilon}{\mu}} \frac{1}{\cos \theta}. \tag{47}$$

The mode function is

$$h_p(y) = \mathbf{x}_0 \frac{1}{\sqrt{AB}} e^{-jk_y y}, \tag{48}$$

with

$$k_y = k \sin \theta; \tag{49}$$

[6] H. Gruenberg, "Theory of wave-guide-fed slots radiating into parallel-plate regions," *J. Appl. Phys.*, vol. 23, pp. 733–737; July, 1952.

and the voltage term becomes

$$V_p = \frac{1}{\sqrt{AB}} \frac{2a'b'}{\pi} \frac{\sin (k_y b'/2)}{k_y b'\ 2} \tag{50}$$

on use of (48) in (17). When (50) is inserted into (18) and comparison is made with the $\theta=0$ result (21), the result for the normalized conductance may be stated as

$$\left(\frac{G}{Y}\right)_\theta = \left(\frac{G}{Y}\right)_{\theta=0} \frac{1}{\cos\theta} \left[\frac{\sin\left(\frac{\pi b'}{\lambda}\sin\theta\right)}{\frac{\pi b'}{\lambda}\sin\theta} \right]^2. \tag{51}$$

The term in brackets is close to unity for narrow slots, so that the conductance is seen to *increase* with scan angle, in contrast to result (46). The dependence of conductance on scan angle is thus essentially opposite for scanning in these two orthogonal planes.

C. Arbitrary Scan Angle

The spherical coordinate system shown in Fig. 9 is

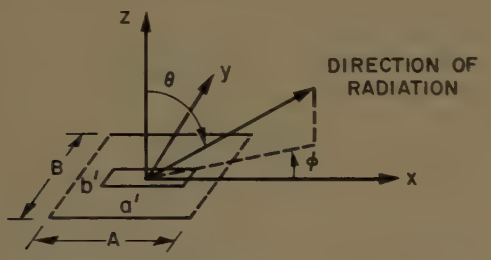

Fig. 9—Spherical coordinate system for description of arbitrary angle radiation.

employed to describe the radiation characteristics for arbitrary scan angle θ, ϕ; $\theta=0$ corresponds to broadside radiation. For arbitrary scan angle all four walls of the unit cell are phase-dependent, and both E_z and H_z field components are created. Thus, *both* the lowest E mode and the lowest H mode are propagating simultaneously in the periodic waveguide, and a superposition of these two modes is required to account for the total far field distribution.

While the calculation of the conductance in terms of these two dominant modes is straight-forward, the evaluation may be simplified by the use of an alternative mode set, the so-called E-type and H-type modes (sometimes referred to as the LSM and LSE modes, respectively). Because of the symmetry of the slot array and the choice of a unidirectional slot electric field, a proper choice of E-type or H-type mode permits the radiation field to be expressed in terms of *one*, rather than two, dominant modes.

The E-type and H-type modes are characterized by a vanishing magnetic or electric field component, respectively, in one of the transverse directions, rather than in the longitudinal direction as in the case of E and H modes. Each of the E-type and H-type modes are orthogonal to each other and the set is complete, but the pertinent orthogonality statement is[7]

$$\iint_{\text{cross section}} z_0 \times e_i \cdot h_j dS = \delta_{ij}, \tag{52}$$

where

$$\delta_{ij} = \begin{cases} 0, & i \neq j \\ 1, & i = j \end{cases}$$

rather than

$$\iint_{\text{cross section}} h_i \cdot h_j dS = \delta_{ij},$$

since

$$z_0 \times e_i \neq h_i,$$

in contrast to E and H modes. However, expression (17) for the voltage is still valid since it is consistent with (52).

An examination of the field lines in the plane containing the slots indicates that while the magnetic field has components in both the x and y directions, the electric field points only in the y direction (since a unidirectional slot field is chosen). Hence, the dominant mode is an *H-type mode with respect to the x direction*, since there is no E_x component.

The appropriate mode function is[7]

$$h_i(x, y) = \frac{e^{-j(k_x x + k_y y)}}{\sqrt{AB}}, \tag{53}$$

with

$$Y_p = \frac{k^2 - k_x^2}{\omega\mu\kappa_p}. \tag{54}$$

where κ_p, k_x and k_y are given by (40), (42) and (49), respectively. The peculiar form taken by Y_p in (54) is important in the analysis. Employment of (53) in expression (17) for the mode voltage yields

$$V_p = \frac{1}{\sqrt{AB}} \frac{2a'b'}{\pi} \frac{\cos (k_x a'/2)}{1 - (k_x a'/\pi)^2} \frac{\sin (k_y b'/2)}{k_y b'/2}. \tag{55}$$

Since only a single propagating mode is present, the simple relation (18) is valid; the use of (9), (19), (54) and (55) in (18) produces the following result for the conductance:

$$\left(\frac{G}{Y}\right)_{\theta,\phi} = \frac{\lambda_g}{\lambda} \frac{ab}{2AB} \left[\frac{1 - (a'/a)^2}{\cos (\pi a'/2a)} \cdot \frac{\cos (k_x a'/2)}{1 - (k_x a'/\pi)^2} \cdot \frac{\sin (k_y b'/2)}{k_y b'/2} \right] \left[\frac{1 - \sin^2\theta \cos^2\phi}{\cos\theta} \right]. \tag{56}$$

[7] H. M. Altschuler and L. O. Goldstone, "On network representations of certain obstacles in waveguide regions," IRE TRANS. ON MICROWAVE THEORY AND TECHNIQUES, vol. MTT-7, pp. 213–221; April, 1959.

Expression (56) can be rephrased by reference to the broadside ($\theta=0$) value (21), and by substituting for k_x and k_y from (42) and (49), to yield

$$\left(\frac{G}{Y}\right)_{\theta,\phi}=\left(\frac{G}{Y}\right)_{\theta=0}\left[\frac{\cos\left(\frac{\pi a'}{\lambda}\sin\theta\cos\phi\right)}{1-\left(\frac{2a'}{\lambda}\sin\theta\cos\phi\right)^2}\right]^2 \cdot\left[\frac{\sin\left(\frac{\pi b'}{\lambda}\sin\theta\sin\phi\right)}{\frac{\pi b'}{\lambda}\sin\theta\sin\phi}\right]^2\left[\frac{1-\sin^2\theta\cos^2\phi}{\cos\theta}\right]. \quad (57)$$

One readily checks that (57) reduces correctly when $\theta=0$. Furthermore, when $\phi=0$ the scanning is performed in the xz plane and (57) reduces to relation (46), while for $\phi=\pi/2$ the scanning occurs in the yz plane and (57) becomes identical with (51).

The field distribution associated with the H-type mode is correct for all scan angles, and becomes identical with that for an H mode when $\phi=0$ and that for an E mode when $\phi=\pi/2$. An additional advantage, then, of the E-type, H-type formalism in this application is that a single mode suffices to describe the radiation field for all scanning positions, in contrast to the E, H mode formalism which requires only an H mode for xz plane scanning, only an E mode for yz plane scanning, but both an E and an H mode for arbitrary angle radiation.

It is clear from the discussion above that the conductance value changes significantly with scan angle and varies differently in different scan directions. As a consequence, unless a compensation scheme is employed, the efficiency of an array will change during scan, and more power will be radiated in some directions than in others.

V. The Array as a Receiving Antenna

Most of the discussion above was based on viewing the array as a transmitting antenna, and the conductance results, in particular, were phrased in that fashion. The periodic structure approach is equally valid, however, when the array is employed as a receiving antenna. The incident plane wave, coming in at some angle, is then phrased as an incident mode in the unit cell, or periodic, waveguide, with the propagation wavenumber κ_p related to the angle of incidence θ by (40), and the characteristic admittance Y_p dependent on the polarization and incidence direction of the incoming wave. If the array spacings are such that only a single propagating mode is present in the periodic waveguide, part of the incident wave power is transmitted into the rectangular waveguide and the remainder is reflected from the array interface in the *same mode* as the incident wave. If the array spacings were large enough to permit more than one propagating mode, the reflected wave would also contain higher order reflected beams.

The geometrical configuration of Fig. 4(a) is also applicable to the receiving case when the unit cell waveguide is regarded as the feed waveguide and the "radiation" occurs into the rectangular waveguide. The equivalent network of Fig. 4(b) must be replaced, however, by that of Fig. 10, in which one should note that

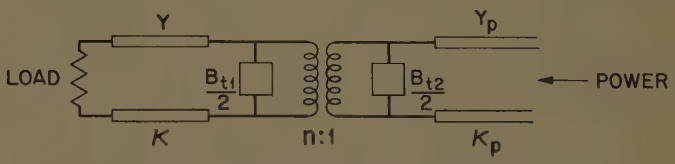

Fig. 10—Equivalent network for slot array as a receiving antenna.

the load terminating the receiving rectangular waveguide need not be matched. Explicit expressions for the susceptances $B_{t1}/2$ and $B_{t2}/2$ and the transformer turns ratio n, which characterize the junction between the unit cell and the rectangular waveguides, are discussed in Section VI. With the knowledge of this equivalent network one may determine many interesting properties of the array, such as its mismatch, its reactive content, and its efficiency.

When the receiving rectangular waveguide is terminated by a *matched load*, the useful power received by the antenna is given simply by

$$P=Y|V|^2, \quad (58)$$

where Y and V have been defined by (9) and (10). If the array spacings are such that only a single propagating mode is possible in the periodic waveguide, the conductance normalized to the characteristic admittance of the periodic waveguide may be stated as

$$\frac{G}{Y_p}=\frac{\text{Power Received}}{Y_p|V_p|^2}, \quad (59)$$

where the numerator is given by (58). When (58) is substituted into (59), one finds

$$\frac{G}{Y_p}=\frac{Y}{Y_p}\left|\frac{V}{V_p}\right|^2, \quad (60)$$

which is the inverse of G/Y as given by (18). Under these conditions one may then write

$$\left(\frac{G}{Y_p}\right)_{\text{receive}}=\frac{1}{\left(\frac{G}{Y}\right)_{\text{transmit}}}; \quad (61)$$

that is, the normalized conductance on reception is the inverse of the normalized conductance on transmission. If the slot were made resonant, *i.e.*, if its susceptance were made zero, a unity normalized conductance would imply a perfect power transfer. In view of (61) and the results of Section IV, however, which indicate that

the conductance varies strongly with scan angle, we must conclude that the efficiency of a receiving array will depend on the incidence angle of the received wave.

Since the slot array under consideration is linearly polarized, it will respond to only half of the possible incident polarizations. With the periodic structure approach, an incoming wave of arbitrary polarization and incidence angle is decomposed into an E-type mode and an H-type mode. These modes are discussed in Section IV. The E-type mode will not be detected by the array and will be totally reflected. The response of the array to the H-type mode is governed by the equivalent network of Fig. 10.

This response is, of course, mirrored in the match between the antenna (plus feed line) and the receiver input. Such a mismatch will cause a decrease in the efficiency of the system; in addition, the noise figure of the receiver will deteriorate badly. Furthermore, if a parametric amplifier is used, mismatch will throw it into oscillation.

VI. Susceptance of Slot Array Elements

The elements of an array are usually made resonant so that susceptance considerations are automatically eliminated, and attention is focused on the conductance behavior. However, the dimensions of the element for resonance are usually based on the isolated element rather than the element in an array, since information for the latter is not ordinarily available. It is shown below, for the case of slot elements, that the susceptance value does change if the array spacing is altered, so that an element which is resonant when isolated is no longer resonant when placed in an array. If the slot is wide, so that its Q is low, this shift in susceptance may not be significant; for a very narrow slot, which has a high Q, the susceptance change may be quite large.

From the periodic structure point of view, the slot in an array couples the rectangular waveguide, which is the feed guide in the transmitting case, to the periodic waveguide, as shown in Fig. 4(a). The slot therefore couples two rectangular waveguides of different cross section dimensions, one of all metallic walls and the other with peculiar walls under scanning conditions. For broadside radiation, the walls of the latter guide are electric and magnetic walls, as shown in Fig. 5, and this case will be considered first. The input susceptance, normalized to the feeding rectangular waveguide, is given by expression (7), where

$$(\text{P.S.})_{\text{total}} = (\text{P.S.})_{\text{interior}} + (\text{P.S.})_{\text{exterior}}, \qquad (62)$$

with P.S. signifying "power stored." The power stored is composed of the higher nonpropagating modes which are excited by the slot and remain in its vicinity; it may be viewed physically as being related to the distortion of the field lines in the neighborhood of the slot.

The power stored in the interior region is found readily by relating it to the susceptance of a transverse slot in a rectangular waveguide. The exterior region, however, is bounded by two electric walls and two magnetic walls, rather than all electric walls. A good approximation of the power stored in the exterior region can be made by the following reasoning. The power stored (or the distortion of the field lines) in the neighborhood of the slot resides primarily above and below the slot [in Fig. 4(a)] and only a little of it extends sideways. For this reason, the susceptance is influenced primarily by the proximity of the top and bottom walls and only slightly by the side walls. These statements have been verified by measurements on noncentered transverse slots in rectangular waveguides. If we therefore replace the magnetic walls at the sides of the slot by metallic (or electric) walls little change would occur in the stored power, although the mode function, and hence the mode voltage, would be affected.

With this replacement in mind, let us rewrite (7) as

$$\left(\frac{B}{Y}\right)_p = \frac{(\text{P.S.})_r}{Y|V|^2} + \frac{(\text{P.S.})_p}{Y_{pe}|V_{pe}|^2}\,\frac{Y_{pe}|V_{pe}|^2}{Y|V|^2}, \qquad (63)$$

where the subscripts r, p and pe signify the interior rectangular waveguide, the exterior periodic waveguide and the equivalent periodic waveguide (with all metallic walls), respectively. Relation (63) for the normalized susceptance of a slot radiating into the periodic waveguide can be expressed in terms of network elements as follows

$$\left(\frac{B}{Y}\right)_p = \left[\frac{1}{2}\,\frac{B_{t1}}{Y}\right] + \frac{1}{n^2}\left[\frac{1}{2}\,\frac{B_{t2}}{Y_{pe}}\right]; \qquad (64)$$

the equivalent network corresponding to (64) is presented in Fig. 11, in which the conductance G has also

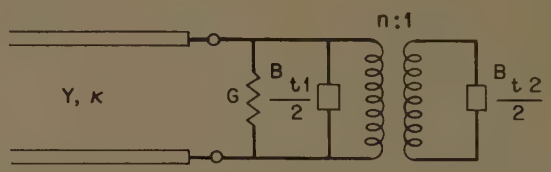

Fig. 11—Equivalent network representing the admittance terminating the rectangular feed guide.

been included for completeness. Turns ratio n in (64) is seen to be

$$n = \frac{V}{V_{pe}}\left[\frac{Y}{Y_{pe}}\right]^{1/2}, \qquad (65)$$

where V is given by (19) for a guide with dimensions a by b consisting of all electric walls; since V_{pe} corresponds to a similar guide with dimensions A by B, (19), with appropriate substitutions, may also be used for V_{pe}. The ratio of characteristic admittances is

$$\frac{Y}{Y_{pe}} = \frac{\kappa}{\kappa_{pe}}, \qquad (66)$$

where κ is given by (9), and κ_{pe} is

$$\kappa_{pe} = \sqrt{k^2 - (\pi/A)^2}, \tag{67}$$

so that n becomes

$$n = \left[\frac{AB}{ab}\cdot\frac{1-(\lambda/2a)^2}{1-(\lambda/2A)^2}\right]^{1/2} \cdot\left[\frac{\cos(\pi a'/2a)}{\cos(\pi a'/2A)}\cdot\frac{1-(a'/A)^2}{1-(a'/a)^2}\right]. \tag{68}$$

The susceptances in (64) are to be interpreted in the following way. B_{t1}/Y is the susceptance of a transverse slot, of dimensions a' by b', coupling identical waveguides with all metal walls of dimensions a by b, while B_{t2}/Y_{pe} is the susceptance of a similar slot coupling identical waveguides of metal walls of dimensions A by B. A reasonably accurate expression for B_{t1}/Y is[8]

$$\frac{B_{t1}}{Y} = \frac{4b}{\lambda_g}\left[\ln\csc\frac{\pi b'}{2b} + \frac{1}{2}\left(\frac{b}{\lambda_g}\right)^2\cos^4\frac{\pi}{2}\frac{b'}{b}\right] - \frac{4b}{\lambda_g}\left(\frac{\lambda_g}{\lambda_{g3}}\right)^2\left[\frac{\cos(3\pi a'/2a)}{\cos(\pi a'/2a)}\cdot\frac{1-(a'/a)^2}{1-9(a'/a)^2}\right] \cdot\left[1+\left(\frac{\pi}{2}\frac{b'}{\lambda_{g3}}\right)^2\right]\ln\left(\frac{4}{\gamma\pi}\frac{\lambda_{g3}}{b'}\right), \tag{69}$$

where

$$\gamma = 1.781$$

$$\lambda_{g3} = \left|\frac{\lambda}{\sqrt{1-(3\lambda/2a)^2}}\right|.$$

A corresponding expression is obtained for B_{t2}/Y_{pe} if in (69) a and b are replaced by A and B, and if similarly appropriate changes are made in λ_g and λ_{g3}.

Expression (64) is therefore the susceptance, normalized to the characteristic admittance of the rectangular feed waveguide, of a typical slot radiating into its associated unit cell, or periodic, waveguide. It was derived for broadside radiation conditions and was subject to certain assumptions regarding the localized nature of the stored power in the vicinity of the slot. These same assumptions also apply when the array is scanned, so that a design for resonance at broadside may be satisfactory during scanning as well. This supposition should certainly be valid for scanning in the xz plane, parallel to the long dimension of the slots, but the susceptance value may change somewhat when scanning is performed in the yz plane. The possible change in the susceptance value during scan (except for end-fire situations) is expected to be much less than the difference between the susceptance values for the slot in an array and the isolated slot radiating into a half-space.

Comparison between the values obtained from (64), using (68) and (69), and those computed from an accurate expression[9] for the susceptance of an isolated slot radiating into a half-space, indicates that if the isolated slot is made resonant the same slot employed in an array may be inductive or capacitive, but will in most instances be *inductive*. The amount by which the slot deviates from resonance depends on the array spacings and the height b' of the slot. A narrow height slot has a larger Q and deviates more rapidly from resonance. If the array spacings A and B are not much larger than the waveguide dimensions a and b, the slot will be inductive. Increasing A serves to make the slot more inductive, while increasing B reduces the inductive content. It is possible, by increasing B sufficiently while maintaining A not much larger than a, to make the slot resonant or even slightly capacitive. This statement is illustrated quantitatively by the calculations summarized in Table I. A slot in an X-band waveguide is chosen

TABLE I

$a=0.900$ inch, $a'=0.609$ inch, $f=9375$ mc
$b=0.400$ inch, $b'=0.120$ inch, $\lambda=1.260$ inches
$A=0.900$ inch

B	0.40 inch	0.80 inch	1.00 inch	1.20 inches
$(B/Y)_p$	−0.510	−0.180	−0.031	+0.158

to be resonant at a frequency of 9375 mc when it is isolated and radiating into a half-space. For a slot height $b'=0.120$ inch, the slot length under these conditions is found to be $a'=0.609$ inch; the waveguide dimensions are $a=0.900$ inch and $b=0.400$ inch, of course. Array spacing A is chosen for simplicity to be equal to a, and the resulting values of $(B/Y)_p$ are computed, using (64), for several values of spacing B. One sees from Table I that when B is less than 1.00 inch the slot is always inductive, while for larger spacings the slot passes through resonance and becomes capacitive.

The permissible values of A and B are limited, however, by the requirement that no higher order beams are created. In addition, it should be noted that as B approaches this critical limit value, the array behavior may become erratic, as indicated in Section III, B. For this reason, the slot should not be made resonant by adjusting the array spacings but rather by choosing the slot dimensions in accordance with (64).

If the slots in the array are not fed by separate waveguides but by a traveling wave arrangement, for example, the quantitative evaluations will be different but the qualitative assertions made above are still applicable.

[8] A. A. Oliner, *op. cit.*, eq. (3.107).

[9] A. A. Oliner, *op. cit.*, eqs. (3.111) and (3.113).

Spiral Antennas*

WALTER L. CURTIS†

Summary—**The radiation fields of the Archimedes spiral are derived by approximating the spiral with a series of semicircles. The calculated patterns are shown to have excellent correlation with experimentally determined patterns. It is shown that the high-frequency limit is determined by the feed configuration and that the low-frequency limit occurs when the outside diameter is a little greater than a half wavelength.**

Introduction

THE spiral antenna[1–7] has, in the past six years, come into widespread use by the aircraft industry because of its large bandwidth and suitability to flush mounting. Much of the work on the spiral up to the present time has been experimental. The purpose of this study is to determine analytically the radiation properties of the spiral antenna. In particular, the report is confined to a balanced spiral free to radiate in all directions.

Theoretical Analysis

The basic approach used in the following analysis is to find the vector potential by the volume integration of the proper Green's function and current distribution. The vector potential, $\boldsymbol{A}$, is defined by

$$\nabla \times \boldsymbol{A} = \boldsymbol{H} \tag{1}$$

where $\boldsymbol{H}$ is the magnetic intensity vector. In free space

$$\boldsymbol{A} = \frac{1}{4\pi}\int_V \frac{Ie^{j(\omega t-\beta R')}}{R'}\,d^V \tag{2}$$

where R' is the distance from the current element. The coordinate system used is shown in Fig. 1.

For the case of a line source, considering only the radiation or far-field component of the field, (2) becomes

$$\boldsymbol{A} = \frac{1}{4\pi R}\int_0^{s_0} Ie^{-j\beta R'}[S_\phi\boldsymbol{\phi} + S_\theta\boldsymbol{\theta}]ds \tag{3}$$

where $e^{j\omega t}$ is understood and

s is a unit of length along the spiral,
s_0 is the total length out to the end of the spiral,
ds is an element of length on the spiral,
R' is the radial distance measured from ds,
$\boldsymbol{\phi}$, $\boldsymbol{\theta}$ and $\boldsymbol{s}$ are unit vectors,
S_ϕ is the direction cosine between $\boldsymbol{s}$ and $\boldsymbol{\phi}$,
S_θ is the direction cosine between $\boldsymbol{s}$ and $\boldsymbol{\theta}$,
I represents the current distribution on the spiral and is thus a function of s,
$\beta = 2\pi/\lambda$,
R, θ, ϕ are regular spherical coordinates,
r, ϕ' are the polar coordinates of the spiral.

It can be easily shown that R', as used in the phase term of (3), is given approximately as

$$R' \approx R - r\sin\theta\cos(\phi - \phi'). \tag{4}$$

The direction cosines and the element of length ds are given in terms of the polar coordinates of the spiral as

$$S_\phi ds = rd\phi'\cos(\phi - \phi') - dr\sin(\phi - \phi') \tag{5}$$

and

$$S_\theta ds = \cos\theta[rd\phi'\sin(\phi - \phi') + dr\cos(\phi - \phi')]. \tag{6}$$

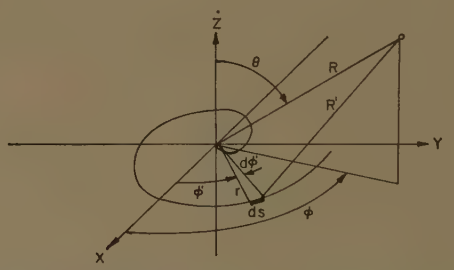

Fig. 1—Coordinate system used for study of spiral.

Description of Spiral

The value of s depends on the particular spiral being studied. The general equation for any spiral is

$$r = f(\phi'). \tag{7}$$

The length s measured along the spiral is given as

$$s = \int_0^{\phi'}\left[\left(\frac{dr}{d\phi'}\right)^2 + r^2\right]^{1/2} d\phi'. \tag{8}$$

In general, s will be a complicated function. For instance, for a simple Archimedes spiral defined by

$$r = r_0 + a\phi', \tag{9}$$

* Manuscript received by the PGAP, October 12, 1959; revised manuscript received January 1, 1960.
† Antennas and Radomes Unit, Boeing Airplane Co., Seattle, Wash.

[1] J. S. Chatterjie, "Radiation field of a conical helix," *J. Appl. Phys.*, vol. 24, pp. 550–559; May, 1953.
[2] J. S. Chatterjie, "Radiation characteristics of a conical helix of low pitch angle," *J. Appl. Phys.*, vol. 26, pp. 331–335; March, 1955.
[3] B. H. Burdine, "The Spiral Antenna," Res. Lab. of Electronics, M.I.T., Cambridge, Mass., Repts. Nos. 1 and 2; March 15, 1955 and April 15, 1955.
[4] J. D. Dyson, "The equiangular spiral antenna," IRE Trans. on Antennas and Propagation, vol. AP-7, pp. 181–188; April, 1959.
[5] E. M. Turner, "Spiral Slot Antenna," Wright Air Dev. Center, Dayton, Ohio, Tech. Note WCLR-55-8; June, 1955.
[6] P. E. Mast, "A Theoretical Study of the Equiangular Spiral Antenna," Electrical Engrg. Res. Lab., University of Illinois, Urbana, Tech. Rept. No. 35, Contract AF 33(616)-3220; September 12, 1958.
[7] V. H. Rumsey, "Frequency independent antennas," 1957 IRE National Convention Record, vol. 5, pt. I, pp. 114–119.

the length is given as

$$s = \left(\frac{r_0 + a\phi'}{2a}\right)[(r_0 + a\phi')^2 + a^2]^{1/2}$$

$$+ \frac{a}{2}\ln\left[r_0 + a\phi' + \{(r_0 + a\phi')^2 + a^2\}^{1/2}\right] - s_1 \quad (10)$$

where

$$s_1 = \frac{r_0}{2a}[r_0^2 + a^2]^{1/2} + \frac{a}{2}\ln\left[r_0 + (r_0^2 + a^2)^{1/2}\right]. \quad (11)$$

If (3) is to be integrable, a spiral whose length is a simple function of ϕ' must be chosen. One such simple function would be s directly proportional to the angle, or

$$s = a\phi'. \quad (12)$$

This, of course, is nothing more than the length of an arc of a circle.

A circle is not usually thought of as a spiral, but, by using several semicircles with different radii, we can construct a spiral of any number of turns. An example of this is shown in Fig. 2. This type of spiral is a good approximation of an Archimedes spiral as shown in Fig. 3.

Current Distribution

For this problem, the general form of sinusoidal current distribution shall be assumed, namely that the current will be made up of two components, one outward traveling wave and one reflected or inward traveling wave. This can be written as

$$I = I_0[e^{-\gamma s} + Ke^{\gamma s}] \quad (13)$$

where $\gamma = \alpha - j\beta$, and α and β are the attenuation and phase constants respectively. K is the reflection coefficient and is a function of the total length of the spiral, which shall be designated as s_0. Since the case of a thin spiral or line source is being considered, the current will be zero at the end of the spiral. Thus, from (13)

$$e^{-\gamma s_0} + Ke^{\gamma s_0} = 0 \quad (14)$$

$$K = -e^{-2s_0\gamma}. \quad (15)$$

The phase constant, β, shall be assumed the same as for a plane wave in free space, namely, $\beta = 2\pi/\lambda$. The value of α depends on the arm width of the spiral and is a measure of attenuation of the current. This attenuation can be thought of as loss due to radiation. For linear antennas less than a wavelength long, a small value of α does not appreciably change the current from what it would be if α were zero and is thus usually neglected. It was found from the spiral used for verification of the theoretical work in this study that α is approximated by $1/(3\lambda)$.

The first step will be to calculate the radiation field of a single semicircle and then to generalize the work to include a spiral of any size made from semicircles.

Radiation from a Semicircle

Let the semicircle be placed in the x-y plane with its center at the origin as shown in Fig. 4. Using the ϕ-component of (3) and a superscript I to designate this particular configuration,

$$A_\phi^{\mathrm{I}} = \frac{1}{4\pi R}\int_0^{s_0} Ie^{-j\beta R'}S_\phi ds \quad (16)$$

where

$$S_\phi ds = ad\phi' \cos(\phi - \phi') \quad (17)$$

$$S = a\phi' \quad (12)$$

$$R' = R - a\sin\theta\cos(\phi - \phi') \quad (4)$$

$$I = I_0(e^{-\gamma s} + Ke^{\gamma s}). \quad (13)$$

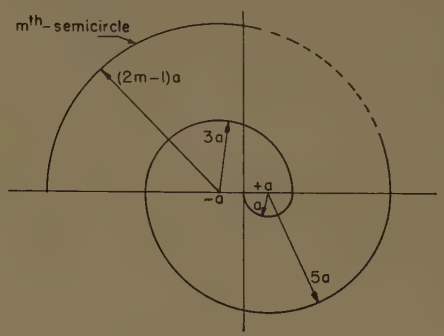

Fig. 2—Spiral made from semicircles.

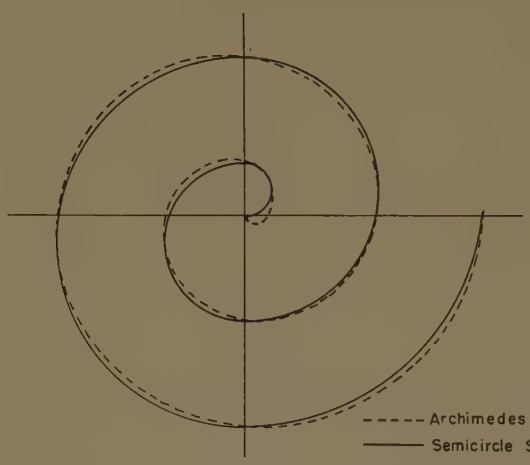

Fig. 3—Comparison of Archimedes spiral and semicircle spiral.

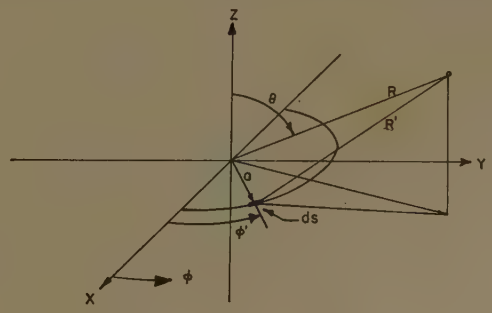

Fig. 4—Coordinate system for calculating radiation field of a semicircle.

Substituting the above into (16) gives

$$A_\phi^{\mathrm{I}} = \frac{I_0 a e^{j(\omega t-\beta R)}}{4\pi R}\int_0^\pi (e^{-\gamma a\phi'} + Ke^{\gamma a\phi'}) \cdot e^{j\beta a \sin\theta\cos(\phi-\phi')}\cos(\phi-\phi')d\phi'. \quad (18)$$

Let

$$C = \frac{I_0 a e^{j(\omega t-\beta R)}}{4\pi R} \quad (19)$$

$$d = \gamma a = (\alpha - j\beta)a \quad (20)$$

$$x = \beta a \sin\theta \quad (21)$$

and (18) becomes

$$A_\phi^{\mathrm{I}} = C\int_0^\pi (e^{-d\phi'} + Ke^{d\phi'})e^{jx\cos(\phi-\phi')}\cos(\phi-\phi')d\phi' \quad (22)$$

$$= C\left[\int_0^\pi e^{-d\phi'+jx\cos(\phi-\phi')}\cos(\phi-\phi')d\phi' + K\int_0^\pi e^{d\phi'+jx\cos(\phi-\phi')}\cos(\phi-\phi')d\phi'\right] \quad (23)$$

$$= C[I_{1\phi} + KI_{2\phi}] \quad (24)$$

where

$$I_{1\phi} = \int_0^\pi e^{-d\phi'+jx\cos(\phi-\phi')}\cos(\phi-\phi')d\phi' \quad (25)$$

$$I_{2\phi} = \int_0^\pi e^{d\phi'+jx\cos(\phi-\phi')}\cos(\phi-\phi')d\phi'. \quad (26)$$

To evaluate the above integrals, it is convenient to use the following Bessel function identity

$$e^{jx\cos(\phi-\phi')} = \sum_{n=-\infty}^{\infty} j^n e^{jn(\phi-\phi')}J_n(x) \quad (27)$$

$$= J_0(x) + 2\sum_{n=1}^{\infty} j^n J_n(x)\cos n(\phi-\phi'). \quad (28)$$

Thus, $I_{1\phi}$ becomes

$$I_{1\phi} = \int_0^\pi e^{-d\phi'}\left(\frac{e^{j(\phi-\phi')} + e^{-j(\phi-\phi')}}{2}\right) \cdot \sum_{n=-\infty}^{\infty} j^n e^{jn(\phi-\phi')}J_n(x)d\phi' \quad (29)$$

$$= \frac{1}{2}\sum_{n=-\infty}^{\infty} j^n e^{jn\phi}J_n(x)\left[e^{j\phi}\int_0^\pi e^{-\phi'[d+j(n+1)]}d\phi' + e^{-j\phi}\int_0^\pi e^{-\phi'[d+j(n-1)]}d\phi'\right], \quad (30)$$

performing the integration results in

$$I_{1\phi} = \frac{1}{2}\sum_{n=-\infty}^{\infty} j^n e^{jn\phi}J_n(x)[(-1)^n e^{-\pi d}+1] \cdot\left[\frac{e^{j\phi}}{d+j(n+1)} + \frac{e^{-j\phi}}{d+j(n-1)}\right]. \quad (31)$$

$$= \sum_{n=-\infty}^{\infty} j^n e^{jn\phi}J_n(x)[(-1)^n e^{-\pi d}+1] \cdot\left[\frac{(d+jn)\cos\phi + \sin\phi}{(d+jn)^2+1}\right]. \quad (32)$$

The value of $I_{2\phi}$ is the same as $I_{1\phi}$ with d replaced with $-d$, thus

$$I_{2\phi} = \sum_{n=-\infty}^{\infty} j^n e^{jn\phi}J_n(x)[(-1)^n e^{\pi d}+1] \cdot\left[\frac{(-d+jn)\cos\phi + \sin\phi}{(-d+jn)^2+1}\right] \quad (33)$$

and

$$A_\phi^{\mathrm{I}} = C\sum_{n=-\infty}^{\infty} j^n e^{jn\phi}J_n(x) \cdot\left[((-1)^n e^{-\pi d}+1)\left(\frac{(d+jn)\cos\phi + \sin\phi}{(d+jn)^2+1}\right) + K((-1)^n e^{\pi d}+1)\left(\frac{(-d+jn)\cos\phi + \sin\phi}{(-d+jn)^2+1}\right)\right]. \quad (34)$$

From (3), the θ component of the field is given as

$$A_\theta^{\mathrm{I}} = \frac{1}{4\pi R}\int_0^{s_0} Ie^{-i\beta R'}S_\theta ds. \quad (35)$$

Substituting the values given by (12), (4), (19), (20) and (21) into (35) results in

$$A_\theta^{\mathrm{I}} = C\cos\theta\int_0^\pi (e^{-d\phi'} + Ke^{d\phi'}) \cdot e^{jx\cos(\phi-\phi')}\sin(\phi-\phi')d\phi'. \quad (36)$$

The integration is performed in the same way as for A_ϕ^{I}:

$$A_\theta^{\mathrm{I}} = C\cos\theta\sum_{n=-\infty}^{\infty} j^n e^{jn\phi}J_n(x) \cdot\left[((-1)^n e^{-\pi d}+1)\left(\frac{(d+jn)\sin\phi - \cos\phi}{(d+jn)^2+1}\right) + K((-1)^n e^{\pi d}+1)\left(\frac{(-d+jn)\sin\phi - \cos\phi}{(-d+jn)^2+1}\right)\right]. \quad (37)$$

Radiation from Two Semicircles Fed Out of Phase

In the previous section, the fields were found for a single semicircle fed from one end. It is, of course, physically impossible to do this. What must be done is to either add a ground system or make the antenna sym-

metrical and feed it from a balanced line. Here will be considered the case of adding a second semicircle to make the configuration symmetrical and feed the two semicircles 180 degrees out of phase as shown in Fig. 5.

The field of the balanced antenna can be found by using the proper translation and rotation of the coordinate system. To shift the origin of the single semicircle, the phase of the vector potential must be adjusted by multiplying by

$$e^{j\beta \boldsymbol{R}\cdot\boldsymbol{a}} = e^{j\beta a \cos\tau} = e^{-j\beta a \cos\phi \sin\theta} \tag{38}$$

where, as shown in Fig. 6, $\boldsymbol{a}$ is the vector distance between the new and old origin, $\boldsymbol{R}$ is the unit vector in the R direction of the new coordinate system, and where τ, by definition of dot product, is the angle between $\boldsymbol{R}$ and $\boldsymbol{a}$. Letting A^{II} be the vector potential for the semicircle shifted as shown in Fig. 6,

$$A^{II} = A^{I} e^{-j\beta a \cos\phi \sin\theta} = \sum_{n=-\infty}^{\infty} \mathfrak{A}_n{}^{I} e^{-jy} \tag{39}$$

where

$$y = \beta a \cos\phi \sin\theta \tag{40}$$

and $\mathfrak{A}^{I}{}_{n}$ equals everything in (34) and (37) except the summation sign.

To find the field (A^{III}) of the semicircle rotated 180 degrees as shown in Fig. 6, position 2, replace ϕ by $(180 + \phi)$ in (34) and (37) and obtain

$$A^{III} = \sum_{n=-\infty}^{\infty} (-1)^{n+1} \mathfrak{A}_n{}^{I}. \tag{41}$$

If the origin of the rotated semicircle is shifted as shown in Fig. 6, position 3,

$$A^{IV} = A^{III} e^{jy} = \sum_{n=-\infty}^{\infty} (-1)^{n+1} \mathfrak{A}_n{}^{I} e^{jy}. \tag{42}$$

The difference between A^{II} and A^{IV} is the field (A^{V}) of the two semicircles fed from a balanced line. Thus

$$A^{V} = \sum_{n=-\infty}^{\infty} \mathfrak{A}_n{}^{I} [e^{-jy} + (-1)^n e^{jy}]. \tag{43}$$

Radiation from a Balanced Spiral Made from Any Number of Semicircles

The next step will be to generalize the above procedure to a spiral of any number of turns. Let m be the number of semicircles in each half of a balanced spiral as shown in Fig. 7. Eq. (14) gives the current in the kth semicircle as

$$I_k = I_{0k} [e^{-\gamma(2k-1)a\phi} + K_k e^{\gamma(2k-1)a\phi}], \quad 0 \leqq \phi \leqq \pi \tag{44}$$

where, by (15),

$$K_k = -e^{-2\gamma(s_0 - s_{k-1})} \tag{45}$$

and s_0 is the total length of the spiral and s_{k-1} is the length of the spiral out to the beginning of the kth semicircle. The lengths s_0 and s_{k-1} are merely the sum of the lengths of each semicircle and therefore are given as

$$s_0 = \pi a m^2 \tag{46}$$

and

$$s_{k-1} = \pi a (k-1)^2. \tag{47}$$

Thus, (45) becomes

$$K_k = -e^{-\gamma\pi a(m^2 - (k-1)^2)}, \tag{48}$$

and

$$I_{0k} = I_0 e^{-\gamma s_{k-1}} = I_0 e^{-\gamma\pi a(k-1)^2}. \tag{49}$$

The complete equation for current in the kth semicircle is

$$I_k = I_0 e^{-\gamma\pi a(k-1)^2} [e^{-\gamma(2k-1)a\phi} e^{-2\gamma\pi a(m-(k-1)^2)} e^{(2k-1)a\phi}], \quad 0 \leqq \phi \leqq \pi. \tag{50}$$

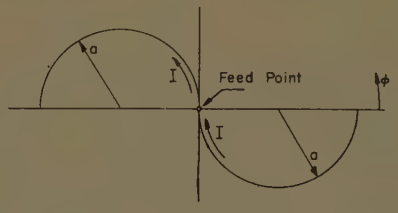

Fig. 5—Balanced spiral made from two semicircles.

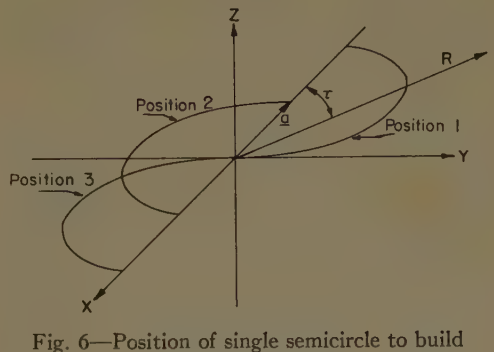

Fig. 6—Position of single semicircle to build up balanced spiral.

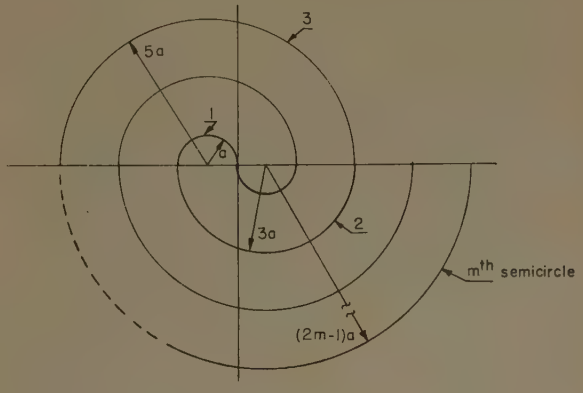

Fig. 7—Balanced spiral made up of m semicircles.

The vector potential from the kth semicircle located with its center at the origin can be found directly from (34) and (37) by writing I_{0k} for I_0, K_kf or K and a_k for a, where

$$a_k = (2k-1)a. \tag{51}$$

Using a notation similar to that previously employed, let A_k represent the vector potential for the kth semicircle located in the upper half plane in Fig. 7. For semicircles in the lower half plane, multiply by $(-1)^{n+1}$. Let A^{VI} be the vector potential for one-half the balanced spiral shown in Fig. 8(a) and A^{VII} for the half shown in Fig. 8(b).

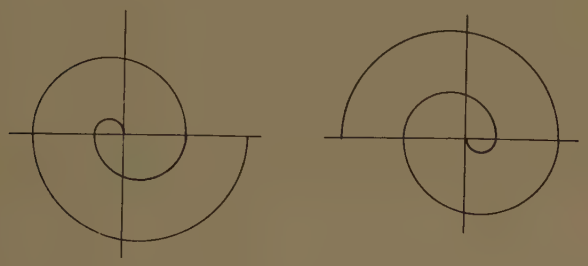

(a) (b)

Fig. 8—Two halves of a balanced semicircle spiral.

The values of A^{VI} and A^{VII} are found by taking the sum of the contributions of each semicircle separately. Thus

$$A^{IV} = \sum_{n=-\infty}^{\infty} [\mathfrak{A}_{1n}e^{-iy} + (-1)^{n+1}\mathfrak{A}_{2n}e^{iy} + \cdots + \mathfrak{A}_{(2k-1)n}e^{-iy} + (-1)^{n+1}\mathfrak{A}_{2kn}e^{iy} + \cdots + m^{th}\text{ term}] \tag{52}$$

and

$$A^{VII} = \sum_{n=-\infty}^{\infty} [(-1)^{n+1}\mathfrak{A}_{1n}e^{iy} + \mathfrak{A}_{2n}e^{-iy} + \cdots + (-1)^{n+1}\mathfrak{A}_{(2k-1)n}e^{iy} + \mathfrak{A}_{2kn}e^{-iy} + \cdots + m^{th}\text{ term}] \tag{53}$$

where $\mathfrak{A}_{km}$ is equal to $\mathfrak{A}^I_n$ with I_0, K, and a replaced with I_{0k}, K_k, and a_k respectively. The complete vector potential for the double spiral in Fig. 9 is the difference between A^{VI} and A^{VII}. That is, $A = A^{VI} - A^{VII}$. Thus

$$A = 2\cos y \sum_{k=1}^{m} (-1)^{k+1}A_k \Big]_{n\text{ even}} + 2j \sin y \sum_{k=1}^{m} (-1)^k A_k \Big]_{n\text{ odd}} \tag{54}$$

where

$$A_k = \sum_{n=-\infty}^{\infty} \mathfrak{A}_{nk}.$$

The double infinite sum contained in A_k can be changed to a single infinite sum by combining the $+n$ and $-n$ terms. The resulting final equations for the θ and ϕ components of the vector potential are:

$$A_\theta = 2C\cos\theta \sum_{k=1}^{m} \{\cos yJ_0(x_k)[\tfrac{1}{2}D_{k,0}\sin\phi - \tfrac{1}{2}C_{k,0}\cos\phi] + \sum_{l=1}^{\infty} [\sin yJ_{2l-1}(x_k)((\cos(2l-1)\phi) \cdot (E_{k,2l-1}\sin\phi + B_{k,2l-1}\cos\phi) + (\sin(2l-1)\phi)(F_{k,2l-1}\sin\phi - G_{k,2l-1}\cos\phi)) + \cos yJ_{2l}(x_k)((\cos 2l\phi)(D_{k,2l}\sin\phi - C_{k,2l}\cos\phi) + (\sin 2l\phi)(H_{k,2l}\sin\phi - A_{k,2l}\cos\phi))]\} \tag{55}$$

$$A_\phi = 2C\sum_{k=1}^{m} \{\cos yJ_0(x_k)[\tfrac{1}{2}C_{k,0}\sin\phi + \tfrac{1}{2}D_{k,0}\cos\phi] + \sum_{l=1}^{\infty} [\sin yJ_{2l-1}(x_k)((\cos(2l-1)\phi) \cdot (-B_{k,2l-1}\sin\phi + E_{k,2l-1}\cos\phi) + (\sin(2l-1)\phi)(G_{k,2l-1}\sin\phi + F_{k,2l-1}\cos\phi)) + \cos yJ_{2l}(x_k)((\cos 2l\phi)(C_{k,2l}\sin\phi + D_{k,2l}\cos\phi) + (\sin 2l\phi)(A_{k,2l}\sin\phi + H_{k,2l}\cos\phi))]\} \tag{56}$$

where

$$y = \beta a\cos\phi\sin\theta, \qquad e_1 = e^{-\pi k^2 d}$$

$$x_k = (2k-1)\beta a\sin\theta, \qquad e_2 = e^{\pi(k-1)^2 d}$$

$$C = \frac{I_0 a}{4\pi R}e^{j(\omega t-\beta R)}, \qquad e_3 = e^{-\pi(2m^2-k^2)d}$$

$$d = \gamma a = (\alpha - j\beta)a, \qquad e_4 = e^{-\pi(2m^2-(k-1)^2)d}$$

$$d_k = (2k-1)d,$$

$$A_{k,2l} = \frac{-4(-1)^k(-1)^l(2k-1)^2 d(2l)}{(d_k^2+(2l-1)^2)(d_k^2+(2l-1)^2)} \cdot [+e_1+e_2+e_3+e_4]$$

$$C_{k,2l} = \frac{2(-1)^k(-1)^l(2k-1)(-d_k^2+4l^2-1)}{(d_k^2+(2l-1)^2)(d_k^2+(2l-1)^2)} \cdot [+e_1+e_2-e_3-e_4]$$

$$D_{k,2l} = \frac{-2(-1)^k(-1)^l(2k-1)d(d_k^2+4l^2+1)}{(d_k^2+(2l-1)^2)(d_k^2+(2l-1)^2)} \cdot [+e_1+e_2+e_3+e_4]$$

$$H_{k,2l} = \frac{2(-1)^k(-1)^l(2l)(2k-1)(-d_k^2-4l^2+1)}{(d_k^2+(2l-1)^2)(d_k^2+(2l-1)^2)} \cdot [+e_1+e_2-e_3-e_4]$$

$$G_{k,2l-1} = \frac{4(-1)^k(-1)^l(2k-1)^2 d(2l-1)}{(d_k^2+(2l-2)^2(d_k^2+(2l)^2)} \cdot [-e_1+e_2-e_3+e_4]$$

$$B_{k,2l-1} = \frac{2(-1)^k(-1)^l(2k-1)(-d_k^2+(2l-1)^2-1)}{(d_k^2+(2l-2)^2)(d_k^2+(2l)^2)} \cdot [-e_1+e_2+e_3-e_4]$$

$$E_{k,2l-1} = \frac{2(-1)^k(-1)^l(2k-1)^2 d(d_k^2+(2l-1)^2+1)}{(d_k^2+(2l-2)^2(d_k^2+(2l)^2)} \cdot [-e_1+e_2-e_3+e_4]$$

$$F_{k,2l-1} = \frac{-2(-1)^k(-1)^l(2l-1)(2k-1)(-d_k^2-(2l-1)^2+1)}{(d_k^2+(2l-2)^2(d_k^2+(2l)^2)} \cdot[-e_1+e_2+e_3-e_4]$$

$$C_{k,0} = \frac{-2(-1)^k(2k-1)}{1+(2k-1)^2d^2}[+e_1+e_2-e_3-e_4]$$

$$D_{k,0} = \frac{-2(-1)^k(2k-1)^2d}{1+(2k-1)^2d^2}[+e_1+e_2+e_3+e_4].$$

Eqs. (55) and (56) can be further reduced if a particular pair of principal planes are considered, namely $\phi=0°$ and 90°. This results in

$$A_\theta\Big]_{\phi=0°} = 2C\cos\theta\sum_{k=1}^{m}\left\{-\frac{1}{2}C_{k,0}J_0(x_k)\cos x_1 + \sum_{l=1}^{\infty}[B_{k,2l-1}J_{2l-1}(x_k)\sin x_1 - C_{k,2l}J_{2l}(x_k)\cos x_1]\right\} \quad (57)$$

$$A_\theta\Big]_{\phi=90°} = 2C\cos\theta\sum_{k=1}^{m}\left\{\frac{1}{2}D_{k,0}J_0(x_k) + \sum_{l=1}^{\infty}(-1)D_{k,2l}J_{2l}(x_k)\right\} \quad (58)$$

$$A_\phi\Big]_{\phi=0°} = 2C\sum_{k=1}^{m}\left\{\frac{1}{2}D_{k,0}J_0(x_k)\cos x_1 + \sum_{l=1}^{\infty}[E_{k,2l-1}J_{2l-1}(x_k)\sin x_1 + D_{k,2l}J_{2l}(x_k)\cos x_1]\right\} \quad (59)$$

$$A_\phi\Big]_{\phi=90°} = 2C\sum_{k=1}^{m}\left\{\frac{1}{2}C_{k,0}J_0(x_k) + \sum_{l=1}^{\infty}(-1)C_{k,2l}J_{2l}(x_k)\right\}. \quad (60)$$

Another very useful component of A is the on axis polarization—A evaluated at $\theta=0$. It makes no difference whether A_θ or A_ϕ is used because the results are the same with a 90-degree rotation of the coordinate system. At $\theta=0$, $x_k=y=0$ which means that all terms involving Bessel functions of higher order than zero will will be equal to zero. Eq. (55) reduces to

$$A_\theta\Big]_{\theta=0°} = C\sum_{k=1}^{m}(D_{k,0}\sin\phi - C_{k,0}\cos\phi). \quad (61)$$

The above equations are for the completely general case of a spiral made up of m semicircles. It can be shown that for the far field

$$E = -j\omega\mu A. \quad (62)$$

This means that the voltage pattern, defined as the absolute value of E, will be proportional to the absolute value of A. In order to get an idea of what the patterns look like, the next step will be to examine them for some specific values of m and compare the results with experimentally determined patterns.

Experimental Verification

A balanced thin wire antenna can be built, but it is next to impossible to feed such a configuration with conventional transmission lines without affecting the radiation patterns considerably. One way of getting around this problem is to use the complement of the thin wire antenna, a thin slot cut in an infinite conducting sheet. Of course an infinite sheet cannot be used, but a relatively large sheet in terms of wavelengths will give sufficiently accurate results. The patterns of the slot antenna are identical with those of the wire antenna when the E and H components of the field are interchanged. This means that E_θ for the wire is equal to E_ϕ for the slot and E_ϕ for the wire is equal to E_θ for the slot. In this report, all patterns, even though they were taken on the slot, will be labeled as though they were taken on the wire antenna so that no confusion will arise when they are compared to the calculated patterns of the wire antenna.

Experimental patterns were taken on the semicircle spiral for m equal to 1, 2 and 3. A photograph of each of these is shown in Fig. 9. They were made by etching a 0.04-inch wide slot in a 0.02-inch thick sheet of copper.

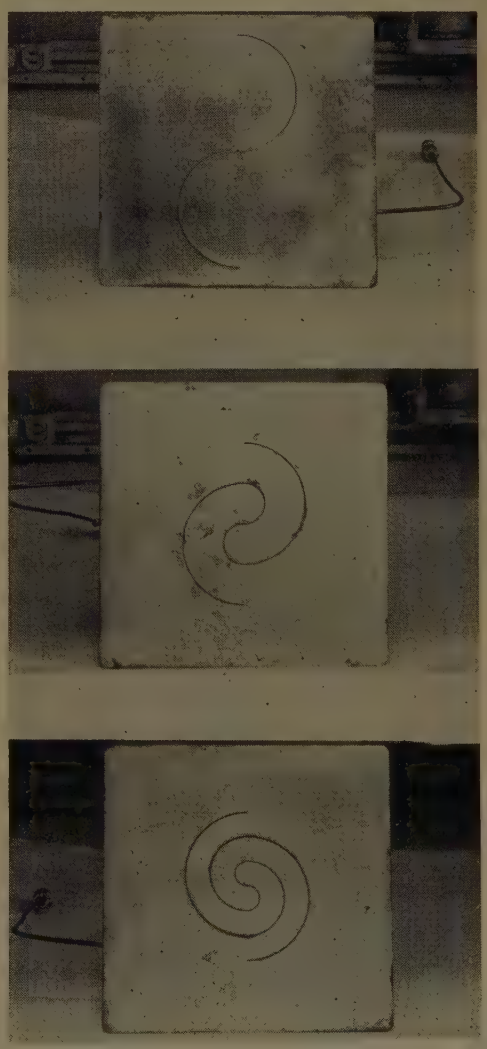

Fig. 9—Experimental models of the semicircle spiral.

The etched piece of copper, which was small for practical reasons, was then mounted in an electrically large aluminum ground plane. The extended ground plane was roughly 36 feet long and 12 feet wide. Each spiral was made with the radius of the largest semicircle equal to 1.88 inches. This means that the length of the largest semicircle is $\lambda/2$ at 1000 mc. Experimental patterns were taken at 1, 2 and 3 kmc. Since the patterns are symmetrical with respect to the ground plane, only half of the pattern was measured.

The experimental and theoretical patterns for the simple cases of m equal to 1, 2 and 3 are shown in Figs. 10–12 respectively. In each case, there is remarkably good correlation.

Typical Calculated Patterns

In general, there will be more use for spirals with more than one to two turns. Typical patterns for a semicircle spiral with m equal to seven are shown in Fig. 13. Only the upper half of the patterns are shown as they are symmetrical about the horizontal axis. Therefore the patterns of the spiral antenna are bidirectional in the direction perpendicular to the plane of the spiral with both polarizations present.

On Axis Polarization

The polarization of the field on the z axis can be found from (61). For the simple case of m equal to one, (61) becomes

$$A_\theta\Big]_{\theta=0^\circ} = \frac{2C}{1+d^2}\left[(e^{-2\pi d}-1)\cos\phi + d(e^{-\pi d}+1)^2\sin\phi\right]. \quad (63)$$

If d is imaginary, the coefficients of $\cos\phi$ and $\sin\phi$ will be in phase and thus $A_{\theta=0^\circ}$ will always be in the form of a figure eight. The position of the minimum in the figure eight pattern, designated as ϕ_0, can be found by equating (63) to zero and obtaining

$$\tan\phi_0 = \frac{1-e^{-2\pi d}}{d(1+e^{-\pi d})^2}, \quad (64)$$

for $d=j\beta a$ (*i.e.*, $\alpha=0$),

$$\tan\phi_0 = \frac{\sin 2\pi\beta a + 2\sin\pi\beta a}{(3+4\cos\pi\beta a+\cos 2\pi\beta a)\beta a}. \quad (65)$$

The plot of ϕ_0 vs βa is given in Fig. 14. If d contains a real term, then (64) will be complex, indicating the field is elliptically polarized.

A measure of the polarization is the polarization ratio, here defined as the magnitude ratio of the minimum value to the maximum value of (61). On this basis,

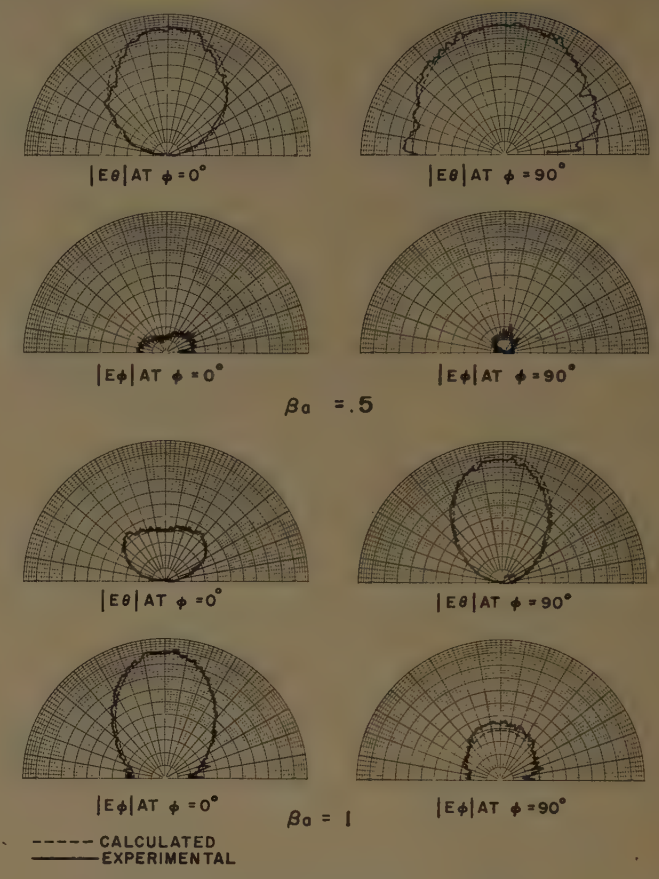

Fig. 10—Far-field radiation patterns of semicircle spiral with $m=1$.

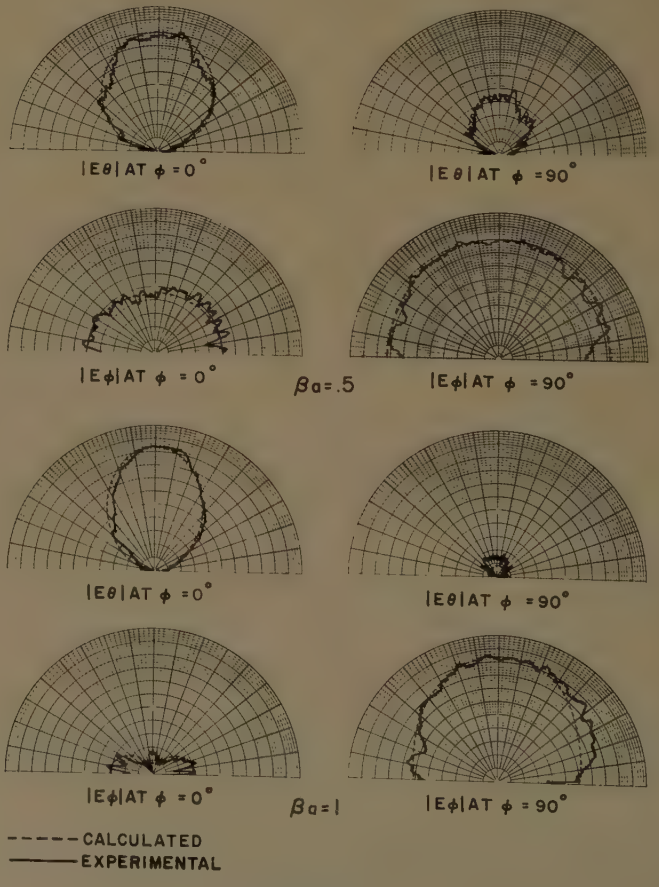

Fig. 11—Far-field radiation patterns of semicircle spiral with $m=2$.

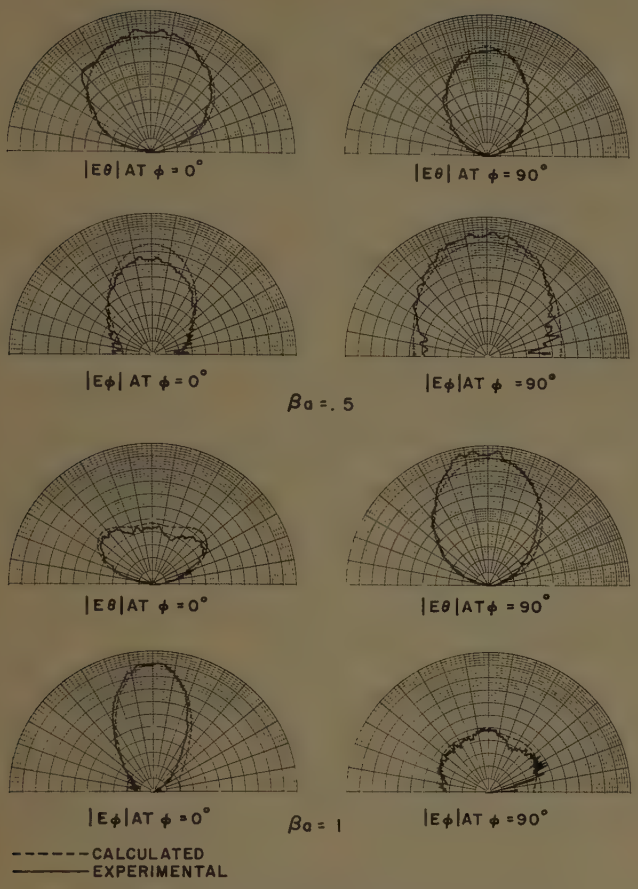

Fig. 12—Far-field radiation patterns of semicircle spiral with $m=3$.

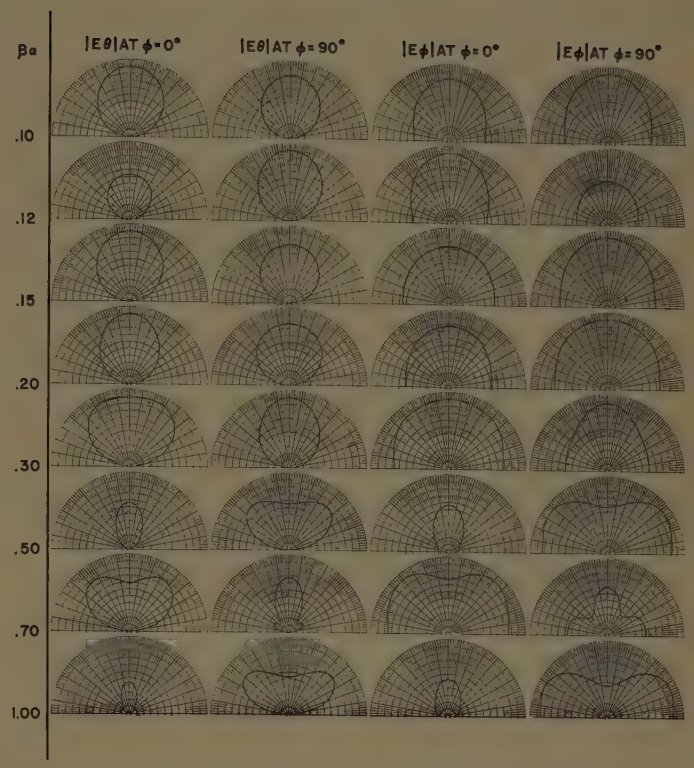

Fig. 13—Typical radiation patterns of semicircle spiral with $m=7$ and $\alpha=1/3\ \lambda$.

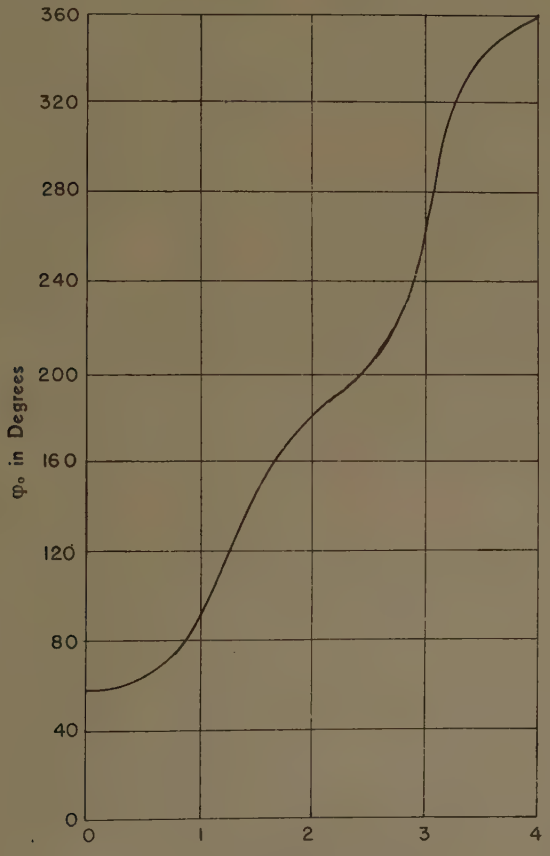

Fig. 14—Plot of ϕ_0 vs $\beta\alpha$ for $m=1$.

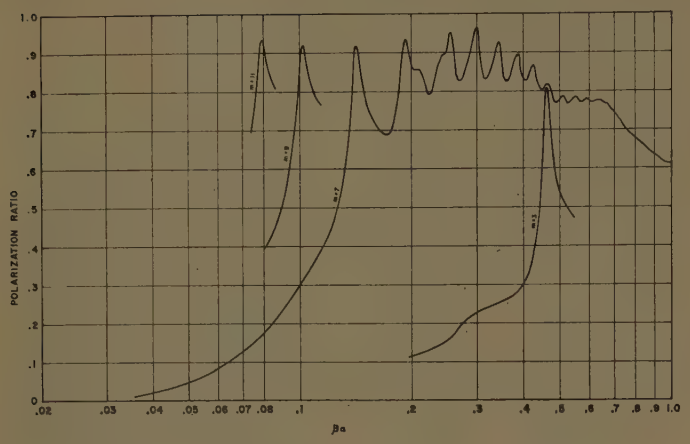

Fig. 15—Polarization ratio of semicircle spiral.

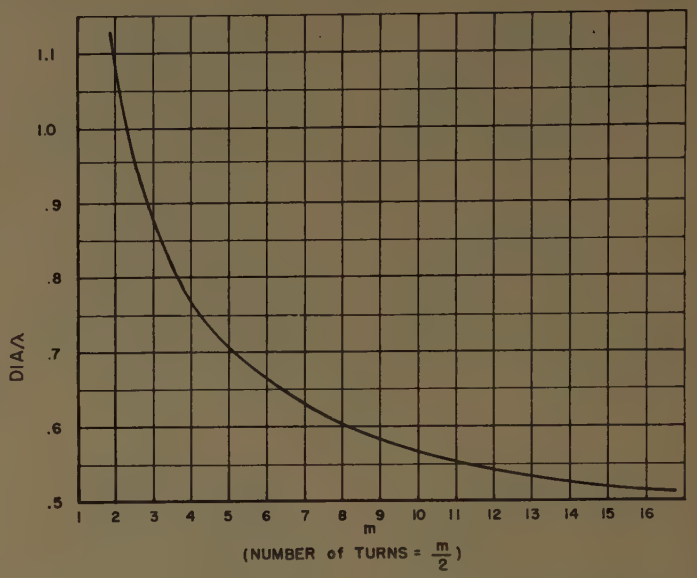

Fig. 16—Ratio of outside diameter to wavelength, corresponding to the first peak in the polarization curve, plotted as a function of m or number of turns.

circular polarization would have a value of one and linear polarization a value of zero. A plot of polarization ratio vs βa for a semicircle spiral for different values of m is shown in Fig. 15. The curve for $m=7$ is typical of the results for any value of m.

In practice, the polarization is sometimes the deciding criterion for determining the useable bandwidth of an antenna. For a spiral antenna, it is often the case that circular or nearly circular polarization is desired. It therefore will be useful to examine the upper and lower frequency limits of the spiral as determined by the polarization ratio. From Fig. 15, we see that a useful lower limit is the first peak in the polarization plot. Fig. 16 shows the outside diameter of the spiral corresponding to this peak plotted as a function of m (number of turns $=m/2$). The significant fact is that as the number of turns in the spiral increases, the diameter corresponding to the first peak in the polarization curve approaches a half wavelength.

There is no convenient way from the polarization plot to determine an upper frequency limit. However, the upper frequency limit can be selected by the radiation pattern which shows that the main lobe of radiation splits into two lobes. This splitting of the pattern occurs when βa is greater than or equal to one, that is, when the length of the first or feed semicircle is a half wavelength. This can be seen in Fig. 15.

Conclusion

The radiation patterns of a balanced spiral antenna made from semicircles has been calculated and shown to be correct by comparison with experimentally measured patterns. The patterns of the spiral are in general single lobed in a direction perpendicular to the plane of the spiral. When the length of the first or feed semicircle is a half wavelength or greater, the pattern breaks into two lobes and thus defines an upper frequency limit. The low frequency limit defined by the polarization ratio occurs when the outside diameter of the spiral is approximately a half wavelength. The exact size is given in Figs. 15 and 16. The above conclusions are based on the semicircle spiral but also apply equally well to an Archimedes spiral of any number of turns.

Acknowledgment

The author wishes to acknowledge the advice and counsel of his adviser, Dr. G. Held, of the University of Washington, Seattle. Appreciation is also extended to R. Vail for programming the equations for solution on the IBM 704 digital computer.

Ground Constant Measurements Using a Section of Balanced Two-Wire Transmission Line*

ERIK J. KIRKSCETHER†

Summary—**When an open-circuited section of unshielded balanced two-wire transmission line is introduced perpendicularly into earth (or some sample under test), the electrical characteristics of the latter may be found by simple input-impedance measurements. By laboratory sample measurements the classical short- and open-circuited method can be used. Some exact and approximate procedures are presented and their utility and practical limitations discussed. Some precautions as to how possible errors and inexactnesses in the measurements and following calculations may be avoided are given. As an example, a typical earth sample is tested in a frequency range from 0.6 to 400 mc, with graphic representation of the most important electrical constants: conductivity, dielectric constant, attenuation, velocity of propagation, etc., which exhibit great variations in the frequency range cited. The measurement method presented seems to be adequate to use in small mobile equipment, with which the ground in general can be tested in its original site and under natural conditions without the necessity of being removed.**

Introduction

THE present paper treats the electric behavior of earth and a method by which its electrical properties may be determined. In the past a variety of methods have been used.[1] Among these, the three most important seem to be:

1) Measure the field intensity of the ground wave as a function of distance from a transmitting antenna. By comparing the measured values with the calculated curves of the ground wave attenuation factor,[2] the conductivity and dielectric constant of the terrain may be deduced. This method is perhaps the most used, especially where transmitting stations already exist; in this case the only instrument needed is a field intensity meter.

2) Near a vertical transmitting antenna measure the electric field vector, its inclination (wave tilt) and the eccentricity of elliptical polarization. From these data the ground constants can be calculated. Besides the transmitter, this method requires elaborate measuring instruments and careful realization. Nevertheless it seems to give the most precise values.

3) Put a sample of the earth or material to be tested into a special cylindrical condenser. By a comparison method or by use of an adequate impedance bridge, the capacitance and loss in the capacitor can be measured and, comparing these values with the corresponding values when the capacitor is empty, the dielectric constant and conductivity is calculated. This method requires special precautions that the earth sample does not change its properties when taken from the ground and put into the capacitor.

A more explicit discussion of the second and third methods is given by Feldman.[3]

The method presented here may be considered an extension of the third method above, but differs from it in various aspects. Instead of putting the earth into a capacitor, a "capacitor" composed of two parallel wires or bars is put into the earth to be tested. In this way, neglecting the small deformation of the earth where the wires are introduced, the measurement is performed in true, natural conditions without fear that the earth should undergo any changes with respect to density, humidity, etc. By letting the wires or bars continue uniformly from within the earth through the air to the impedance measuring device, discontinuities will be practically avoided and, treating the capacitor and its connecting leads as two series-connected uniform transmission lines, the measurements may be realized well into the VHF range. The necessary instruments may easily be installed in a small vehicle, with which great land areas could rapidly be measured.

Set-Up and Instrumentation

The transmission line used in this research is composed of two copper wires of 3-mm diameter and with a center-to-center spacing of 22.2 mm (these dimensions were elected because, due to other reasons, some instruments for this type of line had already been constructed).

Electric parameters of line in air (throughout the paper all symbols referring to air conditions, except c, are primed, while for earth they are not):

$$Z_0' = 323 \text{ ohm}$$

$$L' = 1.075 \cdot 10^{-6} \text{ henry/m}$$

$$C' = 10.32 \ \mu\mu\text{f/m},$$

where

Z_0' = characteristic impedance
L' = series inductance per meter
C' = parallel capacitance per meter.

* Manuscript received by the PGAP, April 27, 1959; revised manuscript received, December 11, 1959.

† Laboratorio de Electrónica y de Comunicaciones, Instituto de Investigaciones Científicas y Técnicas de las Fuerzas Armadas (CITEFA), San Martín, Prov. de Buenos Aires, Argentina.

[1] F. E. Terman, "Radio Engineers Handbook," McGraw-Hill Book Co., Inc., New York, N. Y., pp. 697–709; 1943.

[2] F. E. Terman, *op. cit.*, pp. 675–677, and E. C. Jordan, "Electromagnetic Waves and Radiating Systems," Prentice-Hall, Inc., New York, N. Y., pp. 626–628; 1950.

[3] C. B. Feldman, "The optical behaviour of the ground for short radio waves," PROC. IRE, vol. 21, pp. 764–801; June, 1933.

The series resistance of the line will be neglected throughout.

This paper does not have the intention to establish exact absolute values of the constants of the measured earth, but to test the practical value of the measurement method and to investigate the relative variations of the constants with frequency. Therefore, for convenience, the measurements were realized within the laboratory with the earth sample in a wooden case. The transmission line was installed in the earth in such a way as to permit one end of it (terminating together with the earth) to be short-circuited at will. The other end of the line was prolonged to permit its connection with the measuring device. The transversal dimensions of the earth sample (with respect to the line) were large enough to consider practically all the electromagnetic field to be within the earth.

For frequencies up to 10 mc the sample was measured with the General Radio RF Bridge, type 916-A and, as a control, with the General Radio Twin-T Impedance-Measuring Circuit, type 821-A. Above 10 mc it was not feasible to measure with the mentioned instruments, probably because of the unbalance which they introduced in the balanced transmission line.

In the VHF range the measurements were performed in two different manners. In one, the air line emerging from the earth sample was made long enough to permit measuring the standing waves on the same; the end was connected to a balanced oscillator, and a calibrated balanced standing wave detector, capacitively coupled to the line, was employed to determine the input impedance of the earth line in the frequency band 200–300 mc. In the other manner, the input impedance was determined by the aid of the General Radio type 1602-A Admittance Meter together with the Balun, type 874-UB. The frequencies explored by this procedure ranged from 50 to 400 mc.

Measurement Procedures

Besides the two principal, complete methods of measurement (*Methods 1* and *2* below), under certain conditions and for certain frequency bands some simplified procedures may be used. Some of these will be presented, establishing the conditions under which they can be applied. "Simplified" should be understood in two ways: practically (*e.g.* realizing only one impedance measurement instead of two) and mathematically (less laborious calculations).

Method 1, for Laboratory Measurements Only (Sample Measurements)

The sample will be deposited in a suitable recipient containing the transmission line. The recipient should have a diameter (or transversal dimension) much greater than the line separation. The convenient length of the recipient depends on the characteristics of the material to be tested and should be established in each case; for an earth sample of good conductivity an adequate length would be between 15 and 30 cm.

The input impedance of line in earth will be measured with the other extreme short-circuited and open-circuited. From these measurements the line constants (R, L, G and C) can be calculated in the classical way.[4]

$$Z_0 = \sqrt{Z_{sc} \cdot Z_{oc}} \tag{1}$$

$$\tanh \gamma l = \sqrt{\frac{Z_{sc}}{Z_{oc}}} \tag{2}$$

$$Z = R + j\omega L = Z_0 \gamma \tag{3}$$

$$Y = G + j\omega C = \frac{\gamma}{Z_0} \tag{4}$$

where:

l = length of line in earth
$\gamma = \alpha + j\beta$ = propagation constant in earth
α = attenuation constant in earth
β = phase constant in earth
j = imaginary unit
Z_0 = characteristic impedance of line in earth
Z_{sc} = input impedance of short-circuited line in earth
Z_{oc} = input impedance of open-circuited line in earth
Z = series impedance per meter of line in earth
R = series resistance per meter of line in earth
L = series inductance per meter of line in earth
Y = parallel admittance per meter of line in earth
G = parallel conductance per meter of line in earth
C = parallel capacitance per meter of line in earth
$\omega = 2\pi f$, where f is the frequency.

Further,

$$\sigma = \frac{8.85 \cdot G_{\text{mho}}}{C'_{\mu\mu f}} \text{ mho/meter} \tag{5}$$

$$\epsilon_r = \frac{C}{C'} \tag{6}$$

$$\mu_r = \frac{L}{L'} \tag{7}$$

where:

σ = conductivity of earth
ϵ_r = relative dielectric constant of earth
μ_r = relative permeability of earth.

For the evaluation of (5), see the Appendix.

Method 2, for Measurements in the Terrain and in the Laboratory

The open circuited line is introduced perpendicularly into the earth. Where the line penetrates into the earth, this should be perfectly plane to facilitate an exact measurement of the distance along the air line from

[4] See for example W. L. Everitt, "Communication Engineering," McGraw-Hill Book Co., Inc., New York, N. Y., pp. 168–171; 1937.

the earth's surface to the impedance bridge or, when using the standing-wave method, to a point of minimum voltage. This is especially important in the VHF region. The section of line introduced into earth (by terrain measurements) should preferably be made of rigid bars or tubes to avoid their eventual bending, thus assuring the correct, uniform separation between the two conductors of the same.

Let l be the length of line in earth. The corresponding measured input impedance will be called Z_1. Now the line is introduced further into the earth such that its length (in earth) should be exactly $2l$, calling the corresponding input impedance Z_2. Then Z_0 and γ will be found from the following formulas (see Appendix):

$$Z_0 = \sqrt{Z_1(2Z_2 - Z_1)} \tag{8}$$

$$\tanh \gamma l = \sqrt{\frac{2Z_2 - Z_1}{Z_1}} \tag{9}$$

and the constants result from the formulas (3) to (7) above.

Simplified Procedures

If the permeability of the earth and consequently L of the line are known, the calculations can be simplified. After having computed Z_0 from (1) or (8), or having found it by some other process, we have

$$Y_0^2 = \frac{1}{Z_0^2} = \frac{G + j\omega C}{j\omega L}, \text{ hence } C - j\frac{G}{\omega} = LY_0^2, \tag{10}$$

σ and ϵ_r being found from (5) and (6). Formulas (2) or (9) may also be used alone in a similar way.

When $|\gamma l| \ll 1$ (low frequencies or/and short line in earth), we have, measuring only Z_{oc})

$$Y_{oc} = \frac{1}{Z_{oc}} \approx Yl = (G + j\omega C)l, \tag{11}$$

and as before σ and ϵ_r are calculated from (5) and (6). In this case the line may be considered a capacitor and the permeability μ has no influence upon the measurement. If μ of the earth is known, the other parameters of the earth can be calculated, *e.g.* the intrinsic impedance, velocity of propagation, attenuation, etc. *This capacitor case, using a relative low "standard" frequency, is undoubtedly the one best suited for working in the terrain; it allows rapid measurement and easy calculations.*

A brief study will now be made of Fig. 1. This figure represents the absolute value and argument of Z_{oc} as a function of l, where Z_{oc} is the input impedance of earth line with the far end open-circuited and l is the length of the line in earth; the frequency is 200 mc.

First it will be seen that $\phi = \arg Z_{oc}$ remains practically constant for $0 < l < 4$ cm (these values of course refer only to the present case). On this part of the curve the line acts as a capacitor and we have (for the referred part),

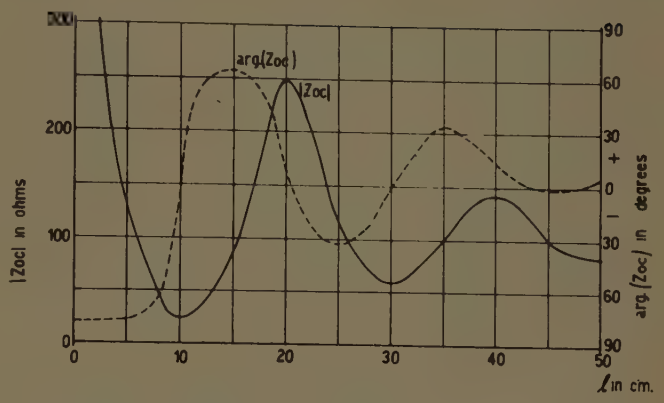

Fig. 1—Curves of magnitude and argument of the input impedance of opencircuited earth line as functions of line length, at 200 mc.

$$\tan \phi = -\frac{\omega C}{G} = -\frac{\omega \epsilon}{\sigma}, \tag{12}$$

where $\epsilon = \epsilon_r \cdot \epsilon'$ and $\epsilon' = (36\pi \cdot 10^9)^{-1}$ farad/m. This result may serve as a control for other methods of measurement.

Further, the distance between $l = 0$ and the length corresponding to the first maximum of $|Z_{oc}|$ or between two successive maxima (or minima) or $|Z_{oc}|$, corresponds to $\lambda/2$, where λ is the wavelength in the earth tested.

At VHF we can introduce the line into earth until the distance between the surface of this and the first voltage minimum is $\lambda'/2$ or $\lambda'/4$, λ' being the free space wavelength. The corresponding values of l (length of line in earth) result as $\lambda/4$ or $\lambda/2$ respectively. If μ is known and $\sigma \ll \omega\epsilon$ (generally true at VHF), we have then

$$\epsilon = \frac{1}{\mu\lambda^2 f^2}, \tag{13}$$

where $\mu = \mu_r \cdot \mu'$ and $\mu' = 4\pi \cdot 10^{-7}$ henry/m. If, on the other hand, arg Z_{oc} for l very small is measured (horizontal part of curve, Fig. 1), σ may be calculated from (12).

For materials of high conductivity, with μ known and at VHF, introduce the line until Z_{oc} practically does not vary with l. In this case $Z_{oc} = Z_0$, and σ and ϵ can be calculated from (10).

Although some of these procedures may be rather restricted in practical usage, they are presented to form an idea of how the transmission line method can be adapted to a variety of conditions.

Experimental Data

Some of the more important constants of one type of earth as functions of frequency are presented in Figs. 2 and 3. In Fig. 2 we find the magnitude and argument of η (the intrinsic impedance of the earth) together with the attenuation constant α and the velocity of propagation v in per cent of free space velocity. In Fig. 3, the conductivity σ, the relative dielectric constant ϵ_r and the dissipation factor $\sigma/\omega\epsilon$ will be found. It is seen that

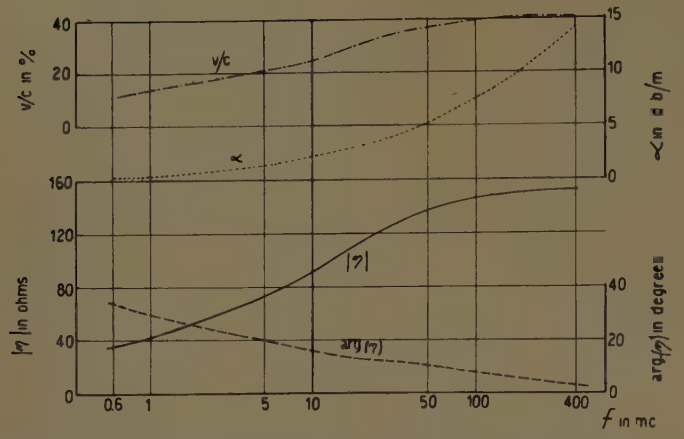

Fig. 2—Magnitude and argument of intrinsic impedance, attenuation factor and velocity of propagation in earth vs frequency.

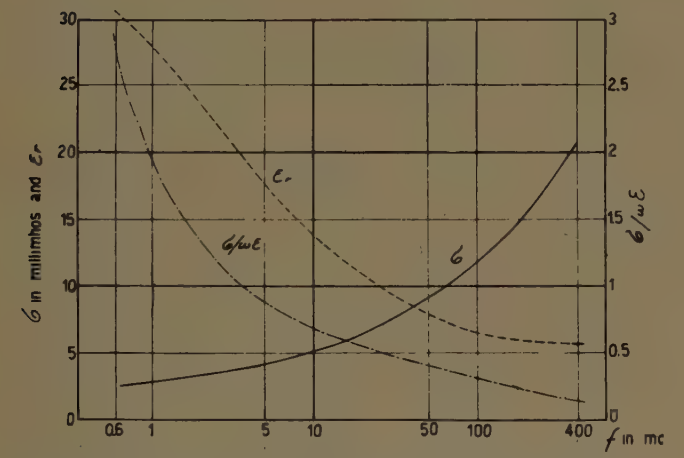

Fig. 3—Curves of the earth's conductivity, relative dielectric constant and dissipation factor as functions of frequency.

$|\eta|$ rises steadily from some small value at low frequencies (in this paper low frequencies will mean frequencies below 1 mc) up to about 150 ohms at 400 mc. Above 200 mc it seems to remain relatively constant. The angle or argument of η diminishes from 35° at 600 kc to about 5° at 400 mc and appears to go asymptotically to zero for higher frequencies. The attenuation constant rises steadily throughout the entire band in the figure. The velocity of propagation, v, rises from about 10 per cent at 600 kc to a practically constant value of 40 per cent at the higher frequencies.

The conductivity (Fig. 3) which appears to approach some constant value of about $3 \cdot 10^{-3}$ mho/m below 600 kc, rises to a value of $21 \cdot 10^{-3}$ mho/m at 400 mc. The rise of σ seems to continue at still higher frequencies. The relative dielectric constant falls from very high values at low frequencies (about 30 at 600 kc) to a value of 6 at 400 mc. At higher frequencies it appears to remain constant. Although σ rises and ϵ_r gets smaller with rising frequencies, the dissipation factor $\sigma/\omega\epsilon$ falls steadily throughout the frequency range, being unity at 4 mc.

To avoid confusion in an eventual comparison of the numerical values of Fig. 1 with those of Figs. 2 and 3, it is made clear that Fig. 1 is based on an earth sample different (though similar) from that of Figs. 2 and 3.

Discussion

A brief analysis follows, to show the agreement between the above results and the general concepts concerning a medium such as earth.

The intrinsic impedance of a medium is

$$\eta = \sqrt{\frac{j\omega\mu}{\sigma + j\omega\epsilon}}.$$

For low frequencies, when $\sigma/\omega\epsilon \gg 1$, we have approximately

$$\eta \approx \sqrt{\frac{j\omega\mu}{\sigma}} = \sqrt{\frac{\omega\mu}{\sigma}} \angle 45°.$$

Assuming σ and μ constant at low frequencies (in agreement with the experimental results), the magnitude of the intrinsic impedance of the measured earth will be proportional to the square root of the frequency, the angle being constant equal to 45°. For the earth sample tested, at 600 kc, the angle of η is only 35°, because $\sigma/\omega\epsilon$ is only equal to 2.8 and not $\gg 1$ as assumed in the above analysis.

For frequencies above 400 mc (present case) the inequality $\sigma/\omega\epsilon \ll 1$ begins to come true, and we may set

$$\eta \approx \sqrt{\frac{j\omega\mu}{j\omega\epsilon}} = \sqrt{\frac{\mu}{\epsilon}}.$$

At these frequencies (again agreeing with the experimental results) we may assume μ and ϵ constants, and therefore the intrinsic impedance is approximately constant and purely resistive.

For the propagation constant in earth we have

$$\gamma = \sqrt{j\omega\mu(\sigma + j\omega\epsilon)}, \tag{14}$$

and the corresponding approximations result: for low frequencies

$$\gamma \approx \sqrt{\omega\mu\sigma} \angle 45°,$$

and for high frequencies

$$\gamma \approx j\omega\sqrt{\mu\epsilon}.$$

Allthough α may be neglected compared with β at the higher frequencies, it has a high value at frequencies above 400 mc. At these frequencies an approximate value for α is[5]

$$\alpha \approx \frac{\sigma}{2}\sqrt{\frac{\mu}{\epsilon}} \text{ neper/m}. \tag{15}$$

That is, again assuming μ and ϵ constants, α is proportional to σ.

[5] E. C. Jordan, "Electromagnetic Waves and Radiating Systems," Prentice-Hall, Inc., New York, N. Y., p. 129; 1950.

From the variation of the dissipation factor it is seen that at low frequencies the measured earth may be considered a conductor and at high frequencies (assuming the interpretation given in this paper concerning low and high frequencies) a lossy dielectric, in agreement with the general concepts exposed above.

The Brewster angle, in the present case, for frequencies above 400 mc, approaches a value of approximately 70°.

The frequency range between 1 and 100 mc (present case) is interesting in that it represents a range of transition in which the electrical behavior of the earth sample changes from that of a conductor to that of a dielectric.

Some of the difficulties which may be met during the measurements and calculations will now be discussed.

When using an RF bridge (similar to the ones employed in this work) at the low frequencies, if the dielectric constant is relatively high, the capacity of the earth capacitor will also be high and the difference in readings between initial balance and balance with earth line connected can be small (referring to reactance dial) and the result unexact. The resulting conductivity will not be greatly affected by this, but the measured value of dielectric constant may suffer great variations. To avoid this difficulty, the earth line should be made as short as possible, taking care that the resistance component does not fall outside the range of resistance dial of the bridge. The ideal solution would of course be to use an impedance measuring device specially built for this purpose.

In the VHF range commercially available VHF coaxial impedance- or admittance-meters together with an appropriate balun can be used. In the present work, both this and a balanced, calibrated standing wave detector has been employed for measurements in the VHF band. The most critical factor, using the standing wave detector, is the exact measurement of the distance from the earth's surface (where the line penetrates into earth) to a voltage minimum on the air line. Employing *Method 1* above, a failure in this distance will greatly affect the value of σ, while ϵ appears relatively unaffected. The difficulty in determining the mentioned distance exactly, probably sets the upper frequency limit for this measurement procedure.

When a measurement, or a pair of measurements, in the VHF range are unexactly realized, they will mostly result in a great calculated series resistance in the line. This fact offers a good control for a correct measurement; *i.e.*, if the measurements are correctly performed, the series resistance of line should result approximately zero.

If the relative permeability is unity as will mostly be the case, there are only two unknowns to be found, σ and ϵ (at the upper range of frequencies the value of σ is frequently unimportant and ϵ only has to be found). However, employing *Method 1* (or *Method 2*), we have four measured quantities at our disposal. Knowing the manner in which the errors may be produced by the instruments and the measuring procedure, one may be able to correct the erroneous results. For example, using the admittance meter and the balun referred to above, and employing *Method 1* together with (1) to (7), the resulting values of σ and ϵ above 100 mc were not acceptable, due to their arbitrary variations with frequency. On the other side, the attenuation constant and the velocity of propagation as functions of frequency resulted in smooth curves up to the higher extreme of the frequency band in question (up to 400 mc). Subsequently, assuming the computed values of α and v (or β) to be correct (a more thorough analysis would make clear if this really is admissable), σ and ϵ can easily be calculated from (14).

In other words, a careful analysis of the measuring procedure employed in each case may provide a means by which eventual errors can be corrected.

The end effect of the open-circuited line has not been accounted for in this paper. Neither has radiation from the earth line been taken into account; this will of course be necessary when the line separation becomes an appreciable fraction of the wavelength in earth. In the present case, at 300 mc, the line separation results about $0.05\ \lambda$ in earth.

Electrolytic action between the transmission line electrodes and the soil could possibly build up small potentials between each electrode and the soil, but because of the symmetry in the set-up, these potentials would cancel and not influence the measurement. This electrolytic action could moreover result in a thin gas film covering the electrodes, but it seems reasonable to assume that the capacitance of the capacitor, whose dielectric is the mentioned gas film, is very much greater than the capacitance of the earth line, and hence will not change the parallel admittance of the line. Therefore it appears that a possible electrolytic action can be neglected.

Although this paper deals with an open, balanced two-wire transmission line, the method is in no way restricted to this type of line. Other configurations can be used as, for example, a coaxial line or a quasi-coaxial line. An unbalanced line has the advantage that commercially available instruments are more readily employed through an extensive frequency range; though in this case a more thorough analysis of an eventual electrolytic action would be desirable. On the other side, in the balanced two-wire line, discontinuities can practically be avoided and it can more easily be introduced into the ground, suffering a minimum of deformation.

Besides the method dealt with in this paper and those mentioned in the Introduction, there exists a variety of laboratory methods for distinct sample measurements.[6]

Though the method described primarily was thought of as a "tool" for terrain measurements, it appears that it could be of value as a laboratory instrument also, as a substitute for the classical sample measurement meth-

[6] See, *e.g.*, R. W. P. King, "Transmission-Line Theory," McGraw-Hill Book Co., Inc., New York, N. Y., pp. 329–341; 1955.

ods, especially in the VHF region. Moreover, the great variations of the constants with frequency, contrary to the commonly accepted "fact" that they should be practically constant, justify the somewhat extensive discussion of the results obtained. In this discussion it is seen that, although the constants vary greatly with frequency, the general behavior of soil as a reflecting layer for radiopropagation compares qualitatively well with the other methods cited.

Though local variations of the soil may be of less importance in radiopropagation, where the average soil condition over a large area should be taken, the present method may prove useful as a means for investigating general physical properties of soil and geological surface phenomena through their relation to the measured electric characteristics, and, in this sense, the knowledge of local variations of soil can be of importance.

Appendix

Demonstration of Formula (5)

From elementary electromagnetic theory we have

$$\frac{G}{\sigma} = \frac{C}{\epsilon}.$$

Hence,

$$\sigma = \frac{\epsilon G}{C} = \frac{\epsilon' G}{C'} = \frac{G}{36\pi \cdot 10^9 C'} = \frac{8.85 \cdot G_{\text{mho}}}{C'_{\mu\mu\text{f}}} \text{ mho/meter.}$$

Demonstration of Formulas (8) and (9)

We have from ordinary transmission line theory

$$Z_1 = Z_{oc}(l) = \frac{Z_0}{\tanh \gamma l}$$

$$Z_2 = Z_{oc}(2l) = \frac{Z_0}{\tanh 2\gamma l}$$

$$\frac{Z_2}{Z_1} = \frac{\tanh \gamma l}{\tanh 2\gamma l} = \frac{1}{2}(1 + \tanh^2 \gamma l),$$

which results in

$$\tanh \gamma l = \sqrt{\frac{2Z_2 - Z_1}{Z_1}},$$

and subsequently

$$Z_0 = Z_1 \cdot \tanh \gamma l = \sqrt{Z_1(2Z_2 - Z_1)}.$$

Acknowledgment

The author wishes to thank the authorities of the "Laboratorio de Electronica y de Communicaciones" (Argentine Armed Forces Research Laboratory) for their encouragement in the present work. He also wishes to acknowledge the stimulus and helpful suggestions of Luís P. Poli.

The Archimedean Two-Wire Spiral Antenna*

JULIUS A. KAISER†

***Summary*—A pair of equally excited but oppositely sensed Archimedean two-wire spirals situated close to one another in the same plane—a doublet—is used to generate a linearly polarized field in which the direction of polarization and phase are controlled or varied independently of each other by rotation of the spiral radiators. An array of these doublets can be made to scan by rotation of the several spiral elements; an eight-doublet array which was made to scan over an 83° sector with small amplitude variation is discussed. A doublet fed from a ring network can be employed as a polarization diversity circuit. A virtual doublet is achieved by placing a single spiral in a right angle trough. A preliminary scanning array comprising four spirals in a trough was made to scan ±36°. The possibility of using a parasitic spiral in conjunction with a driven spiral for obtaining linear polarization of variable direction and phase is indicated. Also, a brief simplified analysis of the two-wire Archimedean spiral is presented, which leads to the concept of higher-order modes of radiation.**

Introduction

THE two-wire Archimedean spiral configurations shown in Fig. 1, when properly excited, have been shown to be circularly polarized radiators with broadband characteristics—broadband with respect not only to input impedance but also to radiation pattern.[1] In practice, either configuration is energized from a transmission line connected to the center terminals of the configuration.

So energized, the configuration radiates a broad circularly polarized beam to each side of the spiral. Each radiated beam is normal to the plane of the spiral, and the sense of circularity of polarization of the beam on one side corresponds to the winding sense of the spiral

* Manuscript received by the PGAP, June 22, 1959; revised manuscript received, October 2, 1959.

† Diamond Ordnance Fuze Labs., Washington, D. C.

[1] E. M. Turner, "Spiral Slot Antenna," Wright-Patterson AFB, Ohio, Tech. Note WCLR-55-8 WADC; June, 1955.

as viewed from the opposite side. Accordingly, the two radiated beams are identical except that the rotational sense of polarization of the radiated field on one side is the opposite of that on the other. For example, the spiral of Fig. 1(a) would radiate a right circularly polarized beam away from a viewer of the figure, and a left circularly polarized beam toward him. In most applications it is desirable that the spiral radiate to one side only; this is readily accomplished by appropriately backing the spiral on one side by a ground plane or cavity.

The spiral antenna described above has received much attention in recent years—principally because its broadband characteristics render it admirably adaptable to the requirements of radar countermeasures.[2-9] This paper presents a simplified analysis of the Archimedean spiral antenna and points out some of the important properties of its radiation field. Earlier work has been reported previously.[10] A few applications utilizing some of the hitherto unexplored properties of the spiral are presented. A spiral doublet array is treated in somewhat greater detail, since, to date, most effort has been directed toward it.[11]

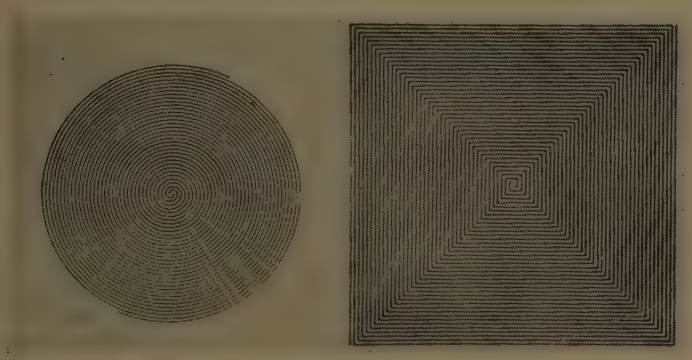

(a) (b)

Fig. 1—Circular and rectangular Archimedean spirals.

[2] Abstracts of the Fifth Annual Symposium on USAF Antenna Res. and Dev., publisher, Monticello, Ill., University of Illinois Press, Urbana; October, 1955.

[3] B. H. Burdine and R. M. McElvery, "The Spiral Antenna," Massachusetts Inst. of Tech., Cambridge Res. Lab. of Electronics, Rept. Nos. 1 and 2.

[4] J. C. Pullara and H. H. Hibbs, "The Study on Flush-Mounted Circularly Polarized Antennas and Polarization Modulation," Melpar, Inc., Falls Church, Va., P.O. 569838, Prime Contractor-Sperry Gyroscope Co., AF 33(600)- 35477; March, 1955.

[5] J. C. Pullara, H. H., Hibbs, and H. T. Ward, "*S*-Band Transmitting and Receiving Antennas," Melpar, Inc., Falls Church, Va., P.O. 520117C, Prime Contractor-Sperry Gyroscope Co., AF 33(038)-14524; February, 1958.

[6] "An Experimental Investigation and Application of the Spiral Antenna," Temco Aircraft Corp., Dallas, Tex., Final Engrg. Rept.; July, 1957.

[7] "Research Studies on Problems Related to ECM Antennas," University of Illinois, Urbana, Rept. Nos. 1–3, 8–11, AF 33(616)–310; October, 1957.

[8] John Dyson, "An Experimental Investigation of the Spiral Antenna," University of Illinois Press, Urbana, Ill.; May, 1957.

[9] "Bibliography of Spiral Antenna Reports and Papers," Melpar, Inc., Falls Church, Va.

[10] J. A. Kaiser, "Scanning Arrays Using the Flat Spiral Antenna," Naval Res. Lab., Washington, D. C., NRL Rept. No. 5103; March, 1958.

[11] J. A. Kaiser, "Spiral Antennas Applied to Scanning Arrays," Electronic Scanning Symposium, AFCRC and RADC, Cambridge, Mass.; April, 1958.

Theoretical Considerations

There has not been any rigorous theory to explain the spiral antenna. However, the following heuristic explanation of the radiating mechanism of the two-wire Archimedean spiral is offered since it is in accord with experimental observations and is of genuine help in understanding the design possibilities of this relatively new antenna.

The point of view taken is that the two-wire spiral antenna behaves as though it were a two-wire transmission line which gradually, by virtue of its spiral geometry, transforms itself into a radiating structure or antenna. It is well known that a two-wire transmission line, of narrow spacing relative to wavelength and of any length, yields a negligible amount of radiation when excited at its terminals. This is due to the fact that the currents in the two wires of the line at any normal cross section are always 180° out-of-phase so that radiation from one line is effectively cancelled by the radiation from the other.

Suppose now that a two-wire transmission line is formed into the spiral configuration of Fig. 2(a). Let P be a point on one wire of the transmission line at a distance measured along the wire from the input terminal A. Then the point Q on the other wire at the same distance from the input terminal B is situated diametrically opposite the point P with respect to the center O, and both P and Q lie on the same circle centered at O. This implies that the point P and its neighboring point P' (on the other wire directly alongside P) lie at such arc distances from A and B, respectively, that the *difference* of these distances is precisely the arc length QP' along the spiral. If Δr, the spacing between wires, is much smaller than r, the arc length QP' is approximately equal to πr. This difference in wire lengths does not depend on the number of turns within r if the spacing between wires is uniform.

A similar situation holds for the square spiral configuration of Fig. 2(b). Here, for a cross-sectional point P-P' on the two-wire line, the path difference in the two wire lengths is given very closely by $4d$, where d is the perpendicular distance from the center O to the side of the square spiral turn on which P-P' lies. Also the circumference of the turn on which P-P' lies is approxi-

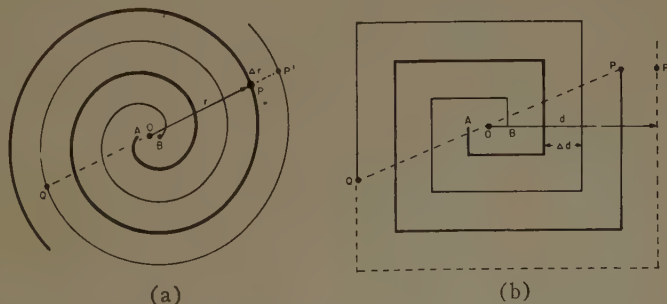

(a) (b)

Fig. 2—Construction of the circular and rectangular Archimedean spirals.

mately $8d$. This difference of $4d$ in wire lengths of the transmission line is independent of the number of turns appearing on the spiral, provided only that the spacing Δd between elements on the spiral is constant and small compared to d.

There are two items of interest that attach to a particular point on the two-wire spiral line: the total difference in wire lengths of the two-wire line to the point P-P' and the circumference or path length of the particular turn on which the point lies. For the rectangular spiral these items are:

$$\text{difference in wire lengths} = 4d$$

$$\text{circumference} = 8d.$$

When d is $\lambda/8$, where λ is the current wavelength on the spiral, the phase change or total difference in wire length is $\lambda/2$, while the total circumferential path length is λ, or a quarter wavelength on each side of the square. Phasing of the radiated field from opposite sides of the square is such as to add in a direction normal to the plane containing the spiral. Moreover, radiation from two adjacent sides is equal in intensity but with a relative phase difference of 90 electrical degrees, so that the radiated field normal to the plane of the spiral is circularly polarized.

For the circular spiral where again the wires are equally spaced, at a point whose radial distance from the spiral center is r, we have

$$\text{difference in line lengths} = \pi r$$

$$\text{circumference} = 2\pi r.$$

When r is $\lambda/2\pi$, the phase change is $\lambda/2$ and the circumference is λ. Assuming that each wire supports a progressive wave of current and that these current waves are anti-phase at the input terminals A and B, it is clear that the difference in phase of the two current elements at any point PP' on the two-wire line, measured in radians, is π (the input phase difference) $+2\pi/\lambda(\pi r)$. Thus neighboring current elements start anti-phase at the feed points A and B, and gradually come into phase as one proceeds outward along the spiral two-wire line. When r is $\lambda/2\pi$, these currents are precisely in phase and radiation is a maximum. Moreover, the condition for precisely in-phase currents occurs at two points diametrically opposite each other relative to the center O. (See Appendix I for typical plots of phases along each filament and for progressive phase changes between filaments.)

Radiation from the spiral then is centered in an annular ring of turns of one wavelength mean circumference. This property makes the spiral antenna an inherently broadband device, the basic requirement being only that the radius be large enough to allow a half wavelength of phase shift. Also, inasmuch as the radiating ring is a wavelength in circumference for all frequencies over which the spiral operates, a constant beamwidth should be maintained.

The input impedance of spiral antennas as a function of filament geometry is not known at this time. However, the impedance of a few spirals with relatively close filament spacings has been found to be on the order of 100 ohms near their centers.

Higher-Order Modes of Radiation

Radiation from the one-wavelength ring as described above has been termed the first mode of radiation, since this represents the first occasion for which conditions are correct for radiation. It can be reasoned that currents existing beyond the one-wavelength ring will continue experiencing phase change as they progress outward. Assuming that the spiral structure is large enough, these currents will be out-of-phase again at a radius where the circumference is two wavelengths and in-phase at the three-wavelength circumference. No radiation occurs from the two-wavelength ring because the currents on adjacent filaments are anti-phase. At the three-wavelength ring radiation can occur if currents exist, giving rise to the third mode of radiation. It follows that currents which are anti-phase at the input terminals can excite only the odd modes of radiation.

If, on the other hand, the two center terminals are tied together and excited in some manner, currents start in-phase at the center of the spiral. In progressing outward, these currents experience phase change. When the one-wavelength circumference is reached, they are anti-phase and no radiation occurs. At the two-wavelength circumference, which is defined as the locus of the second radiation mode, the currents are once again in phase, and radiation is once again strong. Currents around the two-wavelength circumference of a circular spiral, and possibly a rectangular spiral, are in such phase as to cause a radiation pattern of minimum field on-axis and maximum field, which is omnidirectional, in the plane of the spiral. Since the second mode diameter for the circular spiral is approximately $(2\lambda/\pi)$, a very broad pattern in the plane of the spiral axis is obtained. Thus, even modes only are produced when currents are in-phase at the input terminals.

One method of exciting the second mode is shown in Fig. 3. The input is treated as a microstrip line with two branching circuits, connected to the center conductor of a coaxial line, above a ground plane which is connected to the outer conductor of the coaxial line. The part of the spiral immediately above the ground plane can be considered as a microstrip transmission line feeding the second mode radiator with two terminals at the edge of the ground plane. The ground plane is continued only far enough to establish the currents in the microstrip mode. The impedance of the two microstrip line terminals at the edge of the ground plane should match that of the two terminals of the spiral for maximum power transfer.

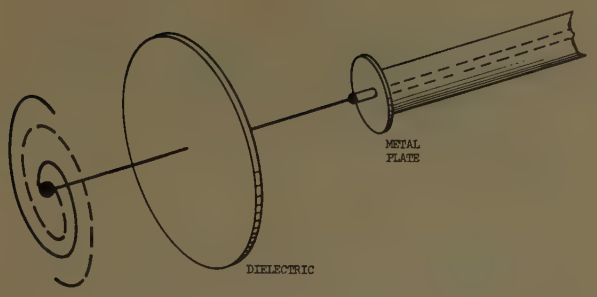

Fig. 3—Second mode excitation method.

Phasing Properties of the Single Spiral Antenna

A property of the spiral which has not been fully exploited is that of circular symmetry about the axis, which allows rotation about the axis to produce a change in phase of the radiated field everywhere in space without variations in the far-field amplitude. One degree of mechanical rotation produces a corresponding change in phase of one electrical degree.[12]

To see, in a simple way, why this phasing property is so, first represent the circular spiral antenna as a circular conductor, one wavelength in circumference, which supports a uniform progressive current wave. Referring to Fig. 4, the arrows on the circular conductor indicate the direction in which current phase fronts move. Consider now two points in the far field of this circular current distribution, $P_1(\theta, \phi_1)$ and $P_2(\theta, \phi_2)$, whose spherical coordinates differ only in the azimuth coordinate ϕ. It is clear that these two points see the same current distribution except for a shift of phase in the current sources along the circle; that is, the sources for the radiation field at P_2 are identical with the sources for the radiation field at P_1 except for a phase lag in the sources for P_2 over those for P_1, of $\Delta\phi$ electrical degrees. Accordingly, the radiation field of the circular one-wavelength current loop depends only with respect to phase on the azimuth coordinate ϕ and this dependence is given by the factor $e^{i\phi}$. It follows immediately that a rotation of the circular current loop, which does not disturb the intrinsic current phasing, changes the phase of the radiation field of the loop everywhere by an amount which in electrical degrees is precisely equal to the number of degrees of mechanical rotation.

Similarly, rotation of the second-mode spiral changes the phase of the radiation field everywhere by an amount which in electrical degrees is twice the number of degrees of mechanical rotation.

Phasing and Polarization Properties of the Spiral Doublet

Two spirals of opposite sense, placed side by side in the same plane and excited equally (Fig. 5), will radiate

[12] Unless specifically excepted, further discussions pertain only to the first mode of radiation.

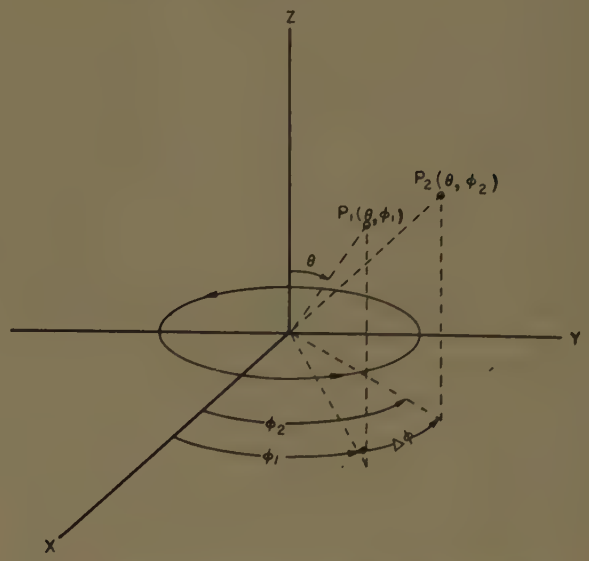

Fig. 4—Phase properties of a single spiral radiator.

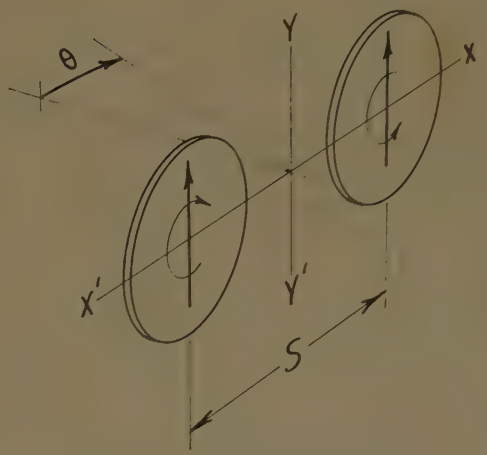

Fig. 5—Spiral doublet schematic.

a combined field which will be linearly polarized everywhere. This is true because both left- and right-hand spirals contribute ellipses of polarization of the same amplitude and orientation, but oppositely sensed, everywhere in space. Although linearly polarized, the direction of polarization of the far field at a particular point will be a function of the relative electrical phasing between the two spirals and the relative space phasing. Consider, first, an on-axis fixed position and let the phase of one spiral be varied with respect to the other by rotation as illustrated in Fig. 6. This figure shows three possible instantaneous orientations for the field vectors radiated from the spiral doublet and the resultant on-axis fields. Fig. 6(a) shows that when both vector fields are simultaneously vertical and in the same direction, the resultant instantaneous field is vertical. Ninety degrees later in time the left vector will be pointing to the left and the right vector will be pointing to the right, producing no net field on-axis. It may be

concluded that the time average field radiated from the doublet as shown in Fig. 6(a) will be linear and vertically polarized. Similarly, as shown in Fig. 6(c) the instantaneous vectors as oriented produce no net vertical field on-axis. Ninety degrees later in time, however, both vectors will be pointing in the same direction, producing a horizontally polarized field. Fig. 6(b) illustrates the condition where the radiated fields are phased orthogonally. The sum of the radiated fields then from the two equally excited spirals remains linear

(a) (b) (c)

Fig. 6—On-axis phasing possibilities of the doublet.

when the phase of one element (the element on the right in Fig. 6) is changed relative to that of the other, but the direction of polarization rotates through an angle $\phi/2$ when the relative phase is changed $\phi°$. If the relative input phasing to the spirals is constant with change in frequency, then the direction of polarization for the doublet at a given point will also be independent of frequency.

Looking again at the spiral doublet schematic shown in Fig. 5, it is clear that symmetry exists in the YY' plane, which bisects the spiral doublet, since no differential space phasing between the elements exists. Direction of polarization in the $X'X$ plane, which bisects the spiral axes, however, will be a function not only of the relative phasing between the spiral elements but also of the differential space phasing between them.

On the other hand, if one spiral is rotated in either direction through an angle θ, while the other spiral is simultaneously rotated in the opposite direction through the same angle θ, the polarization of the radiation field remains unchanged in direction but the phase of this field at all points changes by precisely θ electrical degrees. In this change of phase there is no change in amplitude provided each spiral has perfect axial symmetry. Since the spiral is an inherently broad-band radiator, the above properties hold over a wide band of frequencies.

Applications of the Spiral Doublet

A Spiral Doublet Array

A spiral doublet, as discussed above, is a linear radiator, the direction of polarization of which is varied by rotation of either spiral element and phase is independently varied by rotating simultaneously both spiral elements. An array of such doublets leads to an antenna of any arbitrary linear polarization which can be made to

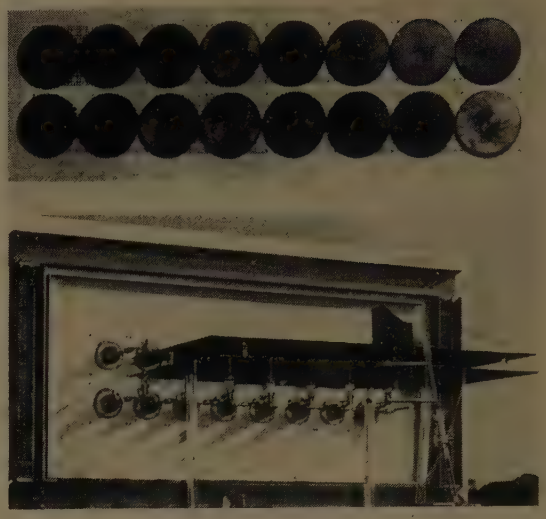

Fig. 7—A spiral doublet array.

scan by changing the relative phase between the spiral doublets. Fig. 7 is a photograph of an array consisting of eight spiral doublets arranged so that each vertical pair of spirals is a doublet. The bottom view is a photograph of the back of the array showing feed harness and dials that indicate phase settings. Spacing between doublets is a half-wavelength for the test frequency of 1430 mc, and the polarization selected here is vertical.

Fig. 8 shows patterns at 1430 mc of a typical spiral element making up this array. The beamwidth for a total variation of 2 db is approximately 104°. The spacing of the spiral above the ground plane is $2\frac{7}{8}$ inches, which at this frequency is correct to give approximately a 1-db dimple in the center of the pattern for vertical polarization. This spacing of the spiral above the ground plane was selected because it results in small amplitude variations over a broad beam, which in turn allows a broad scan. Like the dipole behavior over a ground plane, closer spacing of the spiral to the ground plane would result in less amplitude variation over a smaller angle, while a greater spacing would produce a deeper dimple with correspondingly wider beamwidths and larger amplitude variations. With a linearly polarized antenna—a dipole—used for transmitting, this particular spiral showed a maximum variation in response for reception over the useful portion of the pattern of approximately 1 db for the various angular positions or cuts shown. The maximum variation with rotation for any individual spiral was approximately $1\frac{1}{3}$ db.

Fig. 9 shows patterns of one of the spiral doublets used in the array. The upper group of four curves represents patterns of the vertical doublet set for vertical polarization but for four different phasings. One spiral of the doublet was initially adjusted for maximum response with vertical polarization and the pattern labelled 0° was taken; the phase was changed 90° by rotating one spiral of the doublet 90° in a clockwise direction while simultaneously rotating the other spiral counterclockwise 90° and the pattern labelled 90° was

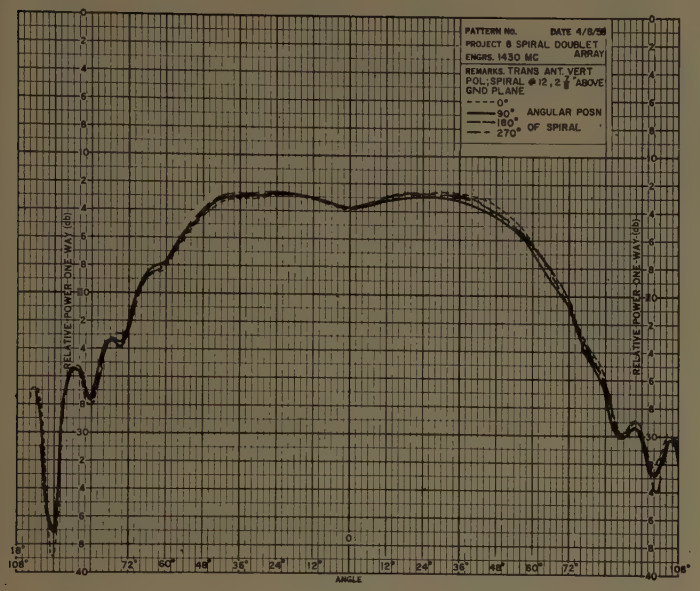

Fig. 8—Single spiral over a ground plane.

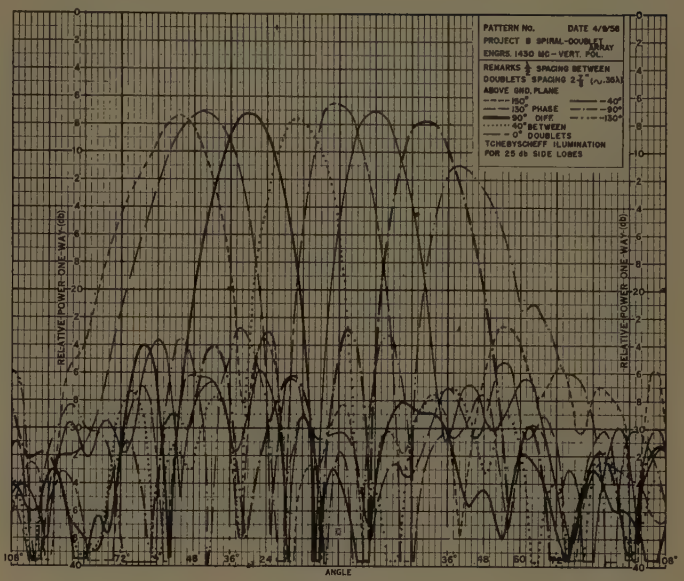

Fig. 10—Eight doublet array patterns.

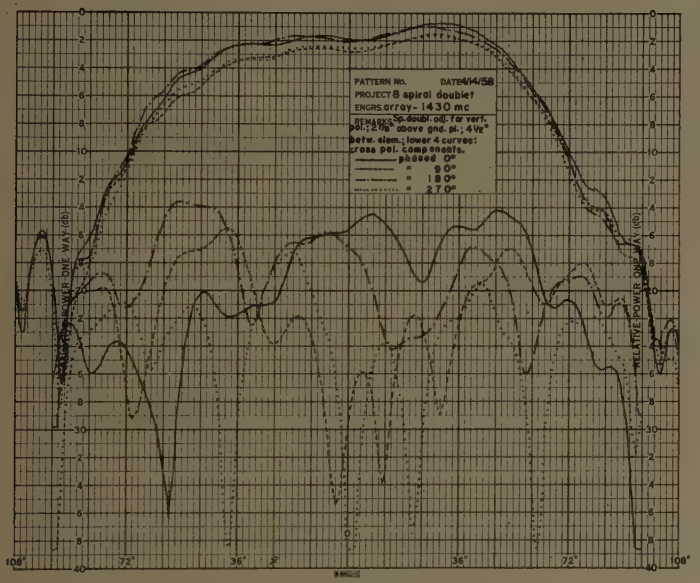

Fig. 9—Spiral doublet patterns.

recorded; similarly, patterns were recorded for relative phasings of 180° and 270° in order to see the variation in doublet response with changes in phasing. The particular doublet shown produces a variation in amplitude with change in phase of as much as 2 db in some places. Also to be noticed from these patterns is a squint or a pointing of the beam off to the right which did not appear in the individual spiral patterns. This is a condition which conceivably can be eliminated.

The lower group of four patterns in Fig. 9 represents the cross-polarized components. For these patterns the transmitting antenna was rotated 90° so that it was radiating with horizontal polarization and patterns were taken of the doublet for the phasings shown while it was still adjusted for vertical polarization. The cross-polarized components are seen to be down only 13 db in some portions of the pattern. Necessity for considerable improvement in doublet performance is clearly indicated.

In Fig. 10 are the patterns taken for the eight doublet array shown in Fig. 7. Patterns considered are only those in the horizontal plane. A Tchebycheff current distribution for a 25-db sidelobe level was obtained using a printed microstrip feed harness. Each pattern shown is for the indicated phase difference between adjacent doublets measured in mechanical degrees.

The direction and width of each main beam is in very close agreement with the theoretically derived array-factor patterns. The scan demonstrated here, ignoring the extreme right pattern, is from 53° to the left of the on-axis direction to 30° to the right, with a total variation in amplitude of the main beam of less than 1½ db. Patterns taken of the individual doublets mounted in the array, and in the presence of all other doublets, indicate that the scan could have been made from 30° to the right of the on-axis direction to approximately 65° on the left for a total useful scan of greater than ±45°. The scan would be symmetrical about the on-axis direction if the spiral doublet patterns were symmetrical about their axes.

The sidelobe levels in Fig. 10 are down approximately 15 db or better, which is considerably above those theoretically predicted—namely, 25 db. The sidelobe level would be more nearly that predicted by the theory if individual doublet performances were uniformly the same.[13]

Because of the squint associated with the individual doublets it was necessary to employ spirals of one sense along the top row in the array and of opposite sense along the bottom row. With this arrangement symmetry

[13] For later results, see J. R. Donnellan, "An Eight Spiral Doublet Electromechanical Scanning Array," Naval Res. Lab., Washington, D. C., NRL Rept. No. 5283; April, 1959.

is maintained in the plane of scan so that, for a given polarization on-axis, the same polarization will obtain throughout the plane of scan. However, in the other principal plane the direction of polarization will tilt from that of the on-axis direction due to the differential space phasing between the two elements of the doublet. If symmetry about the on-axis direction of the doublet can be obtained, an alternating arrangement of doublets can be employed to give symmetry in both principal planes.

Spiral in a Trough

A broad-band linearly polarized radiator of variable phase can be obtained by combining a single spiral with a corner reflector, or right-angled trough open at the ends. The arrangement shown in Fig. 11, where the spiral lies in the plane bisecting the corner reflector, results in a virtual doublet because the spiral radiates right-hand circularly polarized energy in one direction and left-hand circularly polarized energy in the opposite direction. The sides of the trough then reflect two spiral images of opposite sense which are equally energized. Rotation of the single spiral results in simultaneous phase advance or retardation of both images. Constant direction of polarization is therefore maintained and only the phase is changed by spiral rotation. An examination of Fig. 11(a) shows that in the bisecting plane through the vertex those radiated components which appear vertical from the end view cancel in the far field while the horizontal components add. Direction of polarization in the bisecting plane for such an arrangement will always be along the axis of the trough.

There is, in addition, radiation in the plane of the spiral which is down less than 3 db from the on-axis radiation. Furthermore, the direct radiation in the plane of the spiral varies in phase with change of angular position in the bisecting plane of the trough, while the phase of the reflected images described above remains constant. A permanent beam cock is therefore imparted to the radiation field; that is, in the bisecting plane of the trough, the beam, representing the sum of the constant phase fields reflected from the trough sides and the variable phase fields radiated in the plane of the spiral, is in a direction other than that along a normal bisecting the trough vertex. If the beam cock is to one side of this normal for a given spiral, then for a spiral of opposite sense the beam cock will be to the opposite side of the normal.

Spirals of the same sense placed longitudinally along the trough constitute an array with linear polarization which can be made to scan. Phase change is simpler than in a spiral doublet array since rotation of only one spiral accomplishes the same end as rotating both spirals in a doublet. Also there are fewer initial adjustments required; the direction of polarization is predetermined so it does not have to be set initially, nor will it change during the course of adjustments.

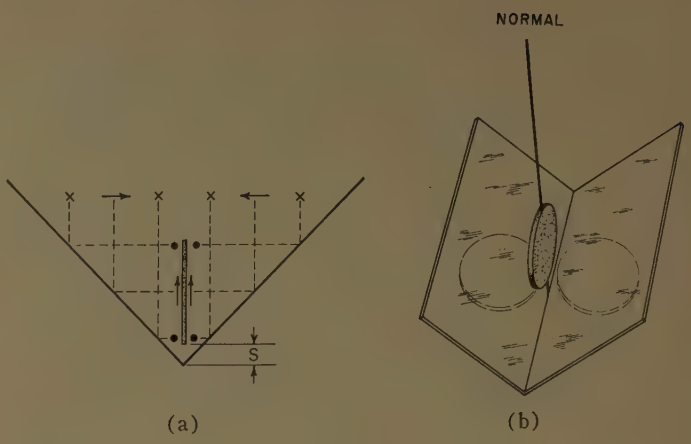

Fig. 11—Spiral in a trough.

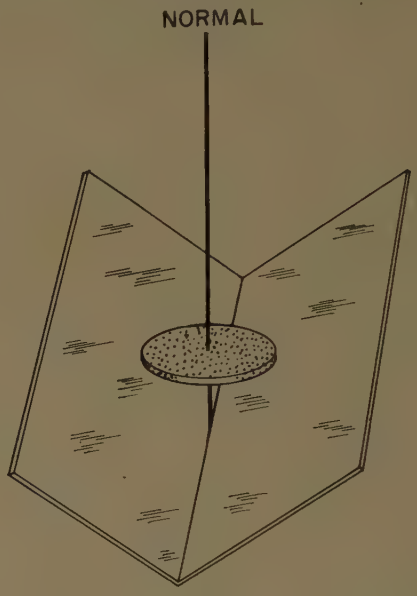

Fig. 12—Spiral in a trough—a variation.

Another arrangement of a spiral in a trough is shown in Fig. 12. Here a spiral is mounted with its axis coincident with a normal bisecting the trough vertex. This arrangement also produces linear polarization, the phase of which can be varied by rotation of the single spiral antenna. In this case, however, the radiation pattern in the bisecting plane of the vertex is symmetrical about the axis of the spiral, and the direction of polarization in a plane normal to the spiral axis is dependent upon the spacing of the spiral above the vertex. Using the plane bisecting the vertex as a reference, the direction of polarization rotates for an increase in the spiral to vertex spacing in a counterclockwise manner when a right circular spiral is used, and rotates in a clockwise manner when a left circular spiral is used. The direction of polarization was found to rotate $\pm 20°$ for a change in spacing of $1\frac{1}{2}$ to 1. The radiated beam had axial ratios of approximately 25 db, while the beamwidths in the bisecting plane ranged from 60° to 70°.

An array of spirals in a trough, where each spiral axis lies in the bisecting plane of the trough, radiates a beam which is linearly polarized and which can be made to

scan symmetrically in a plane bisecting the trough axis. Such an array (Fig. 13), consisting of four equally excited spirals with a half-wavelength separation between centers, was made to scan $\pm 36°$ in the plane bisecting the vertex with less than 1-db variation in the main-beam amplitude. The major-lobe beamwidth was approximately 27° and the sidelobes were down at least 9 db. Spacings of the spirals above the vertex were adjusted to give a direction of polarization along the vertex in order that alternating-sense spirals could be used. A broad-band scanning array would require spirals all of one sense in order to have identical change in direction of polarization with change in frequency.

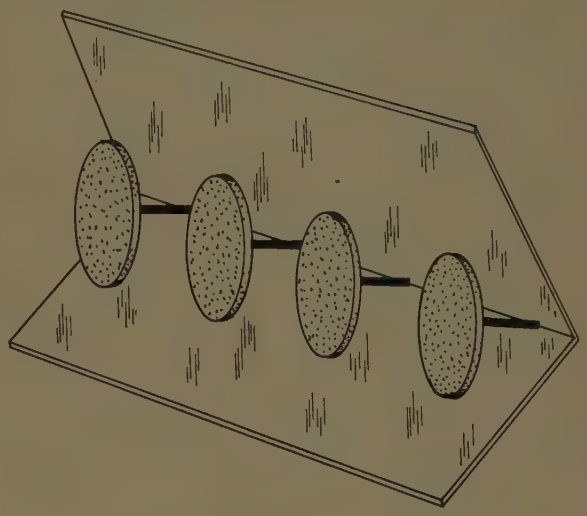

Fig. 13—Spiral trough array.

The Parasitic Spiral

A parasitic spiral placed along the same axis as, and relatively close to, a driven spiral (Fig. 14) radiates circular polarization of opposite sense from that radiated from the driven spiral. The polarization of the combined field varies from near linear to circular, depending upon the degree of coupling between the parasite and driven spirals. The behavior of the parasitic spiral differs from the driven spiral in that the phase of the reradiated energy from the parasitic spiral changes by twice the angle of rotation (rotation signifies here rotation of the parasitic element about its axis or change in phase of the field incident on the parasite). This implies that rotation of the parasite rotates only the major axis of the combined field ellipse; furthermore, the polarization which is assumed along the major axis of the ellipse rotates linearly with rotation of the parasite. By the same token, rotation of the driven element results only in a change of phase of the combined fields, since the phases of both direct and reradiated fields will be affected.

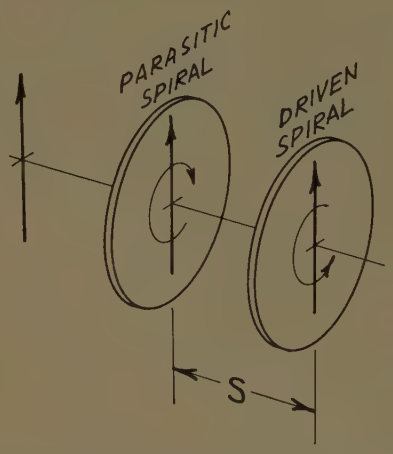

Fig. 14—Parasitic spiral in front of and close to a driven spiral.

The parasitic spiral can presumably be of either sense, regardless of the sense of the driven element, and yet reradiate circular polarization of opposite sense from that of the driven element. This is true because a circularly polarized field incident on a given spiral will cause currents to flow either in toward the center or out toward the edge of the spiral, since the direction of the current flow is a function of the sense of the incident field as well as the sense of the parasitic spiral. Currents reaching either unterminated end would be reflected and travel back out to be reradiated in a sense opposite to that which was received. This means, that linear polarization incident on a parasitic spiral will be reradiated as linear, since a linear field incident on a spiral will cause equal currents to flow in opposite directions.

If sufficient coupling between a driven spiral and a parasitic spiral can be obtained such that the parasite radiates a field equal to that of the driven spiral, the combined fields would be linearly polarized. The direction of polarization would be fixed by the parasite while phase would be determined by the driven element. Patterns recorded with a parasitic spiral separated from the driven element by a $\frac{1}{8}$-inch lucite disk resulted in an axial ratio (or on-axis ellipticity ratio) of 15 db at 1500 mc, which indicates radiation from the parasite was down about 2.5 db from that of the driven spiral (see *Axial Ratio* below). The lucite disk was employed to increase the degree of coupling between the driven spiral and parasitic spiral. Maximum axial ratio without the plastic separator was approximately 10 db. These axial ratios are relatively easy to obtain and do not necessarily indicate the greatest degree of coupling obtainable with proper care.

Polarization Diversity

A spiral doublet with some relative phase between its two elements will radiate a field linearly polarized in some arbitrary direction. If the input (or intrinsic) phasing to one element of the doublet is changed by 180° the direction of polarization will be rotated 90°, just as though that element were rotated mechanically 180°. A doublet fed from a ring network as shown in Fig. 15 allows selection of either of two orthogonal polarizations of arbitrary direction. Currents fed into arm 3 of the ring network divide equally and leave arms 2 and 4 in-

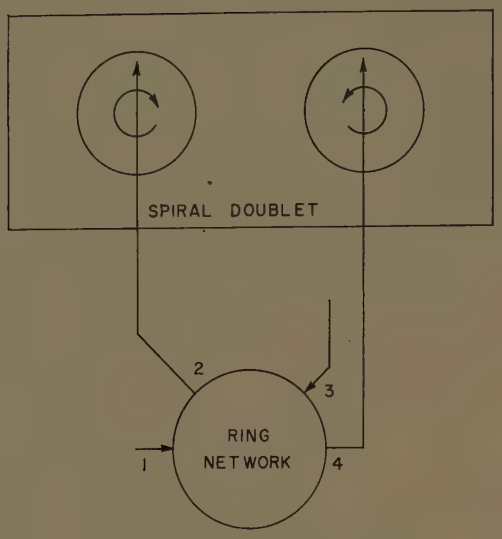

Fig. 15—Polarization diversity circuit.

phase, resulting in a linearly polarized field from the doublet. Currents fed into arm 1 also come out of arms 2 and 4 equally but 180° out-of-phase, resulting in linear polarization orthogonal to that obtained when currents enter arm 3. Similarly, orthogonal shifting of the polarization according to the input terminal used can be arranged for an array of doublets.

Miscellaneous Spiral Antenna Considerations

Axial Ratio

An elliptically polarized wave can be resolved into two circularly polarized waves of opposite sense, which have appropriate relative amplitudes and phases.[14] The relationship is:

$$\text{ellipticity ratio (in db)} = 20 \log \frac{E_L + E_R}{E_L - E_R},$$

where $-E_L$ and E_R are the amplitudes of the opposite sense components. A special case resulting in linear polarization arises when the two amplitudes are equal. Another special case where the amplitude of one circular wave is zero yields circular polarization of the sense corresponding to that of the circular wave of finite amplitude. In general, the latter case is desired of individual spiral radiators.

The Archimedean spiral should in theory radiate a circularly polarized field along its axis with a sense corresponding to the winding sense of the spiral. Frequently in practice the on-axis field of a spiral is found to be elliptically polarized, indicating generally the existence of current flow on the spiral in a sense opposite to that of the currents flowing from the input terminals. For example, when the center terminals shown in Fig. 1(a) are excited, the current flow gives rise to a right circularly polarized field traveling away from the viewer of the figure. Currents originating in some fashion at the spiral periphery, on the other hand, are in a sense opposite to those traveling from the center, resulting in a radiated field which is left circularly polarized. The sum of these two fields of opposite sense from the spiral is a radiation pattern with an axial ratio other than unity. The reverse current flow may arise from reflection at the outer terminals of currents either leaking past the radiation region or being induced on the spiral by the field reflected from a backing ground plane or cavity. In any case, the reflected currents return to the region of the one-wavelength ring and are there radiated in a sense opposite to that desired.

Currents existing beyond the radiation ring are therefore generally undesirable. They can be attenuated quite simply by placing lossy material such as resistive card or aquadag on the outermost turns of the spiral or at some radius less than that necessary for higher-mode radiation. Aquadag painted between the two wires of the last turn of a spiral, for example, will absorb incident currents in both the radiation mode and transmission line mode. This is so because the lossy material is parallel to the electric field for both modes. In practice, axial ratios have been reduced from 2 or 3 db without aquadag to less than $\frac{1}{2}$ db after applying aquadag.

Beam Cock

Another phenomenon frequently encountered in spiral patterns is that of beam cocking or pointing of the beam other than along the axis of the spiral. This is a condition brought about by simultaneously exciting both the first and second modes of radiation. In a transition from a coaxial line to a two-wire transmission line[15] there exists on the two-wire line, unless suitable precautions are taken, an in-phase component of current as well as the usual anti-phase or transmission line mode currents. The in-phase component along the two-wire line is out-of-phase with the corresponding current on some ground system, which may be the outside conductor of the coaxial line. Considering such a discontinuity at the input terminals of a coaxial fed spiral, it follows that the in-phase component of current will excite the second radiation mode if the spiral is sufficiently large, while the usual transmission line mode current excites the first mode of radiation. The resultant field obtained from adding the first radiation mode, characterized by maximum gain along the axis and 360° phase change per spiral revolution, and the second radiation mode, characterized by maximum gain in the plane of the spiral and 720° phase change per revolution, is generally a beam that does not exhibit symmetry about the spiral axis. The amount of beam cock is dependent upon the relative amplitudes of the two radiation modes, and the direction is determined from the relative phases.

Fig. 16 shows two axial cuts of a coax-fed spiral which was large enough to support the first two modes of radia-

[14] J. D. Kraus, "Antennas," McGraw-Hill Book Co., Inc., New York, N. Y.; 1950.

[15] N. Marchand, "Transmission-Line Conversion Transformers," *Electronics*, vol. 17, pp. 142–145; December, 1944.

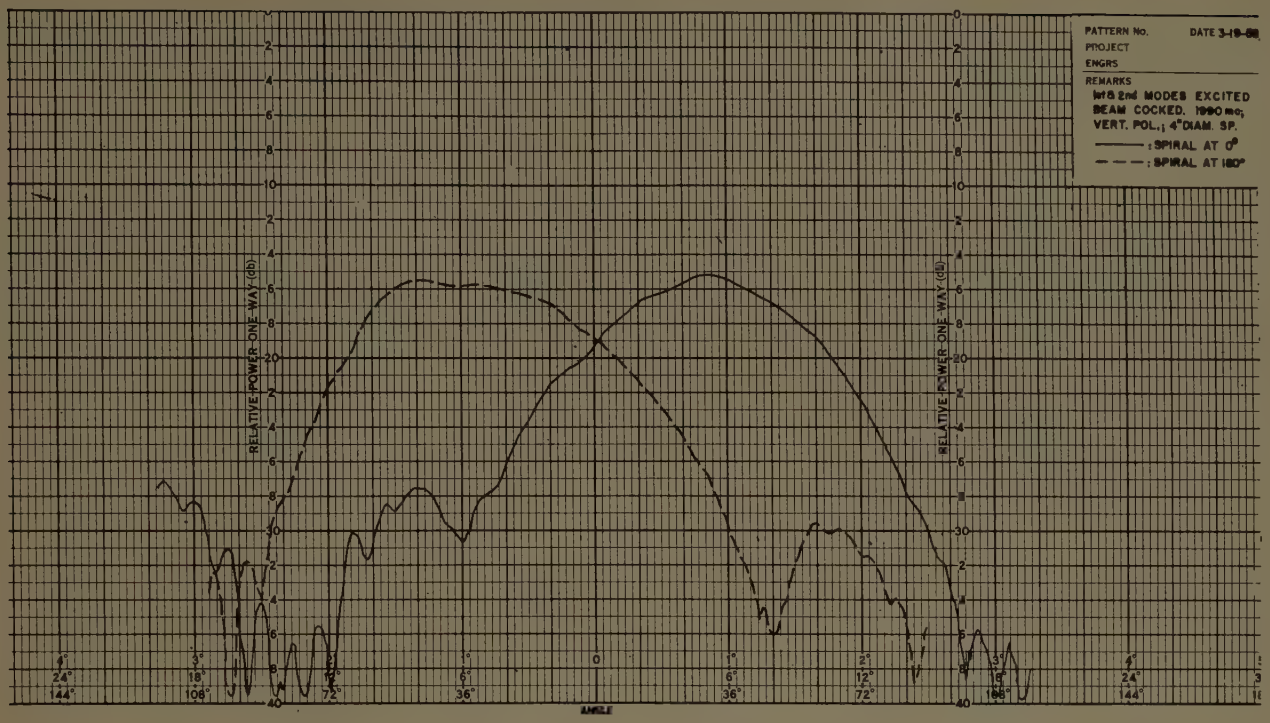

Fig. 16—Beam cock associated with a coaxial line fed spiral. Scale: 360°.

tion. One pattern was recorded with the spiral so oriented as to shift the beam as far as possible off axis in one direction. The spiral was then rotated 180° in its own plane and the other pattern recorded. It can be seen that a beam cock of approximately 30° exists and rotates with rotation of the spiral. In practice it was found that a coax-fed spiral only a little larger than necessary for the first mode of radiation produced sufficient second-mode radiation to cause some beam cock. A balanced feed for the spiral eliminated all evidence of beam cock.

Ground Planes

A flat ground plane is one type of backing used with spiral antennas. The on-axis gain is not much affected by ground-plane size providing the ground plane has a minimum dimension greater than approximately 0.6 wavelength. The far off-axis patterns however are a function of the ground-plane size when it is small. This latter factor assumes importance primarily when arrays of spirals are considered and low sidelobe levels are desired. For low sidelobes in any antenna array, the radiation pattern from each element should coincide exactly with each of the other element patterns. Identical element patterns for all directions in space can only be achieved with adequate ground-plane size.

Conclusions

The flat Archimedean spiral antenna in the first mode —the input terminals excited anti-phase—is a versatile broadband antenna which radiates circularly polarized energy with constant beamwidth whose far-field phase depends upon angular position of the spiral. Excited in the second mode, *i.e.*, the input terminals excited in-phase, the Archimedean spiral becomes a broadband radiator with a beacon pattern; that is, radiation is a maximum in the plane of the spiral and the phase of the far field again is dependent upon angular position.

Two spirals in the first mode, of opposite sense and excited equally, radiate a combined field which is everywhere linearly polarized. The direction of polarization is controlled by rotating one spiral of the doublet relative to the other, while phase is independently controlled by rotating both spirals equal but opposite amounts. An array of doublets can be employed to produce a linearly polarized beam of any arbitrary direction which can be made to scan through an angle of as much as $\pm 50°$ by rotating the individual spiral radiators.

A virtual doublet, with which linear polarization of variable phase is obtained, can be realized by placing a single spiral in a right-angle trough. Direction of polarization is not arbitrary as with the spiral doublet, but linear polarization and scanning can be accomplished with one-half the number of elements.

Nearly linear polarization can be obtained by placing a parasitic spiral in front of and close to a driven spiral. Rotation of the parasite rotates the major axis of the combined far-field ellipse, while rotation of the driven element changes only the phase.

Polarization diversity utilizing any two orthogonal polarizations can be obtained by feeding a spiral doublet from a ring network. An array of doublets with a corporate feed can have one input terminal for linear polarization in one direction while a second input terminal feeds the orthogonal polarization.

Appendix I

The Archimedean spiral is defined by

$$r = a\psi e^{i\sigma} \tag{1}$$

where

r = radius from spiral center
ψ = angular measure (in radians)
a = a constant which controls spiral pitch
$\sigma = 0, \pi$ for a two-wire spiral.

The length (S) of a spiral filament is approximately

$$S = \int_{\psi_1}^{\psi_2} r d\psi = \int_{\psi_1}^{\psi_2} a\psi d\psi = \frac{a}{2}\psi^2 \Big|_{\psi_1}^{\psi_2}. \tag{2}$$

Change of phase due to line length in electrical degrees along a given filament relative to the input is

$$\frac{S}{\lambda}(360°) = \frac{a\psi^2}{2\lambda}(360°) \tag{4}$$

where λ is the current wavelength along the spiral.

Table I shows values of (4) for three wavelengths (assuming $\epsilon = 1$ and input terminals excited anti-phase) and for $a = 0.1$. Fig. 17 is a plot of these phases (small numerals) along each spiral filament starting at the center terminals. Larger numerals represent the differences in phases between adjacent filaments. The shaded circular areas are those regions in which the difference of phases between adjacent filaments is approxi-

TABLE I
Typical Phase Progression Along an Archimedean Spiral Filament

ψ (radians)	$\lambda = 7.88$ inches (1500 mc)		$\lambda = 11.8$ inches (1000 mc)		$\lambda = 15.75$ inches (750 mc)	
	S/λ (360) (degrees)	S/λ (360) + 180 (degrees)	S/λ (360) (degrees)	S/λ (360) + 180 (degrees)	S/λ (360) (degrees)	S/λ (360) + 180 (degrees)
π	22	202	15	195	11	191
2π	90	270	60	240	45	225
3π	203	23	135	315	102	282
4π	361(1)	181	241	61	180	0
5π	564(204)	24	376(16)	196	282	102
6π	812(92)	272	542(182)	2	406(46)	226
7π	1105(25)	205	738(18)	198	553(193)	13
8π	1443(3)	183	964(244)	64	722(2)	182
9π	1826(26)	206	1219(139)	319	914(194)	14
10π	2254(94)	244	1506(66)	246	1128(48)	228

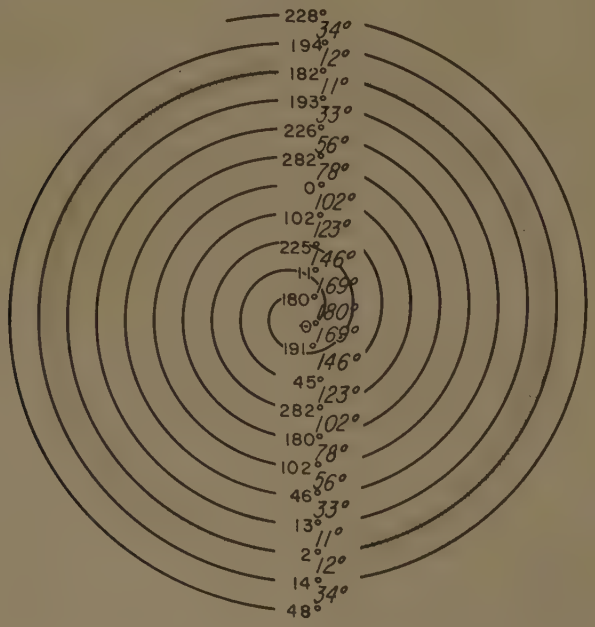

Fig. 17(a)

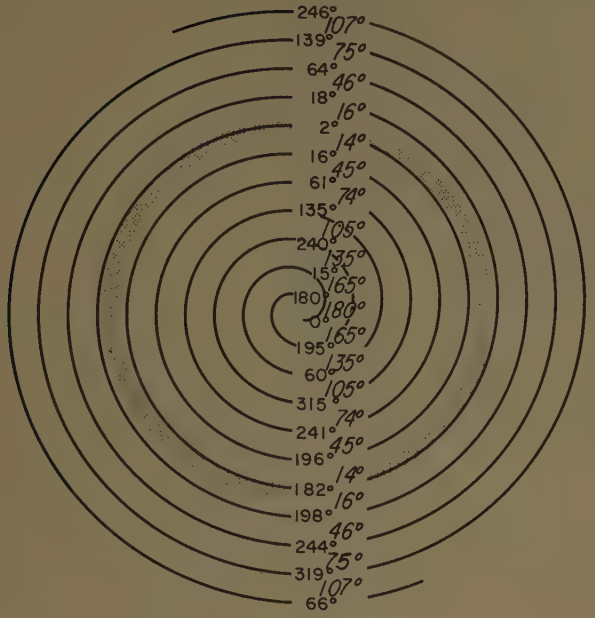

Fig. 17(b)

Fig. 17(c)

Fig. 17—Progressive phase change along a spiral antenna and phase differences between spiral filaments. (a) $A=0.1$, $\lambda=15.75$ inches (750 mc); (b) $A=0.1$, $\lambda=11.8$ inches (1000 mc); (c) $A=0.1$, $\lambda=7.88$ inches (1500 mc).

mately zero. It can be seen that as the wavelength increases, the region where the currents are in phase progresses outward from the center of the spiral. Additionally, it can be noted that the region of in-phase currents at 750 mc is one of anti-phase currents at 1500 mc.

The spiral used for illustrative purposes has five turns, and, since $a=0.1$ inch per turn, the maximum diameter is slightly greater than 6.25 inches.

ACKNOWLEDGMENT

The author wishes to thank A. E. Marston, head of the Microwave Antennas and Components Branch, Electronics Division, Naval Research Laboratory, Washington, D. C., for his contributions and for the enlightening and encouraging discussions. The author also wishes to thank J. Donnellan and R. Wiegand of the same organization for their assistance.

Coupled Leaky Waveguides I: Two Parallel Slits in a Plane*

S. NISHIDA†

Summary—**Theoretical expressions are derived for the effects of mutual coupling between two parallel leaky wave antennas located in an infinite plane. The leaky wave antennas treated are slitted rectangular waveguides, the propagation constants of which are modified by the coupling. It is shown that the attenuation constants are influenced significantly but that the phase constants are changed only slightly, so that the coupling is different from that between neighboring surface wave lines. The nature of the coupling effects are illustrated by numerical calculations.**

* Origin manuscript received by the PGAP, August 8, 1959; revised manuscript received January 18, 1960. The research reported was conducted under Contract AF 19(604)-2031, sponsored by the Air Force Cambridge Res. Ctr., Air Res. and Dev. Command.

† Microwave Res. Inst., Polytechnic Institute of Brooklyn, New York, N. Y.; on leave of absence from Tohoku University, Sendai, Japan.

I. INTRODUCTION

THE longitudinally slitted rectangular waveguide, with radiation characterized by leaky waves, has already been investigated by employing a transverse network representation and a perturbation procedure to solve the resulting network resonance problem.[1] The above investigation has been carried out for a single (isolated) leaky waveguide. In this paper, two coupled leaky waveguides carrying the H_{10} leaky wave

[1] L. O. Goldstone and A. A. Oliner, "Leaky wave antenna I: Rectangular waveguides," accepted for publication in IRE TRANS. ON ANTENNAS AND PROPAGATION.

are treated for the case where they are arranged in a plane[2] and in parallel with each other.

If these two coupled leaky waveguides have identical cross sections and they are excited in the same amplitude and in the same (or opposite) phase, then the leaky wave has a form of exponential change in the direction of the guide axis. Therefore, the problem reduces to a two-dimensional problem in the cross section of the structure. The symmetry (or antisymmetry) also reduces the problem to that for a single leaky waveguide with an electric (or magnetic) wall which bisects the region between the two waveguides in a plane transverse to their cross section. For this reduced problem, the same analytical techniques may be employed as in the single leaky waveguide referred to initially.

If two leaky waveguides with identical cross sections are arbitrarily excited, then the leaky waves may be given as a superposition of the two cases, the in-phase and the out-of-phase excitation, mentioned above because of the symmetry of the structure. In this paper, the leaky waves associated with excitation of only one guide (the other being source-free but acting as a parasite) will also be described.

A cross section of the structure analyzed here is shown in Fig. 1. Numerical results have been calculated

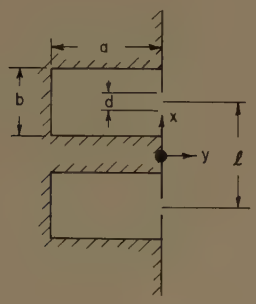

Fig. 1—Cross section of two coupled leaky waveguides arranged on a plane.

for some specific dimensions and are presented in graphical form.

The calculations show that the attenuation constant α is significantly affected by the mutual coupling due to the neighboring leaky waveguide, although the phase constant β is influenced only slightly. These changes in α are a function of the separation between the guides, and may be important in disturbing the aperture illumination, thereby producing pattern deterioration. In particular, the angle of maximum radiation will be shifted only slightly, but the pattern shape may be significantly altered.

Those numerical calculations associated with the excitation of only one of the guides, with the other present as a parasite, indicate that considerable power may be coupled into the parasitic guide.

[2] In the companion paper, entitled, "Coupled leaky waveguide II: Two parallel slits in a cylinder," the corresponding problem dealing with a cylinder will be considered.

II. The In-Phase Excitation

A cross section of the structure considered here is shown in Fig. 1.

Because of the excitation specified, the electric and magnetic fields in the open region, in this case, satisfy the conditions of *electric wall* at $x=0$, which bisects the region between the two waveguides in a plane parallel to the axis of the waveguides, as shown in Fig. 2. Let the

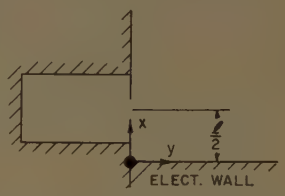

Fig. 2—Equivalent bisected structure corresponding to in-phase excitation of the two leaky waveguides of Fig. 1.

electric field at the aperture of the slit be $\boldsymbol{E}(x)$;[3] then the normalized admittance to be terminated in the transverse network representation is given by[1]

$$Y' = \frac{I_0}{V_0 V_0} = \sum_{n=1}^{\infty} \frac{Y_n V_n V_n^*}{Y_0 V_0 V_0^*} + \frac{\int_{ap} dx \int_{ap} dx' \boldsymbol{y}_0 \times \boldsymbol{E}^*(x) \cdot y(x, x') \cdot \boldsymbol{y}_0 \times \boldsymbol{E}(x')}{Y_0 V_0 V_0^*}, \quad (1)$$

where $\boldsymbol{E}^*(x)$ is the complex conjugate of $\boldsymbol{E}(x)$, $y(x, x')$ is a dyadic admittance in the quarter space to be solved here, and

$$\begin{cases} V_0 = \dfrac{1}{\sqrt{b}} \displaystyle\int_{ap} \boldsymbol{z}_0 \cdot \boldsymbol{y}_0 \times \boldsymbol{E}(x) dx \\ V_0^* = \dfrac{1}{\sqrt{b}} \displaystyle\int_{ap} \boldsymbol{z}_0 \cdot \boldsymbol{y}_0 \times \boldsymbol{E}^*(x) dx. \end{cases}$$

The normalized admittance given in (1) may be decomposed into two terms as follows:

$$Y' = Y_{\text{int}}' + Y_{\text{ext}}',$$

where

$$\left.\begin{aligned} Y_{\text{int}}' &= \sum_{n=1}^{\infty} \frac{Y_n V_n V_n^*}{Y_0 V_0 V_0^*}, \\ Y_{\text{ext}}' &= \frac{b}{d} \cdot \frac{1}{Y_0} \cdot Y_{\text{ext}} \\ Y_{\text{ext}} &= \frac{\displaystyle\int_{ap} dx \int_{ap} dx' \boldsymbol{y}_0 \times \boldsymbol{E}^*(x) \cdot y(x, x') \cdot \boldsymbol{y}_0 \times \boldsymbol{E}(x')}{\dfrac{1}{d} \displaystyle\int_{ap} \boldsymbol{z}_0 \cdot \boldsymbol{y}_0 \times \boldsymbol{E}(x) dx \int_{ap} \boldsymbol{z}_0 \cdot \boldsymbol{y}_0 \times \boldsymbol{E}^*(x) dx}. \end{aligned}\right\} \quad (2)$$

[3] The aperture electric field is assumed to have only an x-component and to be a complex value in general.

To a good approximation, the normalized admittance $Y_{int'}$ may be considered to be independent of the geometry of the open region. Thus, we have[4]

$$Y_{int}' = jB_{int}' \simeq j\frac{\kappa b}{\pi} \ln\left(\csc\frac{\pi d}{2b}\right), \tag{3}$$

where

$$\kappa = \sqrt{k^2 - k_z^2}$$

and k and k_z represent the wave numbers in free space and in z direction in the slitted guide, respectively.

For the external admittance, Y_{ext}, in (2) it can be readily shown that Y_{ext} is stationary for first order variations of $\boldsymbol{E}^*(x)$ and $\boldsymbol{E}(x)$. The distribution of the aperture electric field, in general, is not constant; moreover, it is not symmetrical with respect to a midplane in the aperture because of the asymmetry of the open region looking at the aperture. However, if the quantity $d/b \ll 1$, then it can be easily shown that the stationary value of Y_{ext} is given to a good approximation by taking $\boldsymbol{z}_0 \cdot \boldsymbol{y}_0 \times \boldsymbol{E}(x) = \boldsymbol{z}_0 \cdot \boldsymbol{y}_0 \times \boldsymbol{E}^*(x) = 1$. Therefore, the external admittance in (2) is led to

$$Y_{ext} = \frac{1}{d}\int_{ap} dx \int_{ap} dx' \boldsymbol{z}_0 \cdot y(x, x') \cdot \boldsymbol{z}_0, \tag{4}$$

by putting $\boldsymbol{z} \cdot \boldsymbol{y}_0 \times \boldsymbol{E}(x) = \boldsymbol{z}_0 \cdot \boldsymbol{y}_0 = \boldsymbol{E}^*(x) = 1$. Thus, the problem here has been reduced to the determination of the dyadic admittance, $y(x, x')$, and the evaluation of the integral in (4).

The dyadic admittance is obtained as follows from a Green's function characterized by the quarter space:

$$\left.\begin{aligned} y(\varrho, \varrho') &= -\frac{1}{j\omega\mu}(\nabla \times \nabla \times \boldsymbol{z}_0)(\nabla' \times \nabla' \times \boldsymbol{z}_0) S(\varrho, \varrho') \\ &\text{for } H\text{-type modes,} \\ &\left(\frac{\partial^2}{\partial z^2} + k^2\right) S(\varrho, \varrho') = G(\varrho, \varrho'), \\ &\text{where } \rho \sin\theta = y,\ \rho\cos\theta = x \text{ and } y(x, x') \text{ is found from} \\ &y(\varrho, \varrho') \text{as} \\ &\qquad y(x, x') = y(\varrho, \varrho')]\theta = \theta' = \frac{\pi}{2}. \end{aligned}\right\} \tag{5}$$

The Green's function defined as

$$(\nabla^2 + k^2) G(\varrho, \varrho') = -\delta(\varrho, \varrho'),$$

δ = Dirac's delta function

and subjected to the boundary conditions

G is finite at $\rho \to 0$, satisfies the radiation condition as

$$\rho \to \infty,$$

and

$$\frac{\partial G}{\partial \theta} = 0 \text{ at } \theta = 0 \quad \text{and} \quad \frac{\pi}{2},$$

[4] N. Marcuvitz, "Waveguide Handbook," Rad. Lab. Ser., McGraw-Hill Book Co., Inc., New York, N. Y., vol. 10, p. 218, eq. (2a); 1951.

is obtained as follows:

$$G(\varrho, \varrho') = \sum_{n=0}^{\infty} -j\epsilon_n \cos 2n\theta \cos 2n\theta' J_{2n}(\kappa\rho_<) H_{2n}^{(2)}(\kappa\rho_>), \tag{6}$$

where

$$\epsilon_n = \begin{cases} 1: & n = 0, \\ 2: & n \neq 0 \end{cases}$$

and J and $H^{(2)}$ represent Bessel and the second kind of Hankel functions, respectively, and the notation $\rho_<$ is employed for either ρ or ρ', depending on which is smaller, and conversely for $\rho_>$. From (5) we have

$$\boldsymbol{z}_0 \cdot y(x, x') \cdot \boldsymbol{z}_0 = \frac{\kappa^2}{\omega\mu} \sum_{n=0}^{\infty} \epsilon_n J_{2n}(\kappa\rho_<) H_{2n}^{(2)}(\kappa\rho_>). \tag{7}$$

The right hand side in (7) can readily be led to the following formula:

$$\sum_{n=0}^{\infty} \epsilon_n J_{2n}(\kappa\rho_<) H_{2n}^{(2)}(\kappa\rho_>) = \tfrac{1}{2}\{H_0^{(2)}(\kappa|x - x'|) + H_0^{(2)}(\kappa|x + x'|)\}.$$

Thus, (4) becomes

$$Y_{ext} = \frac{\kappa^2}{2\omega\mu d}\int_{t_1}^{t} dx \int_{t_1}^{t_2} dx' \cdot \{H_0^{(2)}(\kappa|x - x'|) + H_0^{(2)}(\kappa|x + x'|)\},$$

where

$$t_1 = \frac{l}{2} - \frac{d}{2}, \qquad t_2 = \frac{l}{2} + \frac{d}{2}.$$

Furthermore, an appropriate change of variable leads to

$$Y_{ext} = \frac{\kappa^2}{2\omega\mu d}\int_0^d dx \int_0^d dx' \sum_{n=0,1} H_0^{(2)}(\kappa|nl + x - x'|). \tag{8}$$

The first term, corresponding to $n = 0$, in the above integral is an external admittance for the single slit in the the half space (without coupling). The second term, corresponding to $n = 1$, is the additional term that accounts for the presence of coupling with the other slit. Eq. (8) may also be derived directly in the original structure (Fig. 1) from the basic procedure by means of the magnetic field at the aperture which is given by putting the electric field at the aperture as constant.

From (2) we have the normalized external admittance as

$$Y_{ext}' = \frac{b}{d} \sum_{n=0,1} \frac{\kappa}{2d}\int_0^d dx \int_0^d dx H_0^{(2)}(\kappa|nl + x - x'|). \tag{9}$$

The double integral in (9) is transformed into a single integral as follows:

$$Y_{ext}' = \frac{b}{d} \sum_{n=0,1} \frac{1}{2\kappa d}\int_0^{\kappa d} du(\kappa d - u) \cdot \{H_0^{(2)}(|n\kappa l + u|) + H_0^{(2)}(|n\kappa l - u|)\}. \tag{10}$$

When we put

$$Y_{ext}' = G' + jB_{ext}',$$

the circuit parameters, G' and B_{ext}', to be substituted into the transverse network representation are obtained as follows by using an unperturbed real κ:

$$G' = \frac{b}{d}\Bigg[\int_0^{\kappa d} J_0(u)du - J_1(\kappa d) + \frac{l+d}{2d}\left\{\int_{\kappa l}^{\kappa(l+d)} J_0(u)du - J_1(\kappa(l+d))\right\} - \frac{l-d}{2d}\left\{\int_{\kappa(l-d)}^{\kappa l} J_0(u)du - J_1(\kappa(l-d))\right\} + \frac{l}{d}J_1(\kappa l)\Bigg], \tag{11}$$

$$B_{ext}' = \frac{b}{d}\Bigg[-\int_0^{\kappa d} N_0(u)du + N_1(\kappa d) + \frac{2}{\pi\kappa d} - \frac{l+d}{2d}\left\{\int_{\kappa l}^{\kappa(l+d)} N_0(u)du - N_1(\kappa(l+d))\right\} + \frac{l-d}{2d}\left\{\int_{\kappa(l-d)}^{\kappa l} N_0(u)du - N_1(\kappa(l-d))\right\} - \frac{l}{d}N_1(\kappa l)\Bigg], \tag{11a}$$

where N represents Neumann function. If $\kappa d \ll 1$ and the Taylor expansion with respect to κd of the integrand in (10) converges uniformly, we then have

$$G' = \frac{b}{d}\Bigg[\int_0^{\kappa d} J_0(u)du - J_1(\kappa d) + \frac{\kappa d}{2}J_0(\kappa l) + \frac{(\kappa d)^3}{24}J_0''(\kappa l) + \cdots\Bigg], \tag{12}$$

$$B_{ext}' = \frac{b}{d}\Bigg[-\int_0^{\kappa d} N_0(u)du + N_1(\kappa d) + \frac{2}{\pi\kappa d} - \frac{\kappa d}{2}N_0(\kappa l) - \frac{(\kappa d)^3}{24}N_0''(\kappa l) - \cdots\Bigg], \tag{12a}$$

where

$$J_0''(\kappa l) = \left[\frac{\partial^2 J_0(x)}{\partial x^2}\right]_{x=\kappa l}, \text{ etc.}$$

Approximate values of the normalized external admittance for practical computational purposes are

$$\left.\begin{aligned} G' &\simeq \frac{\kappa b}{2}[1 + J_0(\kappa l)], \\ B_{ext}' &\simeq \frac{\kappa b}{2}\left[\frac{2}{\pi}\ln\frac{\pi e}{\gamma\kappa d} - N_0(\kappa l)\right], \end{aligned}\right\} \tag{13}$$

which are valid under the condition that $\kappa d \ll 1$. As usual, $e = 2.718$ and $\gamma = 1.781$.

III. The Out-of-Phase Excitation

In this case, the electric and magnetic fields satisfy the condition of *magnetic wall* at $x = 0$, which bisects the region between the two waveguides, as seen in Fig. 3.

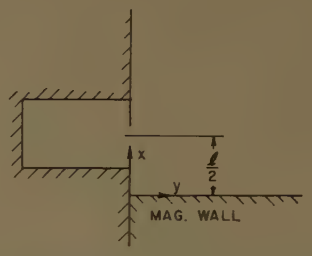

Fig. 3—Equivalent bisected structure corresponding to out-of-phase excitation of the two leaky waveguides of Fig. 1.

For this reduced problem, the same procedure as in Section II may be employed except for the dyadic admittance $y(x, x')$.

The Green's function defined as

$$(\nabla^2 + k^2)G(\varrho, \varrho') = -\delta(\varrho - \varrho'),$$

and subjected to the boundary conditions

$$\left.\begin{aligned} &G \text{ is finite at } \rho \to 0, \text{ satisfies the radiation condition as} \\ &\rho \to \infty, \ G = 0 \text{ at } \theta = 0 \text{ and } \frac{\partial G}{\partial \theta} = 0 \text{ at } \theta = \frac{\pi}{2}, \end{aligned}\right\}$$

is given by

$$G(\rho, \rho') = \sum_{n=0}^{\infty} -j2\sin(2n+1)\theta \cdot \sin(2n+1)\theta' J_{2n+1}(\kappa\rho_<)H_{2n+1}^{(2)}(\kappa\rho_<). \tag{14}$$

Thus, we have

$$z_0 \cdot y(x, x') \cdot z_0 = \frac{\kappa^2}{\omega\mu}\sum_{n=0}^{\infty} 2J_{2n+1}(\kappa\rho_<)H_{2n+1}^{(2)}(\kappa\rho_>)$$

$$= \frac{\kappa^2}{2\omega\mu}\{H_0^{(2)}(\kappa|x - x'|) - H_0^{(2)}(\kappa|x + x'|)\}, \tag{15}$$

and (4) is led to

$$Y_{ext} = \frac{\kappa^2}{2\omega\mu d}\int_{t_1}^{t_2}dx\int_{t_1}^{t_2}dx' \cdot\{H_0^{(2)}(\kappa|x - x'|) - H_0^{(2)}(\kappa|x + x'|)\}$$

$$= \frac{\kappa^2}{2\omega\mu d}\int_0^d dx\int_0^d dx'\sum_{n=0,1}(-1)^n H_0^{(2)}(\kappa|nl + x - x'|). \tag{16}$$

The normalized external admittance, therefore, is given by

$$Y_{ext}' = \frac{b}{d}\sum_{n=0,1}(-1)^n\frac{\kappa}{2d}\int_0^d dx\int_0^d dx' H_0^{(2)}(\kappa|nl + x - x'|). \tag{17}$$

The correction term corresponding to $n=1$ in the above integral differs only in sign from that in (8).

The evaluation of (17) in the same manner as that for (9) results in

$$G' = \frac{b}{d}\Big[\int_0^{\kappa d} J_0(u)du - J_1(\kappa d) - \frac{l+d}{2d}\Big\{\int_{\kappa l}^{\kappa(l+d)} J_0(u)du - J_1(\kappa(l+d))\Big\} + \frac{l-d}{2d}\Big\{\int_{\kappa(l-d)}^{\kappa l} J_0(u)du + J_1(\kappa(l-d))\Big\} - \frac{l}{d}J_1(\kappa l)\Big], \tag{18}$$

$$B_{ext}' = \frac{b}{d}\Big[-\int_0^{kd} N_0(u)du + N_1(\kappa d) + \frac{2}{\pi\kappa d} + \frac{l+d}{2d}\Big\{\int_{\kappa l}^{\kappa(l+d)} N_0(u)du - N_1(\kappa(l+d))\Big\} - \frac{l-d}{2d}\Big\{\int_{\kappa(l-d)}^{\kappa l} N_0(u)du + N_1(\kappa(l-d))\Big\} + \frac{l}{d}N_1(\kappa l)\Big], \tag{18a}$$

or, if $\kappa d \ll 1$,

$$G' = \frac{b}{d}\Big[\int_0^{\kappa d} J_0(u)du - J_1(\kappa d) - \frac{\kappa d}{2}J_0(\kappa l) - \frac{(\kappa d)^3}{24}J_0''(\kappa l)\cdots\Big], \tag{19}$$

$$B_{ext}' = \frac{b}{d}\Big[-\int_0^{\kappa d} N_0(u)du + N_1(\kappa d) + \frac{2}{\pi\kappa d} + \frac{\kappa d}{2}N_0(\kappa l) + \frac{(\kappa d)^3}{24}N_0''(\kappa l) + \cdots\Big]. \tag{19a}$$

For practical computational purposes, we have

$$\left.\begin{aligned} G' &\simeq \frac{\kappa b}{2}[1 - J_0(\kappa l)], \\ B_{ext}' &\simeq \frac{\kappa b}{2}\Big[\frac{2}{\pi}\ln\frac{\pi e}{\gamma\kappa d} + N_0(\kappa l)\Big], \end{aligned}\right\} \tag{20}$$

subject to the condition $\kappa d \ll 1$.

IV. Determination of Propagation Constants

Since the wave number, κ, introduced in the preceding sections is considered as a perturbation of that in the closed guide, it can be written as

$$\kappa = \kappa_0 + \Delta\kappa, \tag{21}$$

where κ_0 is the wave number in the closed guide, equal to π/a in the problem considered here, and $\Delta\kappa$ can be decomposed into its real and imaginary parts as follows:

$$\Delta\kappa = \Delta\kappa_r + j\Delta\kappa_i.$$

The perturbation term, $\Delta\kappa$, is now given by[1]

$$\Delta\kappa \simeq \frac{j}{a}\frac{Z_T'(\Delta\kappa_0) + j\tan\kappa_0 a}{\sec^2\kappa_0 a}, \tag{22}$$

where Z_T' is a normalized impedance to be terminated in the transverse network representation and is written as

$$Z_T' = R' + jX',$$

$$R' = \frac{G'}{G'^2 + B'^2}, \qquad X' = -\frac{B'}{G'^2 + B'^2}.$$

From (22) we have

$$\left.\begin{aligned} \Delta\kappa_r &\simeq -\frac{X'(\kappa_0)}{a}, \\ \Delta\kappa_i &\simeq \frac{R'(\kappa_0)}{a}, \end{aligned}\right\} \tag{23}$$

by using the relation $\kappa_0 = \pi/a$.

The wave number in the longitudinal direction, k_z, is given by

$$k_z = \sqrt{k^2 - \kappa^2} \simeq k_{oz} - \frac{\kappa_0}{k_{oz}}\Delta\kappa,$$

where

$$k_{oz} = \sqrt{k^2 - \kappa_0^2}$$

or

$$k_z \simeq \frac{2\pi}{\lambda_{go}}\Big(1 - \frac{\lambda_{go}^2}{4a\pi}\Delta\kappa\Big). \tag{24}$$

Letting $k_z = \beta - j\alpha$, we have

$$\left.\begin{aligned} \frac{\beta}{k} = \frac{\lambda}{\lambda_g} &\simeq \frac{\lambda}{\lambda_{go}}\left[1 + \frac{\lambda_{go}^2 X'\left(\frac{\pi}{a}\right)}{4a^2\pi}\right], \\ \alpha a &\simeq \frac{\lambda}{2a}\frac{R'\left(\frac{\pi}{a}\right)}{\frac{\lambda}{\lambda_{go}}}, \end{aligned}\right\} \tag{25}$$

where

$$\frac{\lambda}{\lambda_{go}} = \sqrt{1 - \left(\frac{\lambda}{2a}\right)^2}.$$

V. Numerical Example

Fig. 4 shows the propagation constants, that is, the guide wavelength and the attenuation constant of the leaky waves in a typical coupled leaky waveguide with $a=0.9$ inch, $b=0.4$ inch and $d=0.01$ inch, operating at a frequency corresponding to $\lambda/2a=0.7$ ($\lambda=1.26$ inches, frequency $=9385$ mc). In this figure, curves (a) represent guide wavelength and attenuation constant in the z direction in the case of the in-phase excitation described in Section II, and curves (b) that in the case of the out-of-phase excitation described in Section III.

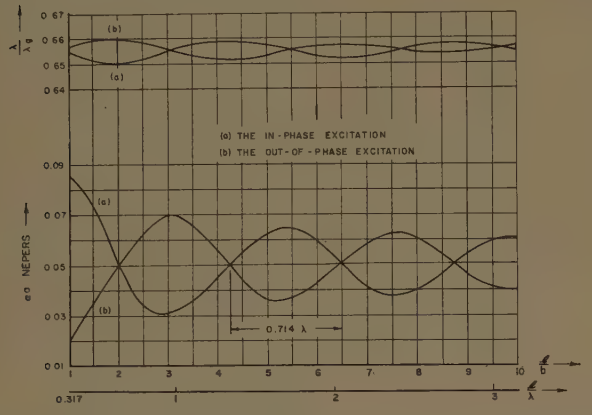

Fig. 4—Variation of propagation characteristics with separation between leaky waveguides ($a=0.9$ inch, $b=0.4$ inch, $d=0.01$ inch, $\lambda/2a=0.7$, $\lambda=1.26$ inches.)

In this example, the waveguides have narrow slits specified by $\kappa_0 d=(\pi/a)d=0.0349\ll 1$. The calculation of propagation constants can, therefore, be carried out to a good approximation from (13) or (20) rather than (11) or (18). It should be noted, however, that the relations

$$\int_0^{\kappa d} J_0(u)du \simeq \kappa d,$$

$$\int_0^{\kappa d} N_0(u)du \simeq -\frac{2\kappa d}{\pi}\ln\frac{2e}{\gamma\kappa d}$$

from which (13) and (20) have been derived can be used within the region $\kappa d<0.5$.

Fig. 4 shows that the variation of λ/λ_g with l/b (>1) is not significant and that the change is less than 15 per cent. However, the variation of αa with l/b is very significant, with a maximum change of 130 per cent. Such characteristics of the coupled leaky waves may physically be explained as follows: The phase constant in the z direction in the slitted waveguide is closely related to the stored energy at the slit. The electromagnetic fields associated with the stored energy are concentrated at the slit and couple only very slightly to the neighboring slit. This means that the phase constant is not significantly affected by the coupling. The attenuation constant in the slitted waveguide, on the other hand, is closely related to the radiated energy from the slit. The pattern of radiated energy may be quite different from that in the case of the uncoupled (isolated) slitted waveguide, and this difference also depends upon the distance between the two slits. This means that the attenuation constant is significantly influenced by the coupling associated with the radiated fields.

The above statement (that the attenuation constant is closely related to the radiated field, which has the form of the Hankel function $H_0^{(2)}(\kappa\rho)$) may also be an explanation for the slow decay of the amplitude of the curves which oscillate along the l/b axis in the figure. The curves (a) and (b) of the attenuation constant, αa, oscillate about the line $\alpha a\simeq 0.05$, which corresponds to the attenuation constant in the uncoupled (isolated) waveguide. The intersections between the curves (a) and (b) also occur on this line and coincide approximately with the roots of $J_0(\kappa_0 l)=J_0(1.396\ l/b)=0$. The intervals between the intersections, which are representative of the radiation pattern changes and which depend on the dimension of the waveguide, are about 0.9 inch ($=0.714\ \lambda$) in this example. With regard to the variations of wavelength, λ/λ_g, there are similar phenomenon to the attenuation, except when the deviations of wavelength from the uncoupled case is at its lowest, the deviations of attenuation are approximately at their highest, and vice versa. This phenomenon may be interpreted that the mutual impedances between the two slits are almost linearly related to the distance between the slits and curve helically on the impedance plane.

VI. Single Guide Excitation

There exist two modes in this structure, the in-phase and the out-of-phase modes mentioned in Sections II and III, respectively, which do not couple with each other because of the symmetry of the structure. An arbitrary excitation of the two guides, therefore, may be expressed by appropriately superposing the two modes mentioned above. In general, both forward and backward waves may exist. In the single guide excitation considered here, only the forward waves associated with the two modes are assumed to be present. Upon representing the in-phase and out-of-phase modes as

$$\begin{pmatrix}1\\1\end{pmatrix} \text{ and } \begin{pmatrix}1\\-1\end{pmatrix},$$

respectively, we have

$$\frac{1}{2}\begin{pmatrix}1\\1\end{pmatrix}+\frac{1}{2}\begin{pmatrix}1\\-1\end{pmatrix}=\begin{pmatrix}1\\0\end{pmatrix} \tag{26}$$

at the excitation point, $z=0$. If the in-phase and out-of-phase waves in the z direction are

$$e^{-jk_z^{(i)}z} \text{ and } e^{-jk_z^{(o)}z},$$

respectively, then at a further point we have

$$\frac{1}{2}\begin{pmatrix}e^{-jk_z^{(i)}z}\\e^{-jk_z^{(i)}z}\end{pmatrix}+\frac{1}{2}\begin{pmatrix}e^{-jk_z^{(o)}z}\\-e^{-jk_z^{(o)}z}\end{pmatrix}$$

$$=\frac{1}{2}\begin{pmatrix}e^{-jk_z^{(i)}z}+e^{-jk_z^{(o)}z}\\e^{-jk_z^{(i)}z}-e^{-jk_z^{(o)}z}\end{pmatrix}. \tag{27}$$

By putting

$$k_z^{(i)} = \alpha_i - j\beta_i, \qquad k_z^{(o)} = \alpha_0 - j\beta_0,$$

the right hand side of (27) can be written as

$$\begin{pmatrix} C_1 & e^{j\Phi_1} \\ C_2 & e^{j\Phi_2} \end{pmatrix}, \tag{28}$$

where

$$\left.\begin{aligned} C_1 &= \frac{1}{2}\left\{e^{-2\alpha_i z} + e^{-2\alpha_0 z} + 2e^{-(\alpha_i+\alpha_o)z}\cos(\beta_i - \beta_0)z\right\}^{1/2}, \\ C_2 &= \frac{1}{2}\left\{e^{-2\alpha_i z} + e^{-2\alpha_o z} - 2e^{-(\alpha_i+\alpha_o)z}\cos(\beta_i - \beta_0)z\right\}^{1/2}, \end{aligned}\right\} \tag{29}$$

$$\left.\begin{aligned} \Phi_1 &= \tan^{-1}\left(-\frac{e^{-\alpha_i z}\sin\beta_i z + e^{-\alpha_o z}\sin\beta_0 z}{e^{-\alpha_i z}\cos\beta_i z + e^{-\alpha_o z}\cos\beta_0 z}\right), \\ \Phi_2 &= \tan^{-1}\left(-\frac{e^{-\alpha_i z}\sin\beta_i z - e^{-\alpha_o z}\sin\beta_0 z}{e^{-\alpha_i z}\cos\beta_i z - e^{-\alpha_o z}\cos\beta_0 z}\right). \end{aligned}\right\} \tag{29a}$$

C_1 in (28) represents the amplitude along the guide originally excited, and will be discussed below in connection with the typical example described in Section V.

From Section IV we can write

$$\left.\begin{aligned} \beta_i - \beta_0 &= \frac{\lambda_{go}}{2a^2}\left\{X_i'(\kappa_0) - X_0'(\kappa_0)\right\}, \\ \alpha_{io} &= \frac{\lambda_{go}}{2a^2}R_{io}'(\kappa_0), \end{aligned}\right\} \tag{30}$$

where $\kappa_0 = \pi/a$, α_{io} represents α_i or α_o, as well as for R_{io}', X_i' and X_o' are X' and R' defined in (23) for the in-phase and out-of-phase waves, respectively, and also for R_i' and R_o'. Since the results in Section V show us that

$$B' \gg G'$$

and

$$B_i' \simeq B_0' \equiv B', \text{ but } B_i' - B_o' \simeq -\kappa_0 b N_0(\kappa_0 l),$$

(30) is led to

$$\left.\begin{aligned} \beta_i - \beta_0 &\simeq \frac{\lambda_{go}}{2a^2}\cdot\frac{B_i'^2 - B_o'^2}{B'^2}, \\ \alpha_{io} &\simeq \frac{\lambda_{go}}{2a^2}\cdot\frac{G_{io}'}{B'^2} \end{aligned}\right\}. \tag{31}$$

Substituting (13) and (20) into (31), we have

$$\left.\begin{aligned} \beta_i - \beta_0 &\simeq \frac{\lambda_{go}}{2a^2}\cdot\frac{\kappa_0 b(-N_0(\kappa l))}{B'^2}, \\ \alpha_{io} &\simeq \frac{\lambda_{go}}{2a^2}\cdot\frac{\frac{\kappa_0 b}{2}\left\{1 \pm J_0(\kappa_0 l)\right\}}{B'^2}, \end{aligned}\right\} \tag{32}$$

and

$$\frac{\beta_i - \beta_0}{\alpha_{io}} \simeq \frac{2\kappa_0 b\left\{-N_0(\kappa_0)l\right\}}{\left\{1 \pm J_0(\kappa l)\right\}}. \tag{33}$$

Since

$$(\beta_i - \beta_0)a = \frac{\pi}{\frac{\lambda}{2a}}\left(\frac{\lambda}{\lambda_{gi}} - \frac{\lambda}{\lambda_{go}}\right),$$

the numerical values in (33) can be found approximately from the curves in Fig. 4.

In the vicinity of the roots of $N_0(\kappa_0 l)$, which correspond to the intersections of the curves of Fig. 4, we have

$$\alpha_{i_0} \gg |\beta_i - \beta_o| \simeq 0. \tag{34}$$

This means that the terms $\cos(\beta_i - \beta_0)z$ in 29 do not exert a significant effect on $|C_1|$ and $|C_2|$. In other words, the amplitudes $|C_1|$ and $|C_2|$ may decay to insignificant values before the term $\cos(\beta_i - \beta_0)z$ needs to be taken into account. Then we can approximate these expressions by

$$\left.\begin{aligned} C_1 &\simeq \tfrac{1}{2}(e^{-\alpha_i z} + e^{-\alpha_o z}), \\ C_2 &\simeq \tfrac{1}{2}(e^{-\alpha_i z} - e^{-\alpha_o z}), \end{aligned}\right\} \tag{35}$$

and, from 32,

$$\left.\begin{aligned} |C_1| &\simeq |e^{-\alpha' z}\cosh\alpha'' z|, \\ |C_2| &\simeq |e^{-\alpha' z}\sinh\alpha'' z|, \end{aligned}\right\} \tag{36}$$

where

$$\left.\begin{aligned} \alpha' &= \frac{1}{2}(\alpha_i + \alpha_o) \simeq \frac{\lambda_{go}}{2a^2}\frac{\frac{\kappa_0 b}{2}}{B'^2}, \\ \alpha'' &= \frac{1}{2}(\alpha_i - \alpha_o) \simeq \frac{\lambda_{go}}{2a^2}\frac{\frac{\kappa_0 b}{2}J_0(\kappa_0 l)}{B'^2} \simeq \alpha' J_0(\kappa_0 l), \\ \kappa_0 &= \frac{\pi}{a}. \end{aligned}\right\} \tag{37}$$

It can be seen from (25) and (37) that α' is very nearly equal to the attenuation constant in the uncoupled waveguide (isolated waveguide). The phase difference between waves 1 and 2 is about π or 0 when $\alpha_i > \alpha_o$ or $\alpha_i < \alpha_o$, respectively, as is clear from (35), since $\Phi_1 \simeq \Phi_2$, in this case $(\beta_i \simeq \beta_0)$.

Far along the slit, *i.e.*, when $\alpha' z \gg 1$, we can obgain the following expression from (29):

$$\left.\begin{aligned} |C_{1_2}| &= \left|\tfrac{1}{2}e^{-\alpha_o z}\left\{1 + e^{-2(\alpha_i - \alpha_o)z} \pm 2e^{-(\alpha_i - \alpha_o)z}\cos(\beta_i - \beta_0)z\right\}^{1/2}\right| \\ &\simeq \tfrac{1}{2}e^{-\alpha_o z}, \qquad (\alpha_i - \alpha_o)z \gg 1. \end{aligned}\right\} \tag{38}$$

In the same way,

$$|C_{1_2}| \simeq \tfrac{1}{2}e^{-\alpha_i z}, \qquad (\alpha_o - \alpha_i)z \gg 1.$$

Eq. (38) coincides with that which is derived from (36) as $\alpha'' z \to \infty$.

In the vicinity of the roots of $J_0(\kappa_0 l)$, which correspond to the intersections in the αa curves in Fig. 4, we can write

$$\left.\begin{aligned} |C_1| &\simeq e^{-\alpha' z}\left|\cos \tfrac{1}{2}(\beta_i - \beta_0)z\right|, \\ |C_2| &\simeq e^{-\alpha' z}\left|\sin \tfrac{1}{2}(\beta_i - \beta_0)z\right|, \end{aligned}\right\} \tag{39}$$

because $\alpha_i \simeq \alpha_o$ in that region. We recall that α' is defined in (37), and

$$\frac{1}{2}|\beta_i - \beta_0| \simeq \frac{\lambda_{go}}{2a^2}\,\frac{\dfrac{\kappa_0 b}{2}\,|N_0(\kappa_0 l)|}{B'^2} = \alpha' |N_0(\kappa_0 l)|\,. \tag{40}$$

The above expression can be shown to be exact when $\alpha_i = \alpha_o$ and when $\alpha' z \gg 1$.

The amplitude in each waveguide is given by (36) and (39). Curves of these amplitudes vs distance along the slit are shown as an example in Fig. 5. The same dimensions as in Section IV or Fig. 4 have been chosen. The value of the amplitudes is normalized so that the amplitude excited initially is unity, as seen in (36) and (39). The distance is also normalized by multiplying the actual distance by l/a. In this figure, three cases are shown: the uncoupled waveguide case is indicated by the solid line, the case of coupled waveguides with $l/b = 1$ by the dashed line, and that for coupled waveguides with $l/b = 2$ by the dotted line. The last two cases are examples which we are able to calculate by means of (36) and (39), respectively. For large values of z, the amplitudes $|C_1|$ and $|C_2|$ may coincide with each other except when $\alpha_i = \alpha_o$, as understood from the derivation of (38). In the case $\alpha_i = \alpha_o$, the amplitudes $|C_1|$ and $|C_2|$ cannot have the same value but must be related, as seen in (39).

The curves with $l/b = 1$ and 2 have been shown as special cases which are expressed by (36) and (39), respectively, as mentioned above. In other cases, it can be seen by referring to Fig. 4 that all curves of $|C_1|$ or $|C_2|$ with l/b of between 1 and 2 lie in the region between the dashed and the dotted lines (see Fig. 5) of $|C_1|$ or $|C_2|$ with $l/b_1 = 1$ and 2, respectively.

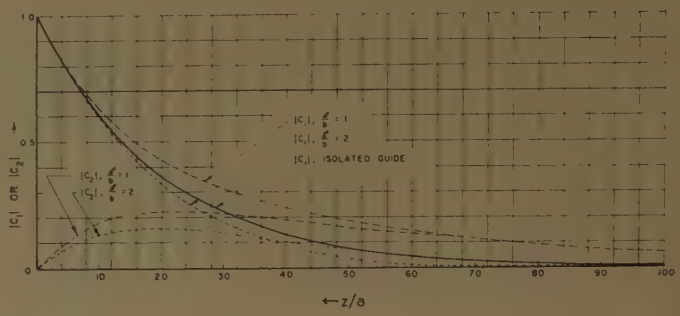

Fig. 5—Wave amplitudes in each of the leaky waveguides vs distance along the guide when only one guide is excited and the second acts as a parasite. ($a = 0.9$ inch, $b = 0.4$ inch, $d = 0.01$ inch, $\lambda/2a = 0.7$, $\lambda = 1.26$ inches.)

It is seen from Fig. 5 that the power coupled into the neighboring guide, which acts as a parasitic guide, can actually be greater than that in the guide initially excited (case for which $l/b = 2$, for $z/a > 40$, approximately), or can be greater than that present in an isolated guide (case for which $l/b = 1$, for $z/a > 30$). While these extreme situations occur only for very large distances along the slit, considerable power is coupled into the parasitic guide even for moderate distances ($z/a > 10$).

Acknowledgment

The author wishes to express his gratitude to Prof. A. A. Oliner for his kind direction. The author also thanks the staff members of the Electrophysics Group of MRI for their encouragement.

Experimental Study of a Diffraction Reflector*

J. H. PROVENCHER†

Summary—**A microwave antenna has been designed and constructed on the principles of parageometric optics formulated by Toraldo di Francia and on principles similar to those of Fresnel rings and the diffraction grating. Its surfaces are all zones of cones and are simple to construct.**

The chosen design parameters were incorporated in two *K*-band ($\lambda=1.24$ cm, $\lambda=1.22$ cm) models. Experimental results show good agreement with theory. Scanning characteristics are superior to those of the paraboloidal or spherical reflector, and spherical aberration and coma are minimized, and the effects of astigmatism are minimized by using a "compromise focus."

I. Introduction

A REFLECTOR recently devised by L. Ronchi and G. Toraldo di Francia[1] of the Centro Microonde, Florence, Italy, is based on the principles of diffraction as well as on the principles of reflection. Unlike conventional reflectors fed by a point source, which almost invariably require doubly curved surfaces, the diffraction reflector uses only conical surfaces and can therefore be constructed from flexible flat sheets. Scanning is accomplished by lateral motion of a point source feed in the focal region.

Theoretical analysis of this reflector indicates that it should have wide-angle scanning capabilities. If imbedded in the earth, it would have a firm support, a low silhouette, and low susceptibility to wind damage. To investigate the practicality and performance of the Ronchi-Toraldo di Francia type of diffraction reflector, a microwave model was designed, constructed, and experimentally tested to verify the theoretical analyses and predictions.

II. Theory of the Diffraction Reflector

For proper design the diffraction (or zoned) reflector must meet two conditions: 1) each zone must individually focus incoming parallel rays to a common focal point, and 2) the contributions from all zones must arrive at the focal point in phase. Because the zoned reflector is a surface of revolution its design can be entirely developed in just two dimensions by working in a single axial cross section plane. Once conditions 1) and 2) are satisfied in a single axial cross section plane, they will, except for polarization effects, be satisfied in all axial cross section planes.

Let Σ be an arc of a circle of radius R with center at C, intersecting the negative x axis at P [see Fig. 1(a)]. Let P_n be a point on Σ other than P and let M_n be the projection of P_n on the x axis. The line segment L_n passes through P_n collinearly with the line segment PP_n.

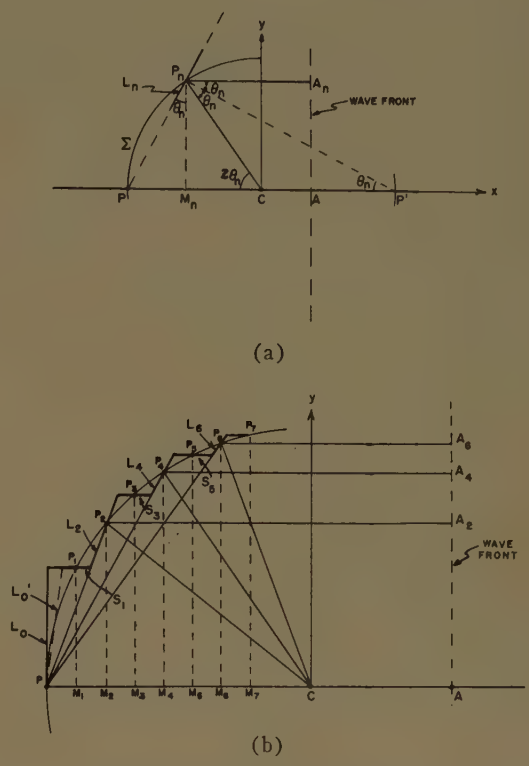

Fig. 1—Coordinate system and determination of optical path difference between two rays.

Consider now an incoming ray A_nP_n reflected by L_n at P_n. The construction of Fig. 1(a) verifies that this ray will be reflected through the point C. Since $A_nP_n=AM_n$ and $P_nC=PC$, it is clear that the path difference along the two ray paths A_nP_nC and $-APC$ is precisely equal to PM_n. Hence, if $PM_n=m\lambda$, $m=1, 2, 3, \cdots$, the rays will be in phase at C.

In Fig. 1(b) the points M_1, M_2, M_3, $\cdots$, are chosen so that $PM_1=M_1M_2=M_2M_3=\cdots=\lambda/2$. The construction of the line segments L_0, L_2, L_4, L_6, $\cdots$, guarantees that the rays AP, A_2P_2, A_4P_4, $\cdots$, are all reflected through the point C and thus condition 1) will be approximately satisfied. Over the zone determined by the line segment L_0, condition 1) would be satisfied to a high degree of approximation if L_0 were replaced by an appropriate arc of a circle of radius 2R with center on the x axis. Significant improvement can, however, be obtained by approximating the circular arc by a straight line, that is, by L_0' as shown in Fig. 1(b).

Since by construction, $PM_2=\lambda$, $PM_4=2\lambda$, $PM_6=3\lambda$, $\cdots$, the rays APC, A_2P_2C, A_4P_4C, $\cdots$, will all be in phase at C. Condition 2) will therefore be satisfied to within a good approximation if the line segments L_0,

* Manuscript received by the PGAP, September 8, 1959.
† U. S. Navy Electronics Laboratory, San Diego, Calif.
[1] L. Ronchi and G. Toraldo Di Francia, "An application of parageometrical optics to the design of a microwave mirror," IRE Trans. on Antennas and Propagation, vol. AP-6, pp. 129–133; January, 1958.

$L_2, L_4, \cdots$, are not too long. It is evident that for this focusing system the focal point is C, and the focal length F is precisely equal to R, the radius of Σ.

Given a desired frequency and beamwidth (or aperture dimension), the focal length (or radius of curvature of Σ) will be determined by the angle-of-scan requirement. Once the frequency, aperture dimension, and focal length are fixed, the reflector design is fixed according to the construction of Fig. 2. The ordinates of the points P_n (Fig. 2) are given by the formula

$$y_n = F \sin 2\theta_n,$$

where

$$\theta_n = 1/2 \cos^{-1} 1 - \frac{n\lambda}{2F}, \tag{1}$$

and λ is the wavelength. θ_n for $n=0, 2, 4, \cdots$, is the complement of the slant angle of L_n, $n=0, 2, 4, \cdots$, (Fig. 2).

Eq. (1) may be written

$$\frac{y_n}{\sin 2\theta_n} = F = \text{constant},$$

which is a form of the sine condition when the reflector is used with parallel incident or emergent rays.[2] The lengths of the line segments S_n [Figs. 1(b) and 2] are the step depths of the reflector and are given by the formula

$$|S_n| = y_n(\tan \theta_{n+1} - \tan \theta_{n-1}), \quad n = 1, 2, 3, \cdots. \tag{2}$$

The surface of the three-dimensional zoned reflector is obtained by rotating the broken line composed of the line segments $L_0', S_1, L_2, S_3, L_4, \cdots$, about the x axis [Fig. 2(b)]. The line segments $L_0', L_2, L_4, \cdots$, generate portions of coaxial right circular cones with common vertex P, and the line segments $S_1, S_3, S_i, \cdots$, generate portions of coaxial right circular cylinders.

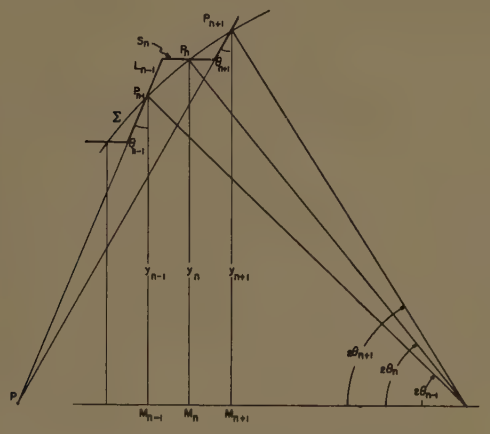

Fig. 2—Determination of zones and step depths.

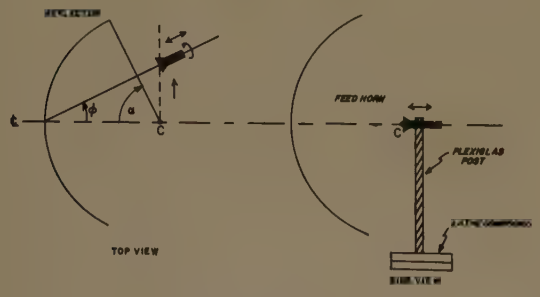

Fig. 3—Setup showing method of scanning.

III. Aberrations

The zoned reflector is a form of stepped spherical surface that is well corrected for spherical aberration and offense against the sine condition.

It can be shown that both sagittal and tangential coma are independent of the first power of the sine of the semiscan angle. Third-order sagittal coma is given by the expression[1]

$$C_s = -\frac{R}{2} \sin^3 \Omega(1 - \cos \alpha), \tag{3}$$

where R is the radius of curvature, Ω is the semiscan angle, and α is the aperture angle (Fig. 3). The expression vanishes when the sine condition is satisfied.

This reflector design does not correct for chromatic aberration, whose value may be found by the relation

$$df = R\frac{d\lambda}{\lambda}, \tag{4}$$

where df is the elemental change in focal length due to an elemental change in wavelength $d\lambda$, λ is the wavelength, and R is the radius of curvature.

The loci of the sagittal and tangential foci can be found from expressions derived by Ronchi and Toraldo di Francia.[1] (A plot of these curves is given in Fig. 9 for a reflector with a 12-inch radius of curvature. The radius of curvature for these curves at F turns out to be R in both cases.)

IV. Construction

From computations carried out and graphed (Fig. 4)

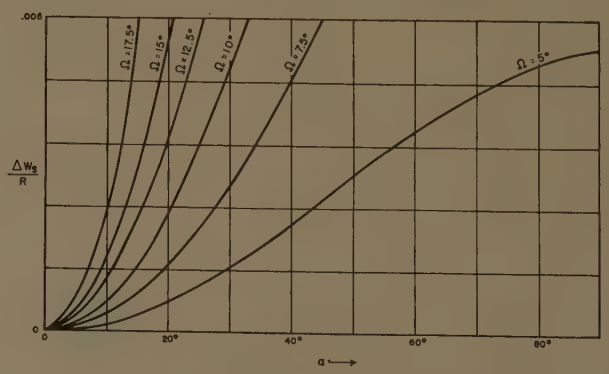

Fig. 4—Total excursion of the wave aberration plotted against α for different values of Ω.

[2] F. A. Jenkins and H. E. White, "Fundamentals of Physical Optics," 2nd Ed., McGraw-Hill Book Co., Inc., New York, N. Y.: 1950.

by Ronchi and Toraldo di Francia, an aperture angle of 30° and a scan angle of ±10° were chosen. The radius of curvature and aberration tolerance were determined from these choices. K band (24.55 kmc) was selected as the design frequency. From the graph the ratio of wave excursion, ΔW_s, to R was selected as 0.005, and with ΔW_s as $\lambda/8$, yielded

$$R = \frac{\Delta W_s}{0.005} = 30.5 \text{ cm.} \tag{5}$$

From the sagittal formula and the derived formulas (1) and (2), a 16-inch reflector at K band was designed and constructed. The reflector was fed with a flared horn supported by a plexiglass rod mounted on a lathe compound. Scanning was accomplished by means of the lathe compound, which allowed lateral, longitudinal, and rotary movements of the feed in the focal planes (Fig. 3). Movements of 0.025-inch increments were possible in either direction, the total possible lateral movement being 10 inches across one-half of the face of the reflector.

Movements in 0.250-inch increments were made across the face of the reflector, followed by movements in 0.025-inch increments along a line at an angle ϕ to the reflector axis (Fig. 3). As the feed was moved off-axis the horn was rotated so that it was always aligned with the vertex of the reflector (Fig. 3). In this way the loci of the sagittal, tangential, and compromise foci were obtained.

Although the first system was designed for 24.55 kmc, all of the tests were made at 24.05 kmc, which was more readily available at that time. To check the results obtained with the first model, a second reflector was designed, also at K band (24.05 kmc), with $R = 30.5$ cm. This reflector had an 18-inch aperture and required two more zones than the 16-inch reflector. The same general pattern for testing was used.

V. Experimental Results

The object of the experiment was twofold: 1) to investigate the properties of the reflector for possible use in radioastronomy, and 2) to attempt to verify the Ronchi-Toraldo di Francia theory by experiment.

The first phase of the experiment consisted in taking radiation patterns for various off-axis feed positions. With the feed on the compromise focus curve, the pattern was symmetric when scanned up to about ±17.5° (approximately 10 beamwidths) off-axis, and had a half-power beamwidth of 1.8°. The sidelobes remained well under 15 db over this range, and no noticeable broadening of the beam was observed (Fig. 5). The gain over this range remained within 2 db of its level on-axis. At K band the measured gain of the 16-inch reflector was 35 db, that of the 18-inch reflector was 36 db.

A comparison of radiation patterns of a 16-inch parabolic reflector, a 15-inch Mangin mirror,[3] and the 16-inch diffraction reflector is shown in Fig. 6. The same feed horn was used in all cases. Table I (next page) compares these reflectors at various scan angles. With respect to both theoretical and experimental data, the beamwidths of the diffraction reflector are narrower than those of the other systems.

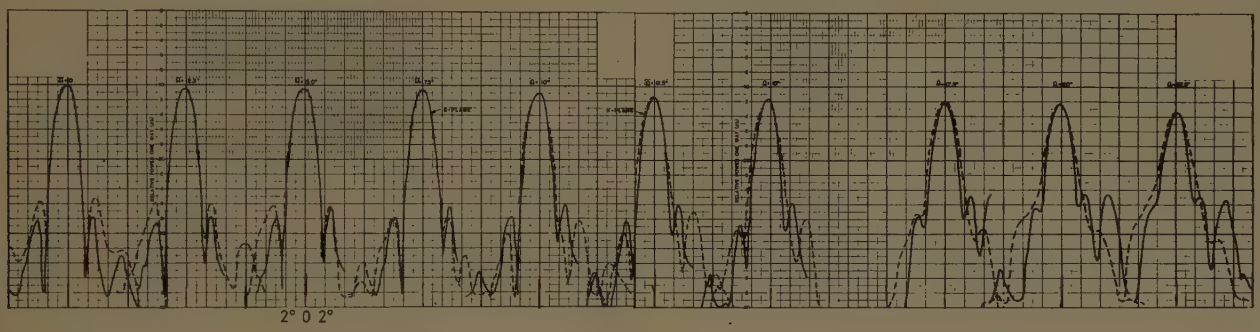

Fig. 5—Patterns along compromise focus of diffraction reflector system.

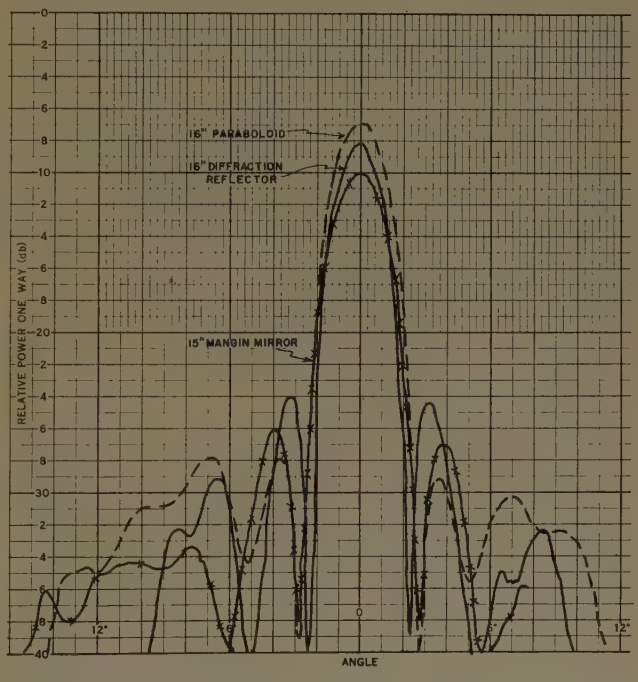

Fig. 6—Comparison of gain and beamwidth: 16-inch paraboloidal reflector, 16-inch diffraction reflector, and 15-inch Mangin mirror system.

[3] R. C. Gunter, F. S. Holt, and C. F. Winter, "The Mangin Mirror," AFCRC Tech. Rept. No. TR-54-161, AF Cambridge Res. Center, Bedford, Mass.; April, 1955.

TABLE I

COMPARISON OF BEAMWIDTH AND SIDELOBE LEVEL OF SCANNING SYSTEMS

Diffraction Reflector—18 inches $\lambda=1.246$ cm							
$R=12$ inches $=F$							
Scan Angle		0	5	12	14	18.5	30
Half-Power	T*	1.8	1.8	1.8	1.8	1.8	1.9
Beamwidth	S*	1.8	1.8	1.8	1.8	1.8	1.9
Sidelobe	T	16	16	17	16	13.5	10.5
Level (-db)	S	18	18	18	17	17	15
Diffraction Reflector—18 inches $\lambda=1.246$ cm (Compromise Focus)							
$R=12$ inches							
Scan Angle		0	5	12	14	18.5	
Half-Power	T	1.8	1.8	1.8	1.9	1.9	
Beamwidth	S	1.8	1.8	1.8	1.9	1.9	
Sidelobe	T	16	16	16	16	14	
Level (-db)	S	18	18	16.5	14	14	
Spherical Mirror—15 inches $\lambda=0.856$ cm							
$R=11.5$ inches							
Scan Angle							
Half-Power	T	2.0	2.1	2.0	2.2	2.5	
Beamwidth	S	2.1	2.3	2.3	2.4	2.4	
Sidelobe	T	12.5	12.0	11.5	10.0	9.0	
Level (-db)	S	17.5	17.5	18.0	19.0	19.5	
Mangin Mirror—15 inches $\lambda=0.856$ cm (Compromise Focus)							
$R=11.5$ inches, $R_1=7.75$ inches							
Scan Angle		0	2.75	6	12.25	18.75	
Half-Power	T	1.7	1.7	1.8	1.9	2.0	
Beamwidth	S	1.8	1.8	1.9	2.1	3.0	
Sidelobe	T	17.5	14.5	15.0	15.0	10.5	
Level (-db)	S	21.5	20.5	20.0	17.5	11.5	
Diffraction Reflector—16 inches $\lambda=0.856$ cm (Compromise Focus)							
$R=12$ inches $=F$							
Scan Angle		0	2.5	5	7		
Half-Power	T	1.4	1.4	1.5	1.5		
Beamwidth	S	1.6	1.5	1.5	1.5		
Sidelobe	T	16	15	14.5	14.5		
Level (-db)	S	25	24	22.0	20.0		

* S = Sagittal, T = Tangential. All angles in degrees, all beamwidths in degrees.

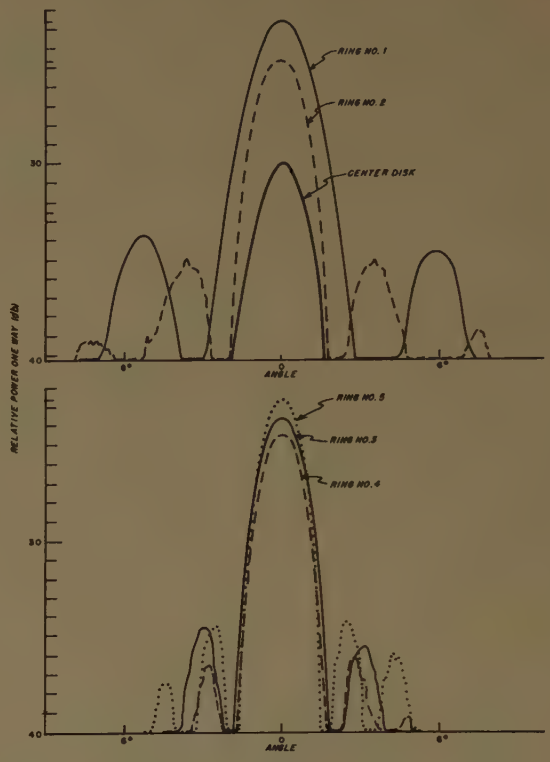

Fig. 7—Contribution of individual rings, diffraction reflector no. 1.

The contributions of individual rings (zones) were investigated by covering the entire reflector with absorbing material and successively exposing separate rings. The radiation pattern of any one ring was similar in shape and showed about the same gain (Fig. 7) as any other ring.

In many respects, the second phase of the experiment confirmed the theoretical design of the reflector. The focal length at the design frequency turned out to be R empirically, as predicted by theory. Chromatic aberration effects were observed in the region of the design frequency, as predicted by (4). In tests of the first reflector at 24.05 kmc ($\lambda=1.247$ cm), the distance to the horn aperture on-axis measured 12.25 inches. The design radius (focal length) of this reflector was 12 inches, but this was at a design frequency of 24.55 kmc ($\lambda=1.222$ cm). Applying (4) with $R=12$ inches, $\lambda=1.247$ cm, and $d\lambda=0.025$ cm, leads to a predicted shift in focal length of 0.24 inch, which agrees well with the measured value. Tests made on the second reflector showed a focal length equal to R at the design frequency.

Incremental increases in the wavelength lengthen the focal length, and incremental decreases shorten the focal length. It was found, however, that (4) is not valid for large wavelength increments. A relatively large shift of focal point was observed when K_a band (34.95 kmc) was used in the tests. By (4), a change of 0.363 cm in wavelength should produce a change of 3.57 inches in the focal length. At this wavelength (0.858 cm) the reflector focused at about $0.77R$ and not at $0.7R$ as predicted by theory. The ratio of the two wavelengths is 0.7, and hence, not a full multiple of the design wavelength. The possibility of other foci at even wavelength multiples was not investigated, owing to the unavailability of the required transmitting tubes. The physical size of the reflector itself limited the use of the lower frequency bands available. The E plane patterns at K_a band at best focus (Fig. 8) were more desirable than those at K band (the design frequency) at the design focus.

The well-focused patterns obtained on-axis in both planes verify the theoretical prediction of very low spherical aberration and on-axis astigmatism. The symmetry of the patterns as the beam was scanned through $\pm 17.5°$ is in agreement with the predicted low comatic aberration. Exceptionally good agreement between the feed loci for best azimuth and elevation patterns as determined experimentally and the traces of the tangential and sagittal surfaces as predicted by theory[1] is seen in Fig. 9. It is clear from this figure that the astigmatism is zero on-axis but increases with lateral feed displacement. It is primarily this growth in astigmatism with off-axis feed displacement that limits the practical scanning

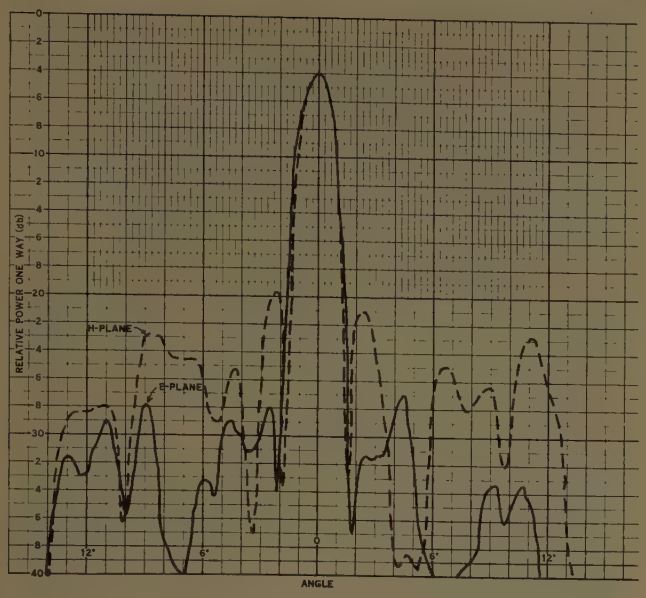

Fig. 8—Radiation patterns at best focus.

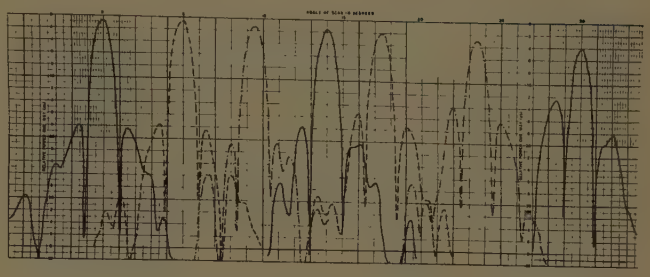

Fig. 10—Patterns along best tangential focal locus of diffraction reflector system.

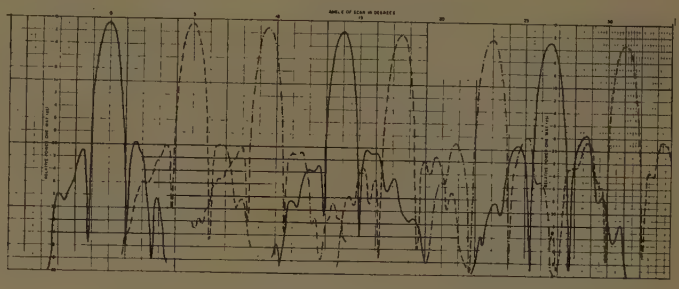

Fig. 11—Patterns along best sagittal focus locus of diffraction reflector systems.

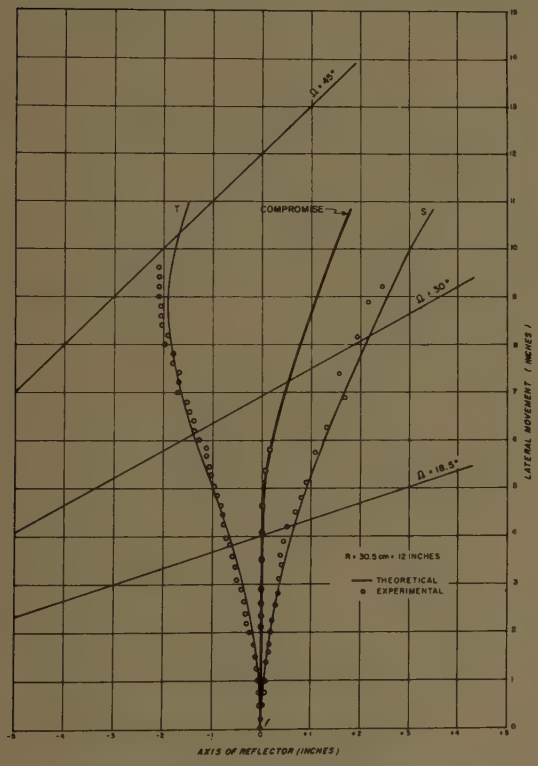

Fig. 9—Theoretical and experimental plot of sagittal and tangential foci.

capability of the diffraction reflector. Also shown in Fig. 9 is an experimental compromise best-focus curve where the effects of astigmatism are minimized. This curve follows the zero line (Gaussian focal plane) to nearly 20° off-axis and then appears to turn away from the reflector as predicted by theory. Beyond 20° the patterns deteriorate rapidly and it is difficult to use lobe level and beamwidth criteria for picking the compromise. Figs. 10 and 11 show the radiation patterns at various scan angles for the sagittal and tangential foci.

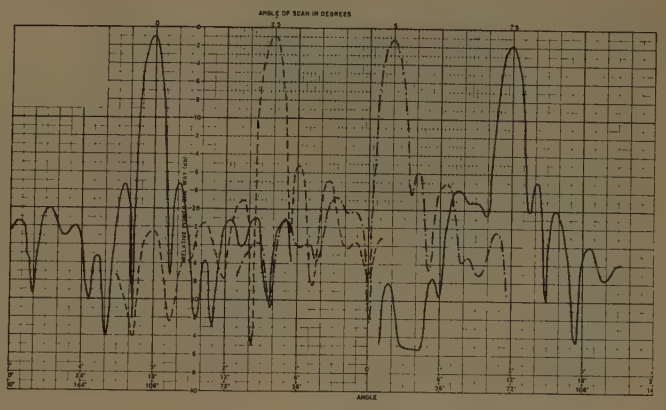

(a)

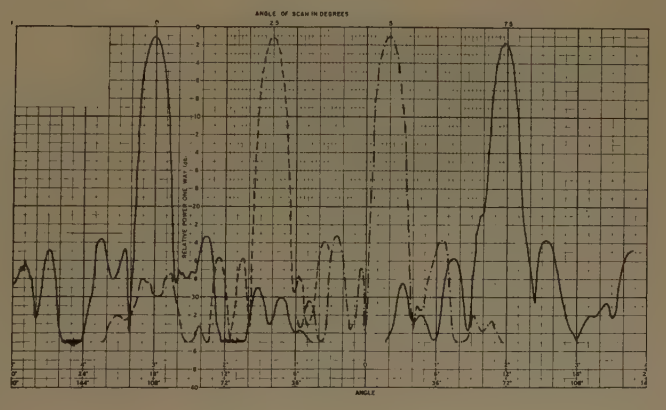

(b)

Fig. 12—(a) Patterns along best tangential focal locus of diffraction reflector system. (b) Patterns along best tangential sagittal focal locus of diffraction reflector system.

Patterns taken along the best tangential focal locus and along the best sagittal focal locus at K_a band were similar to corresponding patterns at K band. Figs. 12(a) and 12(b) show these patterns to $\pm 7°$ scan.

The maximum useful field that can be covered with this particular reflector is $\pm 17.5°$, which is in good agreement with the scan angle chosen for design. The best over-all use of this reflector is made when the feed is placed at the "compromise focus." At this position the system maintains a symmetric beam while being scanned $\pm 17.5°$ in either plane.

VI. Conclusions

The zoned reflector based on diffraction principles and using conical surfaces has been shown to agree with the theoretical predictions of its properties and performance. The principal aberrations present in conventional paraboloidal and spherical reflectors have been greatly minimized in this design. Astigmatism is present but its effects can be reduced by a "compromise focus." The shift of focal point which was noted as the frequency was changed is an effect of chromatic aberration, predicted by theory and verified by experiment.

The system tested could scan a maximum of $\pm 17.5°$ with no appreciable broadening of the beam, with sidelobe level well under 15 db and gain remaining within 2 db of its on-axis level.

Larger diffraction reflectors of the type shown in Fig. 13 are now being constructed at the Air Force Cambridge Research Center, and work on movable feed systems is anticipated.

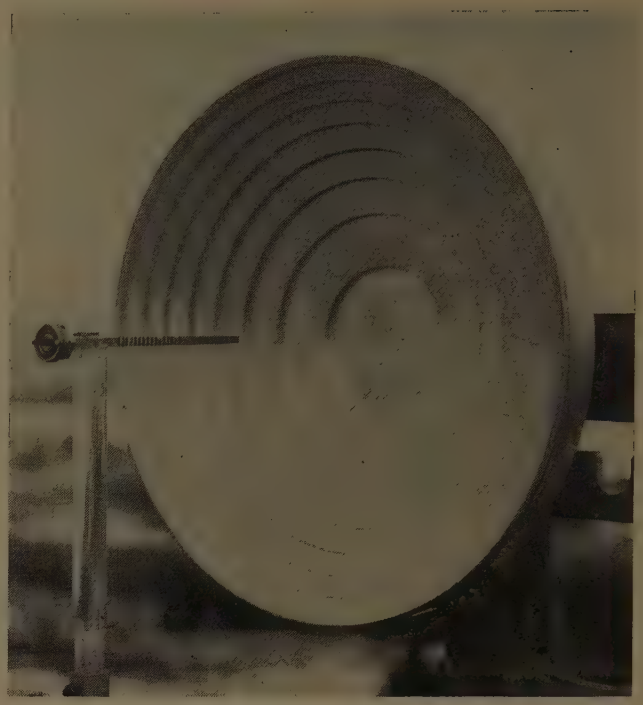

Fig. 13—Diffraction reflector with feed.

VII. Acknowledgment

The author is indebted to his associates at the Air Force Cambridge Research Center Antenna Test Station at Ipswich, Mass., for their cooperation in carrying out the experimental studies of the reflector. He also wishes to thank Dr. F. Sheppard Holt of the Air Force Cambridge Research Center for his suggestions on the writing of the report.

communications

A Note on the Relation Between the "Exact" and "Simplified" Theories for EM Wave Propagation in Ionized Gases*

JOHN M. ANDERSON†

RECENTLY Sisco and Fiskin[1] have discussed the accuracy of a simplified formulation of the conductivity of an ionized gas as compared with a more exact theory. They find a factor of error in the real components of the conductivities of ≈ 0.82. It is the purpose of this note to point up that this error may be eliminated by a proper definition of the average electron collision frequency.

A simple, convenient expression for electrical conductivity of a gaseous medium containing free electrons, developed from the differential equation of motion of an *average* electron, has been much used:

$$\sigma = \sigma_{\text{real}} + i\sigma_{\text{imag}} = \frac{n_e e^2}{m}\left[\frac{\nu - i\omega}{\omega^2 + \nu^2}\right], \tag{1}$$

where n_e is the electron number density, e and m are the electronic charge and mass, respectively, ν is the electron collision frequency with heavier constituents of the gas, and ω is the angular frequency of the applied sinusoidal wave. A more exact expression, developed by Margenau[2] and Ginsburg,[3] is (Maxwellian distribution of electron velocities)

$$\sigma = \frac{8}{3\sqrt{\pi}}\frac{n_e e^2}{m}\left[\int_0^\infty \frac{\nu(u)u^4 \exp(-u^2)du}{\omega^2 + \nu^2(u)} - i\omega\int_0^\infty \frac{u^4 \exp(-u^2)du}{\omega^2 + \nu^2(u)}\right] \tag{2}$$

where

$$u = \left(\frac{m}{2kT_e}\right)^{1/2} v,$$

v is the electron velocity, k is the Boltzmann constant and T_e is the temperature of the gas of electrons.

Assuming initially that $\nu^2 \ll \omega^2$, the real terms of (1) and (2) may be equated and it is determined that a *desired* definition of average electron collision frequency $\bar{\nu}$ evolves as

$$\bar{\nu} = \frac{8}{3\sqrt{\pi}}\int_0^\infty \nu(u)u^4 \exp(-u^2)du. \tag{3}$$

* Manuscript received by the PGAP, December 14, 1959.
† General Electric Res. Lab., Schenectady, N. Y.

[1] W. B. Sisco and J. M. Fiskin, "Effects of relatively strong fields on the propagation of EM waves through a hypersonically produced plasma," IRE TRANS. ON ANTENNAS AND PROPAGATION, vol. AP-7, pp. 240–244; July, 1959.

[2] H. Margenau, "Conduction and dispersion of ionized gases at high frequencies," *Phys. Rev.*, vol. 69, pp. 508–513; May, 1946.

[3] V. L. Ginsburg, "On the absorption of radio waves and the number of collisions in the ionosphere," *J. Phys. (USSR)*, vol. 8, pp. 253–256; April, 1944.

The collision frequency $\nu(u)$ is related to the probability P_m of momentum transfer collisions between electrons and gas molecules,

$$\nu(v) = p_0 P_m v, \tag{4}$$

where p_0 is the gas pressure normalized to 0°C and *1* mm Hg. It follows from the assumptions made by Sisco and Fiskin that P_m is a constant, equal to the reciprocal of the electronic mean free path λ in the gas. If P_m varies with electron energy, as it does in almost every real experimental situation, a power series,

$$P_m = \sum_n a_n v^n, \tag{5}$$

may approximate P_m and (3) may be readily integrated. However, for constant P_m,

$$\bar{\nu} = \frac{4}{3} p_0 P_m \left(\frac{8}{\pi m}\right)^{1/2} (kT_e)^{1/2}. \tag{6}$$

Frequently the density of gaseous ions may be sufficiently high that significant momentum transfer is effected by electron-ion collisions. For this case it has been shown[3,4] that an approximate collision frequency follows from the equating of (1) and (2),

$$\bar{\nu} = A \frac{n_i}{T_e^{3/2}} \ln\left[\frac{BT_e}{n_i^{1/2}}\left(\frac{2T_eT_i}{T_e + T_i}\right)^{1/2}\right], \tag{7}$$

where n_i is the density of ions, and T_i is their temperature. The constants A and B have been found experimentally[4] to be 3.6 and 3.7×10^3, respectively. A total collision frequency for use in (1) must therefore be a sum, in the first approximation, of the two types of collisions expressed in (6) and (7).

A consideration of the low frequency or dc situation $\nu^2 \gg \omega^2$ would follow in analogy to the above. This gives a slightly different result than (6), namely,

$$\bar{\nu} = \frac{3\pi}{8} p_0 P_m \left(\frac{8}{\pi m}\right)^{1/2} (kT_e)^{1/2}. \tag{8}$$

Caution must be exercised in the use of (8) since for those cases where the electric field strength forces a rise in mean electron energy appreciably above that of the gas, a Maxwellian distribution most probably no longer exists.

In the above the electron temperature may be an elevated value in the presence of the electromagnetic wave. The extent of a variation of T_e may be calculated by the method of Margenau, as outlined by Sisco and Fiskin, or may be calculated by the method employed in a description of the phenomenon of ionospheric cross-modulation, as outlined by Anderson and Goldstein.[4,5]

Quite incidentally, it should be pointed out that the factor B_2 should replace the factor B_1 in (20) of Sisco and Fiskin's article, and also in their (26) the factor 2 should replace the factor π.

[4] J. M. Anderson and L. Goldstein, "Interaction of electromagnetic waves of radio frequency in isothermal plasmas: collision cross section of helium atoms and ions for electrons," *Phys. Rev.*, vol. 100, pp. 1037–1046; November, 1955.

[5] J. M. Anderson and L. Goldstein, "Variation with electron energy of the collision cross section of helium for slow electrons," *Phys. Rev.*, vol. 102, pp. 933–938; May, 1956.

A Note on "Effects of Relatively Strong Fields on the Propagation of EM Waves Through a Hypersonically Produced Plasma"*

J. M. FISKIN† AND W. B. SISCO‡

THE comments of Anderson[1] regarding the typographical errors of B_2 and π, and the definition of $\bar{\nu}$, an effective collision frequency, for insertion into the classical equations are correct. The deviation in our simplified conductivity based on a mean velocity f_0 is, however, essentially 0.18 and not 0.82.

* Received by the PGAP, January 18, 1960.

† Douglas Aircraft Co., Santa Monica, Calif.

‡ National Engineering Science Co., Pasadena, Calif.; formerly with Douglas Aircraft Co., Santa Monica, Calif.

[1] J. M. Anderson, "A note on the relation between 'exact' and 'simplified' theories for Em wave propagation in ionized gases," this issue, pp. 337–338.

It is interesting to note that under the assumption $\omega^2\lambda^2 \gg \nu^2$ (equivalent to our $\omega^2\lambda^2 > v^2$) where ω is the angular frequency, λ is the mean-free path, and v is the velocity, the dependence of f_0, the velocity distribution on λ is removed. This allows values of λ that are functionally dependent on v to be conveniently handled in the expression for the conductivity as noted in (5) by Anderson.

A case in which a variation of λ with v can be handled quite easily without assumptions is the one in which v/λ or ν is a constant. Beginning with the expression of

Margenau[2] for f_1

$$f_1 = -\frac{\lambda}{v^2 + \omega^2\lambda^2}\cdot\frac{\partial f_0}{\partial v} \tag{1}$$

and taking,

$$\frac{v}{\lambda} = \nu = \text{constant},$$

$$f_1 = \frac{2n\nu A^2\sqrt{A}}{\pi\sqrt{\pi}(\nu^2 + \omega^2)}\, e^{-Av^2} \tag{2}$$

where,

$$A = \frac{m/2}{kT + \dfrac{M\gamma^2}{6(\nu^2 + \omega^2)}}$$

and

$$\gamma = \frac{eE}{m}.$$

[2] H. Margenau, "Conduction and dispersion of ionized gases," *Phys. Rev.*, vol. 69, pp. 508–513; May, 1946.

Here m is the mass of the electron, M is the mass of the positive ion, k is Boltzmann's constant, T is the temperature of the plasma, e is the charge of the electron, and E is the external applied field strength. The real part of the conductivity is then

$$\sigma_r = \frac{I}{E} = \frac{4\pi e\gamma}{3E}\int_0^\infty f_1 v^4 dv = \frac{ne^2}{m}\left(\frac{\nu}{\nu^2 + \omega^2}\right). \tag{3}$$

This is, of course, the classical expression for the conductivity of a gas which is identical with the exact expression when v/λ is a constant. Eqs. (1), (2), and (3) thus constitute a very simple proof of the conditions[3] under which the classical expression is valid.

We wish to express our appreciation to Dr. Anderson for pointing out the typographical errors and the definition of an effective $\bar{v}$ that may be used in the classical expression for the conductivity.

[3] E. Everhart and S. C. Brown, "The admittance of high frequency gas discharges," *Phys. Rev.*, vol. 76, pp. 839–842; September 1, 1946.

A Reciprocity Theorem for Nonperiodic Fields*

G. GOUBAU†

THE reciprocity theorem, first derived by H. A. Lorentz in 1895, formulates a general relation between two arbitrary electromagnetic fields of stationary sources of the same frequency, within an arbitrary space which does not include the sources of the fields. The space may contain dielectric and conductive bodies of isotropic or even anisotropic media, provided the tensors ϵ, μ and σ are symmetrical. The reciprocity theorem is usually written in the form:

$$\int_S \{E_1 \times H_2 - E_2 \times H_1\}\cdot ndS = 0 \tag{1}$$

where E_1, H_1 and E_2, H_2 are the complex amplitude vectors of the two fields, having both the same time factor $e^{j\omega t}$. The integration is performed over the entire surface S bounding the considered space. S may be composed of several closed surfaces; for instance, surfaces to exclude the sources from the space of integration. In cases where the space is unbounded, one part of S is a sphere whose radius approaches infinity.

The integrand in (1) represents a complex vector R which is a function of ω:

$$R(\omega) = E_1(\omega) \times H_2(\omega) - E_2(\omega) \times H_1(\omega). \tag{2}$$

Since (1) is satisfied for any frequency, it is satisfied also for the Fourier transform of $R(\omega)$ that is

$$R(t) = \int_{-\infty}^{+\infty} R(\omega)e^{j\omega t}d\omega. \tag{3}$$

Thus, the reciprocity theorem of (1), when transformed into the time domain, reads:

$$\int_S R(t)ndS = 0. \tag{4}$$

In order to perform the Fourier transformation of $R(w)$, we consider $E_1(\omega)$, $H_1(\omega)$, and $E_2(\omega)$, $H_2(\omega)$ as Fourier components of the fields $E_1(t)$, $H_1(t)$ and $E_2(t)$, $H_2(t)$ having arbitrary time dependence:

$$E_1(\omega) = \frac{1}{2\pi}\int_{-\infty}^{+\infty} E_1(\tau)e^{-j\omega\tau}d\tau \text{ etc.} \tag{5}$$

* Manuscript received by the PGAP, August 17, 1959. Presented at the 1958 URSI-IRE Fall Meeting, Pennsylvania State University, University Park, Pa.; October 21–22.

† U. S. Army Signal Research and Development Laboratory, Fort Monmouth, N. J.

This is permissible since every Fourier component of a field satisfies Maxwell's equations with the boundary conditions. Replacing $E_1(\omega)$, $H_1(\omega)$ by their Fourier transforms, we can write $R(t)$ in the form

$$R(t) = \frac{1}{2\pi}\int_{\omega=-\infty}^{+\infty} e^{j\omega t}\int_{\tau=-\infty}^{+\infty}\{E_1(\tau)\times H_2(\omega) - E_2(\omega)\times H_1(\tau)\}e^{-j\omega\tau}d\tau d\omega. \quad (6)$$

If we integrate first over ω and consider that

$$\int_{-\infty}^{+\infty} H_2(\omega)e^{j\omega(t-\tau)}d\omega = H_2(t-\tau);$$

$$\int_{-\infty}^{+\infty} E_2(\omega)e^{j\omega(t-\tau)}d\omega = E_2(t-\tau) \quad (7)$$

where $E_2(t)$ and $H_2(t)$ are the Fourier transforms of $E_2(\omega)$, $H_2(\omega)$, we obtain:

$$R(t) = \frac{1}{2\pi}\int_{-\infty}^{+\infty}\{E_1(\tau)\times H_2(t-\tau) - E_2(t-\tau)\times H_1(\tau)\}d\tau. \quad (8)$$

The integration at the right side of this equation is identical with the formation of the cross-correlation function between two time functions $f_1(t)$ and $f_2(-t)$. Therefore, $R(t)$ can be interpreted as a cross-correlation vector between the field vectors $E_1(t)$, $H_1(t)$ and $E_2(-t)$, $H_2(-t)$.

The reciprocity theorem in the time domain can thus be written in the form

$$\int_S\{\overline{E_1(\tau)\times H_2(-\tau)} - \overline{E_2(-\tau)\times H_1(\tau)}\}ndS = 0 \quad (9)$$

where the bars indicate the formation of the cross-correlation functions.

This theorem yields all the results which can be derived with the classical reciprocity theorem. However, it is more general in that it can be also extended to cases where one or both of the sources are moving. The classical theorem fails in this case because the field of a moving source is not periodic in the entire space, even if the source itself is periodic.

Before applying (9) to the case of moving sources, we consider a simple example, namely the case of the two resting dipoles.

We apply (9) to the entire space with the exclusion of small spheres around the dipoles $P_1(t)$ and $P_2(t)$. The infinitely remote boundary of the space does not contribute to the surface integral of (9), since the integrand is identically zero at infinity for any t and τ. Thus, the surface integral in (9) can be split into two parts:

$$\int_{S_1} R(t)ndS + \int_{S_2} R(t)ndS = 0 \quad (10)$$

where S_1 and S_2 are the surfaces of the spheres around the dipoles.

In order to evaluate the integrals of (10), we interchange the integrations over τ and S. The integration of S_1 and S_2 yield

$$\int_{S_1}\{E_1(\tau)\times H_2(t-\tau) - E_2(t-\tau)\times H_1(\tau)\}ndS = -E_2(t-\tau)\frac{\partial}{\partial\tau}P_1(\tau) + \frac{1}{3}\frac{\partial}{\partial\tau}(P_1(\tau)E_2(t-\tau))$$

$$\int_{S_2}\{\ \}ndS = -E_1(\tau)\frac{\partial}{\partial\tau}P_2(t-\tau) + \frac{1}{3}\frac{\partial}{\partial\tau}(P_2(t-\tau)E_1(\tau)). \quad (11)$$

The term containing the factor $\frac{1}{3}$ disappears when the integration over τ is performed, since $P_1(t)$ and $P_2(t)$ are zero for $t=\pm\infty$.

Thus, (10) becomes

$$-\int_{-\infty}^{+\infty} E_2(t-\tau)\frac{\partial}{\partial\tau}P_1(\tau)d\tau = \int_{-\infty}^{+\infty} E_1(\tau)\frac{\partial}{\partial\tau}P_2(t-\tau)d\tau. \quad (12)$$

If we introduce on the left side the variable $t-\tau$, instead of the variable τ, the equation can also be written in the form:

$$\int_{-\infty}^{+\infty} E_2(\tau)\frac{\partial}{\partial\tau}P_1(t-\tau)d\tau = \int_{-\infty}^{+\infty} E_1(\tau)\frac{\partial}{\partial\tau}P_2(t-\tau)d\tau. \quad (13)$$

This equation shows at once that if P_1 and P_2 have the same time dependence, the same is true for the components of E_1 and E_2 measured in the direction of P_2 and P_1 respectively. We can formulate the result in the following manner:

Choose two arbitrary points A and B in space (Fig. 1) and assign them unit vectors t_1 and t_2, respectively,

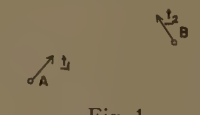

Fig. 1.

which indicate arbitrary directions in space. Place a time-variable dipole $P(t)$ at A in the direction of t_1 and record at B the component of the electric field $E(t)$ in the direction of t_2. Now place the same dipole at B in direction of t_2 and record at A the component of the electric field in the direction of t_1. Eq. (13) then states that the observed electric field components have in both cases identical amplitude and time dependence, no matter whether there is free space transmission between the two points or the transmission is affected by diffraction, refraction or reflection phenomena, provided ϵ, μ and σ of the matters involved are scalars or are characterized by symmetrical tensors.

This result is not at all new, although it has been derived in a different manner, However, the example will be helpful in the interpretation of the result which is obtained when the reciprocity theorem of the time domain, as formulated by (9) is applied to the case of movable sources. It must be remembered that (1) is based on the condition div $R(\omega)=0$ within the entire space bounded by the surface of integration. Similarly (9) is based on the condition div $R(t)=0$ within this space. This condition implies that the sources at no time enter into this space.

The space which is occupied by a moving source at one time or another is a cylinder, the cross-sectional dimensions of which are given by the size of the source and by the path length during the period of emission. Fortunately, the integration of $E\times H$ over the surface of such a volume can be transformed into an integration which is easily performed.

In the following, we assume for simplicity reasons that E_1, H_1 is the field of a source (Source I) fixed in space and E_2, H_2 that of a moving source (Fig. 2). The

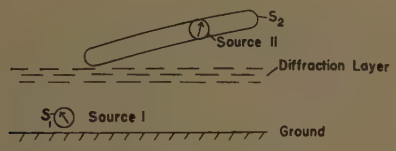

Fig. 2.

stationary source may be a transmitter located near the surface of the earth and the moving source (Source II) a transmitting satellite. The two sources may be separated by a refracting layer like the ionosphere, but we assume that there is no gyromagnetic effect involved which would invalidate (1).

As in the previous example, we apply (9) to the entire space, with the exception of a sphere around Source I and the cylindrical space occupied by the moving source. Eq. (9) can then be written in the form of (10), where S_1 is the surface of the sphere around Source I and S_2 the surface of the cylindrical space. In order to evaluate (10), we again perform first the integration over the two surfaces and then the integration over τ.

It is well known that for any distributed source (such as a radiating antenna structure) there is a multipole point source which yields the identical field at distances greater than the geometrical extension of the distributed source. If we replace Source II by such an equivalent source, the integral over S_1 in (10) obviously remains unchanged, because S_1 is beyond the geometrical extension of Source II. Therefore, with (10), the integral over S_2 must remain unchanged too. In the case of a moving point source, the space occupied by the source reduces to a filament-like space. If the integration is performed over the surface of this filament for any values of t and τ, only the near-field components of the source will contribute to the integral, because, at larger distances from the source, E_1, H_1 and E_2, H_2 can be considered constant along the circumference of a cross section of the filament. Therefore, the surface integral may be taken over a small sphere surrounding the equivalent point source.

Assume both sources radiate dipole fields. Then the evaluation of the surface integrals leads to the same expressions as if both dipoles were standing still; in other words, (13) is also applicable to the case of the moving source. However, $E_1(\tau)$ is now the field at the location of the dipole P_2 at the time $t-\tau$. $E_1(\tau)$ differs from the field which would be recorded by a receiver moving along with the source $P_2(\tau)$, because $P_2(t-\tau)$ corresponds to a movement of P_2 in the opposite direction. Thus, reciprocity in the usual sense does not exist any more if one of the sources is moving. Nevertheless, (13) formulates a relation for the mutual transmission between a moving and a resting source, which may be useful in certain instances.

Assume, for example, the hypothetical case that P_2 varies in time in such a manner that

$$\frac{\partial P_2(\tau)}{\partial \tau} = A\cdot\delta(\tau - t_1) \tag{14}$$

where δ represents a Dirac-pulse occurring at the time t_1. Then the right side of (13) becomes:

$$\int_{-\infty}^{+\infty} E_1(\tau)\frac{\partial}{\partial \tau}P_2(t-\tau)d\tau = -A\cdot E_1(t-t_1).$$

The correlation integral performed at the resting source [left side of (13)] is then proportional to the field of this source at the location where the pulse emission took place.

It shall be mentioned that (13) is restricted to velocities which are very small compared to the velocity of light. Otherwise, Lorentz transformation must be applied to the dipole field before (11) is evaluated.

The problem of a moving source can also be treated from the viewpoint of relativity theory. In this case, the total space is divided into two halves (Fig. 3), one half

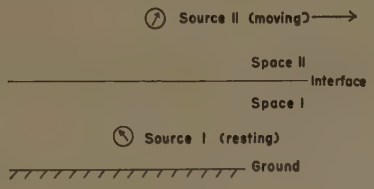

Fig. 3.

(Space I) containing the resting source (Source I) and the other half (Space II) containing the moving source (Source II). We assume a straight path for the moving source and a plane interface between the two half spaces parallel to this path. We furthermore assume that Space I contains no resting matter so that this space may be thought to be moving with the source.

The field of the source in the one space, when observed in the other space, is subjected to Lorentz transformation. The reciprocity relation (10) can be applied to each space. Each source is in rest with respect to its surrounding space. One surface of integration is the sphere around the source. The other surface is the interface between the two spaces. The problem is to find a relation between the two reciprocity integrals extended over the two sides of the interface. This problem is complicated for two reasons:

1) The integrals contain not only the field components which are parallel but also those which are perpendicular to the interfaces. The latter components are introduced by the Lorentz transformation.

2) τ being constant in one system means a progressive time in the other system.

If the velocity of the source is small compared to the velocity of light the relation simplifies and it is not very difficult to show that this kind of treatment yields the same result, *i.e.*, (13).

Concluding, it is apparent that the signal transmission between a satellite and a ground station is quite complicated, if studied in detail. The ordinary reciprocity in transmission is invalid, not only because of the gyromagnetic effects in the ionosphere but also because of the fact that a moving source is involved. The question as to the practical consequences requires further study.

Checking Design of Stepped Luneberg Lens*

H. F. MATHIS†

A PROCEDURE is presented in this note which may be used to check the design of a stepped Luneberg lens. This procedure is based on geometrical optics, using Snell's law and ignoring reflections.

In order to introduce the notation which will be used, a stepped Luneberg lens is shown in Fig. 1. It is assumed that all radii are normalized with respect to the radius of the lens. The steps are numbered from the outside toward the center. The ith step is bounded by $r=r_i$ and $r=r_{i-1}$. The index of the ith step is denoted by n_i. A ray is designated by its value of θ_0. Although only three steps are shown in Fig. 1, the procedure may be used for any finite number of steps.

It is well known and easy to derive from Snell's law that at any point $P(r, \theta)$ on the path of a ray,

$$nr \sin \phi = \sin \theta_0 \tag{1}$$

where n is the index of refraction at the point and ϕ is the angle between the path and the line OP. If follows from the law of sines and (1) that

$$\theta_2 - \theta_1 = \sin^{-1}\left(\frac{\sin \theta_0}{n_2 r_2}\right) - \sin^{-1}\left(\frac{\sin \theta_0}{n_2 r_1}\right). \tag{2}$$

Due to symmetry,

$$\theta_4 - \theta_3 = \theta_2 - \theta_1. \tag{3}$$

In Fig. 1, it may be observed that there is a minimum value of r for a specific ray. This minimum value of r is denoted by r^* and it must satisfy the equation

$$nr = \sin \theta_0. \tag{4}$$

* Received by the PGAP, December 28, 1959.
† Goodyear Aircraft Corp., Akron, Ohio.

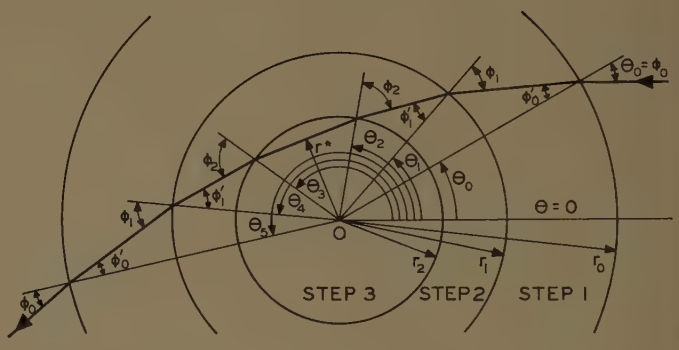

Fig. 1—A stepped Luneberg lens.

There may be more than one value of r which satisfies (4). If this is the case, the largest of these is the proper value of r to use for r^*. Let N denote the number of the step in which r^* is located. It follows from (1) and simple geometry that

$$\theta_3 - \theta_2 = 180° - 2 \sin^{-1}\left(\frac{\sin \theta_0}{n_3 r_2}\right). \tag{5}$$

A stepped lens with an assumed external focus at $(R_f, 180°)$ is considered first. An arbitrary ray, identified by θ_0, will go through the point (R_f, θ_x), where

$$\theta_x = 180° + 2\theta_0 - \sin^{-1}\left(\frac{\sin \theta_0}{R_f}\right) + 2\sum_{k=1}^{N-1} \sin^{-1}\left(\frac{\sin \theta_0}{n_k r_k}\right) - 2\sum_{k=1}^{N} \sin^{-1}\left(\frac{\sin \theta_0}{n_k r_{k-1}}\right), \tag{6}$$

with $r_0=1$. For an ideal lens, $\theta_x=180°$. If the assumed focus is located at $(R_f=1, 180°)$, an arbitrary ray goes through the point $(R_f=1, \theta_x)$, where

$$\theta_x = 180° + \theta_0 + 2\sum_{k=1}^{N-1} \sin^{-1}\left(\frac{\sin\theta_0}{n_k r_k}\right) - 2\sum_{k=1}^{N} \sin^{-1}\left(\frac{\sin\theta_0}{n_k r_{k-1}}\right). \quad (7)$$

A stepped lens with an assumed internal focus at $(R_f, 180°)$ is considered next. Let M denote the step in which the assumed focus is located. It may be found for some values of θ_0 that $R_f<r^*$, which indicates that the corresponding rays cannot go through the assumed focus. Other rays go through the points (R_f, θ_x), where

$$\theta_x = 180° + \theta_0 - \sin^{-1}\left(\frac{\sin\theta_0}{n_M R_f}\right) + \sum_{k=1}^{M-1} \sin^{-1}\left(\frac{\sin\theta_0}{n_k r_k}\right) - \sum_{k=1}^{M} \sin^{-1}\left(\frac{\sin\theta_0}{n_k r_{k-1}}\right) + 2\sum_{k=M}^{N-1} \sin^{-1}\left(\frac{\sin\theta_0}{n_k r_k}\right) - 2\sum_{k=M+1}^{N} \sin^{-1}\left(\frac{\sin\theta_0}{n_k r_{k-1}}\right). \quad (8)$$

If the point $(R_f, 180°)$ lies on a boundary between steps, it is convenient to assume that the point is in the inner step.

Since the angle θ_0 has all values for $-90°$ to $+90°$ and the lens has only a finite number of steps, it is impossible to design an ideal stepped Luneberg lens. Therefore, one must decide upon some allowable range for θ_x. If the range must be small, a large number of steps must be used.

A Note Concerning the Precise Measurements of Dipole Antenna Impedance*

SEYMOUR KREVSKY†

A RECENT discussion of an apparent anomaly in the measured values of reactance and other parameters of importance in the utilization of dipole type antennas at or near resonance[1] emphasizes the importance of refined techniques for precise measurement of dipole antennas. A perusal of the literature,[2–4] and some results of similar measurements made by others,[5–7] indicate the difficulty involved in obtaining data with a reliability grade of better than one per cent in a statistical as well as absolute sense.

One of the inescapable difficulties of this measurement problem is that arising from the apparent discontinuity that must exist between the external antenna and the driving transmission line.[8] It is noted that the physical measurements depend on the separation of the shunt driving point admittance into two parts, as it is treated theoretically,[9] that is, an antenna admittance and a shunt driving point terminal admittance. Fig. 1 shows a measured and a calculated curve for a particular whip antenna having an L/D ratio of 183 and a total length of 84 inches as used from 38 to 54 mc in a vehicular communications system.[5] It was found that an additional constant shunt network was required to provide a "best fit" of curves. The network elements consisted of a fixed resistance of 2850 ohms and a fixed capacitance of 12.15 $\mu\mu$f. Since "Q" meter measurements of the mast base showed a negligible shunt resistance and a capacitance of approximately 8 $\mu\mu$f, one must postulate the sources for the manifest values of these elements. First,

* Manuscript received by the PGAP, December 28, 1959.

† Surface Communications Systems Lab., RCA, New York, N. Y.

[1] L. Lewin, "A contribution to the theory of cylindrical antennas—radiation between parallel plates," IRE TRANS. ON ANTENNAS AND PROPAGATION, vol. AP-7, pp. 162–168; April, 1959.

[2] G. H. Brown and O. M. Woodward, "Experimentally determined impedance characteristics of cylindrical antennas," PROC. IRE, vol. 33, pp. 257–262; April, 1945.

[3] D. D. King, "The measured impedance of cylindrical dipoles," *J. Appl. Phys.*, vol. 17, pp. 844–852; October, 1946.

[4] S. Silver, "Microwave Antenna Theory and Design," M.I.T. Rad. Lab. Series No. 12, McGraw-Hill Book Co., Inc., New York, N. Y., ch. 15; 1949.

[5] S. Krevsky, "VHF Whip Antenna System Design," M.S. thesis in electrical engrg., Newark College of Engrg., Newark, N. J.; June, 1950.

[6] B. F. Barton, "The Design of an Efficient Wideband Antenna System," Engrg. Res. Inst., University of Michigan, Ann Arbor, Tech. Rept. No. 45; August, 1955.

[7] S. A. Schelkunoff, "Antenna theory and measurement," *J. Appl. Phys.*, vol. 15, pp. 54–60; January, 1944.

[8] R. W. P. King, "The Theory of Linear Antennas," Harvard University Press, Cambridge, Mass., ch. VIII, section 12; 1956.

[9] S. A. Schelkunoff, "Advanced Antenna Theory," John Wiley & Sons, Inc., New York, N. Y., ch. II, section 2.6; 1952.

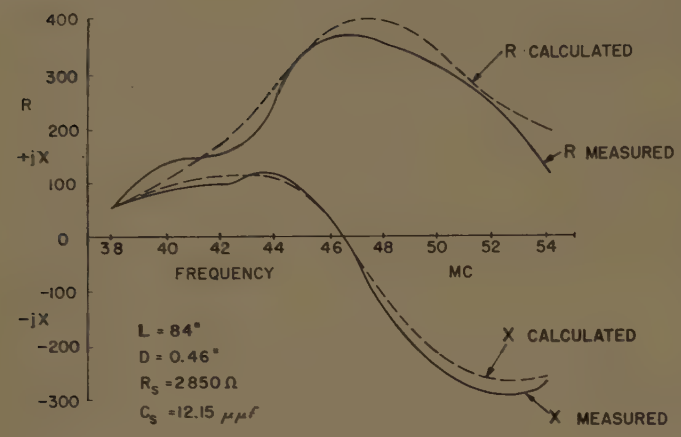

Fig. 1—Whip antenna impedance curves.

the finite shunt resistance is indicative of a small but real loss in the actual ground plane involved, *e.g.*, the soil at Coles Signal Laboratory, Fort Monmouth, N. J. Secondly, the additional shunt capacitance is indicative not only of the terminal effects discussed[2,7,8] but is also due to the effect of the imperfect ground with a finite dielectric constant, reflecting an imperfect image whose effective length must be less than that which a perfect ground reflects to the driving point.

Nevertheless the point made here is to the nature of the additional shunt elements affecting the correlation between measured and computed cylindrical dipole input impedance.

The second objective of this note relates to a technique used for improving the precision of measurements of this type. There is one principal precaution that can be taken to eliminate many otherwise cumulative sources of error that is apparently not covered in the literature. This precaution is the calibration of the driving transmission line by open and short circuit measurement.[10] It has been found that presumably constant characteristic impedance cable such as RG9B/U shows periodicity of as much as 5 per cent in amplitude in 5 mc periods at VHF in characteristic impedance, phase velocity and net attenuation. If these deviations from the mean accepted values are not accounted for, they reflect large errors into the indicated antenna driving point impedance measurement. The calibration of the driving cable wipes out all anomalies behind it, eliminating the source of a whole set of cumulative errors.

Three conclusions are drawn from the information given above. First, it is an extremely difficult problem to correlate a computed dipole input impedance to measurements made even in a controlled environment. Secondly, assuming complete control of all parameters, including the anomalies of the reflected image across the driving point as well as the precise data on the behavior of the driving transmission line at the driving point, it may well be possible to describe, to a statistically satisfactory degree, the correlation between measured and computed dipole input impedances.

Finally it is concluded that it is of importance to pursue the details of this correlation in light of the possibility of the existence of the anomaly referenced by L. Lewin.[1]

[10] W. L. Everett, "Communications Engineering," second edition McGraw-Hill Book Co., Inc., New York, N. Y., pp. 168–175; 1937.

Fresnel Region Field Distributions of Circular Aperture Antennas*

MING-KUEI HU†

IN the study of field distributions of linearly-polarized uniform phase plane aperture antennas,[1] the following formula[2] or a slightly different form given by Silver[1] may be used:

$$E(x, y, z) = \frac{jk}{4\pi}\int_A F(\xi, \eta)\,\frac{e^{-jkr_0}}{r_0}\left(1 + \frac{z}{r_0}\right)dA, \qquad (1)$$

where

$E(x, y, z)$ = the complex magnitude (amplitude and phase) of the electric field intensity at the field point (x, y, z)

$F(\xi, \eta)$ = the illumination at the point $(\xi, \eta, 0)$ in the aperture A. For uniform phase illumination, $F(\xi, \eta)$ can be taken as a real function of ξ and η,

$$r_0 = \sqrt{(x-\xi)^2 + (y-\eta)^2 + z^2}$$

$$k = \frac{2\pi}{\lambda} \quad \text{with} \quad \lambda = \text{the wavelength.}$$

In this communication, it is assumed that the aperture is circular and the illumination is of circular symmetry.

* Manuscript received by the PGAP, December 3, 1959. This work is a part of a project sponsored by Rome Air Development Center under Contract No. AF 30(602)-928.

† Elec. Engrg. Dept., Syracuse University, Syracuse, N. Y.

[1] S. Silver, "Microwave Antenna Theory and Design," Mass. Inst. Tech. Rad. Lab. Ser., McGraw-Hill Book Co., Inc., New York, N. Y., vol. 12, pp. 170–173; 1949.

[2] M. K. Hu, "Study of Near-Zone Fields of Large Aperture Antennas," Syracuse University Res. Inst., Syracuse, N. Y., Final Rept., pt. 2; April, 1957.

Fresnel Region Approximation

For a circular aperture of radius a, (1) can be rewritten as

$$E(r, \theta, \phi) = \frac{jk}{4\pi}\int_0^{2\pi}\int_0^a F(\rho, \phi')\frac{e^{-jkr_0}}{r_0}\left(1+\frac{r}{r_0}\cos\theta\right)\rho d\rho d\phi', \quad (2)$$

where (r, θ, ϕ) and $(\rho, \pi/2, \phi')$ are the spherical coordinates of the field point and source point respectively, and

$$r_0 = \{(r\sin\theta\cos\phi - \rho\cos\phi')^2 + (r\sin\theta\sin\phi - \rho\sin\phi')^2 + (r\cos\theta)^2\}^{\frac{1}{2}}.$$

The evaluation of the integral in (2) is very difficult without further approximation. In order to facilitate its evaluation, different approximations are generally used. Depending upon the approximation used, the result may be classified as the far field approximation, the Fresnel region approximation, etc. The most widely used approach to such approximations is to expand the distance r_0, appearing in the exponential, into a power series involving r and θ. The truncated series, obtained by neglecting all terms of order higher than one or two, is generally considered as the far field approximation or the Fresnel region approximation. As far as the remaining r_0's under the integral sign are concerned, much less accurate approximations are satisfactory. If the field point in consideration is not too close to the aperture and θ is not too large, then the factor $1/r_0(1+r/r_0\cos\theta)$ can be approximated to good accuracy by using the relation

$$\frac{1}{r_0}\left(1+\frac{r}{r_0}\cos\theta\right) \cong \frac{2}{r}. \quad (3)$$

A rather different approach to the Fresnel region approximation is used in this communication. Instead of using the truncated power series expansion, the well-known Newton's iteration formula for finding square root of a given number is employed. This formula has the following special property. If an approximation B_1 of $\sqrt{A}$ is known to be correct to n significant figures, then the approximation B_2 of $\sqrt{A}$, obtained by using the iteration formula

$$B_2 = \frac{1}{2}\left(B_1 + \frac{A}{B_1}\right), \quad (4)$$

will be correct to $2n$ significant figures. If this formula is applied to the approximation of r_0 in Fresnel region, with r as the first approximation, we have simply

$$r_0 \cong r - \rho\sin\theta\cos(\phi-\phi') + \frac{\rho^2}{2r}. \quad (5)$$

This approximation of r_0 gives a simpler form than that given by Silver,[1] but it is by no means less accurate. This particular form makes possible the analytical evaluation of such integrals. The use of Newton's formula is not limited to circular apertures; it applies just as well for antennas of any other shape.

Fresnel Region Field Distributions

With circular symmetric aperture illumination, $F(\rho, \phi')$ may be written as $F(\rho)$, and $E(r, \theta, \phi)$ as $E(r, \theta)$. Using the approximations given by (3) and (5), (2) gives:

$$E(r, \theta) = jk\frac{e^{-jkr}}{r}\int_0^a F(\rho)J_0(k\rho\sin\theta)e^{-jk(\rho^2/2r)}\rho d\rho. \quad (6)$$

If a normalized variable ζ is defined as

$$\zeta = \frac{\rho}{a}, \quad (7)$$

then (6) becomes

$$E(r, \theta) = jka^2\left(\frac{e^{-jkr}}{r}\right)\int_0^1 F(\zeta)J_0(u\zeta)e^{-j(\gamma/2)\zeta^2}\zeta d\zeta, \quad (8)$$

where

$$u = ka\sin\theta \quad \text{and} \quad \gamma = \frac{ka^2}{r}. \quad (9)$$

For aperture illumination of the following general form,

$$F(\zeta) = (1-\zeta^2)^n, \qquad n = 0, 1, 2, \cdots. \quad (10)$$

The author found that $E(r, \theta)$ can be expressed in terms of a new class of function $W_0^n(\gamma, u)$, as

$$E(r, \theta) = e^{-jkr}(\gamma e^{j(\pi-\gamma)/2})\cdot W_0^n(\gamma, u), \quad (11)$$

with

$$W_0^n(\gamma, u) = \int_0^1 (1-\zeta^2)^n J_0(u\zeta)e^{j(\gamma/2)(1-\zeta)^2}\zeta d\zeta. \quad (12)$$

Some properties of $W_0^n(\gamma, u)$ will be given in the next section.

Eq. (11) gives the Fresnel region field of a circular aperture with illumination of the special form $(1-\zeta^2)^n$. It is clear that this includes the uniformly illuminated aperture as a special case. For nonuniform illumination of the more general type, it is possible to express the field as a sum of the fields of the above special forms.[2] Field distribution curves (both amplitude and phase) due to illumination of these special forms are given in reference 2 for $n=0, 1, 2, 3, 4$ and

$$r = \frac{1}{4}\left(\frac{D^2}{\lambda}\right), \frac{1}{3}\left(\frac{D^2}{\lambda}\right), \frac{1}{2}\left(\frac{D^2}{\lambda}\right), \left(\frac{D^2}{\lambda}\right), 2\left(\frac{D^2}{\lambda}\right) \text{ and } \infty.$$

Only the case of uniform illumination, *i.e.* $n=0$, is given in Figs. 1 and 2 of this communication.

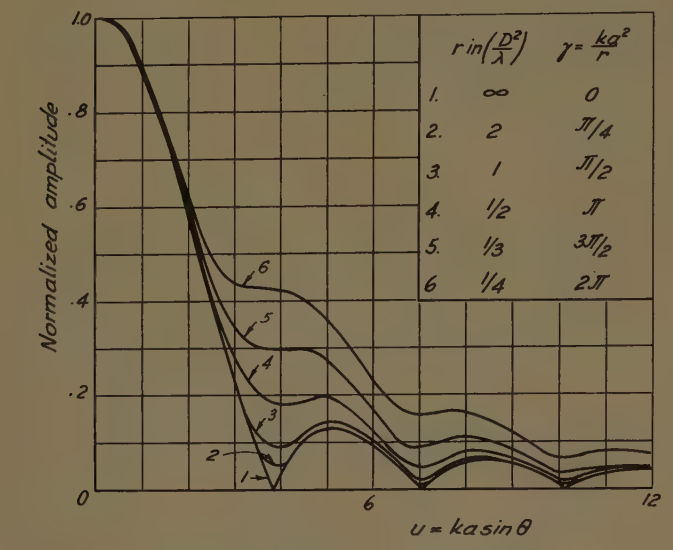

Fig. 1—Normalized Fresnel region amplitude distribution curves from a uniformly illuminated circular aperture.

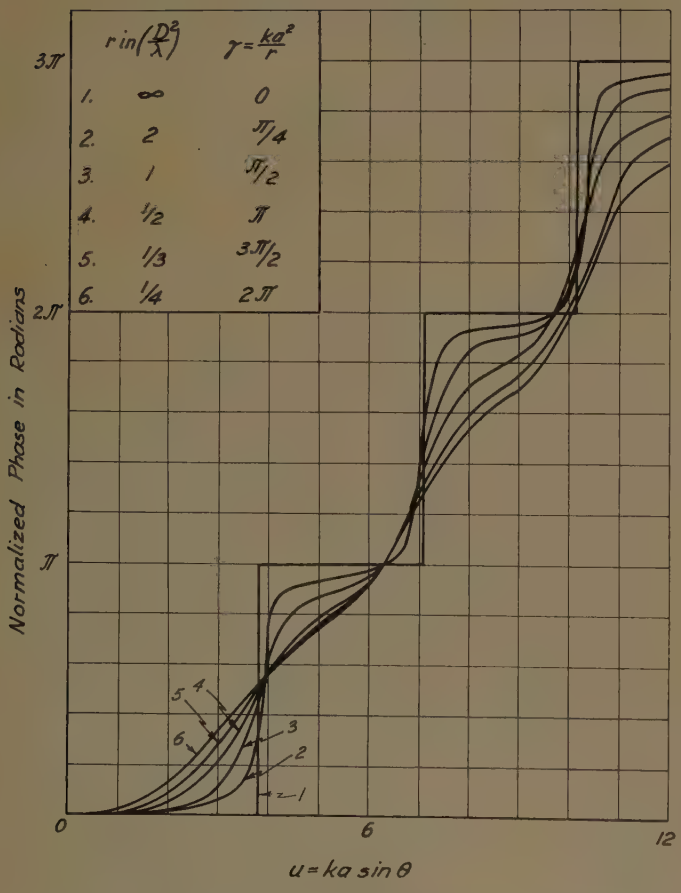

Fig. 2—Normalized Fresnel region phase distribution curves from a uniformly illuminated circular aperture.

Some Properties of $W_0^n(\gamma,u)$

The new function $W_0^0(\gamma, u)$ can be expressed in terms of the following two Lommel's functions of two variables as

$$W_0^0(\gamma, u) = \frac{U_1(\gamma, u)}{\gamma} + j\frac{U_2(\gamma, u)}{\gamma}. \tag{13}$$

These two Lommel's functions,[3] $U_1(\gamma, u)$ and $U_2(\gamma, u)$, are usually given either in integral forms as

$$U_1(\gamma, u) = \gamma \int_0^1 J_0(u\zeta) \cos\frac{\gamma}{2}(1-\zeta^2)\cdot\zeta d\zeta,$$

$$U_2(\gamma, u) = \gamma \int_0^1 J_0(u\zeta) \sin\frac{\gamma}{2}(1-\zeta^2)\cdot\zeta d\zeta, \tag{14}$$

or in series forms, in terms of Bessel functions, as

$$U_1(\gamma, u) = \left(\frac{\gamma}{u}\right)J_1(u) - \left(\frac{\gamma}{u}\right)^3 J_3(u) + \left(\frac{\gamma}{u}\right)^5 J_5(u) - \cdots,$$

$$U_2(\gamma, u) = \left(\frac{\gamma}{u}\right)^2 J_2(u) - \left(\frac{\gamma}{u}\right)^4 J_4(u) + \left(\frac{\gamma}{u}\right)^6 J_6(u) - \cdots. \tag{15}$$

For $n>0$, it is found that the following recurrence relation holds:

$$W_0^{n+1}(\gamma, u) = \frac{2}{j}\frac{\partial}{\partial\gamma} W_0^n(\gamma, u). \tag{16}$$

By repeated applications of this relation, we have

$$W_0^n(\gamma, u) = \left(\frac{2}{j}\right)^n \left\{\frac{\partial^n}{\partial\gamma^n}\frac{U_1(\gamma, u)}{\gamma} + j\frac{\partial^n}{\partial\gamma^n}\frac{U_2(\gamma, u)}{\gamma}\right\}. \tag{17}$$

Highly convergent series expansions for $W_0^n(\gamma, u)$ can be derived from (15) and (17). These series can then be used for numerical evaluation.

Justifications of the results and statements appearing in this communication and some other results were given by this author.[2] In that report, near-zone and Fresnel region fields of large aperture antennas other than circular ones were also treated.

[3] G. N. Watson, "A Treatise on the Theory of Bessel Functions," Cambridge University Press, Cambridge, Mass., second ed., pp. 537, 540; 1952.

On the Beam Deviation Factor of a Parabolic Reflector*

Y. T. LO†

IN a parabolic reflector antenna, the scanning can be achieved for a range by displacing the feed in the focal plane without resorting to a costly steerable mechanism for the whole antenna system. It is well-known that the range of scan by this method is limited by the increasing coma and astigmatism. However, it is still widely used in some specific applications. It is not the intention of this paper to investigate the aberrations of such a system, which may be referred to elsewhere, but rather to derive a formula for another characteristic of interest, namely the beam deviation factor. Such a formula does not seem to appear in literature, although there are available some experimental results for specific cases.

The beam deviation factor has been defined as the ratio of the beam deflection angle Θ_b to the angular displacement of the feed Θ_f, both measured from the axis of the reflector with the vertex as origin. Let the feed be at F' at a distance d from the focus F and let d be much smaller than the focal length f; then with a certain plausible approximation, the field at $P(R, \Theta\Phi)$, in Fig. 1 is given by

$$I = K \iint_A \frac{f(\phi, \theta)}{r} \cos [\beta\rho \sin \Theta \sin \Phi \sin \phi] \times \cos [\beta\rho(\sin \Theta \cos \Phi - d/r) \cos \phi] \rho d\phi d\rho, \quad (1)$$

where (ρ, ϕ, z) or (r, θ, ϕ) are the coordinates of a typical point q of integration.

K is a proportional constant, including the inverse R factor and the phase delay function due to r and R; A is the aperture of the reflector, *i.e.*, for $\rho = 0$ to $D/2$ (D = diameter), and $\phi = 0$ to 2π,

$r = f \sec^2 \theta/2$, and

$f(\phi, \theta)$ is the primary pattern of the feed.

If the plane containing F' is defined as one for which $\Phi = 0$ and π, the maximum of I must appear in the same plane, since in practice $f(\theta, \phi)$ is real and positive for q in A. Thus if the maximum of I, I_m, occurs at Θ_m,

$$I_m = K \iint_A \frac{f(\phi, \theta)}{r} \cos [\beta\rho(\sin \Theta_m - d/r) \cos \phi] \rho d\phi d\rho, \quad (2)$$

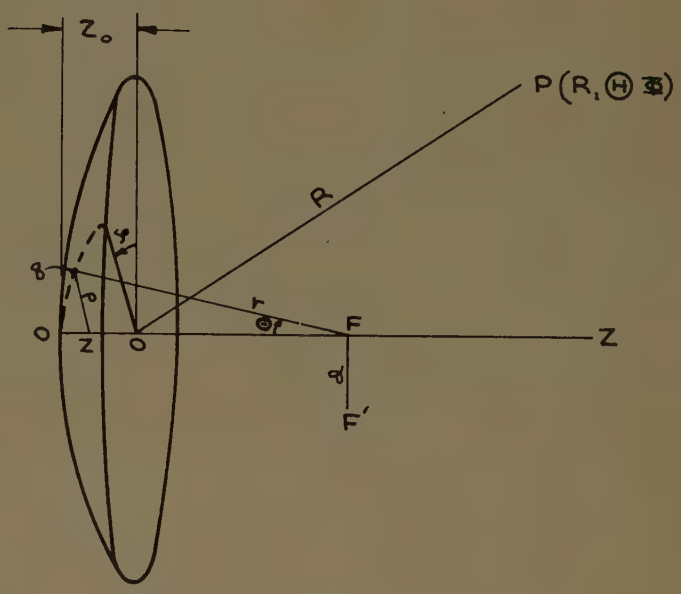

Fig. 1—Geometry of the reflector.

and Θ_m satisfies the following equation:

$$\iint_A \frac{f(\phi, \theta)}{r} \sin [\beta\rho(\sin \Theta_m - d/r) \cos \phi] \beta\rho^2 \cdot \cos \phi d\phi d\rho = 0. \quad (3)$$

Since for (ρ, ϕ) in A, $f(\phi, \theta) > 0$, and

$$\sin [\beta\rho (\sin \Theta_m - d/r) \cos \phi] \cos \phi$$

is a continuous function of ρ and ϕ. This equation will be satisfied

$$\sin [\beta\rho (\sin \Theta_m - d/r) \cos \phi] \equiv 0$$

for some (ρ, ϕ) in A, by invoking mean value theorem for integrals. As $d = 0$, the first condition can be met with $\Theta_m = 0$, as expected. Were r a constant the condition could still be satisfied with $\Theta_m = \sin^{-1} d/r$. Now r is a variable with a range from f to $f + Z_0$ where Z_0 = the depth of the dish. Therefore, it will be expected that in general there are many solutions of Θ_m to satisfy this second condition. For the maximum of the main beam, as shown in Fig. 2, the following inequality must be satisfied:

$$(1 + Z_0/f)^{-1} d/f < \sin \Theta_b < d/f.$$

It is easily seen that for a shallow dish Θ_b can be determined accurately without going to the complicated

* Manuscript received by the PGAP, February 8, 1960. This work was supported in part by Westinghouse Electric Corp., Baltimore, Md., during 1957.
† University of Illinois, Urbana, Illinois.

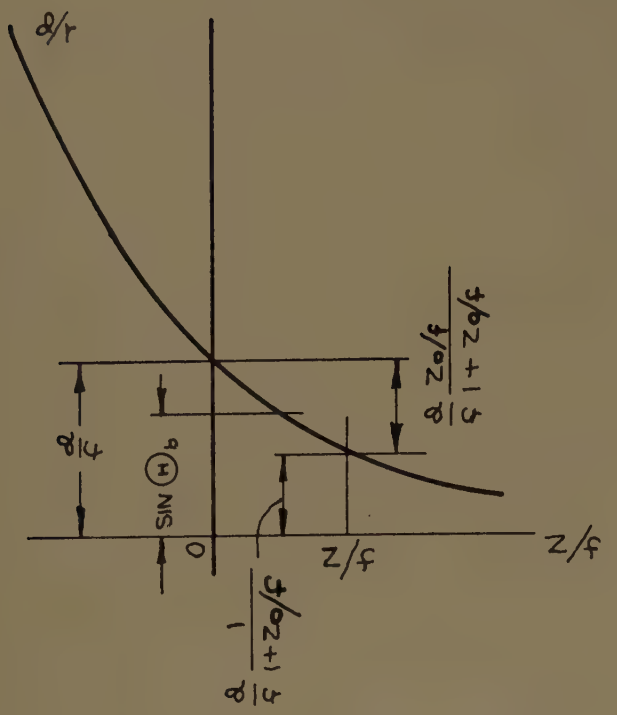

Fig. 2—The range of $\sin \Theta_b$ which is a portion of the hyperbola d/r.

integration in (3). Now we can write

$$\sin \Theta_b = \frac{d}{f}\left(\frac{1}{1 + Z_0/f} + k\,\frac{Z_0/f}{1 + Z_0/f}\right)$$

$$= \frac{d}{f}\,\frac{1 + kZ_0/f}{1 + Z_0/f} = \frac{d}{f}\,\frac{1 + k(D/4f)^2}{1 + (D/4f)^2}, \qquad (4)$$

where $k < 1$. Or

$$\frac{\sin \Theta_b}{\tan \Theta_f} = \frac{1 + k(D/4f)^2}{1 + (D/4f)^2}. \qquad (5)$$

If the usual definition of the beam deviation factor (BDF) is used,

$$\text{BDF} = \frac{\Theta_b}{\tan^{-1} d/f} = \frac{\sin^{-1}\left[\dfrac{d}{f}\,\dfrac{1 + k(D/4f)^2}{1 + (D/4f)^2}\right]}{\tan^{-1} d/f}$$

$$\approx (\text{BDF})_0\left\{1 + \tfrac{1}{3}(d/f)^2\left[\tfrac{1}{2}(\text{BDF})_0^2 + 1\right] + O(d/f)^4\right\},$$

where

$$(\text{BDF})_0 = \frac{1 + k(D/4f)^2}{1 + (D/4f)^2}. \qquad (6)$$

It is seen that by the usual definition the BDF, up to the approximations assumed so far, depends also upon (d/f).[1]

Although k is a function of f, D, f (θ, ϕ), its value is not critical, especially for large f/D as seen from (5) and (6). From one experimental point (or computation) it should be possible to predict the rest as a function of f/D with good accuracy. In Fig. 3, there shows the

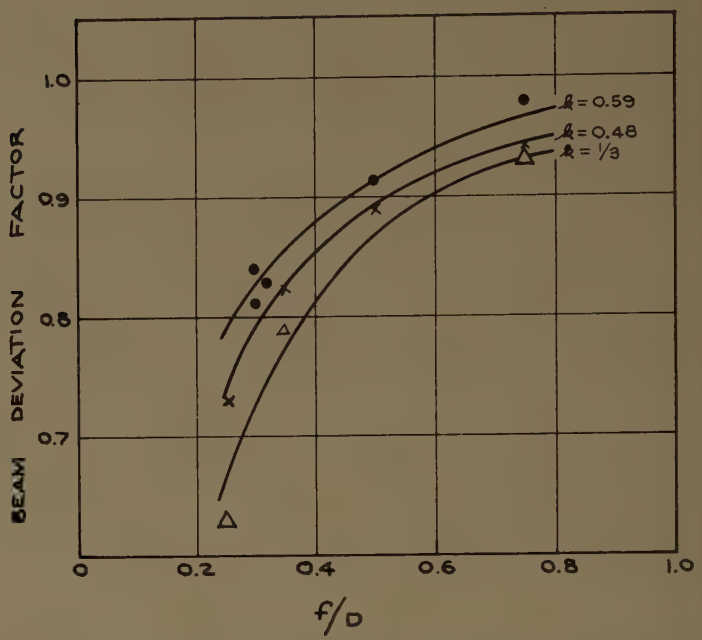

Fig. 3—Beam deviation factor as a function of f/D. Experimental data: Silver and Pao: ●; Keller and Coleman: x20-db taper, Δ 10-db taper; computed curve: ———.

computed curves and the experimental results by Silver and Pao,[2,3] and by Kelleher and Coleman.[1] For the former, there is no information available for f (θ, ϕ) function, and $k = 0.59$ is established by its point where $f/D = 0.5$. For the latter, one case has a 10-db tapering, the other 20 db with $k = \frac{1}{3}$ and 0.48 respectively. The extraction of the experimental data from Kelleher and Coleman's report is rather difficult because they measured for various values of Θ_b, those indicated here being for $\Theta_b = 2 \times$ beamwidth. It seems that one can conclude that the values of k are from about 0.3 to 0.7, and that k becomes larger with higher tapering, as expected.

A second method to determine Θ_b is by assuming that the system is circularly symmetrical and $f(\theta, \phi) = \cos^n \theta$.

[1] K. S. Kelleher and H. P. Coleman, "Off-Axis Characteristics of the Paraboloidal Reflector," NRL Rept. No. 4088, Washington, D. C.; December, 1952.

[2] S. Silver and C. S. Pao, "Paraboloid Antenna Characteristics as a Function of Feed Tilt," Rad. Lab. Rept. No. 479, Cambridge, Mass.; 1944.

[3] S. Silver, "Microwave Antenna Theory and Design," Rad. Lab. Ser., McGraw-Hill Book Co., Inc., New York, N. Y., vol. 12, p. 487; 1949.

In this case (3) becomes

$$\int_0^{D/2} \frac{\cos^n\theta}{1+(\rho/2f)^2} J_1\left[\beta\rho\left(\sin\Theta_b - \frac{d/f}{1+(\rho/2f)^2}\right)\right] \cdot\rho^2 d\rho = 0. \quad (7)$$

Since

$$\rho' \equiv \rho/2f = \tan\theta/2,$$

$$\cos^n\theta = (1-\rho'^2)^n(1+\rho'^2)^{-n}.$$

It does not seem that (7) can be evaluated in a closed form. However, by using the series-expansion for the Bessel Function it can be integrated term by term since the integrand involves algebraic functions only. Suppose that D is so small that only the first term is significant; then

$$\Theta_b = \sin^{-1}\frac{d}{f}\left[1 - \frac{2}{3}\frac{Z_0}{f} + k'\left(\frac{Z_0}{f}\right)^2\right]$$

$$= \sin^{-1}\frac{d}{f}\left[1 - \frac{2}{3}\left(\frac{D}{4f}\right)^2 + k'\left(\frac{D}{4f}\right)^4\right], \quad (8)$$

where $k' = 1/2, 13/18, 15/18$ for $n = 0, 2, 3$, respectively. For small d/f, the first term corresponds to the reflection by a flat sheet, and the remaining terms appear as a result of the curvature of the reflector. If the result in (4) is expanded in Z_0/f and compared with (8), it will be found that $k = \frac{1}{3}$, a value we obtained before. It may also be mentioned that the same method can be carried out if the illumination function $f(\theta)$ be any polynomial in ρ, such as $(1-\rho^2)^n$ type.

Contributors

P. S. Carter, Jr. (S'48–A'50–M'56) was born on May 23, 1926, in Marion, Mass. He received the B.E.E. degree from Cornell University, Ithaca, N. Y., in 1948. From Stanford University, Stanford, Calif., he received the M.S. degree in 1952 and the Ph.D. degree in 1954, both in electrical engineering.

P. S. Carter

From 1949 to 1950 he was a laboratory instructor in electronics at Stanford. From 1948 to 1949 he was employed by Airborne Instruments Laboratories, Inc., in Mineola, Long Island, where he was engaged in the research and development of flush-mounted aircraft antennas. In 1950 he joined the staff of Stanford Research Institute. His work at the Institute has included research in the development of airborne direction-finding antenna systems, studies of radio-frequency properties of rocket exhaust gases, and investigations of mutual impedance properties of electronically-scanned antenna arrays. From 1958 to 1959 he was employed by Lockheed Missile and Space Division, Sunnyvale, Calif., where he was engaged in research in solid-state microwave applications. In June, 1959 he returned to the Institute, where he is continuing this research.

Dr. Carter is a member of the Scientific Research Society of America, and the American Physical Society.

❖

David K. Cheng (S'44–A'48–M'48–SM'50–F'60) was born on January 10, 1918, in Kiangsu, China. He received the B.S.E.E. degree from the National Chiao-Tung University, Shanghai, China, in 1938, and the M.S. and Sc.D. degrees from Harvard University, Cambridge, Mass., in 1944 and 1946, respectively. While at Harvard, he was a Charles Storrow Scholar and a Gordon McKay Scholar.

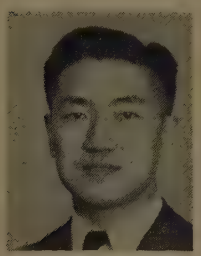

D. K. Cheng

From 1938 until he came to the U. S. in 1943, he was an engineer at the Central Radio Corporation of the National Resources Commission of China. In 1946 he joined the Communications Laboratory of the USAF Cambridge Field Station, Cambridge, Mass., as an electronics engineer and, later, as a project engineer. Since 1948 he has been on the faculty of Syracuse University, Syracuse, N. Y., where he now a professor of electrical engineering. He also has been a project director for antenna research projects contracted through the Syracuse University Research Institute.

Dr. Cheng is a member of the American Society for Engineering Education, Sigma Xi, and Eta Kappa Nu.

❖

Walter L. Curtis (S'51–M'55) was born on May 11, 1931, in Seattle, Wash. He received the B.S. degree and the M.S. degree in electrical engineering from the University of Washington, Seattle, in 1953 and 1958, respectively.

W. L. Curtis

During 1953 he worked part time at the University of Washington wind tunnel and designed and built a servo-operated automatic positioning control for use in the tunnel. While attending graduate school in 1954, he was employed as a Research Fellow at the University of Washington Experiment Station on a study of radio propagation. During the summer of 1954, he worked on instrumentation for the wind tunnel at Boeing Airplane Co., Seattle, Wash.

In 1955, he joined the Physical Research Staff of the Boeing Airplane Co., and has been engaged in research and development on aircraft antennas. Mr. Curtis is presently working for the Antenna Research Group of the Electronic Sciences Section.

❖

Seymour Edelberg was born on November 21, 1923, in Brooklyn, N. Y. He received the B.E.E. degree from the College of the City of New York in 1944; the M.E.E. degree in 1947 and the D.E.E. degree in 1953, both from the Polytechnic Institute of Brooklyn, Brooklyn, N. Y. From 1944 to 1947 he was at Haskins Laboratory working on electronic aids for the blind. From 1947 to 1949 he was a research fellow at the Microwave Research Institute of P.I.B. At the Sperry Gyroscope Company during the period 1949 to 1952 he was part of a group doing research and development on microwave components, and from 1952 to 1955 he was employed at the Balco Laboratories where he was responsible for the microwave and antenna efforts.

S. Edelberg

Since 1955, he has been with the M.I.T. Lincoln Laboratory, Lexington, Mass., where he has done research in the antenna and electromagnetic scattering fields, and is currently working in the area of plasma physics. He is assistant group leader of the Electromagnetics group.

Dr. Edelberg is a member of the American Physical Society, A.A.A.S., Sigma Xi, and Eta Kappa Nu.

❖

Allen R. Edison (M'59) was born in Plainview, Neb. on September 21, 1926. He received the B.S. and M.S. degrees in electrical engineering from the University of Nebraska, Lincoln, in 1950 and 1957, respectively.

A. R. Edison

From 1944 to 1946 he served as an electronic technician with the U. S. Navy and from 1950 to 1953 he was an engineer for the Silas Mason Company at the Iowa Ordnance Plant, Burlington. In 1953 he joined the staff of the electrical engineering department at the University of Nebraska where he is an assistant professor. For two years he has been on leave of absence from the University of Nebraska while doing graduate work and working as a research associate at the University of New Mexico, Albuquerque.

Mr. Edison is a member of Pi Mu Epsilon, Eta Kappa Nu, Sigma Tau, Sigma Xi and the AIEE.

❖

Warren L. Flock (S'42–A'44–M'54) was born in Kellogg, Idaho on October 26, 1920. He received the B.S.E.E. degree from the University of Washington, Seattle, in 1942, and the M.S.E. E. degree from the University of California, Berkeley in 1948.

W. L. Flock

From 1942 to 1945, he was a staff member of the Radiation Laboratory, Massachusetts Institute of Technology, Cambridge. At present he is an associate engineer and lecturer in the Department of Engineering, University of California, Los Angeles, where his work has been in the areas of radio-wave propagation, plasmas, and natural resources. During the summer of 1958, he served as an electronics engineer in the Radio Propagation Engineering Division, National Bureau of Standards, Boulder, Colo.

Mr. Flock is a member of AIEE, Tau Beta Pi, and Sigma Xi.

W. D. Hershberger (A'37–SM'45–F'54) was born on May 10, 1903 in Wellman, Iowa, He received the B.A. degree in mathematics from Goshen College, Goshen, Ind. in 1927, the M.A. degree in physics from George Washington University, Washington, D. C., in 1930, and the Ph.D. degree in electrical engineering from the University of Pennsylvania, Philadelphia, in 1937.

W. Hershberger

From 1927 to 1931, he was employed in the Sound Division at the Naval Research Laboratory, Washington, D. C., working in ultrasonics for submarine detection. From 1931 to 1936 he was engaged in short wave and microwave work for radio detection at the Signal Corps Laboratories, Fort Monmouth, N. J. From 1937 to 1942 he was employed in the Research Laboratories of RCA, Camden, N. J., and from 1942 to 1949 at RCA Laboratories in Princeton, N. J. He was active in the development of the altimeter and obstacle detection equipment operative in flight in 1937. During this period he contributed to the fields of radar, microwave spectroscopy, frequency stabilization with ammonia absorption lines, and paramagnetic resonance. Since 1949 he has served as professor of engineering at the University of California, Los Angeles, working in electromagnetic theory, paramagnetic resonance, and plasma research. From 1955 to 1956 he attended the University of Leiden, The Netherlands, as a Fulbright research scholar.

Dr. Hershberger holds fifty patents. He is a member of the AAAS, the American Physical Society, Tau Beta Pi and Sigma Xi.

❖

Dwight E. Isbell (A'55) was born on May 23, 1929, in Seattle, Wash. He received the B.S. degree in physics at the University of Illinois, Urbana, and is currently completing the requirements for the M.S. degree in electrical engineering at the University of Washington, Seattle.

D. E. Isbell

He has been engaged in the field of antenna research and development since 1950, and was with Dorne & Margolin Inc., Westbury, N. Y., for approximately five years. As chief project engineer his efforts were devoted to the design of aircraft communication antennas and direction finder systems. He spent three years at the University of Illinois doing research on broadband antennas. He has recently rejoined Boeing Airplane Company, Seattle, Wash., as a research specialist with the Electro-Dynamics Staff of Transport Division, having previously worked in the Boeing Physical Research Unit on problems related to radome research during 1951 and 1952.

The University of Illinois has filed two of his patent applications on the design of logarithmically periodic antennas.

❖

Julius A. Kaiser, Jr. (S'48–A'50–M'53) was born in Washington, D. C. on February 26, 1920. He received the B.S. degree in engineering from the University of Maryland, College Park, in 1948.

J. A. Kaiser

From 1948 to 1955, he was a member of the RF Research Branch at the Naval Research Laboratory, Washington, D. C., where he was engaged in the development of millimeter wavelength components. In 1955, he joined the Microwave Antenna and Components Branch at the same establishment, doing research and development in microwave antennas. Currently Mr. Kaiser is located at the Diamond Ordnance Fuze Laboratories, Washington, D. C., working on antenna problems.

❖

Isadore Katz (SM'56) was born in Philadelphia, Pa., on October 21, 1916. He received the B.S. degree in physics and mathematics from Temple University, Philadelphia, Pa., in 1937.

I. Katz

From 1938 until 1941 he worked for the U. S. Weather Bureau, in Philadelphia, Pa., and Tucson, Ariz. In 1942 he joined the staff of Massachusetts Institute of Technology Radiation Laboratory, Cambridge, Mass., where he was engaged in research in radiometeorological problems. In 1946 he joined the Naval Research Laboratory, Washington, D. C., where he did research on microwave propagation and atmospheric physics. Since 1952 he has been with the Applied Physics Laboratory of Johns Hopkins University, Silver Spring, Md., where he is studying various phases of radar propagation and atmospheric turbulence.

Mr. Katz is a member of the American Physical Society and a professional member of the American Meteorological Society.

❖

Erik J. Kirkscether (A'53–M'56–SM'59) was born January 5, 1924 in Oslo, Norway. He received the B.S. degree in 1942 in Oslo and from 1943 to 1945 studied at the Technical University of Norway (communication engineering). He worked until 1948 at A/S Elektrisk Bureau of Oslo as a draftsman. From 1949 to 1951 he was with Compañía Cotelma, Buenos Aires, Argentina, engaged in design of pneumatic tube conveyer systems. From 1951 to 1954 he was employed at Transradio Internacional, Buenos Aires, on research and development, especially concerning rhombic antennas. In 1954 he joined the Argentine Armed Forces Research Laboratory (Laboratorio de Electrónica y de Comunicaciones, Instituto de Investigaciones Científicas y Técnicas de las Fuerzas Armadas), where he is now the head of the Antenna Section. His principal work has been in the field of VHF and microwave antennas, and related fields.

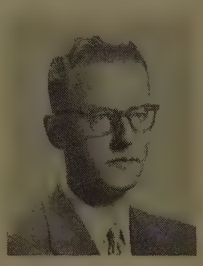

E. J. Kirkscether

❖

Michael Leichter was born in Bucharest, Rumania, on March, 20, 1922. He received the B.S. degree in 1948 from the City College of New York, and the Ph.D. degree from Ohio State University, Columbus, in 1952, both in physics.

M. Leichter

From 1952 to 1953, he taught at Alabama Polytechnic Institute, Auburn, and from 1953 to 1954 he was Fulbright Lecturer at the University of Ceylon.

Since 1954 he has worked in the fields of electromagnetic scattering, random processes and antenna theory. He is presently employed at the System Development Corporation, Santa Monica, Calif.

Dr. Leichter is a member of the American Physical Society.

❖

Mark T. Ma (S'58) was born in Kiangsu, China, on March 21, 1933. He received the B.S.E.E. degree from the National Taiwan University, Taiwan, China, in 1955, and afterwards taught there until 1956 when he came to the U. S. He received the M.S.E.E. degree from the University of Illinois, Urbana, in 1957.

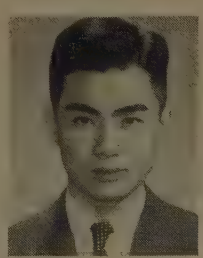

M. T. Ma

From 1957 to 1958, he was employed by the IBM Laboratory, Poughkeepsie, N. Y. He is now employed as a research engineer in the Department of Electrical Engineering of Syracuse University, Syracuse, N. Y.

Richard C. Mackey (S'50–A'53–M'57) was born in Los Angeles, Calif. on July 27, 1926. He received the B.S.E.E. degree in 1950 and the M.S. degree in 1952, both from the University of California, Los Angeles.

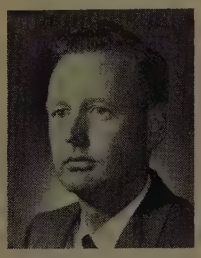

R. C. MACKEY

Mr. Mackey was employed at the University of California as a research engineer and associate in engineering from 1950 through 1956. His work concerned the properties of materials at microwave frequencies including gas spectroscopy, paramagnetic resonance, frequency stabilization and instrumentation. From January, 1957 to February, 1958 he was a member of the technical staff of the Ramo-Wooldridge Corp., Los Angeles, working in the area of electronic countermeasures. Since February, 1958 he has been with the University of California, Los Angeles, as assistant professor of engineering, and has been advising in the fields of microwave instrumentation, electronic countermeasures and counter-countermeasures at Space Technology Laboratories, Los Angeles, Calif.

Mr. Mackey holds two patents. He is a member of Tau Beta Pi and Sigma Xi.

❖

Richard K. Moore (S'43–A'46–M'50–SM'54) was born on November 13, 1923 in St. Louis, Mo. He received the B.S. degree in electrical engineering at Washington University, St. Louis, Mo. in 1943 and the Ph.D. degree from Cornell University, Ithaca, N. Y., in 1951 after doing graduate work both at Cornell and at Washington. He also attended the Bowdoin College-M.I.T. Navy Radar School, Brunswick, Me., during the war.

R. K. MOORE

During 1943 and 1944 he was a test equipment engineer with the RCA Victor Division in Camden, N. J. He then entered the Navy and served as Communication and Electronics Officer of the U.S.S. *Rehoboth* (AVP-50). He was an instructor and research engineer at Washington University from 1947 to 1949 and research associate at Cornell from 1949 to 1951. He served as research engineer and section supervisor in the field of radar terrain return and radio propagation at Sandia Corporation in Albuquerque, New Mexico from 1951 to 1955. He taught evening graduate courses at the University of New Mexico, Albuquerque, from 1953 to 1955, at which time he became Associate Professor and Acting Chairman of the Department of Electrical Engineering. He is currently professor and Chairman of the Department of Electrical Engineering at the University of New Mexico.

Dr. Moore is a member of the AIEE, the ASEE, Sigma Xi, Tau Beta Pi, and Sigma Tau. He is a member of Commission II (radio and troposphere) of the U.S.A. National Committee of URSI.

❖

Shigeo Nishida was born in Nagoya, Japan, on March 7, 1924. He graduated from Tohoku University, Sendai, Japan, in 1949, and received the Doctor of Engineering degree in 1959.

S. NISHIDA

From 1949 to 1955, he was a research assistant at the Research Institute of Electrical Communication at Tohoku University, and since 1955 he has been an assistant professor at the latter. Two years, 1957 to 1959, were spent as a research associate at the Microwave Research Institute of the Polytechnic Institute of Brooklyn. New York, N. Y., where his major interests were in microwave waveguide and antenna problems.

Mr. Nishida is a member of Sigma Xi and the Institute of Electrical Communication of Japan.

❖

Arthur A. Oliner (M'47–SM'52), for a photograph and biography please see page 443 of the October, 1959, issue of these TRANSACTIONS.

❖

Joseph H. Provencher was born in Lawrence, Mass., on January 19, 1923. He attended Merrimack College, Andover, Mass., and received the A.B. degree in physics from Boston University, Boston, Mass., in 1953. From 1952 to 1959, he was a member of the Ground Antenna Section of the Antenna Laboratory of Air Force Cambridge Research Center, where he worked on the development of microwave antennas at the Ipswich, Mass., test site.

J. H. PROVENCHER

He joined the U. S. Navy Electronics Laboratory, San Diego, Calif., in 1959 and is presently a member of the microwave components section working on the design of fixed scanning arrays for the radar branch. Mr. Provencher is also working towards the M.A. degree in physics at San Diego State College.

❖

L. M. Spetner (SM'57) was born in St. Louis, Mo., on January 17, 1927. He received the B.S.M.E. degree from Washington University, St. Louis, Mo., in 1945, and the Ph.D. degree from Massachusetts Institute of Technology, Cambridge, Mass., in 1950.

L. M. SPETNER

He was a lecturer in the Department of Applied Mechanics at Washington University from 1946 to 1947, and during that time also worked as a research engineer on missile guidance and control problems with the Washington University Research Foundation. During the summer of 1948 he worked in the servomechanism group at Emerson Electric Co., St. Louis, Mo. From 1949 to 1950 he was a research assistant at Massachusetts Institute of Technology and, later, a research associate. From 1951 to the present he has been a physicist with the Applied Physics Laboratory of Johns Hopkins University, Silver Spring, Md., where he has been engaged in research in electromagnetic propagation and noise theory.

Dr. Spetner is a member of the American Physical Society and Tau Beta Pi, and an associate member of Sigma Xi.

❖

Billie D. Warner (S'56–M'58) was born in El Dorado, Kan. on April 11, 1930. He attended Wichita University, Wichita, Kan., from 1953 to 1955, and in 1957 received the B.S. degree in electrical engineering from the University of Oklahoma, Norman.

B. D. WARNER

From 1957 to 1958 he was a component engineer at the Sperry Utah Engineering Laboratory, Salt Lake City. Since 1958, he has been a research assistant in radar terrain return studies at the University of New Mexico, Albuquerque.

Mr. Warner is a member of Eta Kappa Nu, Tau Beta Pi, Sigma Tau, and an associate member of Sigma Xi.

PROCEEDINGS OF THE URSI INTERNATIONAL SYMPOSIUM ON ELECTROMAGNETIC THEORY, Toronto, Canada, JUNE 15-20, 1959

PGAP members and subscribers are urged to order their copies now, accompanied by remittance made payable to The Institute of Radio Engineers, 1 East 79th Street, New York 21, N.Y., at the following rates:

	Price per Copy
PGAP Members	$ 8.00
Other IRE Members	$12.00
Libraries	$12.00
Nonmembers	$16.00

AVAILABLE BACK ISSUES OF IRE TRANSACTIONS ON ANTENNAS AND PROPAGATION

PUBLICATION	PRICES		
	Group Members	IRE Members	Non-* Members
Vol. AP-2, No. 2, April, 1954	$2.00	$3.00	$6.00
Vol. AP-4, No. 4, Oct., 1956	$2.10	$3.15	$6.30
Vol. AP-5, No. 1, Jan., 1957	$3.20	$4.80	$9.60
Vol. AP-5, No. 2, April, 1957	$1.75	$2.60	$5.25
Vol. AP-5, No. 3, July, 1957	$2.00	$3.00	$6.00
Vol. AP-5, No. 4, Oct., 1957	$1.70	$2.55	$5.10
Vol. AP-6, No. 1, Jan., 1958	$3.85	$5.80	$11.55
Vol. AP-6, No. 2, April, 1958	$1.15	$1.75	$3.45
Vol. AP-6, No. 3, July, 1958	$2.40	$3.60	$7.20
Vol. AP-6, No. 4, Oct., 1958	$1.50	$2.25	$4.50
Vol. AP-7, No. 1, Jan., 1959	$2.50	$3.75	$7.50
Vol. AP-7, No. 2, April, 1959	$1.75	$2.60	$5.25
Vol. AP-7, No. 3, July, 1959	$1.75	$2.60	$5.25
Vol. AP-7, No. 4, Oct., 1959	$2.55	$3.85	$7.65
Vol. AP-7, SS†, Dec., 1959	$8.00	$12.00	$16.00

* All Libraries and Subscription Agencies may purchase at the IRE Member rate.

† Special supplement.

INSTITUTIONAL LISTINGS

The IRE Professional Group on Antennas and Propagation is grateful for the assistance given by the firms listed below, and invites application for Institutional Listing from other firms interested in the field of Antennas and Propagation.

AERO GEO ASTRO CORP., 1200 Duke St., Alexandria, Va.
Research and Development; Antennas; Transponders; Command Receivers; Augmenters; Telemetry-Radar.

ANDREW CORPORATION, 363 E. 75th St., Chicago 19, Ill.
Antennas, Antenna Systems, Transmission Lines, Development and Production.

ANTLAB, INC., 6330 Proprietors Rd., Worthington, Ohio
Antenna Pattern Range Systems—Recorders & Mounts.

BLAINE ELECTRONETICS, INC., 14757 Keswick St., Van Nuys, Calif.
Antennas, Paraboloids, Scale Models, Antenna Radiation Pattern Measurement Towers.

DEVELOPMENTAL ENGINEERING CORP., 1001 Conn. Ave. N.W., Washington, D. C. and Leesburg, Va.
Research, Development, Installation of Antennas and Antenna Equipment for Super Power Stations.

GABRIEL ELECTRONICS, Division of The Gabriel Company, Main & Pleasant Sts., Millis, Mass.
Research, Engineering and Manufacture of Antenna Equipment for Government and Industry.

I-T-E CIRCUIT BREAKER CO., Special Products Div., 601 E. Erie Ave., Philadelphia 34, Pa.
Design, Development and Manufacture of Antennas, and Related Equipment.

JANSKY & BAILEY, INC., An Affiliate of Atlantic Research Corp.,
1339 Wisconsin Ave., N.W., Washington, D. C.
Complete Engineering Services for Antennas and Propagation Programs.

MARK PRODUCTS CO., 6412 W. Lincoln Ave., Morton Grove, Ill.
Multi Element Grid Parabolas, Antennas for Two-Way Communications, R & D.

THE W. L. MAXSON CORP., 475 Tenth Ave., New York 18, N.Y.
Research, Development, & Manufacture of Airborne, Missile & Ordnance Systems & Equipment.

TRANSCO PRODUCTS, INC., 12210 Nebraska Ave., Los Angeles 25, Calif.
Res., Design, Dev., & Mfr. of Antenna Systems & Components for Missile, Aircraft & Ground Installations.

WEINSCHEL ENGINEERING COMPANY, INC., Kensington, Md.
Antenna Pattern Receivers; Bolometer Amplifiers; Modulated Microwave Sources;
Insertion Loss Measuring Systems; Calibrated Attenuators.

WHEELER LABORATORIES, INC., Great Neck, N. Y.; Antenna Lab., Smithtown, N. Y.
Consulting Services, Research and Development, Microwave Antennas and Waveguide Components.

The charge for Institutional Listing is $25 for one issue or $100 for six consecutive issues (one year). Application may be made to the Technical Secretary, The Institute of Radio Engineers, 1 East 79th Street, New York 21, N. Y.